A Simple Strategy for Dynamic Substructuring and its Application to Soil-Foundation-Structure Interaction

by

Aikaterini Stefanaki

February 1, 2017

A dissertation submitted to the

Faculty of the Graduate School of the

State University of New York at Buffalo

in partial fulfillment of the requirements for the degree of

Doctor of Philosophy

Department of Civil, Structural and Environmental Engineering

Acknowledgements

First and foremost, I would like to express my sincere gratitude to my advisor Professor Mettupalayam Sivaselvan whose continuous support and guidance made the completion of this dissertation possible. His enthusiasm, scholarship and attention to detail has set an example I hope to match some day.

I would also like to thank my committee members for reviewing this work. Specifically, I would like to extend my gratitude towards Professor Andrew Whittaker for his support throughout my studies and Professor Amjad Aref for his support during the course of the experimental work performed for the purposes of this study. I would also like to thank Professor Tarunraj Singh for his insightful comments on control design and Professor Anthony Tessari for his significant contributions in the geotechnical aspects of this work.

I also wish to thank the faculty of the CSEE department who taught and inspired me through their dedication and hard work. Especially, I would like to thank Professor Michael Constantinou, Professor Andrei Reinhorn, Professor Panos Anastasopoulos and Professor Andreas Stavridis for their help and support throughout my studies.

I would also like to gratefully acknowledge the contribution of Dr. Eric Stauffer for providing me with a software for modal identification based on eigenrealization algorithm, which facilitated the identification of the testbed used for the experiments presented in this work.

Many thanks also go to the SEESL staff, Mr. Mark Pitman, Mr. Scot Weinreber, Mr. Robert Staniszewski, Mr. Lou Moretta, Mr. Jeffrey Cizdziel, Mr. Christopher Budden and Mr. Chris Zwierlein, for their significant contribution in the conduction of the experiments.

Their expertise and hard work made this dissertation possible. Importantly, I gratefully acknowledge the contributions of late Duane Kozlowski who passed during the early stages of this work.

Many thanks go to the CSEE staff Ms. Margaret Poniatowski, Ms. Kellie Stanchak, Ms. Eva Mcgovern and Ms. Sarah D'Iorio for their assistance during my studies at UB.

This work was made possible with financial support from MCEER. It was also partly supported by a University at Buffalo RENEW seed grant and a National Science Foundation grant. These contributions are gratefully acknowledged.

I am also grateful to my colleagues and friends at UB. Especially, I would like to thank my good friends Dr. Yannis Kalpakidis, Dr. Chandu Bolisetti, Dr. Katerina Ziotopoulou, Ms. Revekka Papagianni, Ms. Danai Constantinou, Dr. Ioannis Karampelas, Mr. Alexis Nikellis and Dr. Ifigeneia Marinou for their encouragement and support.

Last but not least, I wish to thank my parents Stefanos and Zampia, my sister Andriani and my husband Kostis, for their love, support and encouragement throughout my life and studies. This dissertation is dedicated to them.

Contents

List of Figures

List of Tables

Abstract

Dynamic substructuring (DS), also known as hybrid simulation, is an experimental method used to study the dynamic behavior of complex engineering systems. Models are created that consists of two parts actively interacting during the experiment, (i) a physical subsystem - an experimental component representing a portion of a system and (ii) a virtual subsystem - a computer model the remainder of the system. Since only the key components need to be physically constructed, this form of simulation results in reduced costs and more effective use of the laboratory equipment. Furthermore, using this approach, the properties of the virtual subsystem can be easily varied, providing for a means of readily performed parametric studies in the laboratory. During DS experiments, the interface conditions between the two subsystems are imposed using actuators and the response of the physical subsystem is measured using sensors and fed back to the computer model. Accurate control design is required to achieve a stable feedback system and ensure that the effect of the virtual subsystem is represented accurately during the experiment.

DS has been extensively studied in recent years in the earthquake engineering field. The approaches conventionally used involve development of a tracking controller and delay compensators to account for actuator dynamics. Due to the complicated control design required in these approaches, DS has been limited to relatively modest configurations.

In the current study, DS is approached using a strategy conceptually different from the conventional methods, aimed at challenging configurations such as the Soil-Foundation-Structure-Interaction (SFSI). The new strategy is characterized by simplicity of control design decoupled from the physical subsystem, and results in robustly stable and accu-

rate testing. Experiments were performed using a specially designed versatile testbed to demonstrate the effectiveness of this strategy. Moreover, preliminary, proof of concept, experiments of the SFSI DS were performed, showing the feasibility of such experiments.

Chapter 1

Introduction

Dynamic substructuring (DS), also termed hybrid simulation and model-in-the-loop testing, refers to combining physical and virtual components to study the dynamic behavior of complex engineering systems. A physical subsystem, i.e. an experimental component, is coupled with a virtual subsystem, i.e. a computer model, and the two subsystems actively interact during an experiment. The interface conditions between the physical and virtual subsystems are effected by actuators, while the response of the physical subsystem is measured by means of sensors and fed back to the computer model. Proper controls are necessary to ensure that this feedback system is stable, and that the effect of the virtual subsystem is represented in the experiment sufficiently accurately. The main objective of the work presented here is to develop a simple and effective strategy for designing such controls, particularly aimed at challenging DS configurations such as the soil-foundation-structure interaction (SFSI) application shown in Figure 1.1.

In a DS experiment, the role of the virtual subsystem is to enact meaningful or realistic boundary conditions (or boundary impedances) on the physical subsystem; DS may therefore also be appropriately dubbed "active-boundary testing". Clearly, this adds value to experimentation when, and only when, such dynamic boundary conditions significantly influence the behavior of the physical subsystem. Since the components represented by the virtual subsystem need not actually be constructed, substructuring could reduce costs, and

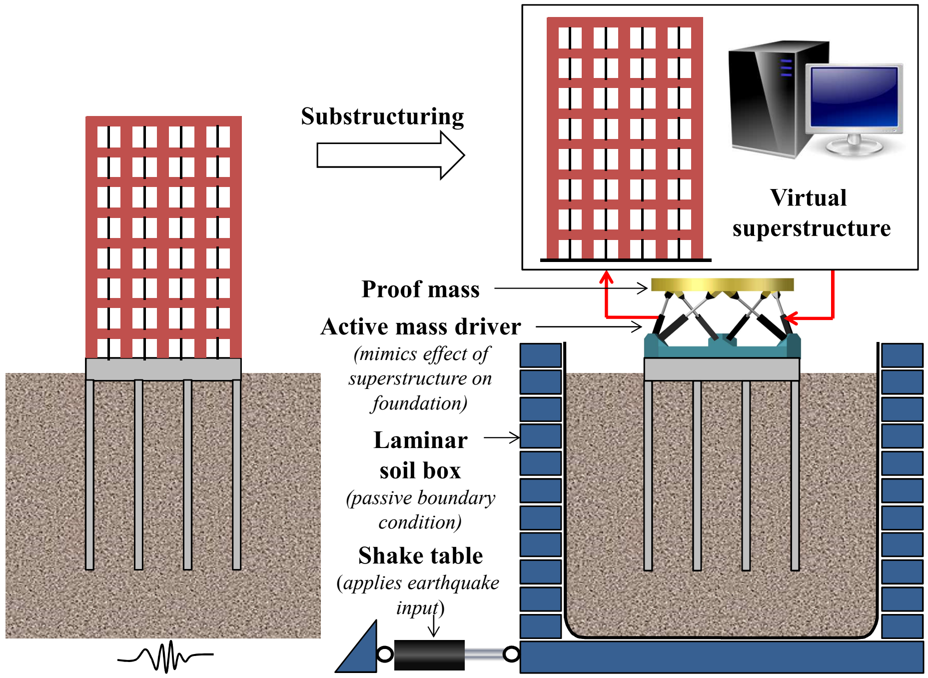

Figure 1.1: Example of dynamic substructuring (DS) concept — the soil-foundation system is the physical subsystem, the superstructure is the virtual subsystem

lead to more effective use of laboratory space and equipment.

DS has received considerable attention in the earthquake engineering field in recent years. Within earthquake engineering, DS originated as substructure pseudo-dynamic testing, motivated by thinking of the physical substructure as an "experimental finite element". Consequently, much of the work on DS has retained artifacts of this thinking; principally, a displacement- or force-tracking controller is so central in these conventional approaches that a number of recent publications related to DS are in fact on developing tracking controllers. Extending pseudo-dynamic substructuring to DS led to the need for delay-compensators. Thinking in terms of these components significantly complicates control design, and has therefore limited DS to relatively modest configurations and applications. A review on conventional approaches to DS and associated challenges is given in Chapter 2.

1.1 Scope and goals of this study

The strategy adopted in this work is conceptually different from the conventionally used approaches. A view akin to model-matching is considered, asking what the controller should be so that the interface actuator produces the same effect on the physical subsystem as the virtual subsystem would. This greatly simplifies the control design. For DS configurations with a single actuator and stable linear virtual substructures, the process is almost trivial. Importantly, the control design is decoupled from the physical substructure; in fact, how closely the actuator with control resembles the virtual subsystem can be tested independently of the physical subsystem. As demonstrated in Chapter 4, this strategy results in robustly stable and accurate DS. Although this strategy is applicable more generally, the main focus of the work reported here is on DS configurations such as shown in Figure 1.1, where interface conditions are effected by an active mass driver (AMD). The considered configurations mainly employ a one-degree-of-freedom (1DOF) AMD and stable linear virtual substructures. It should be noted that the specific AMD along with an elastomeric bearing assembly constitute a testbed which was specifically designed and constructed for the needs of this work, as described in Chapter 3.

In summary, the main goals of this work are:

- Development and characterization of a testbed to be used in DS applications
- Development of a strategy for DS testing which
  - is easy and simple enough to use, in comparison with conventional approaches
  - is robustly stable
  - enables an accurate representation of the virtual subsystem in the experiment
  - utilizes a control design independent of the physical subsystem
- Exploration of the applicability of the method in complex engineering systems, such as soil-foundation-structure-interaction systems

1.2 Dissertation organization

This dissertation is organized as follows. In Chapter 2, a review on conventional approaches to DS in earthquake engineering is presented, tracing their motivations to the origins of DS. The main ingredients of these approaches, the associated challenges and developed solutions are discussed.

To facilitate development and validation of the new DS strategy, an experimental testbed was constructed consisting of a uniaxial hydraulic shake table to serve as a 1DOF AMD, a resonant physical substructure, and hardware and software for controls. The architecture and design of this testbed and its detailed characterization through modeling and experiments are presented in Chapter 3.

Chapter 4 contains the main contribution of this work. Here, the new DS strategy is described, and its three essential features — simple control design, physical subsystem decoupling, and robust stability and accuracy, are demonstrated by means of shake table experiments using the 1DOF AMD and linear virtual substructures. Robustness is not discussed from a theoretical point of view, but rather by showing insensitivity to model variations in experiments. This chapter also contains a brief description of the path towards multi-input configurations and nonlinear virtual substructures.

Chapter 5 discusses a preliminary realization of the of the SFSI DS concept shown in Figure 1.1, using a 1DOF AMD. This is intended to be a proof of concept; design of the experiment is described and some interesting measurements are presented. Chapter 6 summarizes the conclusions and original contributions of this study.

Chapter 2

Background

This chapter discusses previous research on dynamic substructuring (DS), primarily in the earthquake engineering field, to provide context for the current work. A review of the evolution of DS that led to these approaches is presented, which consists of three ingredients — a tracking controller, a compensator and a time-integration scheme. Almost all DS strategies that can be found in the literature fall in this category, and these are called "conventional" in the following discussion. Developing algorithms within this framework has restricted the versatility of DS and its robustness in practical applications. The alternate approach presented in Chapter 4 departs from the conventional framework, resulting in much simpler control design, decoupling from the physical subsystem, and robust stability and accuracy.

2.1 Origins and evolution of substructuring

Experimental substructuring has been widely used in civil engineering testing applications during the last years. Seismic testing performed by (Reinhorn et al. [3] ; Shing et al. [4]) is an example.

The original conception of experimental substructuring in earthquake engineering was that of replacing one or more elements in a finite element model by physical elements. Mahin et al. [5] and Shing et al. [4] provide a comprehensive exposition of this approach. The intention then was that the physically constructed elements would have no rate-dependent behavior, and that all such effects would be represented in the computer model. This form of testing was therefore termed *substructure pseudo-dynamic* testing. The test could be performed arbitrarily slowly (*asynchronous pseudo-dynamic substructuring*) and therefore, actuator dynamics was not an issue. The only extraneous features of concern were measurement noise and disturbance. These were considered in the same light as numerical round off and truncation errors, using adaptations of time-integration schemes. Again motivated by the modus operandi of the finite element method, a desired displacement would be imposed on the physical substructure using an actuator driven in closed-loop position control, and the interface force would be measured and fed back to the computer model. A typical substructure pseudo-dynamic test is shown schematically in Figure 2.1. The origins of the important roles played by a displacement-tracking controller and a time-integration scheme in the finite-element way of thinking is clear. Real-time substructure pseudo-dynamic experiments were also performed later for cases where the rate-dependent behavior of the system was important, using modified time-integration algorithms. In this case, the testing can be categorized as *real-time pseudo-dynamic substructuring*.

Dynamic substructuring was the next logical step, to investigate systems for which the inertia effects of the physical subsystem cannot be accurately represented in a computer model. It is obvious that such experiments must be performed in real-time. The main challenge in these configurations is the compensation for the additional actuator dynamics. The specific method can be used to perform experiments on configurations such as the one shown in Figure 2.2, specified to test a soil-structure interface. In this case, while the foundation system and the surrounding soil is physically constructed, the superstructure is simulated computationally. The earthquake excitation of the soil and the foundation system is provided by an earthquake simulator (shake table) while the interface conditions with the superstructure are imposed by an actuator. In this experiment, the physical subsystem has inertia effects. In other words, it offers resistance not only to deformation and rate of

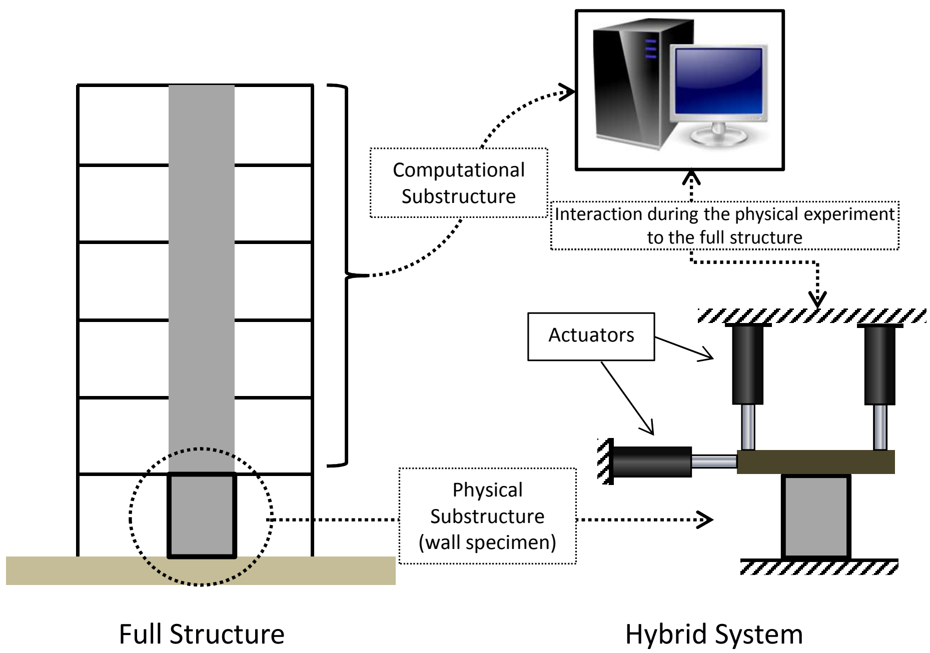

Figure 2.1: Schematic of a typical substructure pseudo-dynamic test configuration — suppose it is known from analyses or observations in past earthquakes that only a portion of the multi-story building could potentially suffer severe damage; substructuring allows just this critical portion to be physically constructed, and yet be tested as though it were part of the whole building.

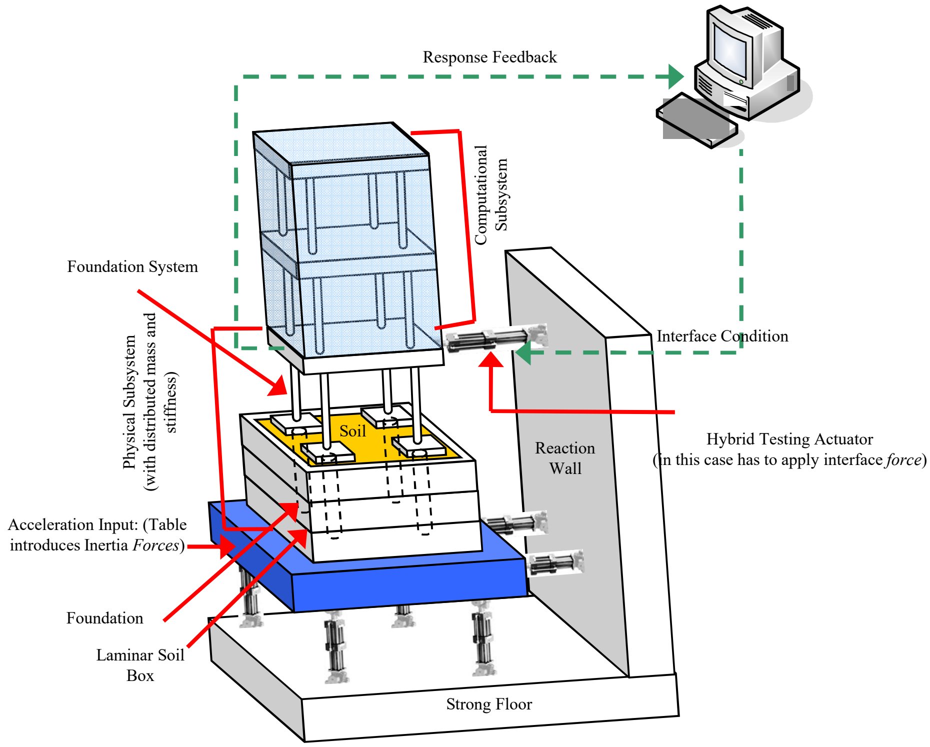

Figure 2.2: Dynamic substructuring example

deformation, but also to acceleration.

Following the above discussion, there are different forms of experimental substructuring evolved in the past years depending on the system of interest. The classification of these forms of substructuring is shown schematically in Figure 2.3.

2.2 Approaches on Substructuring Algorithms

As discussed above, experimental substructuring consists of physical and virtual substructures interacting with each other. An interface condition between the subsystems is imposed on the physical subsystem and the work conjugate of the imposed condition is measured and fed back to the computational subsystems. Referring to the examples discussed earlier, the applied condition in the example shown in Figure 2.1 is displacement and the measured work conjugate is force. In the setup shown in Figure 2.2, the applied condition is force and the measured quantity is displacement. If the full structure were built, the interface be-

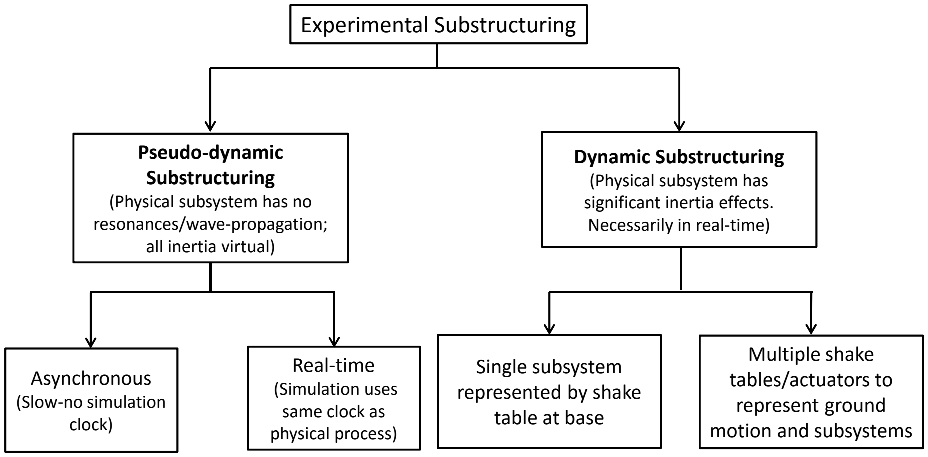

Figure 2.3: Experimental substructuring classification

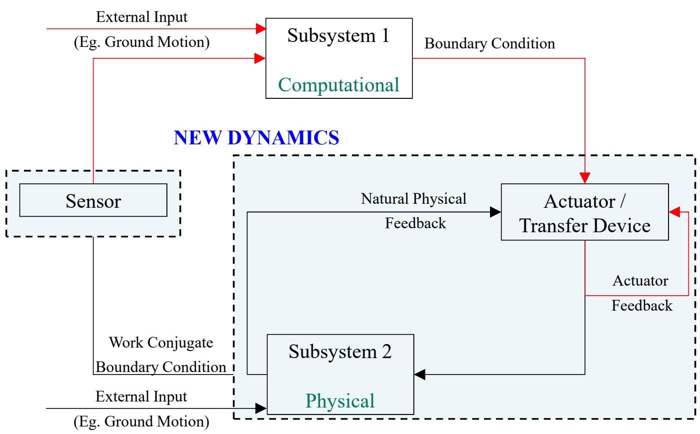

Figure 2.4: Additional dynamics in DS experiment

tween the substructures is intrinsic—the substructures impose power-conjugate conditions at the interface depending on their relative impedance. For example, the stiffer substructure would determine the velocity at the interface and the more flexible substructure, the force. Gawthrop et al. [6] introduce the bond graph approach to thinking about substructuring in this way in terms of impedances. For the hybrid system however, an actuator is required to impose the desired condition at the interface and sensors are needed to measure the power-conjugate interface condition. These components introduce their own dynamics. The concept of substructuring with the additional dynamics is illustrated in Figure 2.4.

Hence, in the hybrid system some features are introduced that are extraneous to both the full system and its mathematical model. More specifically, the additional features are: (1) the additional dynamics of the actuators and the transducers, (2) the natural feedback paths resulting from Newton's third law and those used to control the actuators to track their reference signals, (3) the measurement noise and (4) the external disturbance.

An algorithm for substructuring must be composed of two components: (a) simulation of the computational subsystem and (b) compensation for the dynamics of the actuator and servo-control system. Accordingly, algorithms for substructuring experiments have been developed from two perspectives. The first one is the *Numerical Analysis Approach*, in which a numerical method conventionally used to computationally simulate the entire system is also used for experimental substructuring. For example, when a finite element discretization along with a time integration scheme such as Newmarks method is used, the physical subsystem is viewed as a special finite element. Another approach is the *Control Systems Approach*, in which the hybrid test system is viewed as a feedback system. The computational model plays the role of a controller and the physical subsystem, that of a plant. Such a viewpoint allows more convenient stability and robustness analysis.

In general, depending on the challenges of the several types of substructuring, different approaches have been considered. Murray et al. [7], Shao et al. [8] and, recently, McCrum et al. [9] provide an overview and discuss the difficulties associated with such experiments. In the case of pseudo-dynamic testing, for instance, the challenges are mainly related to numerical errors, while in dynamic substructuring the main issue is the addition of the actuator dynamics in the system. The approaches that have been considered by researchers to overcome these difficulties are presented here. However, it should be noted that it is not desired to produce an exhaustive literature review, rather than to create a broad classification of the different approaches on experimental substructuring.

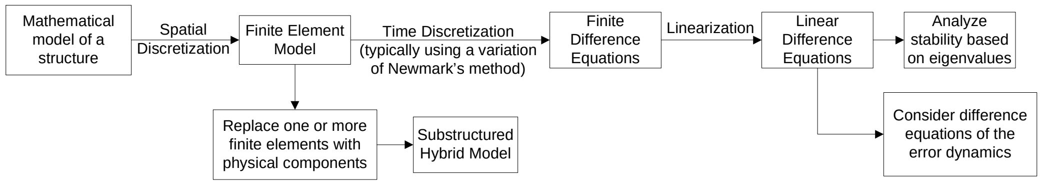

Figure 2.5: Approach motivated Time-discretization in the Finite Elements context

2.2.1 Algorithms motivated by time-discretization strategies in Finite Element Analysis

A schematic representation of the approach motivated by time-discretization in the finite elements context is shown in Figure 2.5. This approach is primarily referred to pseudo-dynamic testing.

Techniques have been developed in the finite elements context to tailor the eigenvalues of the linearization to damp out the spurious effects of higher modes that are excited by numerical error. An example is the well-known α-method of Hilber et al. [10]. Such techniques have been applied to substructure pseudo-dynamic testing as well, (see for example [11]) where measurement error and disturbance are even more significant than numerical error. On the other hand, Bursi et al. [12] makes use of linear implicit algorithms. An example is the Rosen-brock algorithm which was used for real-time substructuring testing (Bursi et al. [13]). Such algorithms have been modified for testing of non linear structures as well (Bursi et al. [14]). Shing et al. [15] proposed a method so that the Hibler-Hughes-Taylor (HHT) α-algorithm can be implemented in real-time testing, using a fixed number of sub-step iterations. The particular algorithm was later modified by Chen and Ricles [16] for real-time pseudo-dynamic testing on non-linear structures. Ou et al. [17] proposed a Runge-Kutta integration algorithm to reduce computational delays.

The term "unconditionally stable" is often used which implies that the linearization has stable eigenvalues independent of the time step. The linearized finite difference equations corresponding to the error dynamics are also considered and this is termed "error propagation analysis". Approached in this manner, implicit time integration schemes are found to possess better stability properties. However, the main problem with implementing an implicit scheme for experimental substructuring is that the operations on the physical substructure are not causal. In other words, it is not possible to iterate over the physical substructure in the same manner as with a numerical model. As a work-around for this problem, several strategies have been suggested including (a) various types of predictor-corrector methods (see for example Combescure et al. [18], Bonelli et al. [11], Zhang et al. [19], Wu et al. [20], Kolay et al. [21] and Mosqueda et al. [22]) (b) time-step staggering between the numerical and experimental components (Pegon et al. [23]) and (c) strategies that try to ensure that the physical substructure is loaded monotonically by using a Newton stiffness matrix that is more positive than the tangent stiffness matrix and by applying only a fraction of the Newton perturbation in every iteration (Shing et al. [24]). The analysis of stability in these cases becomes somewhat heuristic. Chen and Ricles [25] performed a stability analysis procedure at discrete time content. The actuator delay and the integration algorithm are both modeled by discrete transfer functions, combined together to represent the real-time hybrid structure.

2.2.2 Modified numerical algorithms for real-time pseudo-dynamic testing

Modifications of the algorithms discussed in the previous subsection have been developed to perform pseudo-dynamic testing in real-time. This is of interest when the physical substructure has rate-dependent behavior, such as in the case of commonly used damping and seismic isolation devices. Nakashima et al. [26] was the first to perform this type of simulation, using a staggered central difference method. Two interesting strategies under this category are those developed by Shing et al. [27] and Bayer et al. [28]. Both these strategies employ multi-rate sampling with two sampling times. The larger sampling interval corresponds to the time-step of the difference equation while a Newton iteration is performed at every instance of the smaller sampling time. In an attempt to enure monotonic loading of the physical substructure within every time-step, after every Newton iteration, only a fraction of the computed perturbation was applied to the physical substructure. A linear interpolation was used for this purpose by Bayer et al. [28] and a quadratic interpolation by Shing et al. [27]. In both strategies, actuator dynamics is implicitly recognized by using the measured displacement at the interface instead of the desired displacement in the Newton iterations. Interestingly, the example presented by Bayer et al. [28] also includes inertia effects in the physical substructure. It can also be shown that these approaches are closely related to the idea of internal model control presented by Sivaselvan [29].

2.2.3 Approaches on actuator dynamics compensation

In the case of dynamic substructuring, in order to perform successful experiments, it is crucial to compensate for the additional dynamics of the actuator. Extensive research has been conducted to overcome this difficulty and several approaches have been considered. Some of them, model the actuator dynamics as pure time-delay, while others consider the dynamics of the actuator as part of the system to be controlled. In some cases, the actuator dynamics are recognized but not compensated for. These different approaches are discussed in detail below.

2.2.3.1 Approaches that model actuator dynamics as a pure time-delay

Horiuchi et al. [30,31] were the first to explicitly consider actuator dynamics. In this work, the actuator is modeled as a pure time-delay and a compensation technique is developed using polynomial extrapolation. Nakashima et al. [32] also used a variation of this approach for real-time pseudo-dynamic testing of seismic isolation bearings. Darby et al. [33–35] present polynomial compensation as well as linear lead compensation as strategies to compensate for actuator delay. Blakeborough et al. [36] and Nakashima [37] present comprehensive discussions of this approach. Wallace et al. [38] present an adaptive polynomial compensation strategy.

Similarly, Chen and Tsai [39] used a dual compensation strategy using adaptive time delay estimation to compensate for the phase lead and the restoring force of the actuator. An adaptive-lead compentator was also used by Chen and Tsai [40] for the test of an isolation system consisted of magnetorheological (MR) dampers and elastomeric bearings. Mercan and Ricles [41] performed stability analysis using a procedure called pseudo-delay technique. An extrapolation procedure was used by Ahmadizadeh et al. [42] to compensate for the delay of the hybrid system.

Gonzalez-Buelga et al. [43] look the hybrid simulation of a pendulum (nonlinear component) coupled to a mass-spring-damper system (linear system). The former is the physical substructure while the latter is virtual. The interface displacement is imposed by a position servo and the resulting interface force is measured and fed back to the numerical model of the virtual substructure. The dynamics of the servo is considered to be a pure-time delay and is compensated for using a (linear) polynomial predictor. The hybrid system is shown to exhibit parametric resonances that are shown by the full system. Kyrychko et al. [44] also study the same problem. They also consider the actuator dynamics to be a pure time-delay. However, instead of compensating for it, they explore the stability boundaries of the hybrid system with the delay using the theory of delay differential equations and show that for certain critical values of the delay a Hopf bifurcation occurs. This approach to stability analysis was presented by Wallace et al. [45]. When the physical substructure is mechanically stiff, a mixed force-displacement control strategy is presented by Pan et al. [46].

2.2.3.2 Systems approach without compensation of actuator dynamics

Outside of civil engineering, experimental substructuring has been considered in terms of the feedback interaction between the two substructures. In some of these cases, while effect of actuator dynamics of destabilizing the feedback system is recognized, no explicit measure is taken to compensate for it. The work of Peterson [47] is an example. Plummer [48] discusses two applications of hybrid simulation (which he terms *Model-in-the-loop Testing - MiL*) in automotive testing, in particular, testing of motor sports cars. In the first application, a hydraulically actuated four poster test rig is used, the entire car is the physical substructure and the virtual substructure is a numerical aerodynamic model. In the second application, a hub-coupled rig is used, the car without its wheels and tyres is the physical substructure and a numerical model of the tyres is the virtual substructure. The actuators are operated in closed-loop position- or force-control depending on whether the interface element in the physical substructure is a stiffness or a mass. A "framework" is presented that provides for these possibilities. The closed-loop dynamics of the actuators is compensated for in one of the applications using a lead compensator. The author suggests that compensation for the closed-loop dynamics of the actuator would be effective in improving the performance of the MiL system and proposes using more general linear filters for this purpose.

2.2.3.3 Approaches that consider general actuator dynamics

These approaches use what is usual in control engineering, of considering the dynamics of the actuator as part of the system to be controlled. In all of the reported work, the actuator is considered along with a tracking feedback controller. This feedback loop is referred to as the "inner loop." The control loop implementing the hybrid simulation is then referred to as the "outer loop." As mentioned previously, lead compensation strategies have been used for actuator delay compensation. In the place of a lead-compensator, Carrion and Spencer [49] use an inverse dynamics compensation procedure. This method was combined with Darby's online delay estimation procedure (Darby et al. [35]) to develop an "integrated compensation" method by Liu et al. [50].

Gawthrop et al. [51] consider the *robust stability* of a feedback system by treating it as a perturbation of the system, shown in Figure 2.6. They consider the nominal system to have linear dynamics and formulate the hybrid system dynamics in such a way that the actuator dynamics is a multiplicative perturbation of the full system dynamics. Then, they use standard results from SISO robust control theory (see for example Doyle et al. [52]) to obtain conditions on the actuator transfer function for stability of the hybrid system. They also present three "robustness compensators" that result in a larger set of actuator dynamics that result in a stable hybrid system — (a) increasing the damping in the virtual subsystem, (b) a linear lead compensator and (c) and internal model compensator. The first

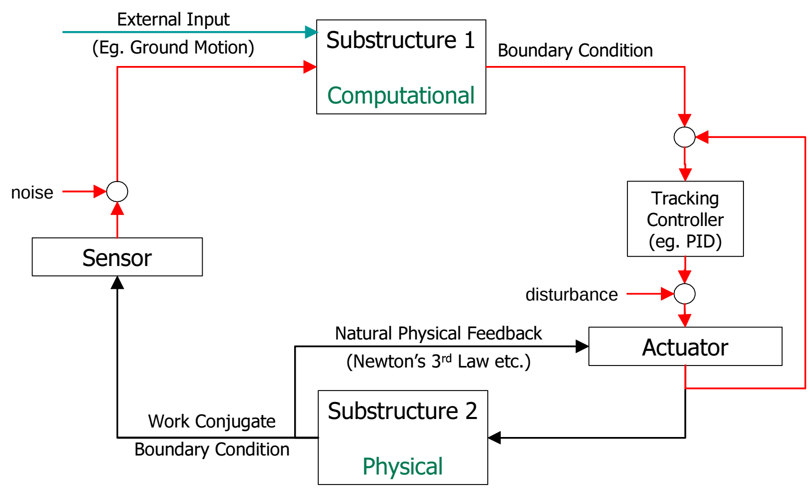

Figure 2.6: Interaction between components in the hybrid system

two strategies result in misrepresentation of the virtual substructure while the third requires a reasonable mathematical model of the physical substructure. To overcome the problems related with instabilities caused by the actuator dynamics, Gawthrop [53] also proposes an emulated-based control strategy, which emulates the inverse of a transfer system which is not causally invertible.

Another control systems approach that has been taken to substructuring is *model reference control* (Wagg et al. [54], Neild et al. [55], [56]). The idea is to break up the feedback system of Figure 2.6 as shown in Figure 2.7a, and pose the problem as finding a control u, that results in the output y_2 of the physical substructure tracking the output y_1 of the virtual substructure, i.e., the conditions at the boundary are compatible. Figure 2.7a can be rearranged as shown in Figure 2.7b [57] along with feedforward and feedback. Stoten et al. [57] develop linear controllers as well as an adaptive controller using the "Minimal Control Synthesis" idea and show using a numerical example that the the adaptive controller performs better than the linear controller.

Other control systems strategies include the use of advanced adaptive controllers. Bonnet et al. [58] developed a method which involves the use of a minimal control synthesis with modified demand (MCSmd) controller combined with a multi-tasking strategy. In this particular study, a controller was created for each controller without considering the cou-

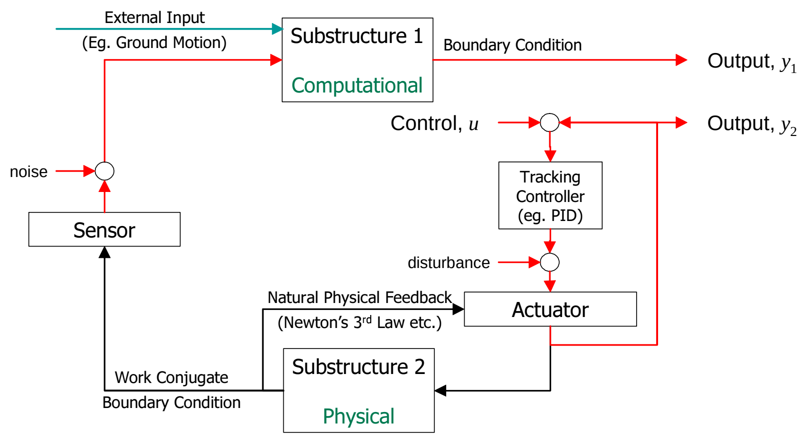

(a) Basic idea

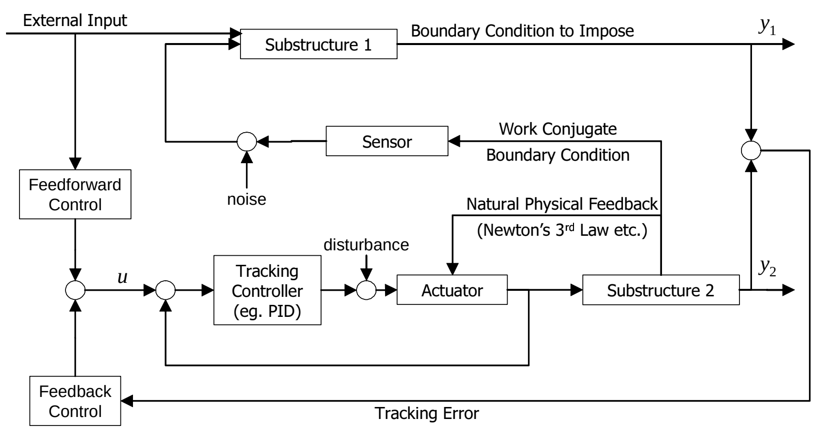

(b) Rearranged block diagram

Figure 2.7: Model Reference Control

pling of the actuators. To overcome this issue, Phillips and Spencer [59] proposed a method which deals with the control of multiple actuators.

Gao et al. [60] introduces a strategy which includes the use of a digital H_∞ controller to control the actuator's motion, while Ou et al. [61] uses a similar approach for actuator's control. Li et al. [62] uses an antiwindup (AW) technique to deal with the actuator's saturation. As an alternative approach, Li et al. [63] also made use of an online model predictive control (MPC) approach, utilizing a framework which totally separates the numerical from the experimental substructure. This framework is further refined (Li [64]) to explicitly define the relation of the substructure and the signals of the overall system.

Elorza [65] discusses broader possibilities for real-time substructuring. More specifically, the actuators are not viewed as a transfer system in the contrast, a generic differential notation is introduced. Tu [66] uses numerical-substructure-based (NB) and output based controllers using transfer function and state space techniques to classify control systems in a systematic way. Tu et al. also [67] use this frameworks by adding output-based adaptive techniques, and test their effectiveness on isolated structural systems. Tu et al. [68] also performs an investigation into substructurability and synchronization of this approach. Chae et al. [69] propose the use of an adaptive compensator, which updates the gains of the hydraulic actuator at each time step of the real-time testing. Since this approach does not include user-defined adaptive gains it provides an improved approach compared to the methods where the gains should be calibrated before the experiment.

In order to systematically predict the robustness of an individual substructure, termed "dominative substructure" and to evaluate the performance of the dynamic substructuring system during an experiment, Huang et al. [70] proposes a method using techniques of Lyapunov function and linear matrix inequalities (LMI).

In recent studies, measure of the performance of real-time experimental substructuring is investigated. Mosqueda et al. [71] provides qualitatively the effect of the error in the actuator tracking. Guo et. al [72] proposes a more quantitative frequency response approach to estimate the error of the actuator tracking using a frequency evaluation index. Maghareh et al. [73] introduce a predictive performance indicator (PPI) to estimate how sensitive the simulation is to phase discrepancies caused by the actuator dynamics and other delays. Chen et al. [74] used this approach on multi-degree-of freedom (MDOF) systems to identify the effect of the tracking error of the actuator for the case when multiple structural models exist.

2.2.4 Dynamic Substructuring using shake tables

While there has been significant work on real-time substructuring in the last several years, there have been relatively limited applications of dynamic substructuring using shake tables. Igarashi et al. [75,76], Lee et al. [77] and Ji et al. [78] use a shake table to virtually represent lower stories of a building model. Neild et al. [56] discuss control systems issues in this type of testing. Günay and Mosalam [79] perform hybrid simulation of electrical insulator posts, which are an example of distributed mass systems, representing support structures virtually by means of a shake table. Later [80, 81], they develop and perform real-time experiments and parametric studies on high voltage disconnect switches. They also propose an enhancement of the real-time hybrid simulation control approach by adding velocity and acceleration in the conventional displacement control, [82]. Zhang et al. [83] investigate the challenges of DS using shake tables, utilizing an acceleration tracking controller.

Although not shake tables, similar devices were used by Bayer et al. [28] and Gonzalez-Buelga et al. [43].

Studies using multiple shake tables and actuators to represent substructures as proposed here are even fewer. This necessitates use of dynamic force control, which is a challenging problem in itself (Sivaselvan et al. [84]). The authors have used a combination of shake tables and external actuators for dynamic hybrid testing of building models (Reinhorn et al. [3]). Shao et al. [85] perform such tests to model numerical substructures at the top and bottom of the experimental substructures. Nakata and Stehman [86] present a numerical simulation of a shake table representing building upper stories.

2.3 Conventional approach to SFSI DS

It is clear from the previous discussion that extensive research has been conducted in the last decades to overcome challenges related to substructuring. Specifically, for the case of dynamic substructuring, significant effort has been made to deal with the additional dynamics of the actuators. However, the application of such experiments is limited to relatively simple experimental configurations. Therefore, the investigation of the response of complex systems, such as SFSI, cannot be successfully performed using the conventional approach. Wang et al. [87] attempted to perform DS experiments on SFSI systems, for which the soil was numerically simulated, i.e. it was the virtual subsystem. However, due to the complexity of the response of the soil during an earthquake, it is preferable to perform experiments for which the physical subsystem is the soil and the superstructure, which can be more accurately modeled, is the virtual subsystem. The challenges of such an experiment are summarized in the following section, underlying the need for a simpler approach in DS experiments. The simplified approach proposed in this dissertation is briefly described in contrast with the conventional approach.

2.4 Problem formulation of SFSI DS

A conceptual example of a DS configuration is shown in Figure 1.1 (a preliminary realization of this concept is presented in Section 5.1).

Here, the soil-foundation model is the physical subsystem (PS), and a superstructure model is the virtual subsystem (VS). The active mass driver (AMD), described in Chapter 3, is to mimic the superstructure impedance. This could be accomplished by using feedback of the foundation motion, and driving the proof mass appropriately, to produce forces representative of the virtual superstructure on the foundation.

This suggests thinking in terms of the arrangement shown in Figure 2.8a. Indeed, the conventional approach starts here. The AMD has to operate in a control mode in which it has to track a reference force command. One quickly recognizes that the AMD feels the

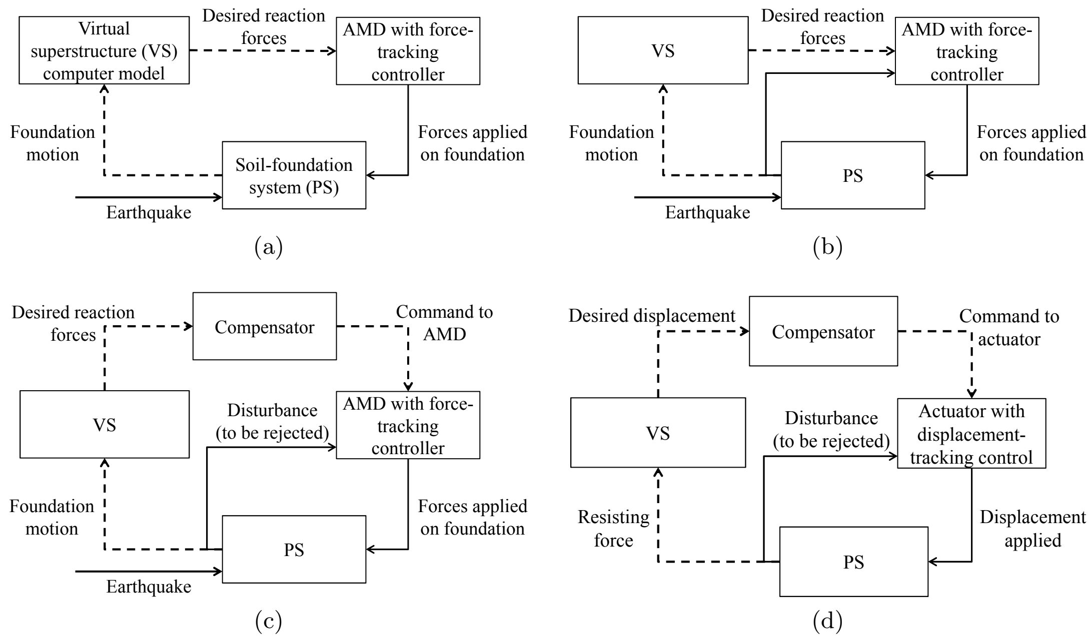

Figure 2.8: Conventional DS arrangement (solid lines depict mechanical interactions associated with large power, and dashed lines electronic signals of low power; additional dynamics from sensors have not been shown); (a) using foundation motion feedback, desired force is computed from VS model, and AMD is to track this force; (b) AMD also feels the foundation motion — control-structure interaction; (c) AMD cannot track desired force exactly — need for compensator; (d) dual of (c) where the input to PS is displacement — more common form of substructuring.

motion of the foundation as well, as shown in Figure 2.8b. This is called control-structure interaction [88, 89]; thus the tracking controller has the PS in its feedback path. The AMD cannot track a force command exactly over all frequencies; in fact, deviation from exact tracking could result in instability, particularly when the PS is lightly damped [45, 53]. To alleviate the effects of inexact tracking, a "compensator" is used as shown in Figure 2.8c. Finally, the conventional approach also typically consists of a numerical time integration scheme to simulate the VS independently of the controls. In Figure 2.8d, a more typical DS arrangement is shown, where the input to the DS is displacement.

Thus, the three ingredients common to most conventional approaches are

1. A *tracking controller* with the PS in its feedback path

2. A *compensator* to mitigate inexact tracking

3. A *numerical integration* scheme for the VS

As described previously in this chapter, most of the literature on DS, is on one or a combination of these ingredients.

2.5 Concluding remarks

Significant effort has been made to successfully perform DS experiments. The approaches conventionally used are formed with the finite-element approach in mind, leading to the need of tracking controllers, compensators and time-integration schemes. Attempts to perform DS experiments using these techniques are complicated and prone to inaccurate results or even instability of the entire simulation, limiting the effectiveness of DS.

Moving towards the development of a simpler approach, there is need to depart from the three-ingredient conventional framework. During the simulation the focus of the study should be the response of the physical substructure, while the virtual substructure needs only to be represented to the extent of meaningful boundary conditions, exact tracking of the displacement or force is, hence, not necessary.

Using the control design presented in Chapter 4, the compensation of the actuator's dynamics and the use of complicated integration schemes is not required. This largely simplifies the controller design, however it is necessary to remedy situations for which the computed controller is unrealistic.

Chapter 3

Development testbed for dynamic substructuring

3.1 Introduction

As an environment to implement and evaluate the new dynamic substructuring (DS) strategy described in Chapter 4, a development testbed is built. As shown in Figure 3.1, it consists of

1. a uniaxial hydraulic shaker to serve as a 1DOF active mass driver (AMD)
2. a resonant physical subsystem
3. various hardware and software components for measurement and control.

The goals in building this testbed are that

- it be amenable to reliable mathematical modeling, so that the testbed can be used with confidence to evaluate DS results subsequently,
- it allows for repeatable experiments over a wide range of frequencies,
- it be forgiving of errors during development (for example, if an instability occurred, it would not damage the system)

(a) AMD with resonant physical subsystem (b) Hardware and software components

Figure 3.1: Testbed components

- its hardware and software components be flexible enough to accommodate a variety of modifications and extensions.

This chapter discusses the architecture and design of the testbed that reflect the above objectives, and presents the mathematical modeling and experimental characterization of this testbed.

3.2 Uniaxial hydraulic shaker

3.2.1 Concept

In dynamic substructuring applications, shakers can be used to apply interface conditions between virtual and physical subsystems. Such use may be of two types, (a) to apply motion from a virtual subsystem at the base of a physical subsystem (for example, [82]), and (b) to apply forces from a virtual subsystem atop of a physical subsystem. The former configuration is similar to the use of shake tables in usual seismic testing, while the latter is

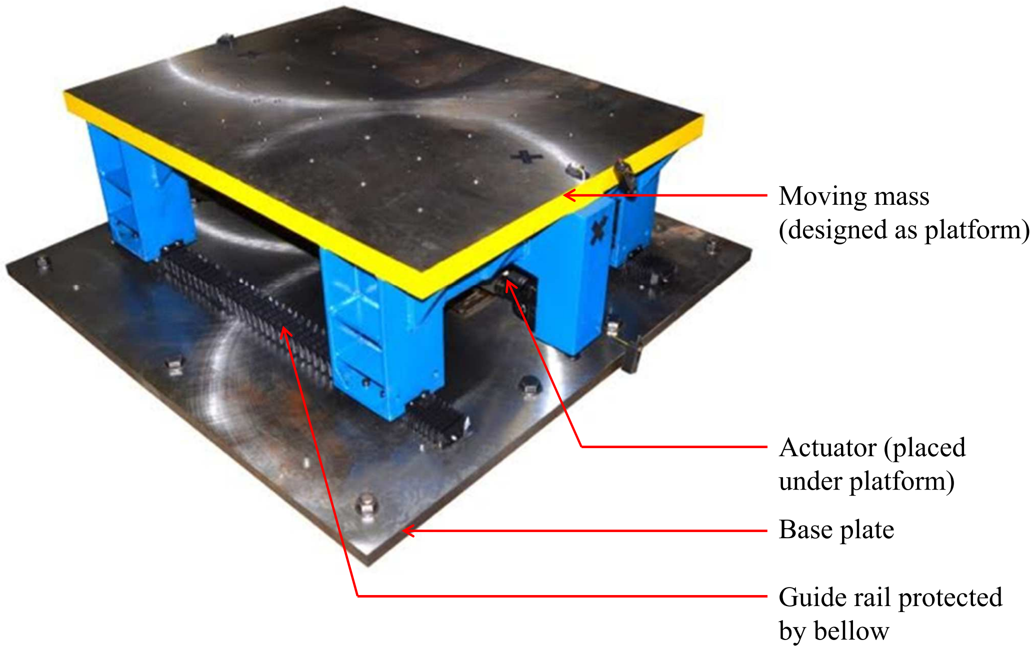

Figure 3.2: Uniaxial shaker used as an active mass driver (AMD); details are shown in Figure 3.8

reminiscent of the active mass driver (AMD) concept in structural control, and of eccentric mass shakers.

The uniaxial shaker presented in this chapter is intended primarily for the latter purpose, to function as an AMD. It consists of a moving mass, called proof mass in the AMD context [90], driven by a hydraulic actuator mounted on a base plate (Figure 3.2); when the actuator drives the proof mass with a certain acceleration, a force equal to the mass times that acceleration is applied at the base. The proof mass is designed as a platform, so that the shaker can also be used as a shake table in other applications. To be able to readily place the shaker as an AMD over different physical subsystems, including on a foundation model in the Soil-Foundation-Structure Interaction (SFSI) application described in Chapter 5, it is desirable for the the shaker to have a compact footprint. For this, the hydraulic actuator is placed *under* the platform as seen in Figure 3.2. The platform is consequently elevated by means of four posts. The posts are supported by low-friction recirculating ball bearings that slide on guide rails attached to the base plate. To connect the actuator symmetrically to the platform, the closed housing on what is usually the reaction side of the actuator [91] is removed, so that both piston ends are exposed. Swivels are attached on both piston ends, and tied to the platform through connecting blocks. The body of the actuator is mounted on the base plate by means of angle brackets bolted to the end caps as shown in Figure 3.8. The elevated configuration of the platform makes it more flexible, potentially lowering its natural frequency. In order to ensure that the natural frequency of the platform itself is much higher than all frequencies of interest, it is stiffened suitably. The proof mass is thus made up of the platform, posts, connecting blocks, bearings, swivels, the actuator piston and the stiffening elements. Detailed design of the various components of the shaker is presented in Section 3.2.3. A representative mathematical model is used to guide this design. This model, discussed next, is also used in dynamic substructuring control design in Chapter 4.

3.2.2 Modeling

The behavior of a hydraulic actuator has a number of nonlinear features. Several researchers [92–94] have developed mathematical models for such systems. This subsection begins by discussing a nonlinear shaker model. For the purposes of the work reported here, specifically for the control design in Chapter 4, a linear model is found to much simpler and adequate. Implications of using a controller designed based on a linear model even in the presence of nonlinear effects in the system are illustrated in Section 4.4.1.1. As discussed at the end of Section 3.2.2.1, the nonlinear model has more parameters that are difficult to identify separately. For these reasons, the nonlinear model is linearized. The linear model reveals the concepts of oil column frequency and damping, which characterize dynamic performance of the shaker. Understanding of the essential dynamics gained from these models forms the basis for its design and construction, described in the next subsection.

3.2.2.1 Nonlinear model

The modeling of the hydraulic shaker presented here mainly follows Merritt [95]. A simplified representation is shown in Figure 3.3. The system consists of a 4-port type servovalve and a double-ended actuator that is connected to the proof mass. It should be noted that this is referred to as the *platform* when the shaker is used as a shake table, or the *proof mass* in the AMD context. The servovalve ports have identical properties, and both sides of the actuator piston have the same area, A_{p}, resulting in a symmetric configuration. A_{p} is the area exposed to oil pressure, and excludes the area of the piston rod. The servovalve spool itself is generally driven by hydraulic flow, and its position is regulated by mechanical feedback (in two-stage valves) or servo control (in three-stage valves). However, to begin with, it is assumed that the spool position is directly controlled, and considered as the input, u_{v}, in the model. The servovalve dynamics will be included in the model later, in Section 3.2.2.4. The model is developed in three steps.

1. Flow through the servovalve ports: For each servovalve port, the flow through the port depends on the pressure difference ΔP across the port and the area of opening of the port. The area of opening in turn depends on the spool position, u_{v}. Thus the port flow (volume per second) can be expressed as a function, $Q(\Delta P, \pm u_{\mathrm{v}})$. The specific form of the function Q is discussed later in this section. Referring to Figure 3.3, taking the spool displacement to be positive going left, the flows in the four ports of the servovalve can be written as

$$Q_1 = Q(P_{\mathrm{S}}-P_1, u_{\mathrm{v}}); \quad Q_2 = Q(P_1-P_{\mathrm{R}}, -u_{\mathrm{v}}); \quad Q_3(P_2-P_{\mathrm{R}}, u_{\mathrm{v}}); \quad Q_4(P_{\mathrm{S}}-P_2, -u_{\mathrm{v}}) \quad (3.1)$$

where P_{S} and P_{R} are the hydraulic pump supply and return pressures.

2. Conservation of oil mass in the actuator chambers: Conservation of mass for each of the two chambers of the actuator can be stated as

$$\rho(P_i)(Q_{\mathrm{in},i} - Q_{\mathrm{out},i}) = \frac{d}{dt}(\rho(P_i)V_i), \quad i = 1, 2$$

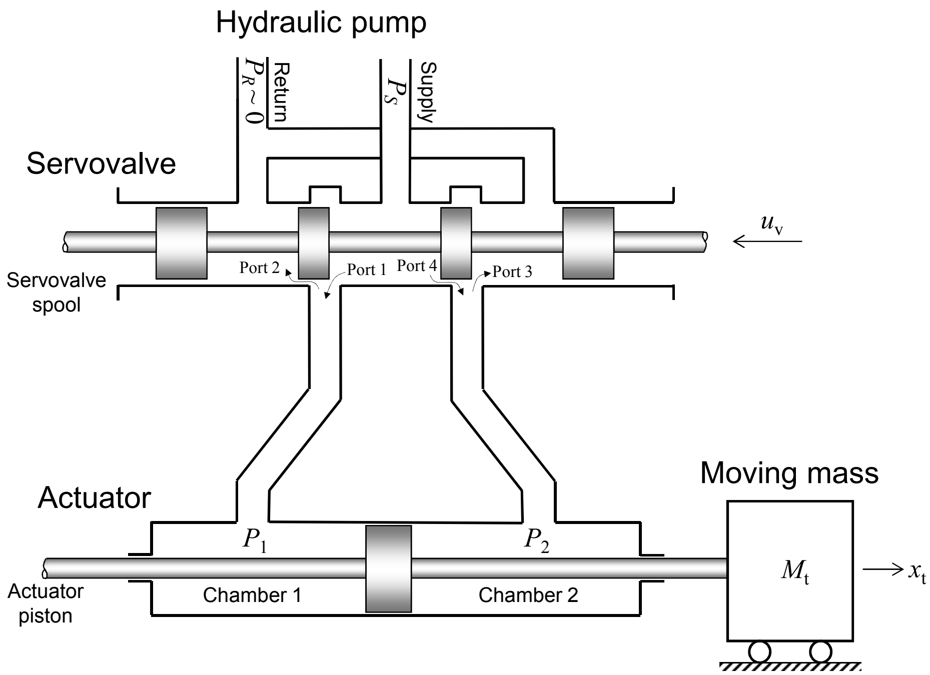

Figure 3.3: Schematic of a uniaxial hydraulic shaker (P_S and P_R are the supply and return pressures, u_v is the servovalve spool displacement considered here to be the input to the model, P_1 and P_2 are the pressures in actuator chambers 1 and 2, and M_t and x_t are the mass and displacement of the proof mass)

where ρ is the oil density, a function of the pressure, Q_{in} and Q_{out} are the flows into and out of the chamber, and V_i is the volume of the chamber. Dividing through by ρ, and using the relationship $\rho \frac{dP}{d\rho} = \kappa$, the bulk modulus of the hydraulic oil, we get

$$Q_{\mathrm{in},i} - Q_{\mathrm{out},i} = \dot{V}_i + V_i \frac{\dot{P}_i}{\kappa}$$

If x_{m} is the midstroke position of the actuator piston, then $V_1 = A_{\mathrm{p}}(x_{\mathrm{m}} + x_{\mathrm{t}})$ and $V_2 = A_{\mathrm{p}}(x_{\mathrm{m}} - x_{\mathrm{t}})$. Some leakage flow is accounted for across the piston from chamber 1 to chamber 2, and is modeled as laminar flow proportional to the pressure difference between the chamber. Such a leakage flow is of the form, $K_l(P_1 - P_2)$, K_l being a leakage coefficient. Putting all this together, conservation of mass in the two actuator chambers leads to

$$\begin{aligned}
\dot{P}_1 &= \frac{\kappa}{A_{\mathrm{p}}(x_{\mathrm{m}} + x_{\mathrm{t}})}(Q(P_{\mathrm{S}} - P_1, u) - Q(P_1 - P_{\mathrm{R}}, -u) - K_l(P_1 - P_2) - A_{\mathrm{p}}\dot{x}_{\mathrm{t}}) \\
\dot{P}_2 &= \frac{\kappa}{A_{\mathrm{p}}(x_{\mathrm{m}} - x_{\mathrm{t}})}(Q(P_{\mathrm{S}} - P_2, -u) - Q(P_2 - P_{\mathrm{R}}, u) + K_l(P_1 - P_2) + A_{\mathrm{p}}\dot{x}_{\mathrm{t}})
\end{aligned} \tag{3.2}$$

3. Equation of motion of the proof mass: The total force on the proof mass is $A_{\mathrm{p}}(P_1 - P_2)$. Thus, again referring to Figure 3.3, the equation of motion of the proof mass is

$$M_{\mathrm{t}}\ddot{x}_{\mathrm{t}} = A_{\mathrm{p}}(P_1 - P_2) \tag{3.3}$$

Combining equations (3.2) and (3.3), the nonlinear model can be written as

$$\begin{aligned}
\dot{x}_1 &= x_2 \\
\dot{x}_2 &= \frac{A_{\mathrm{p}}}{M_{\mathrm{t}}}(x_3 - x_4) \\
\dot{x}_3 &= \frac{\kappa}{A_{\mathrm{p}}(x_{\mathrm{m}} + x_1)}(Q(P_{\mathrm{S}} - x_3, u_{\mathrm{v}}) - Q(x_3 - P_{\mathrm{R}}, -u_{\mathrm{v}}) - K_{\mathrm{l}}(x_3 - x_4) - A_{\mathrm{p}}x_2) \\
\dot{x}_4 &= \frac{\kappa}{A_{\mathrm{p}}(x_{\mathrm{m}} - x_1)}(Q(P_{\mathrm{S}} - x_4, -u_{\mathrm{v}}) - Q(x_4 - P_{\mathrm{R}}, u_{\mathrm{v}}) + K_{\mathrm{l}}(x_3 - x_4) + A_{\mathrm{p}}x_2)
\end{aligned} \tag{3.4}$$

where

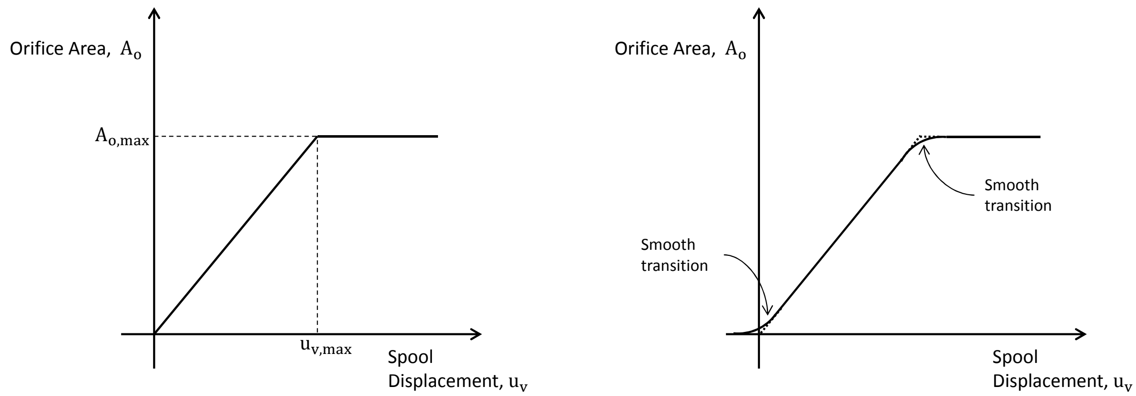

(a) Ideal orifice with abrupt opening and saturation

(b) Real orifice with clearance between the spool and the landings, so that there is leakage in the closed position and gradual saturation

Figure 3.4: Qualitative nature of the servovalve orifice opening function $A_\text{o}(u_\text{v})$

x_1 = table displacement (x_t)
x_2 = table velocity (v_t)
x_3 = pressure in chamber 1 (P_1)
x_4 = pressure in chamber 2 (P_2)
u_v = valve spool displacement (input)

Flow equation A specific form of the port flow function used in equation (3.1) is now considered. This stems from Bernoulli's equation, and is applicable in the turbulent flow regime, where the ports primarily operate [95]. The flow through the servovalve port depends on the pressure difference across the port, and on the area of opening of the port, A_o.

$$Q(\Delta P, u_\text{v}) = C_\text{d} A_\text{o}(u_\text{v}) \sqrt{\frac{2\Delta P}{\rho}} \tag{3.5}$$

The area of opening is itself a function of the spool displacement, $A_\text{o}(u_\text{v})$. This function is difficult to define exactly, since it would depend of the exact geometry of the ports, but is shown qualitatively in Figure 3.4. The hydraulic fluid density, ρ, can be taken as $8.5 \times 10^{-6} \frac{\text{lbs}^2}{\text{in}^4}$, and the discharge coefficient, C_d, for the port orifices as 0.6 [95]. For practical use, the flow function can be written by aggregating the various parameters, as

$$Q(\Delta P, u_\mathrm{v}) = K_\mathrm{V} a_\mathrm{o}(u_\mathrm{v}) \sqrt{|\Delta P|}\,\mathrm{sgn}(\Delta P) \tag{3.6a}$$

where K_V is a valve coefficient, and a_o is a function that varies between zero when the port is closed, and one when fully open. Corresponding to the idealized shape of Figure 3.4a, a_o may be written as

$$a_\mathrm{o} = \min(\max(u_\mathrm{v}, 0), 10)/10 \tag{3.6b}$$

so that it is zero when the valve command is zero and one when the valve command is 10V.

Model parameters

1. **Area of the piston, $A_\mathbf{p}$, and midstroke position, $x_\mathbf{m}$**: These properties are given by the manufacturer's specifications of the actuator used in the system.

2. **Proof mass, $M_\mathbf{t}$**: The proof mass of the system is equal to the mass of the moving part of the shaker and can be almost exactly (except for the piston rod) measured directly using a scale.

3. **Supply and return pressures, $P_\mathbf{S}$ and $P_\mathbf{R}$**: The supply pressure P_S is determined by the hydraulic pump used, and is typically 3000psi, while the return pressure is taken to be approximately equal to the atmospheric pressure, hence $P_\mathrm{R} \simeq 0$.

4. **Bulk modulus of the oil, κ**: This is a property of the hydraulic oil flowing through the ports of the servovalve. According to the literature [95], a value of $\kappa = 10^5 \frac{\mathrm{lb}}{\mathrm{in}^2} = 10^5$ psi is considered to be a good approximation for the bulk modulus of oil; however, its value can fluctuate due to several factors, such as changes in temperature.

5. **Valve coefficient, $K_\mathbf{V}$**: K_V can be obtained from the specifications of the servovalve. For example, the specifications for the MTS252.25 servovalve [96] (see section 3.2.3) state that its rated flow is 15gpm (57.75in^3/s) at a load pressure of 1000psi. This means that the piston velocity is constant, and $P_1 - P_2 = 1000$psi at $u_\mathrm{v} = 10$V.

From equations, (3.4), at steady state, $P_1 + P_2 = P_\mathrm{S} + P_\mathrm{R} = 3000\mathrm{psi}$. Solving, we get $P_1 = 2000\mathrm{psi}$ and $P_2 = 1000\mathrm{psi}$. The pressure drop across a servovalve port, $P_\mathrm{S} - P_1 = P_2 - P_\mathrm{R} = 1000\mathrm{psi}$. Substituting in equation (3.6a), $57.75\mathrm{in}^3/\mathrm{s} = K_\mathrm{V} \cdot 1 \cdot \sqrt{1000\mathrm{psi}}$, giving $K_\mathrm{V} = 1.826\mathrm{in}^3/\mathrm{s}/\sqrt{\mathrm{psi}}$.

6. **Leakage coefficient,** K_l: The leakage coefficient K_l is used to approximate flow around the piston, and cannot be estimated from any accessible measurements. It is back-calculated from the experimentally determined damping ratio using equation (3.9).

Sources of nonlinearity It is evident from equation (3.4) that the model is nonlinear. The sources of the nonlinearity in the system are (i) the terms $\frac{\kappa}{A_\mathrm{p}(x_\mathrm{m} \pm x_1)}$, which are nonlinear in the displacement x_1, and (ii) the flow equation Q which is given by the nonlinear equation (3.5). Additional nonlinear phenomena, such as friction, have not been explicitly included in the model. However, friction in the system is characterized in Section 3.5.1. Experimental observations described in Section 4.5.4, show that even a small amount of friction can play a critical role in dynamic substructuring experiments. For the purpose of control design for dynamic substructuring, a linear model is preferable; hence the nonlinear model (3.4) is linearized next.

3.2.2.2 Linearization

For input $u_\mathrm{v} = 0$, it is readily seen that the equilibrium points of the model (3.4) are given by

$$x_1^* \in (-x_\mathrm{m}, x_\mathrm{m}); \quad x_2^* = 0; \quad x_3^* = x_4^* = \frac{P_\mathrm{S} + P_\mathrm{R}}{2}$$

Assuming that the orifice opening function $A_\mathrm{o}(u_\mathrm{v})$ has the realistic form shown in Figure 3.4b, it is differentiable at $u_\mathrm{v} = 0$. Since $(P_\mathrm{S} - P_\mathrm{R})/2 \gg 0$, the flow function (3.5) is also differentiable at the equilibrium point. Therefore, equation (3.4) can be linearized as

$$\dot{x} = Ax + Bu_{\mathrm{v}} \tag{3.7a}$$

where

$$\begin{aligned}
A &= \begin{bmatrix}
0 & 1 & 0 & 0 \\
0 & 0 & \frac{A_{\mathrm{p}}}{M_{\mathrm{t}}} & -\frac{A_{\mathrm{p}}}{M_{\mathrm{t}}} \\
0 & -\frac{\kappa}{x_{\mathrm{m}}} & -\frac{\kappa}{A_{\mathrm{p}}x_{\mathrm{m}}}\left(K_{\mathrm{l}} + 2\,\mathrm{D}_1\,Q\left(\frac{P_{\mathrm{S}}-P_{\mathrm{R}}}{2}, 0\right)\right) & \frac{\kappa K_{\mathrm{l}}}{A_{\mathrm{p}}x_{\mathrm{m}}} \\
0 & \frac{\kappa}{x_{\mathrm{m}}} & \frac{\kappa K_{\mathrm{l}}}{A_{\mathrm{p}}x_{\mathrm{m}}} & -\frac{\kappa}{A_{\mathrm{p}}x_{\mathrm{m}}}\left(K_{\mathrm{l}} + 2\,\mathrm{D}_1\,Q\left(\frac{P_{\mathrm{S}}-P_{\mathrm{R}}}{2}, 0\right)\right)
\end{bmatrix} \\
B &= \begin{bmatrix} 0 & 0 & \frac{2\kappa}{A_{\mathrm{p}}x_{\mathrm{m}}}\,\mathrm{D}_2\,Q\left(\frac{P_{\mathrm{S}}-P_{\mathrm{R}}}{2}, 0\right) & -\frac{2\kappa}{A_{\mathrm{p}}x_{\mathrm{m}}}\,\mathrm{D}_2\,Q\left(\frac{P_{\mathrm{S}}-P_{\mathrm{R}}}{2}, 0\right) \end{bmatrix}^{\top}
\end{aligned} \tag{3.7b}$$

In the above, D_i denotes derivative with respect to argument i.

The eigenvalues and eigenvectors of the linearization can be calculated symbolically, and written in the form

$$\begin{aligned}
\lambda_1 &= 0 & v_1 &= (1, 0, 0, 0)^{\top} \\
\lambda_{2,3} &= -\zeta_{\mathrm{oil}}\omega_{\mathrm{oil}} + i\omega_{\mathrm{oil}}\sqrt{1-\zeta_{\mathrm{oil}}^2} & v_{1,2} &= \left(x_{\mathrm{m}}\frac{\lambda_{2,3}}{\lambda_{3,2}}, x_{\mathrm{m}}\lambda_{2,3}, \kappa, -\kappa\right) \\
\lambda_4 &= -\frac{2\kappa}{A_{\mathrm{p}}x_{\mathrm{m}}}\,\mathrm{D}_1\,Q\left(\frac{P_{\mathrm{S}}+P_{\mathrm{R}}}{2}, 0\right) & v_4 &= (0, 0, \kappa, \kappa)^{\top}
\end{aligned} \tag{3.8}$$

Remarks:

- Mode v_1 is the proof mass moving as a rigid body without resistance.
- The complex conjugate pair of eigenvalues corresponds to what is commonly referred to as the *oil-column resonance*, with frequency and damping ratio

$$\begin{aligned}
\omega_{\mathrm{oil}} &= \sqrt{\frac{2A_{\mathrm{p}}\kappa}{M_{\mathrm{t}}x_{\mathrm{m}}}} \\
\zeta_{\mathrm{oil}} &= \left(K_{\mathrm{l}} + \mathrm{D}_1\,Q\left(\frac{P_{\mathrm{S}}-P_{\mathrm{R}}}{2}, 0\right)\right)\sqrt{\frac{M_{\mathrm{t}}\kappa}{2{A_{\mathrm{p}}}^3x_{\mathrm{m}}}}
\end{aligned} \tag{3.9}$$

- The oil-column frequency may be thought of as that of a mass M_{t} connected to two springs (the oil in the two actuator chambers) of stiffness $\kappa A_{\mathrm{p}}/x_{\mathrm{m}}$.

- It is interesting to note from equation (3.9) that the damping ratio of the oil-column resonance is associated with imperfections — leakage flows in the actuator and servo-valve.

- The chamber pressures appear in the oil-column resonance mode in the form of *difference* of chamber pressures. It is also this differential pressure that is most commonly measured in hydraulic actuators.

- The mode v_4 consists of the *sum* of the chamber pressures. It is associated with a negative real eigenvalue, and is therefore stable. It is orthogonal to the other three modes, and $v_4^\top B = 0$. Therefore, this mode is uncontrollable with the valve displacement input in the linearization about the midstroke equilibrium point. v_4 also does not have any motion components, and is therefore unobservable from the shake table position and differential pressure measurements.

The last two observations suggest that the number of states can be reduced by a coordinate transformation, so that the difference and sum of the pressures are states rather than the chamber pressures themselves. Therefore the following coordinate transformation is applied,

$$T = \begin{bmatrix} 1 & 0 & 0 & 0 \\ 0 & 1 & 0 & 0 \\ 0 & 0 & 1 & -1 \\ 0 & 0 & 1 & 1 \end{bmatrix}$$

In the new coordinates, dropping the sum of the pressures state, rewriting in terms of ω_{oil} and ζ_{oil}, and also adding a base acceleration as an additional exogenous input, the model becomes

$$\begin{pmatrix} \dot{x}_1 \\ \dot{x}_2 \\ \dot{x}_3 \end{pmatrix} = \begin{bmatrix} 0 & 1 & 0 \\ 0 & 0 & \frac{A_{\text{p}}}{M_{\text{t}}} \\ 0 & -\frac{\omega_{\text{oil}}^2 M_{\text{t}}}{A_{\text{p}}} & -2\zeta_{\text{oil}}\omega_{\text{oil}} \end{bmatrix} \begin{pmatrix} x_1 \\ x_2 \\ x_3 \end{pmatrix} + \begin{bmatrix} 0 \\ 0 \\ d \end{bmatrix} u_{\text{v}} + \begin{bmatrix} 0 \\ -1 \\ 0 \end{bmatrix} w \tag{3.10}$$

where

$x_1 =$ table displacement (x_{t})
$x_2 =$ table velocity (v_{t})
$x_3 =$ differential pressure in actuator's chambers ($P_1 - P_2$)
$u_{\mathrm{v}} =$ valve command
$w =$ base acceleration (exogenous) input

and

$$d = \frac{4\kappa}{A_{\mathrm{p}} x_m} \, \mathrm{D}_2 \, Q\left(\frac{P_{\mathrm{S}} - P_{\mathrm{R}}}{2}, 0\right) \tag{3.11}$$

3.2.2.3 Hydraulic controller

The shake table is driven by a hydraulic controller (Section 3.4.1), which in all of the configurations discussed here, is operated in closed-loop displacement mode. The command to the controller is a reference displacement, u, and it implements the feedback,

$$u_{\mathrm{v}} = K_{\mathrm{e}}(u - x_1) - K_{\mathrm{d}} x_2 - K_{\mathrm{p}} x_3 \tag{3.12}$$

where again, it is assumed that the valve spool position can be commanded directly. K_{e}, K_{d} and K_{p} are the proportional, derivative and ΔP gains of the hydraulic controller. Substituting equation (3.12) into the linearized model (3.10), the following dynamics of the closed-loop shaker are obtained.

$$\begin{pmatrix} \dot{x}_1 \\ \dot{x}_2 \\ \dot{x}_3 \end{pmatrix} = \begin{bmatrix} 0 & 1 & 0 \\ 0 & 0 & \frac{A_{\mathrm{p}}}{M_{\mathrm{t}}} \\ -dK_{\mathrm{e}} & -(dK_{\mathrm{d}} + \frac{\omega_{\mathrm{oil}}^2 M_{\mathrm{t}}}{A_{\mathrm{p}}}) & -(dK_{\mathrm{p}} + 2\zeta_{\mathrm{oil}}\omega_{\mathrm{oil}}) \end{bmatrix} \begin{pmatrix} x_1 \\ x_2 \\ x_3 \end{pmatrix} + \begin{bmatrix} 0 \\ 0 \\ dK_{\mathrm{e}} \end{bmatrix} u + \begin{bmatrix} 0 \\ -1 \\ 0 \end{bmatrix} w \tag{3.13}$$

Equation (3.13) is one of two models used repeatedly in what follows to represent the closed-loop shaker dynamics (the other is equation (3.14) below, including servovalve dynamics). It should be mentioned that for the experiments presented in this work, only the proportional, K_{e}, and ΔP, K_{p}, gains were used.

3.2.2.4 Model including servovalve dynamics

So far, the dynamics of the servovalve have not been accounted for. Instead, it has been assumed that the spool position can be controlled directly. However, experiments suggest that the servovalve plays a noticeable role in the system dynamics (Section 3.5.1). A physics-based model of the servovalve is difficult to build, since the parameters of such a model cannot be readily determined. Furthermore, manufacturers' technical specifications of servovalves often do not provide sufficient detail. The servovalve is therefore modeled here as a generic first order transfer function,

$$x_4 = \frac{\alpha_\mathrm{s}}{s + \alpha_\mathrm{s}} u_\mathrm{v}$$

or equivalently, as a differential equation,

$$\dot{x}_4 = -\alpha_\mathrm{s} x_4 + \alpha_\mathrm{s} u_\mathrm{v}$$

where u_v is now the valve command, and x_4 is the spool displacement. It will be seen later that such a model is appropriate for the servovalve used in this work. The linearized shake table model can be thus modified to include servovalve dynamics as

$$\begin{pmatrix} \dot{x}_1 \\ \dot{x}_2 \\ \dot{x}_3 \\ \dot{x}_4 \end{pmatrix} = \begin{bmatrix} 0 & 1 & 0 & 0 \\ 0 & 0 & \frac{A_\mathrm{p}}{M_\mathrm{t}} & 0 \\ 0 & -\frac{\omega_\mathrm{oil}^2 M_\mathrm{t}}{A_\mathrm{p}} & -2\zeta_\mathrm{oil}\omega_\mathrm{oil} & d \\ -\alpha_\mathrm{s} K_\mathrm{e} & -\alpha_\mathrm{s} K_\mathrm{d} & -\alpha_\mathrm{s} K_\mathrm{p} & -\alpha_\mathrm{s} \end{bmatrix} \begin{pmatrix} x_1 \\ x_2 \\ x_3 \\ x_4 \end{pmatrix} + \begin{bmatrix} 0 \\ 0 \\ 0 \\ \alpha_\mathrm{s} K_\mathrm{e} \end{bmatrix} u + \begin{bmatrix} 0 \\ -1 \\ 0 \\ 0 \end{bmatrix} w \qquad (3.14)$$

The mathematical models developed thus far guide the design and construction of the shaker to be used as an AMD in this work. This process is described in the next subsection.

3.2.3 Design and construction

This subsection describes detailed design of the shaker concept outlined in Section 3.2.1. The different requirements and constraints that arise in designing a shaker for use as an AMD in dynamic substructuring, and the measures taken to satisfy them are discussed.

1. Compact footprint requirement The shaker is to be used as an AMD (a) as part of the testbed configuration (Section 3.5) in DS experiments described in Chapter 4, and (b) in the soil-foundation-structure interaction application of Chapter 5. In view of the latter application, the shaker's plan dimensions are chosen so that it can be placed in the 16.5ft $\times$ 9ft internal space of the SEESL geotechnical laminar box [97] with sufficient clearance from the boundaries of the box. For this, the plan dimensions of the shaker have to be in the range of 4 to 5ft square. For the configurations of Section 3.5 and Chapter 4, the shaker and testbed are attached to the SEESL strong floor and the extension frames of a SEESL 6-DOF shake table [98], both of which have a 2ft$\times$2ft hole pattern. Therefore, the plan dimensions of the shaker are selected to be 4.5ft $\times$ 4.5ft, so that it can be tied to the strong floor and to the shake table extension at eight points, with enough clearance from the tie holes to the edges of its base plate (see the eight $1\frac{1}{4}$in diameter holes in the plan view in Figure 3.5; Figure 3.2 also shows the tie points on the base plate). To accommodate a sufficiently large platform and an actuator to meet the force and stroke demands anticipated in the above applications, while keeping the footprint as small as possible, the actuator is placed *under* the platform as shown in Figure 3.8 and in the elevation in Figure 3.5.

2. Actuator and servovalve characteristics A MTS 244.12 actuator (serial number 585) is selected, with a 5.5kip nominal force rating [91]. The effective piston area, $A_{\mathrm{p}} = 2.10\mathrm{in}^2$. The dynamic stroke of the actuator is 6in (i.e., $x_{\mathrm{m}} = 3\mathrm{in}$) and the static stroke is 7.2in. The actuator is fitted with an MTS 252.25 (MOOG model number 760F264A) servovalve with a rated flow of 15gpm [96, 99]. This actuator, when placed under the platform fits within the desired plan dimensions. It also meets the force, stroke and velocity demands anticipated in the intended applications. Performance curves for MTS 252 series servovalves, taken from reference [96], are shown in Figure 3.6. The curve for the 252.25 valve shows a significant change of slope at 30Hz. This is used as the cutoff frequency when modeling the servovalve. Thus in equation (3.14), $\alpha_{\mathrm{s}} = 2\pi 30\mathrm{rad/s}$.

3. Trade off between frequency bandwidth and stroke/velocity limits With the actuator specifications established, the proof mass can be sized. In doing so, a fundamental

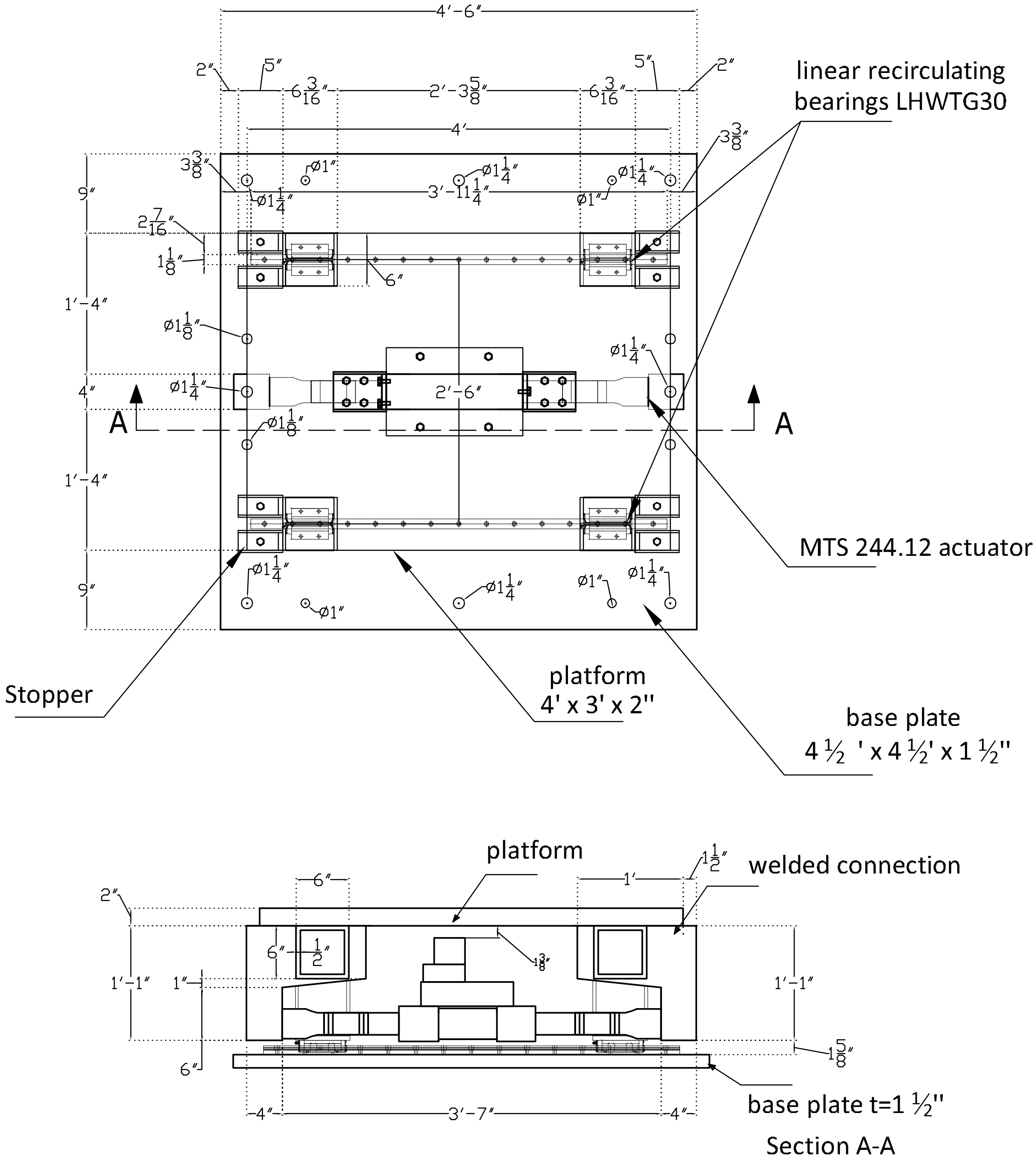

Figure 3.5: CAD drawing of the uniaxial shaker

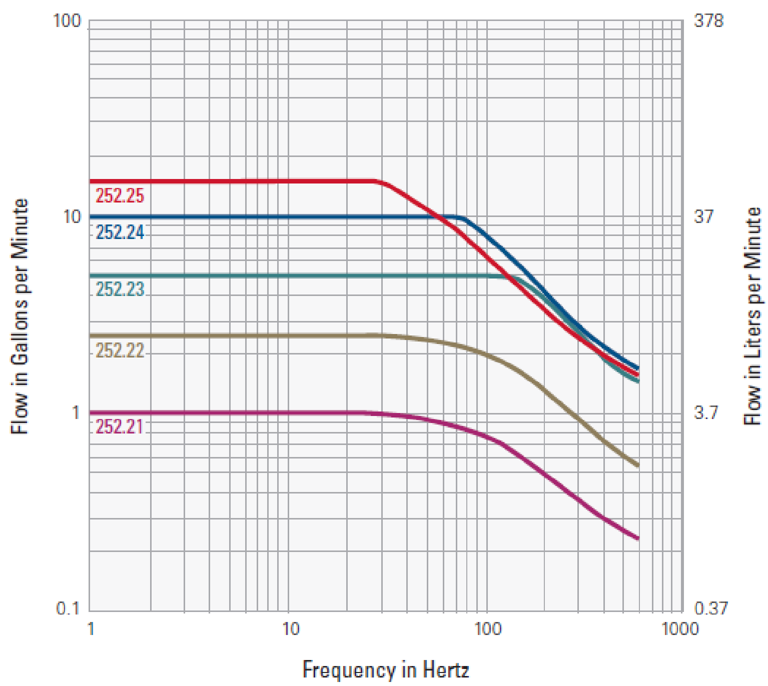

Figure 3.6: Servovalve performance curve [96] — see curve corresponding to MTS 252.25 valve

tradeoff becomes apparent. On one hand, in order to obtain a high-bandwidth system, i.e., for the oil column frequency, ω_{oil}, to be as large as possible, equation (3.9) suggests *reducing* the proof mass. On the other hand, to maximize the utility of the shaker, it is desirable that the actuator can be operated close to its force capacity. It is also beneficial to operate at higher force levels to minimize the contribution of effects such as friction to the applied force. To produce a desired force, reducing the proof mass would result in the need for increased acceleration. A larger acceleration requirement in turn implies greater stroke and velocity demands. The proof mass must be *large enough* to not exceed stroke capacity and force-velocity envelop of the actuator. Therefore, in determining the proof mass, there is an inherent tradeoff between the bandwidth of the shaker on one hand, and its stroke and force-velocity limits on the other. This tradeoff is particular to the use of the shaker as an AMD.

4. Proof mass design

(i) Preliminary weight estimate As a starting point to determine the proof mass, for a target oil column frequency of 40Hz, from equation (3.9), the proof mass, $M_{\text{t}} = 2.22\frac{\text{lb-s}^2}{\text{in}}$, i.e. the weight is 858lb. To understand the stroke demand this implies, consider a desired force of 3000lb at a steady state operating frequency of 10Hz. This requires a displacement of

$$\frac{3000\text{lb}}{2.22\frac{\text{lb-s}^2}{\text{in}} \times (2\pi \times 10\text{Hz})^2} = 0.34\text{in}$$

less than the 3in dynamic stroke of the actuator. On the other hand, the same force at a frequency of 2Hz requires a displacement of

$$\frac{3000\text{lb}}{2.22\frac{\text{lb-s}^2}{\text{in}} \times (2\pi \times 2\text{Hz})^2} = 8.55\text{in}$$

much larger than the stroke. Larger displacements and velocities are necessary at lower frequencies. In dynamic substructuring, when the dominant frequency of the virtual subsystem is low, larger velocity and flow demands arise, possibly resulting in servovalve saturation. Implications of this are discussed in Section 4.4.1.1. The 858lb proof mass is used as preliminary estimate for design.

(ii) Plan dimensions To space the guide rails away from the tie points, the platform is designed to be 3ft wide. For the platform to stay within the extent of the base plate at full stroke, the length (in the actuator direction) is taken to be 4ft.

(iii) Elevation and need for stiffening To elevate the platform above the actuator and servovalve, the posts are made 13in tall, considering also the heights of the guide rails and recirculating bearings (described later). While the elevated configuration helps reduce the shaker footprint, it results in the proof mass being more flexible. The proof mass needs to be stiffened adequately, so that its own natural frequencies are not in the range of interest for testing; for instance, it is desirable for the fundamental frequency of the proof mass to be several times larger than the oil column frequency. The fundamental frequency of the proof mass is estimated using a finite element model.

(iv) Finite element model of the proof mass A finite element model in ABAQUS [100] is used to guide the addition of stiffening elements and the selection of their sizes. An eigenvalue analysis is performed to determine the fundamental frequency of the proof mass model. The model is updated with stiffening elements, and the analysis repeated, until a satisfactorily large fundamental frequency is obtained. This results in the four posts supporting the platform over the bearings being W6 $\times$ 20 sections placed as shown in Figure 3.5. The connecting blocks attaching the platform to the actuator are extended into the platform as shown in elevation view in Figure 3.5, to increase the bending stiffness of the platform. To increase the stiffness associated with relative rotation between the connecting blocks and the posts, HSS6 $\times$ 6 $\times$ 1/2 section tubes are added. Additional stiffeners are welded between the posts and platform, between the tube sections and between the flanges and web of the posts; these additional stiffeners are however not represented in the finite element model.

In modeling the proof mass in ABAQUS CAE, the direction of motion of the shaker is aligned with the global X axis, and the vertical direction with the global Z axis, so that the Y axis is a transverse direction. The platform, posts, connecting blocks and stiffening tubes are created as separate parts. The tubes are discretized using shell elements, and all other parts using solid elements. The parts are then put together in an assembly, and connected using different constraints. The top surfaces of the posts and the connectors are "tied" to the bottom surface of the platform. The tubes are connected to the platform, connecting blocks and posts using shell-to-solid coupling constraints. Boundary conditions are applied by means of reference points. Six reference points are created — four at the base of the posts representing the recirculating bearings, and two at the hinge locations of the actuator swivels. The bottom surfaces of the posts are constrained to the reference points representing the corresponding bearings by rigid-body constraints. The displacements of reference points are constrained in the Y and Z directions; rotations are kept free, a conservative assumption in estimating frequency. The faces of the connecting blocks that attach to the swivels are constrained to the respective swivel reference points by rigid-body constraints. The swivel reference points are fixed from translating, but are free to rotate. The finite element mesh is refined until there is no significant change in the fundamental frequency. The computed fundamental frequency is 213Hz, over five times the estimated oil-column frequency. The corresponding mode shape is shown in Figure 3.7. This was not validated experimentally upon building the shaker, but no frequencies of the proof mass were observed in the 100Hz range of testing.

(v) Total mass With the posts, connecting blocks, tubes and stiffeners added, the total weight becomes 1520lb, which corresponds to a mass of $3.93\frac{\text{lb-s}^2}{\text{in}}$. This does not include the other moving parts — bearings, swivels and actuator piston. The oil column frequency of 30Hz computed based on this mass is therefore approximate. It is measured experimentally in Section 3.5.2 to be 27Hz. At this stage, the design process can be iterated, for example by reducing the thickness of the plate, and instead increasing the size of the supporting posts and the extent of the connecting posts, so that original target oil column frequency of 40Hz is achieved. However, we terminate the design at this stage, deeming the approximately 30Hz oil column frequency as sufficiently high.

Other components and connecting elements

(i) Linear recirculating bearings To minimize friction as the proof mass slides, ball-type

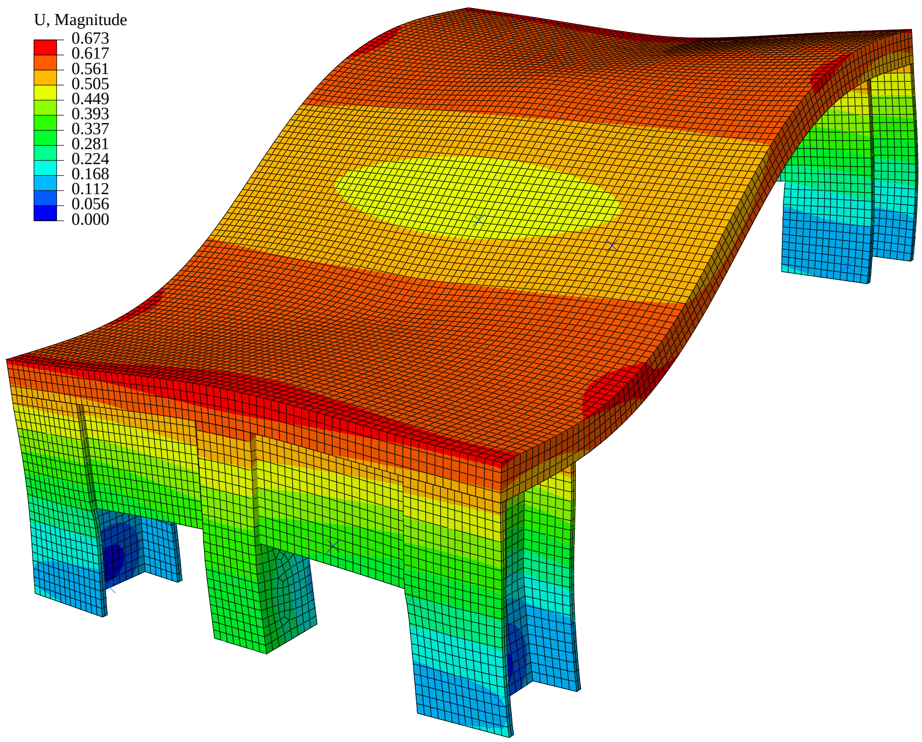

Figure 3.7: First mode of proof mass with computed frequency 213Hz

linear recirculating bearings, IKO LFHTG30 [101], are used. The bearings have fittings to inject lubricant. Apart from having low friction, the specific bearings also provide high rigidity. The load rating for these bearings is shown in Table 3.1. In the use of the shaker as an AMD, the load expected on the bearings comes from a combination of the weight of the proof mass, and resistance to the overturning moment produced by the at most 5.5-kip actuator force at a small elevation from the bearings. This load is small compared to the rated capacity of the bearings. When used as a shake table, care must be taken to ensure that the the additional weight and overturning moment due to the specimen result in loads within the rated capacity of the bearings. The two rails on which the bearings slide extend over the entire length between the bearings plus the stroke of the shaker to avoid alignment errors. The rails are covered with bellows to prevent accumulation of dust, particularly when used in the soil-structure interaction application described in Chapter 5. The surfaces of the base plate, on which the rails are bolted, are machined to minimize

Model	Force rating	Piston area, A_{p}	Dynamic stroke	Static stroke
MTS 244.12, S/N 585	5.5kip	$2.1\mathrm{in}^2$	6in (±3in)	7.2in

(a) Actuator

Model	Nominal flow rate	Operating pressure	Cutoff frequency
MOOG 760 (MTS 252.25)	$15\mathrm{gpm} = 57.75\frac{\mathrm{in}^3}{\mathrm{s}}$	3000psi	30Hz

(b) Servovalve

Model	Dynamic load rating	Static load rating
Ball type, IKOLFHTG30	9.6kip	11.96in

(c) Linear recirculating bearing

Model	Dynamic loading	Static compression	Rotation	Tilt
Shore Western model 981	5.5kip	7.5kip	±90°	±7°

(d) Swivels

Table 3.1: Specifications of shaker components

distortion of the rails.

(ii) Actuator brackets The actuator body is bolted to the base plate using stiffened angle brackets as shown in Figure 3.8c.

(iii) Swivels The actuator piston ends are attached to the platform connecting blocks using Shore Western model 981 swivels as shown in Figures 3.8b and 3.8c. [102,103]. Specifications for these swivels are shown in Table 3.1. The swivels help reduce friction in the actuator seals that could result from misalignment.

(iv) Spiral washers Following standard practice, spiral washers (MTS part 601.11 [104]) are fitted on either side of the load cells (see Section 3.2.4) at the piston ends to reduce backlash.

3.2.4 Instrumentation

The shaker is equipped with the following sensors.

1. **LVDT** A linear variable differential transformer (LVDT) is used to measure the po-

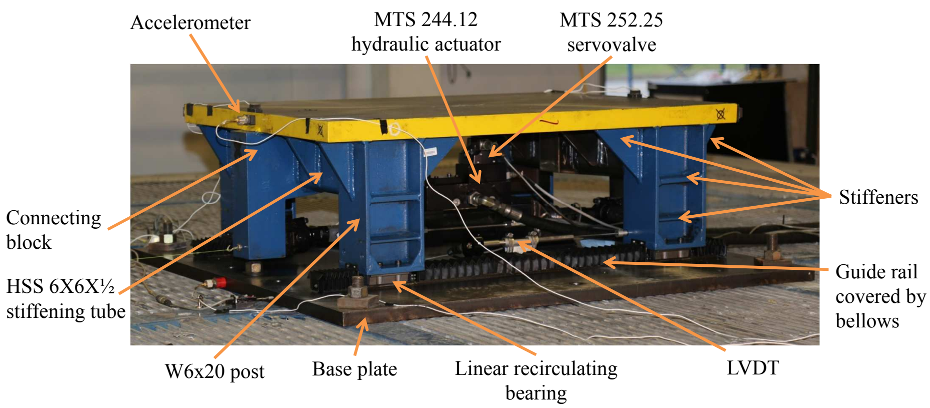

(a) Shaker components

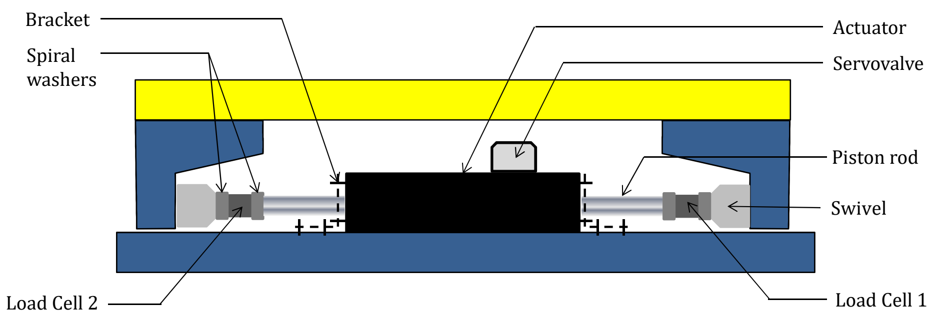

(b) Schematic of shaker assembly

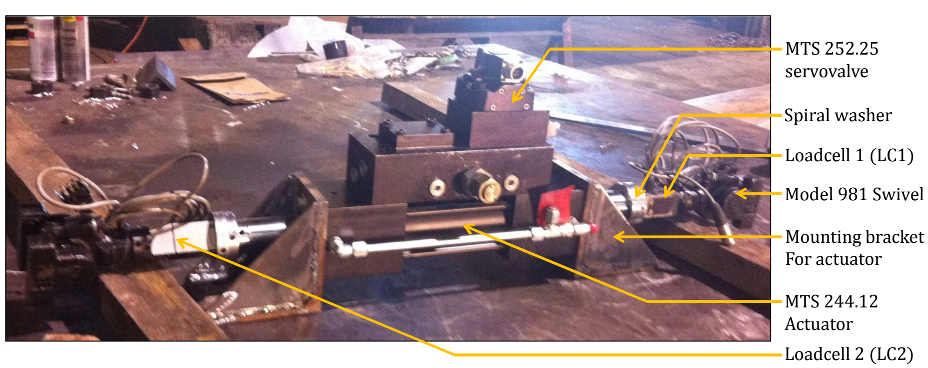

(c) Actuator assembly

Figure 3.8: Uniaxial shaker used as a 1-DOF AMD

Sensor	Calibration factor
LVDT	$0.4\frac{\text{in}}{\text{V}}$
Accelerometer	$1\frac{\text{g}}{\text{V}} = 386.4\frac{\text{in/s}^2}{\text{V}}$
ΔP	$498.8\frac{\text{psi}}{\text{V}}$
LC1 and LC2	$1000\frac{\text{lb}}{\text{V}}$

Table 3.2: Calibration factors for shaker sensors

sition of the proof mass relative to the base plate. Usually, such an LVDT would be located coaxially with the piston in the housing on the reaction side of the actuator. However, since this housing is removed as described in Section 3.2.1, the LVDT body is mounted on the base plate, and the core is connected to one of the platform posts as shown in Figure 3.8a.

2. **Differential pressure (ΔP) cell** A ΔP cell is used to measure the pressure difference between the actuator chambers. Use of the ΔP plays a crucial role in controls for dynamic substructuring.

3. **Load cells** The actuator is furnished with two load cells, LC1 and LC2, one on each end of the piston (see Figures 3.8b and 3.8c). A comparison of the sum of the forces measured by these load cells with the force as estimated from the ΔP cell gives an indication of frictional effects within the actuator itself.

4. **Accelerometer** An accelerometer of 800Hz bandwidth is used to measure the total acceleration of the proof mass.

Signal conditioning hardware for these sensors are described in Section 3.4. The sensor calibration factors are shown in Table 3.2.

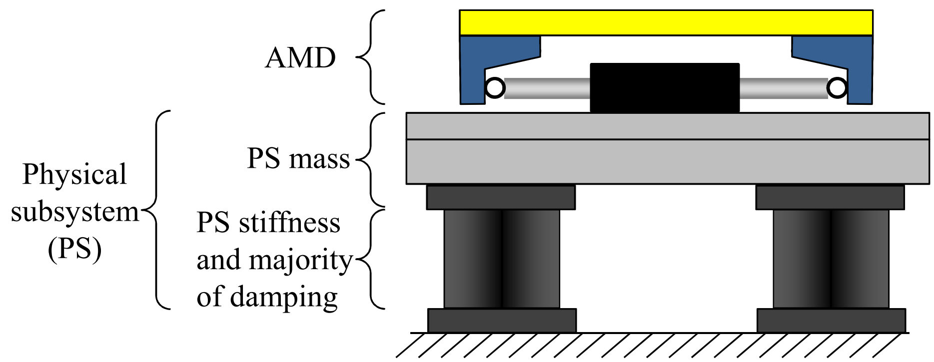

Figure 3.9: Concept of the AMD mounted on a simple physical subsystem. The base plate of the AMD and an additional plate constitute the mass of the physical subsystem; the elastomeric bearings provide the stiffness and majority of the damping. The actuator body and the top end plates of the elastomeric bearings also add to the mass of the physical subsystem, but these are small compared to the two main plates. The concept only shows the vertical bearings; the system also consists of two bearings in the horizontal direction, as seen in Figure 3.10, to restrain out-of-plane motion.

3.3 Resonant physical subsystem

3.3.1 Concept

To facilitate development, a simple instance of the canonical configuration of Figure 4.1a is developed. This consists of a 1DOF physical subsystem with the AMD (shaker) mounted on it, as shown conceptually in Figure 3.9. The physical subsystem is referred to as a *resonant* to contrast it from most conventional DS configurations where the physical subsystem does not have significant inertia effects. Its mass is made of the base plate of the AMD and an additional plate as seen in Figure 3.9. The flexibility of the physical subsystem comes of an assembly of elastomeric bearings; these also provide most of the damping in the physical subsystem.

The assembly consists of six bearings — four in the vertical direction positioned at the four corners similar to a seismic isolation system, and two in the horizontal direction to restrain out-of-plane motion, making the motion of the physical subsystem predominantly planar. The horizontal bearings are attached using a T-section and brackets as indicated in Figures 3.10b and 3.10c. Details of the bearing assembly are provided in Figures 3.11 and

3.12.

The assembly of bearings is chosen as the restoring-force component for the physical subsystem, because it can undergo large reversible deformations, and is therefore forgiving of potential errors or instabilities that might occur during development. Remarkably, as a testament to the simplicity and robustness of the proposed dynamic substructuring strategy, no such instabilities occurred during the experiments described in Chapter 4. It should be noted that the bearing assembly is not intended to represent a particular seismic isolation system; its role is to simply serve as the restoring-force component of a generic 1DOF system.

3.3.1.1 Elastomeric bearings

The elastomeric bearings used are nominally identical low damping rubber bearings from past SEESL projects (serial numbers: 15180, 15174, 15196, 15160, 15163 and 15186 [1, 2]), with properties shown in Figure 3.13 and Table 3.3. The approximate horizontal stiffnesses of the bearings, are obtained using free vibration tests. Each bearing is tested twice with weights of 990lb and 1590lb placed on top. The average value of the horizontal frequency for the six bearings is measured as 3.3Hz and 2.6Hz for the two weights. Based on this, the horizontal stiffness of each bearing is determined as about 1200lb/in. For the assembly of six bearings, the total horizontal stiffness is therefore about 7000lb/in. At higher amplitudes of motion, the stiffness of the bearings decreases [105]. In the experiments of Sections 4.4 and 4.5, when the input excitation is only from the AMD, the amplitude of motion is smaller, and the total horizontal stiffness is about 7000lb/in as above. When the excitation is from the shake table, the displacements are larger, and the stiffness is closer to 6000lb/in. The damping coefficient of the bearings, on the other hand, increases with increasing amplitude of motion [105]. This is also observed in the experimental measurements.

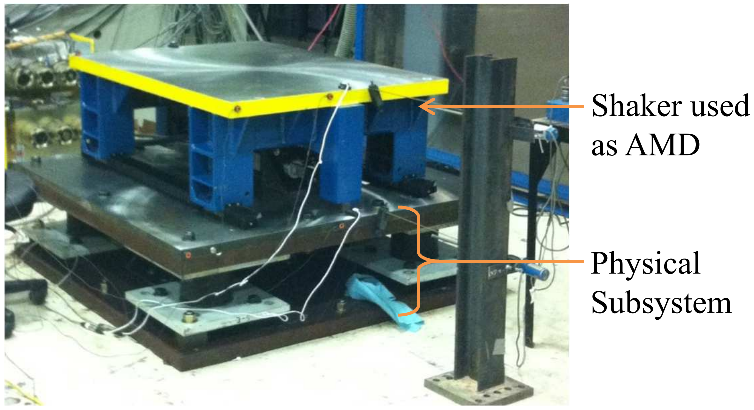

(a) Overview

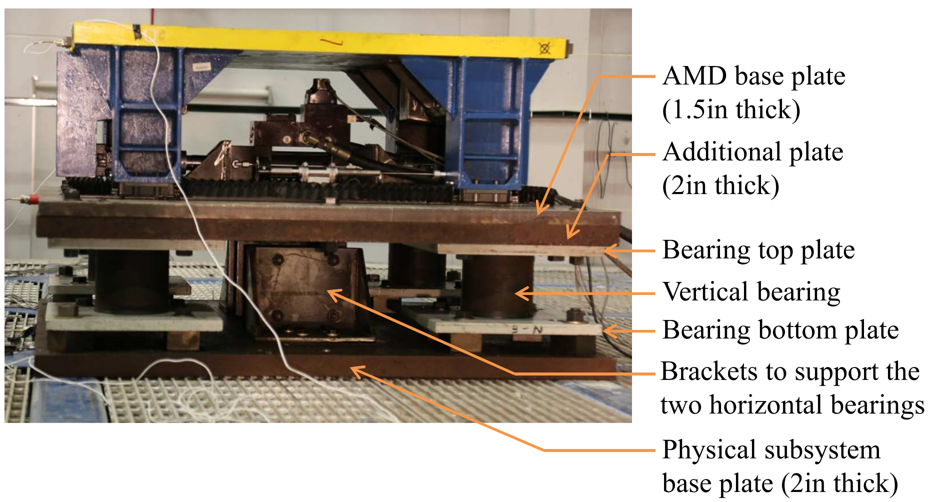

(b) Front view

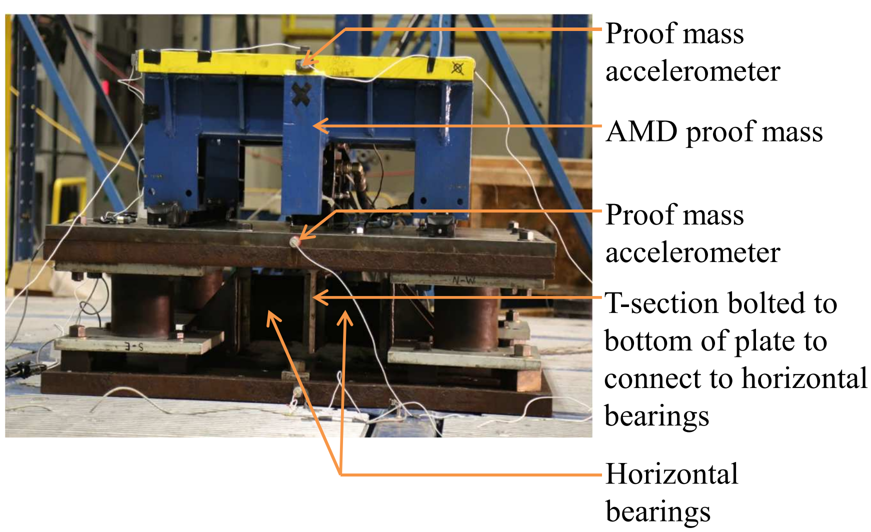

(c) Side view

Figure 3.10: AMD mounted on physical subsystem

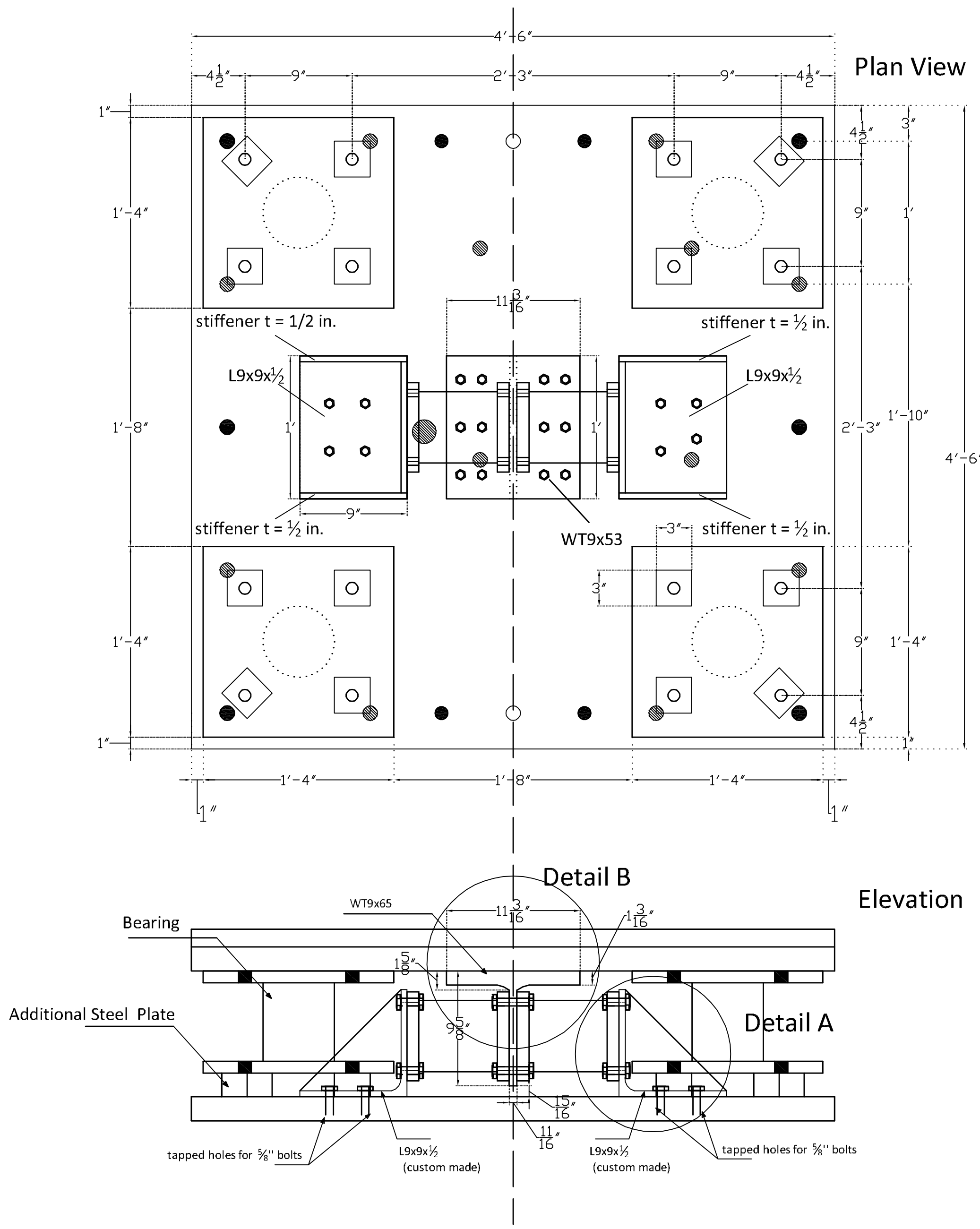

Figure 3.11: CAD drawing of elastomeric bearing assembly in physical subsystem — plan and elevation

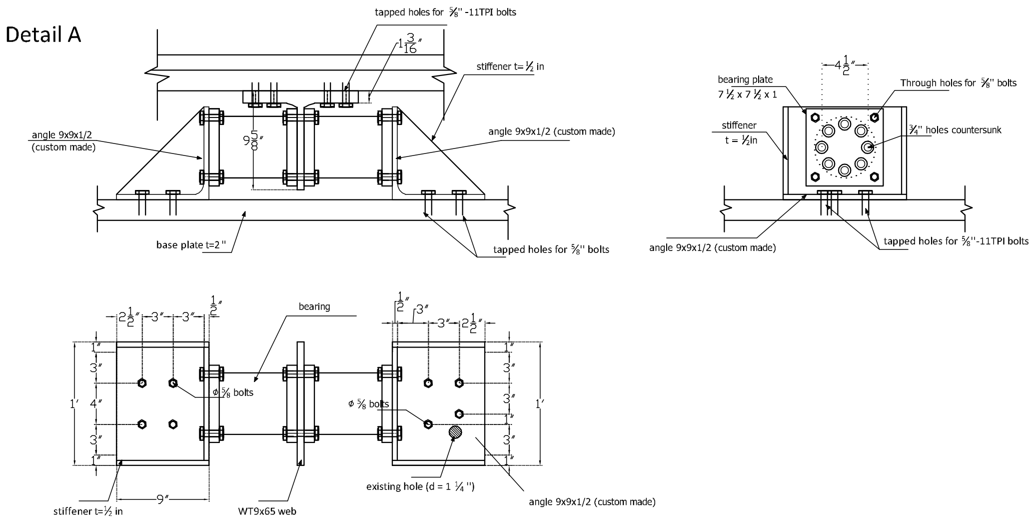

(a) Detail A

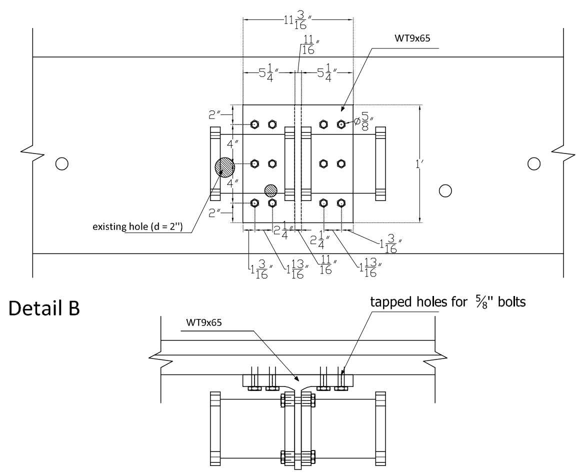

(b) Detail B

Figure 3.12: CAD drawing of elastomeric bearing assembly in physical subsystem — details A and B

Total height	6.418in
Diameter	6.5in
Center hole diameter	1.18in
Area	37.4in^2
Thickness of rubber layer	0.125in
Number of rubber layers	25
Thickness of steel shims	0.0747in
Number of steel shims	24
Cover thickness	0.25in

Table 3.3: Elastomeric-bearing specifications [1, 2]

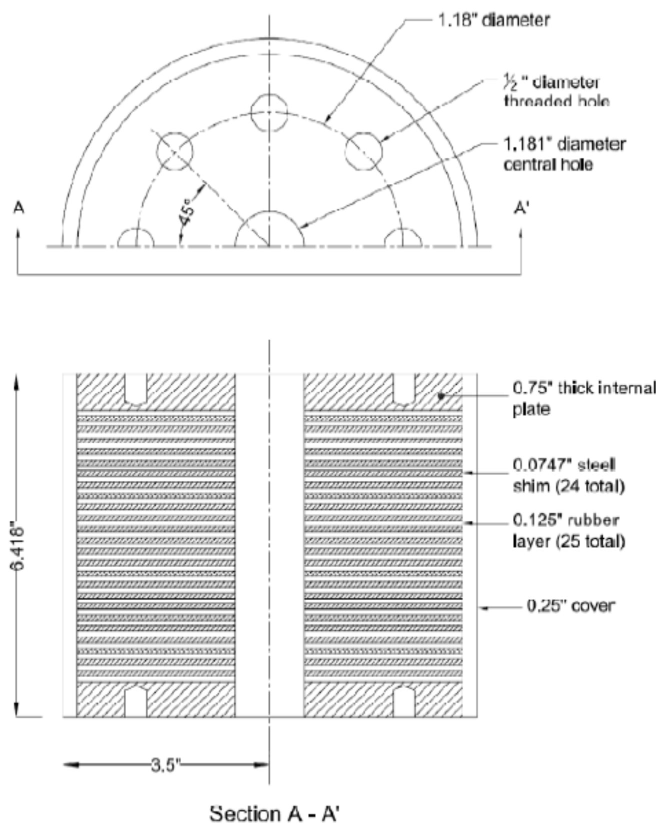

Figure 3.13: Elastomeric-bearing internals [1]

3.3.1.2 Additional instrumentation

In addition to the sensors on the shaker described in Section 3.2.4, an additional accelerometer is added in the horizontal direction at the level of the physical subsystem mass (see Figure 3.10c. The calibration factor for this accelerometer is also 1g/V = $386.4\frac{\text{in/s}^2}{\text{V}}$.

3.3.2 Exploration of rotational motion

Although it is intended that the physical subsystem be 1DOF, with its dominant mode of response in the horizontal direction, subsequent frequency response measurements suggest that there are other resonances at higher frequencies. The hypothesis is that this is due to rotational motion, involving axial deformation of the vertical elastomeric bearings (something not typically considered in the domain of seismic analysis, which is in the low frequency range). To test this hypothesis, two additional sets of instrumentation are used.

1. Vertical accelerometers at the top of the proof mass and base plate (Figure 3.14)

2. A vision-based 3D position tracking system (Figure 3.16)

3.3.2.1 Experiments using accelerometers in the vertical direction

Accelerometers AccelI and AccelIII are placed on the platform of the AMD proof mass, and AccelII and AccelIV on the plates constituting the physical subsystem mass, as shown in Figure 3.14. The frequency responses from the AMD position command to the sums and differences of these vertical accelerometers are measured experimentally with a 2V(0.8in)-amplitude multisine input (see Section 3.5.2.1 on this type of input).

It is observed that the measured acceleration of each side is similar, of the same sign and of quite significant magnitude. The accelerometers on opposite sides, however, show accelerations of opposite signs. These observations suggest that there is vertical motion and/or rocking in the system. Transfer functions are obtained, where the input is the shaker program command, u, and the outputs are the sum and difference of the acceleration obtained by AccelI and AccelIII, and AccelII and AccelIV, shown in Figure 3.15. There are

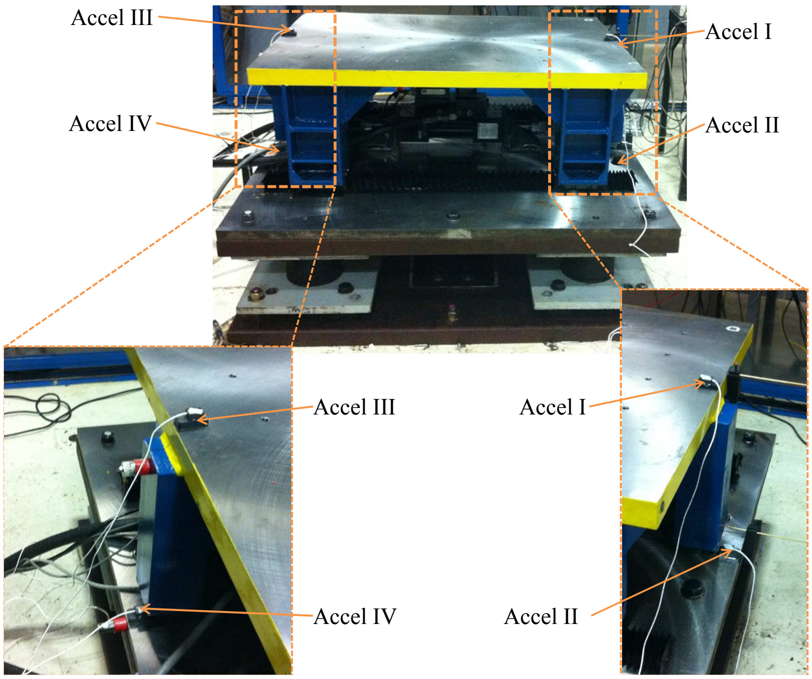

Figure 3.14: Vertical accelerometers for rotation investigation

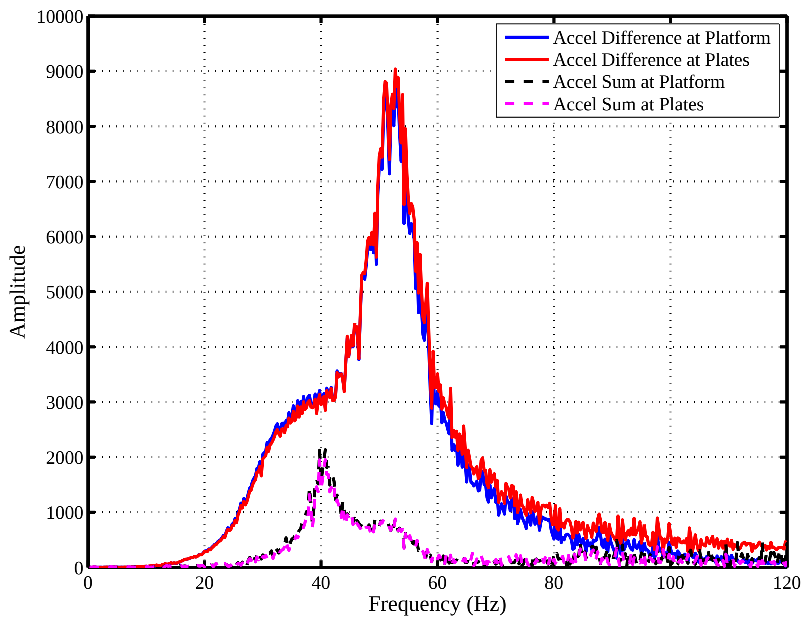

Figure 3.15: Amplitude frequency response of vertical and rotational acceleration

two peaks, one at 40Hz and one close to 55Hz, corresponding to the vertical and rotational degrees of freedom of the system. It is evident that the rotations of both the proof mass and the physical subsystem mass are identical, leading to the conclusion that rotation results from vertical deformation of the bearings. Figure 3.15 also shows that there is coupling between the rotational and vertical translation degrees of freedom.

3.3.2.2 Vision-based 3D position tracking

The 3D rigid body motions of the platform and base are measured using a vision-based 3D position tracking system (Krypton K600 [106]). This system consist of a stereoscopic camera that tracks 3D positions of infrared LEDs by triangulation with 8×10^{-4}in (0.02mm) resolution. With three LEDs each on the proof mass and physical subsystem mass as shown in Figure 3.16b, their rigid body motions can be estimated. The Krypton system can be configured to directly output such rigid motion in terms of screw vectors [107].

For the purposes of the 3D position tracking experiment, a sinusoidal position command of 0.4in amplitude and of increasing frequencies is used, with frequency varying from 1Hz to 70Hz, to investigate how the system responds over a sufficiently large bandwidth. The time range corresponding to the excitation frequencies is shown in Figure 3.17.

Figures 3.18 and 3.19 show the estimated displacements and rotations of the proof mass and the physical subsystem. From these, the following conclusions can be drawn.

1. Comparing the two columns in Figures 3.18 and 3.19, it is clear that there is no relative motion between the proof mass and the physical subsystem mass, except in the X-direction (the direction of shaking).

2. With reference to Figure 3.17, Figures 3.19c and 3.19d show that there is significant rotational motion about the Y-direction over the same frequency range where the frequency response magnitude is large in Figure 3.15 for the difference of accelerations.

3. Figures 3.18e and 3.18f show that there is significant translation in the Z-direction over the same frequency range where the frequency response magnitude is large for

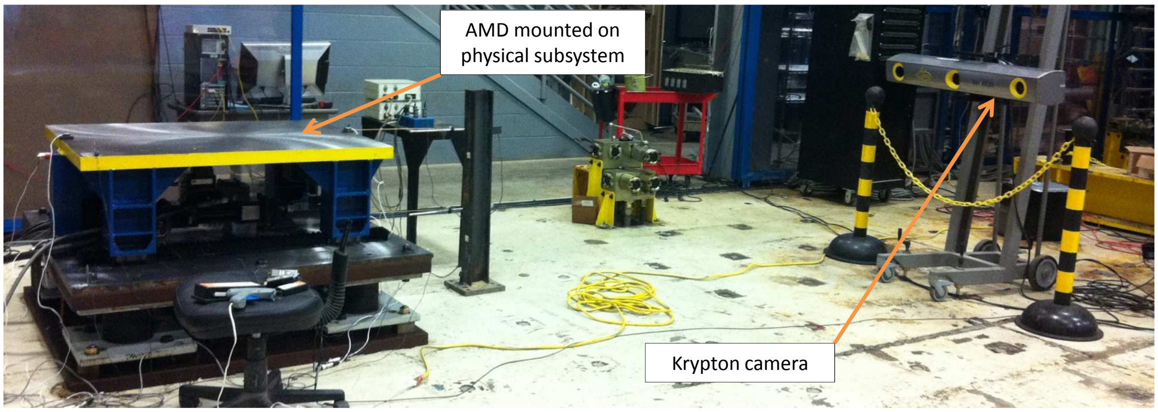

(a) AMD-physical subsystem and Krypton camera

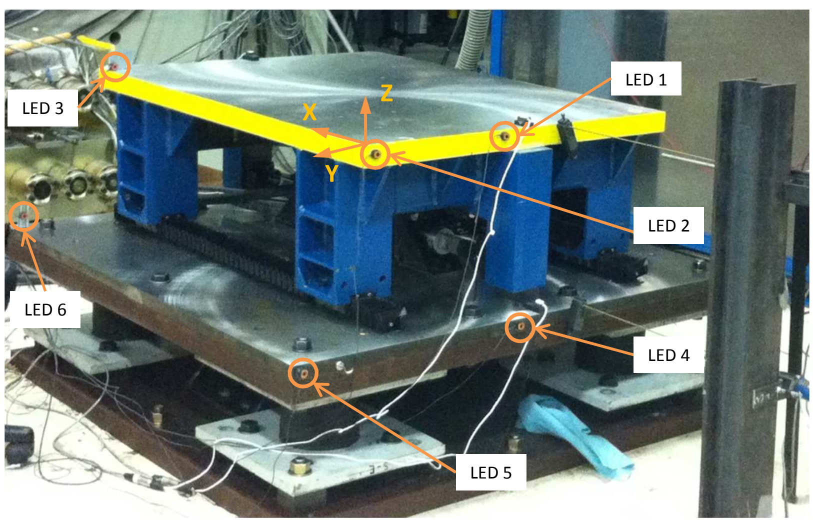

(b) Positions of infrared LED targets and the measurement coordinate system

Figure 3.16: 3D vision-based position tracking (Krypton system)

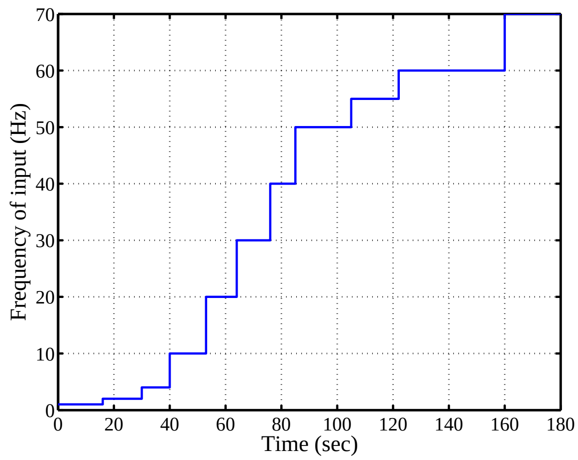

Figure 3.17: Input for 3D position tracking experiment

the sum of accelerations.

4. The X-displacement of the physical subsystem in Figure 3.18b shows a 4Hz-resonance.

5. Figures 3.18c, 3.18d, 3.19e and 3.19f show that despite the horizontal bearings, there is some rotation about the Z-direction (torsion), and displacement in the Y-direction (out-of-plane), which are ignored in further modeling, because these are uncoupled from the in-plane dynamics.

The experimental measurements discussed in Sections 3.3.2.1 and 3.3.2.2 clearly show that vertical displacement and rotational degrees of freedom, and the vertical deformations of the bearings must be modeled to represent the combined AMD-physical subsystem dynamics over a wide frequency range. This is taken in to account in the modeling in the next section.

3.3.3 Modeling the AMD-physical subsystem combination

In this section, the AMD-physical subsystem combination is modeled. This model is not used either for designing DS controls or for assessing DS performance. It is developed simply to obtain a more complete understanding of the testbed, to approach DS with confidence. The model also serves to highlight the role of servovalve dynamics and incidental rotational

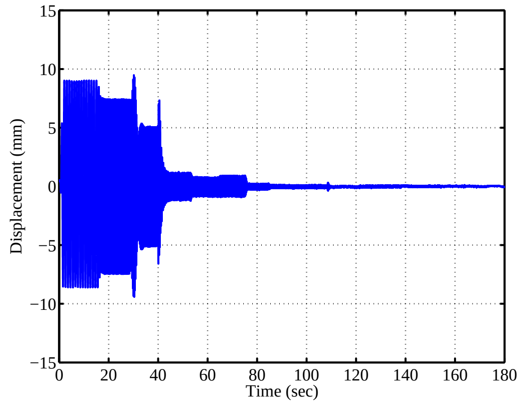

(a) Proof mass X displacement

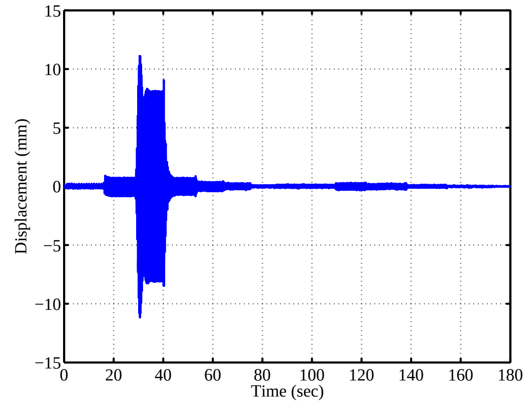

(b) Physical subsystem X displacement

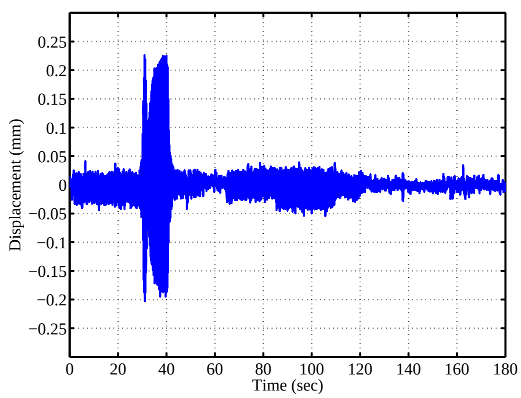

(c) Proof mass Y displacement

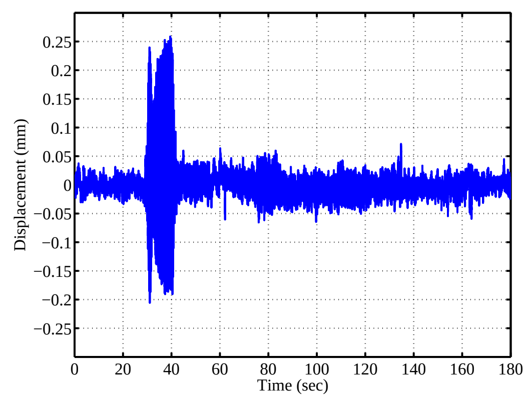

(d) Physical subsystem Y displacement

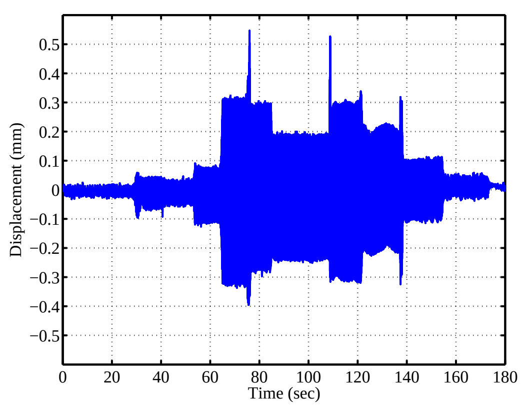

(e) Proof mass Z displacement

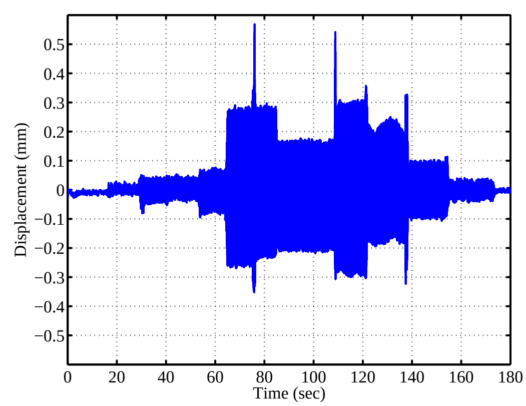

(f) Steel plates z displacement

Figure 3.18: Displacement components of screw vector representing 3D configuration of proof mass and physical subsystem mass

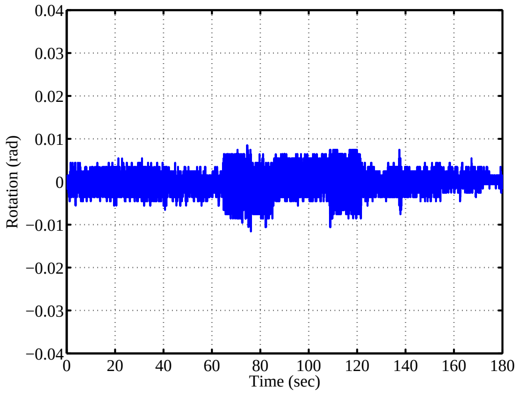

(a) Proof mass X component of rotation vector

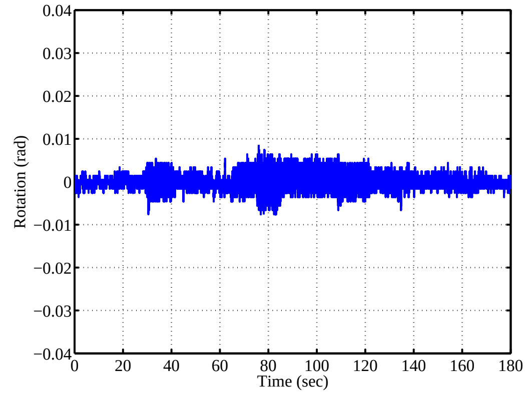

(b) Physical subsystem X component of rotation vector

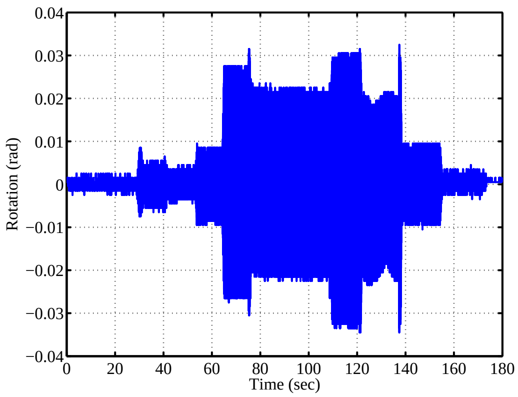

(c) Proof mass Y component of rotation vector

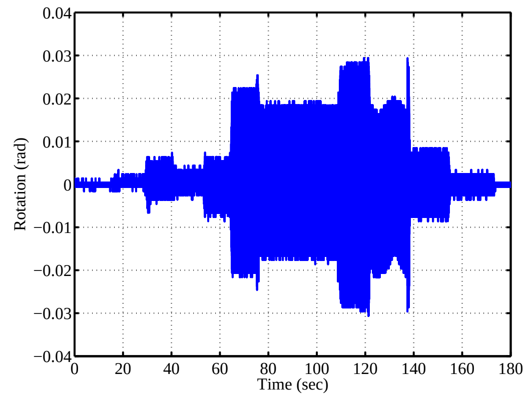

(d) Physical subsystem Y component of rotation vector

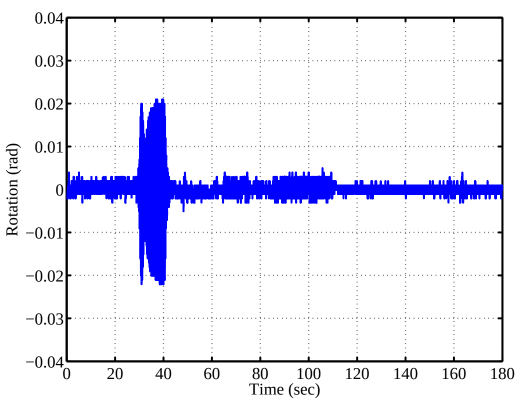

(e) Proof mass Z component of rotation vector

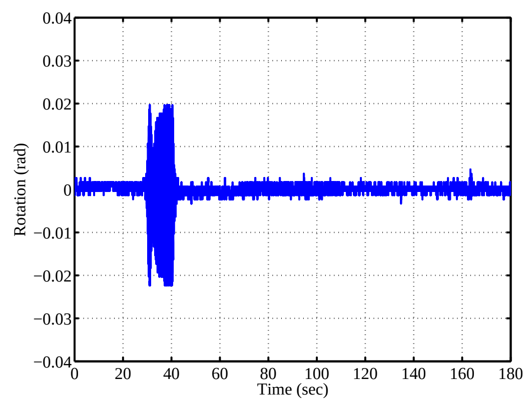

(f) Physical subsystem Y component of rotation vector

Figure 3.19: Rotation components of screw vector representing 3D configuration of proof mass and physical subsystem

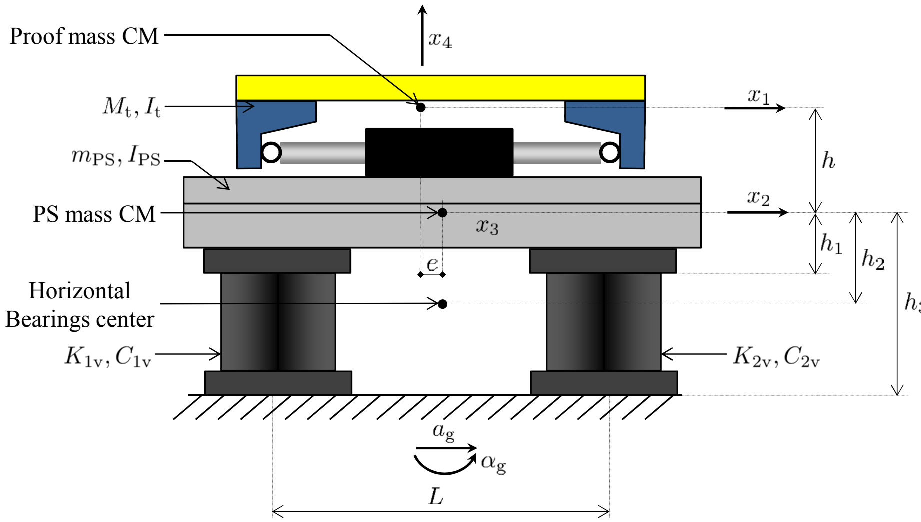

Figure 3.20: Schematic of the AMD mounted on the physical subsystem showing the degrees of freedom of the system, some of the parameters, and translational (a_g) and rotational (α_g) base acceleration components applied to the system

acceleration at the base. Figure 3.20 shows a schematic model of the AMD mounted on the physical subsystem, with a translational acceleration, a_g, and rotational acceleration α_g applied at the base. The degrees of freedom of this model are

x_1 = horizontal displacement of the proof mass relative to the plates making up the mass of the physical subsystem (this is the displacement measured by the shaker LVDT)

x_2 = horizontal displacement of the physical subsystem mass

x_3 = rotation of the physical subsystem mass and AMD (these have the same rotation as established from the experiments in Section 3.3.2)

x_4 = vertical displacement of the physical subsystem mass and AMD

The corresponding velocities are $x_5 = \dot{x}_1, \ldots, x_8 = \dot{x}_8$, and the differential pressure in the actuator is denoted x_9. When servovalve dynamics are considered, the x_{10} is the servovalve state. With this notation, the free body diagrams (FBD) of the proof mass and the combination of the physical subsystem mass and AMD are shown in Figure 3.21 and 3.22.

Writing the equilibrium equations,

1. sum of the horizontal forces in the FBD in Figure 3.21

2. sum of the horizontal forces in the FBD in Figure 3.22

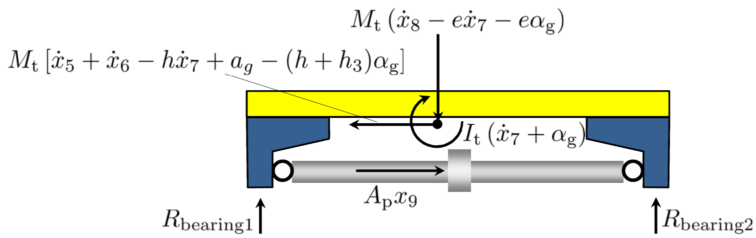

Figure 3.21: Free body diagram of the proof mass; the diagram shows the vertical reactions from the bearings supporting the proof mass, but these reactions do not appear in any of the equilibrium equations considered

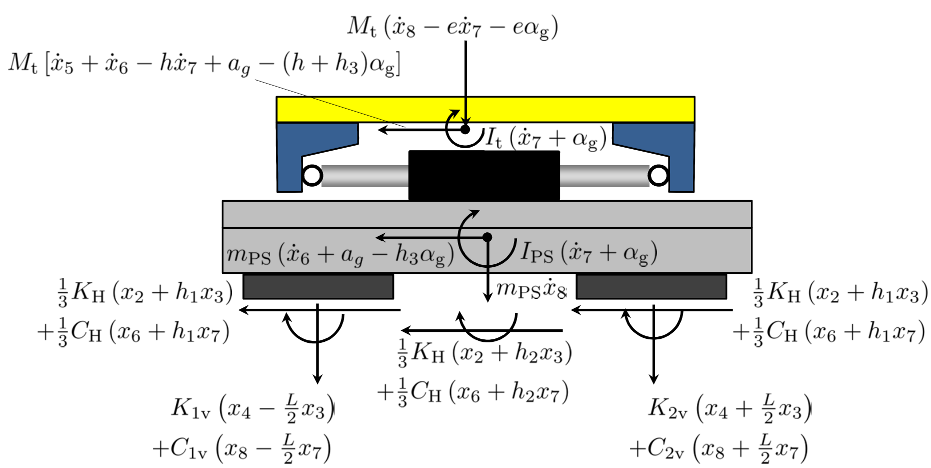

Figure 3.22: Free body diagram of the AMD together with the physical subsystem mass; the diagram shows the bending moments in the vertical bearings and the torsion in the horizontal bearings, but the contributions of these to the restoring moment are small, and are omitted in the equations of equilibrium

3. sum of the moments in the FBD in Figure 3.22 about the center of mass of the physical subsystem mass
4. sum of the vertical forces in the FBD of Figure 3.22

gives in order the four equations represented by

$$\mathcal{M}\ddot{x}_{1:4} + \mathcal{C}\dot{x}_{1:4} + \mathcal{K}x_{1:4} - A_{\mathrm{p}}e_1x_9 + \mathcal{M}e_2a_{\mathrm{g}} + \mathcal{M}(e_3 - h_3e_2)\alpha_{\mathrm{g}} = 0 \tag{3.15a}$$

where the mass matrix

$$\mathcal{M} = \begin{bmatrix} M_{\mathrm{t}} & M_{\mathrm{t}} & -hM_{\mathrm{t}} & 0 \\ M_{\mathrm{t}} & M_{\mathrm{t}} + m_{\mathrm{PS}} & -hM_{\mathrm{t}} & 0 \\ -hM_{\mathrm{t}} & -hM_{\mathrm{t}} & I_{\mathrm{t}} + I_{\mathrm{PS}} + M_{\mathrm{t}}(h^2 + e^2) & -eM_{\mathrm{t}} \\ 0 & 0 & -eM_{\mathrm{t}} & M_{\mathrm{t}} + m_{\mathrm{PS}} \end{bmatrix} \tag{3.15b}$$

the stiffness matrix

$$\mathcal{K} = \begin{bmatrix} 0 & 0 & 0 & 0 \\ 0 & K_{\mathrm{H}} & K_{\mathrm{H}}\left(\frac{2}{3}h_1 + \frac{1}{3}h_2\right) & 0 \\ 0 & K_{\mathrm{H}}\left(\frac{2}{3}h_1 + \frac{1}{3}h_2\right) & K_{\mathrm{H}}\left(\frac{2}{3}h_1^2 + \frac{1}{3}h_2^2\right) + (K_{1\mathrm{v}} + K_{2\mathrm{v}})\frac{L^2}{4} & (K_{2\mathrm{v}} - K_{1\mathrm{v}})\frac{L}{2} \\ 0 & 0 & (K_{2\mathrm{v}} - K_{1\mathrm{v}})\frac{L}{2} & K_{1\mathrm{v}} + K_{2\mathrm{v}} \end{bmatrix} \tag{3.15c}$$

the damping matrix, $\mathcal{C}$, is identical in form to the stiffness matrix $\mathcal{K}$, with the stiffnesses K_{H}, $K_{1\mathrm{v}}$ and $K_{2\mathrm{v}}$ replaced with the damping coefficients C_{H}, $C_{1\mathrm{v}}$ and $C_{2\mathrm{v}}$, $e_1 = \{1, 0, 0, 0\}^\top$, $e_2 = \{0, 1, 0, 0\}^\top$ and $e_3 = \{0, 0, 1, 0\}^\top$. It should be mentioned here that the stiffness K_{H} refers to the total horizontal stiffness of the bearing system and the stiffnesses $K_{1\mathrm{v}}$ and $K_{2\mathrm{v}}$ are the vertical stiffness of the two elastomeric bearings located on each side respectively. The distances h, h_1, h_2, e and L in these matrices are as shown in Figure 3.20.

Combining equation (3.15a) with the differential pressure equation (third of equation (3.13)), or the differential pressure and servovalve equations (third and fourth of equations (3.14)), we get the state space representation

$$\begin{aligned} \dot{x} &= Ax + Bu + E\left(\begin{smallmatrix} a_{\mathrm{g}} \\ \alpha_{\mathrm{g}} \end{smallmatrix}\right) \\ y &= Cx \end{aligned} \tag{3.16a}$$

where

$$
\begin{aligned}
A &= \begin{bmatrix} 0_{4\times 4} & I_{4\times 4} & 0_{4\times 1} \\ -\mathcal{M}^{-1}\mathcal{K} & -\mathcal{M}^{-1}\mathcal{C} & A_{\mathrm{p}}\mathcal{M}^{-1}e_1 \\ -dK_{\mathrm{e}}e_1^\top & -\left(dK_{\mathrm{d}} + \frac{\omega_{\mathrm{oil}}^2 M_{\mathrm{t}}}{A_{\mathrm{p}}}\right)e_1^\top & -\left(dK_{\mathrm{p}} + 2\zeta_{\mathrm{oil}}\omega_{\mathrm{oil}}\right) \end{bmatrix} \\
B &= \begin{bmatrix} 0_{1\times 8} & dK_{\mathrm{e}} \end{bmatrix}^\top \\
E &= \begin{bmatrix} 0_{4\times 1} & 0_{4\times 1} \\ -e_2^\top & -(e_3 - h_3 e_2) \\ 0 & 0 \end{bmatrix}
\end{aligned}
\tag{3.16b}
$$

if servovalve dynamics are not modeled, and

$$
\begin{aligned}
A &= \begin{bmatrix} 0_{4\times 4} & I_{4\times 4} & 0_{4\times 1} & 0_{4\times 1} \\ -\mathcal{M}^{-1}\mathcal{K} & -\mathcal{M}^{-1}\mathcal{C} & A_{\mathrm{p}}\mathcal{M}^{-1}e_1 & 0_{4\times 1} \\ 0_{1\times 4} & -\frac{\omega_{\mathrm{oil}}^2 M_{\mathrm{t}}}{A_{\mathrm{p}}}e_1^\top & -2\zeta_{\mathrm{oil}}\omega_{\mathrm{oil}} & d \\ -\alpha_{\mathrm{s}}K_{\mathrm{e}}e_1^\top & -\alpha_{\mathrm{s}}K_{\mathrm{d}}e_1^\top & -\alpha_{\mathrm{s}}K_{\mathrm{p}} & -\alpha_{\mathrm{s}} \end{bmatrix} \\
B &= \begin{bmatrix} 0_{1\times 9} & \alpha_{\mathrm{s}}K_{\mathrm{e}} \end{bmatrix}^\top \\
E &= \begin{bmatrix} 0_{4\times 1} & 0_{4\times 1} \\ -e_2^\top & -(e_3 - h_3 e_2) \\ 0_{2\times 1} & 0_{2\times 1} \end{bmatrix}
\end{aligned}
\tag{3.16c}
$$

if servovalve dynamics are included as discussed in Section 3.2.2.4. The output y consists of measured quantities,

$y_1 =$ horizontal displacement of the proof mass relative to the physical subsystem (LVDT measurement)

$y_2 =$ differential pressure in the actuator

$y_3 =$ total acceleration of the proof mass relative to an inertial reference, i.e., $\dot{x}_5 + \dot{x}_6 - h\dot{x}_7 + a_{\mathrm{g}} - (h + h_3)\alpha_{\mathrm{g}}$

$y_4 =$ total acceleration of the physical subsystem, i.e., $\dot{x}_6 + a_{\mathrm{g}} - h_3\alpha_{\mathrm{g}}$

Then, if servovalve dynamics are not considered,

$$
C = \begin{bmatrix} 1 & 0 & 0 & 0 & 0 & 0 & 0 & 0 & 0 \\ 0 & 0 & 0 & 0 & 0 & 0 & 0 & 0 & 1 \\ 0 & 0 & 0 & 0 & 0 & 0 & 0 & 0 & \frac{A_{\mathrm{p}}}{M_{\mathrm{t}}} \\ 0 & -\frac{K_{\mathrm{H}}}{m_{\mathrm{PS}}} & -\frac{K_{\mathrm{H}}}{m_{\mathrm{PS}}}\left(\frac{2}{3}h_1 + \frac{1}{3}h_2\right) & 0 & 0 & -\frac{C_{\mathrm{H}}}{m_{\mathrm{PS}}} & -\frac{C_{\mathrm{H}}}{m_{\mathrm{PS}}}\left(\frac{2}{3}h_1 + \frac{1}{3}h_2\right) & 0 & -\frac{A_{\mathrm{p}}}{m_{\mathrm{PS}}} \end{bmatrix}
\tag{3.16d}
$$

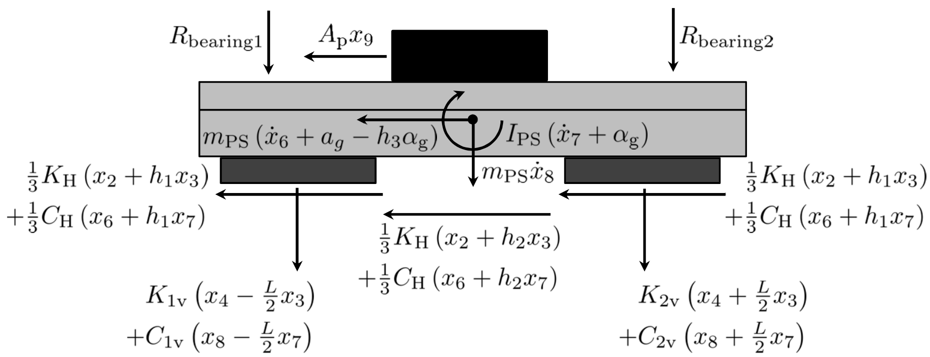

Figure 3.23: Free body diagram of the physical subsystem mass

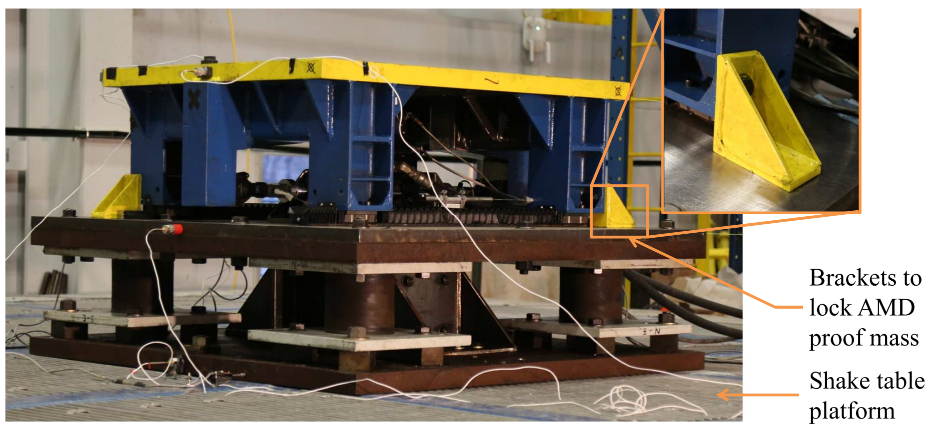

Figure 3.24: Configuration with proof mass locked — AMD and PS with AMD proof mass locked placed on shake table

The third row of C comes from the first of equations (3.15a), the sum of horizontal forces in the FBD of Figure 3.21. The fourth row of C is obtained by substituting the first of equations (3.15a) in the second, or equivalently from summing the horizontal forces in the FBD of the physical subsystem mass (Figure 3.23). If servovalve dynamics are included, then matrix C has a tenth column consisting of zeros.

3.3.3.1 Model of combined AMD-PS with proof mass locked

To further characterize the testbed, experiments are carried out with the proof mass of the AMD locked as shown in Figure 3.24. There is then clearly no control input to the AMD. The shake table applies base acceleration input. The equation of motion for this configuration can be obtained by setting $x_1 = 0$, $\dot{x}_1 = 0$ and $\ddot{x}_1 = 0$ in equation (3.15a).

Formally, this is done using the transformation

$$x_{1:3}^{\text{locked}} = \mathcal{T} x_{1:4} \tag{3.17}$$

where $\mathcal{T} = \begin{bmatrix} 0_{3\times 1} & I_{3\times 3} \end{bmatrix}^\top$. The velocities are also related by $x_{4:6}^{\text{locked}} = \mathcal{T} x_{5:8}$. Substituting in equation (3.15a), and multiplying from the left by $\mathcal{T}^\top$, we get

$$\mathcal{M}^{\text{locked}} \ddot{x}_{1:3}^{\text{locked}} + \mathcal{C}^{\text{locked}} \dot{x}_{1:3}^{\text{locked}} + \mathcal{K}^{\text{locked}} x_{1:3}^{\text{locked}} + \mathcal{M}^{\text{locked}} e_1 a_{\text{g}} + \mathcal{M}^{\text{locked}} (e_2 - h_3 e_1) \alpha_{\text{g}} = 0 \tag{3.18a}$$

where

$$\mathcal{M}^{\text{locked}} = \mathcal{T}^\top \mathcal{M} \mathcal{T}; \quad \mathcal{C}^{\text{locked}} = \mathcal{T}^\top \mathcal{C} \mathcal{T}; \quad \mathcal{K}^{\text{locked}} = \mathcal{T}^\top \mathcal{K} \mathcal{T} \tag{3.18b}$$

and $e_1 = \{1, 0, 0\}^\top$. The state space representation is

$$\begin{aligned} \dot{x}^{\text{locked}} &= A^{\text{locked}} x + E^{\text{locked}} \left(\begin{smallmatrix} a_{\text{g}} \\ \alpha_{\text{g}} \end{smallmatrix} \right) \\ y^{\text{locked}} &= C^{\text{locked}} x \end{aligned} \tag{3.19a}$$

where

$$\begin{aligned} A^{\text{locked}} &= \begin{bmatrix} 0_{3\times 3} & I_{3\times 3} \\ -\left(\mathcal{M}^{\text{locked}}\right)^{-1} \mathcal{K}^{\text{locked}} & \left(\mathcal{M}^{\text{locked}}\right)^{-1} \mathcal{C}^{\text{locked}} \end{bmatrix} \\ E^{\text{locked}} &= \begin{bmatrix} 0_{1\times 3} & 0_{1\times 3} \\ -e_1^\top & -(e_2 - h_3 e_1) \end{bmatrix} \end{aligned} \tag{3.19b}$$

The output of interest, y^{locked}, consists of the accelerations at the levels of the of the PS mass and the AMD proof mass, and

$$C^{\text{locked}} = \begin{bmatrix} A_{4,:}^{\text{locked}} \\ A_{4,:}^{\text{locked}} - h A_{5,:}^{\text{locked}} \end{bmatrix} \tag{3.19c}$$

Here, MATLAB notation has been used; $A_{i,:}^{\text{locked}}$ refers to the i^{th} row of A^{locked}.

Parameter	Value
Proof mass weight (mass, M_{t})	1520lb ($3.93\frac{\text{lb-s}^2}{\text{in}}$)
Actuator piston area (A_{p})	2.1in^2
Physical subsystem weight (mass, m_{PS})	2890lb ($7.50\frac{\text{lb-s}^2}{\text{in}}$)
Distance L in Figure 3.20	36in
Distance h in Figure 3.20	16in
Distance h_1 in Figure 3.20	2.75in
Distance h_2 in Figure 3.20	5.625in
Distance h_3 in Figure 3.20	14.5in

Table 3.4: Parameters of the AMD-PS model that are directly measured

3.3.4 Model parameters

The parameters of the AMD-PS model are presented here. Some of these parameters, such as distances and weights, are measured directly. Other parameters, for instance the horizontal stiffness of the bearings and damping, are deduced from other experimental measurements. The parameters that are directly measured are shown in Table 3.4.

The combined horizontal stiffness of the bearing system is $K_{\mathrm{H}} = 7000\text{lb/in}$ at low amplitudes and could reduce to 6000lb/in at higher amplitudes as described in Section 3.3.1.1. The approximate horizontal frequency of the system can then be calculated as

$$\frac{1}{2\pi}\sqrt{\frac{K_{\mathrm{H}}}{M_{\mathrm{t}} + m_{\mathrm{PS}}}} = 3.94\text{Hz}$$

The moment of inertia of the physical subsystem mass is computed as

$$I_{\mathrm{PS}} = \frac{(7.5\frac{\text{lb-s}^2}{\text{in}})(54\text{in})^2}{12} = 1820\text{lbs}^2\text{in} \tag{3.20}$$

where 54in is the width of the plates comprising the physical subsystem mass. The computation of the moment of inertia, I_{t}, of the proof mass (platform) is however more involved, since it consists of a number of different components. It is therefore computed using AutoCAD based on the 3D CAD model shown in Figure 3.25. I_{t} is computed as 1038lbs^{2}in.

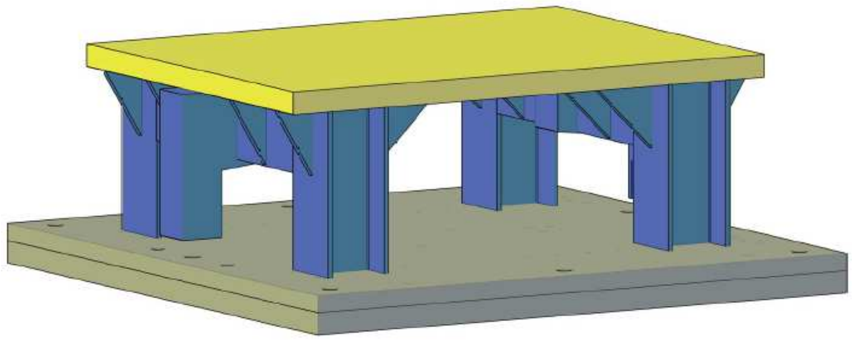

Figure 3.25: 3D AutoCAD model for moment of inertia calculation

Parameter	Value
I_{t}	$1038 \mathrm{lbs}^2\mathrm{in}$
I_{PS}	$1820 \mathrm{lbs}^2\mathrm{in}$

Table 3.5: Computed parameters of the AMD-PS model

A number of other parameters, shown in Table 3.6, are deduced from experimental measurements. These include the AMD oil-column frequency, damping and input coefficient d, and the stiffness and damping properties of the elastomeric bearing system. In particular, the estimated vertical stiffness of the bearings differs significantly from that calculated from empirical formulas [105, 108]. This is attributed to the bearings used in here having been subjected to past destructive testing in the vertical direction [1, 2]).

3.4 Hardware and software components

This section describes the different hardware and software components used for measurement and control in the testbed. An overview of these components is shown in Figure 3.26.

Table 3.6: Parameters of the AMD-PS model deduced from experimental measurements

Parameter	Value
From experiments in Section 3.5.2	
Oil column frequency, $\omega_{\text{oil}}/2\pi^{a}$	27Hz
Oil column damping, ζ_{oil}	0.14
Input coefficient, d (equation (3.11))	12×10^4psi/s/V
From experiments in Section 3.5.4 (see Figures 3.20 and 3.22 for notation)	
Horizontal stiffness of bearing system, K_{H} (see Section 3.3.1.1)	6,000-7,000lb/in
Horizontal damping coefficient of bearing system, C_{H}	$22.9\frac{\text{lb-s}}{\text{in}}$
Vertical stiffness of bearings, $K_{1\text{v}}$ (see also Section 3.3.2)	360,000lb/in
Vertical stiffness of bearings, $K_{2\text{v}}$	380,000lb/in
Vertical damping coefficient of bearings, $C_{1\text{v}}{}^{c}$	$81.1\frac{\text{lb-s}}{\text{in}}$
Vertical damping coefficient of bearings, $C_{2\text{v}}{}^{c}$	$83.4\frac{\text{lb-s}}{\text{in}}$

[a] Oil column frequency calculated from equation (3.9) is also close to this value
[b] $\frac{C_{\text{H}}}{2\sqrt{K_{\text{H}} m_{\text{PS}}}} = 0.05$, damping ratio for horizontal vibration = 5%
[c] $\frac{C_{1\text{v}}+C_{2\text{v}}}{2\sqrt{(C_{1\text{v}}+C_{2\text{v}})(M_{\text{t}}+m_{\text{PS}})}} \approx 0.03$, damping ratio in the vertical direction is 3%; when calibrating $C_{1\text{v}}$ and $C_{2\text{v}}$ to experimental measurements, the trial and error process is carried out on the damping ratios, rather than directly on the damping coefficients.

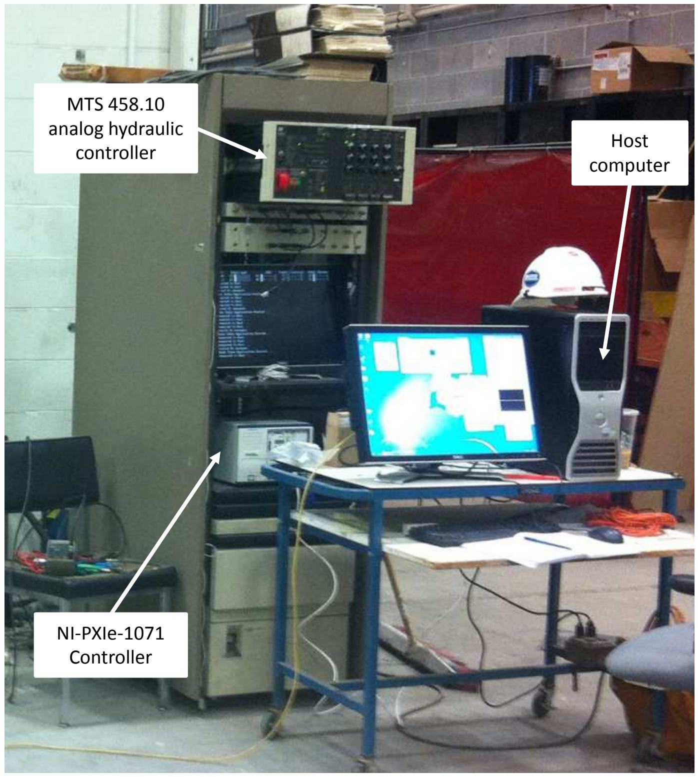

(a) Hardware components

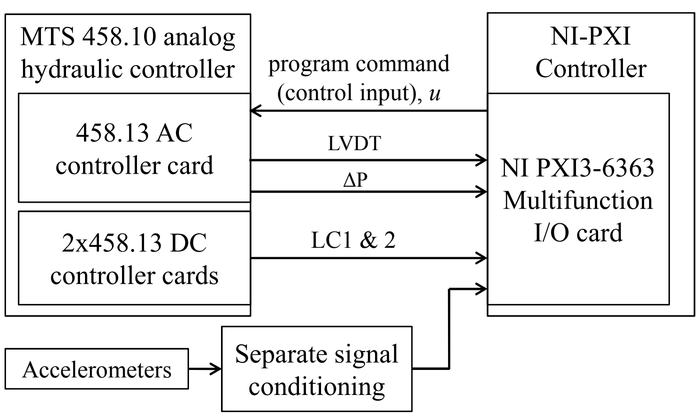

(b) Schematic of measurement and control hardware

Figure 3.26: Overview of hardware components

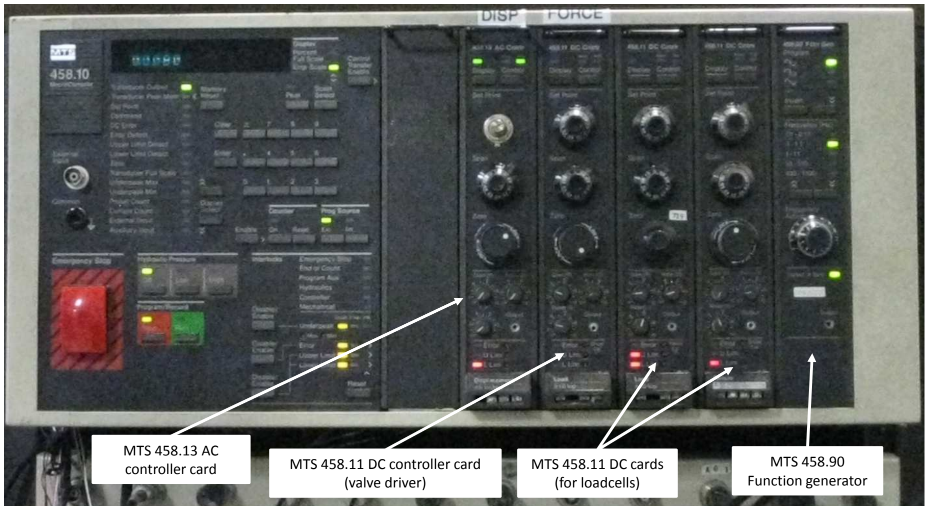

Figure 3.27: MTS 458 analog hydraulic controller

3.4.1 Hydraulic controller

The shaker is driven by an MTS 458 analog hydraulic controller, shown in Figure 3.27. The specific controller is selected because it provides access to internal signals such as the error and valve command, and allows for the adjustment of the ranges of gains and filters through jumper settings and circuit modifications such as switching out resistors. For the purposes of this work, the following two modules are used.

1. An MTS 458.13 AC controller card with a ΔP daughter board, which conditions the LVDT and ΔP signals, and implements a PID loop and ΔP feedback. As described in Section 3.2.2.3, only the proportional and ΔP gains are used, and not the derivative and integral gains.

2. Two MTS 458.11 DC controller cards, used simply to condition signals from the two actuator load cells.

It should be reiterated here that the purpose of the feedback implemented in the hydraulic controller is not to track position, but simply to reduce the effects of nonlinearities and model uncertainties. The control gains are therefore not tuned for tracking. The effects of varying control gains are demonstrated in Section 3.5.2. The proportional gain K_{e} and the

ΔP gain K_p can be adjusted using knobs in the front panel of the controller (Figure 3.27). The K_e knob has settings from 1 to 10, and the K_p knob from 0 to 10. To incorporate these gains in modeling, these knob settings must be related to the gain values in engineering units. This relationship can be obtained from the resistance values used for gain adjustment in the controller circuit shown in Figure 3.28. Let α denote the fraction of the full range to which the gain knob is turned. Then the two gains in engineering units are given by

$$\begin{aligned} K_\mathrm{e} &= \frac{100\mathrm{K}}{\frac{(1-\alpha)(20\mathrm{K})(200\mathrm{K})}{(1-\alpha)20\mathrm{K}+200\mathrm{K}} + 2\mathrm{K}} \mathrm{V/V} \frac{1}{0.4\mathrm{in/V}} \\ K_\mathrm{p} &= \frac{100\mathrm{K}}{(1-\alpha)500\mathrm{K} + 2.3\mathrm{K}} \mathrm{V/V} \frac{1}{498.8\mathrm{psi/V}} \end{aligned} \tag{3.21}$$

which include the LVDT and ΔP calibration factors from Table 3.2. To verify these equations, experiments are performed with different knob settings and using various signals as program command (control input), u. The program command u, valve command u_v, LVDT signal x_1, and differential pressure x_3 are measured. Recalling that the valve command is given by (equation (3.12) with $K_\mathrm{d} = 0$)

$$u_\mathrm{v} = K_\mathrm{e}(u - x_1) - K_\mathrm{p} x_3$$

K_e and K_p are estimated in each case using linear regression (in MATLAB, simply `[u-x1 -x_3]\uv`). Results are shown in Figure 3.29 and Table 3.7. The values given here are average values of the different tests.

3.4.2 Other hardware components

NI PXI realtime controller An NI PXI-8115 controller is used as the realtime platform. An NI PXIe 6363 Multifunction IO card is used for input and output of signals as shown in Figure 3.26b. The controller is run as a sampling frequency of 1024Hz.

Acceleration signal conditioning hardware This component is used to interface with accelerometers (Figure 3.30).

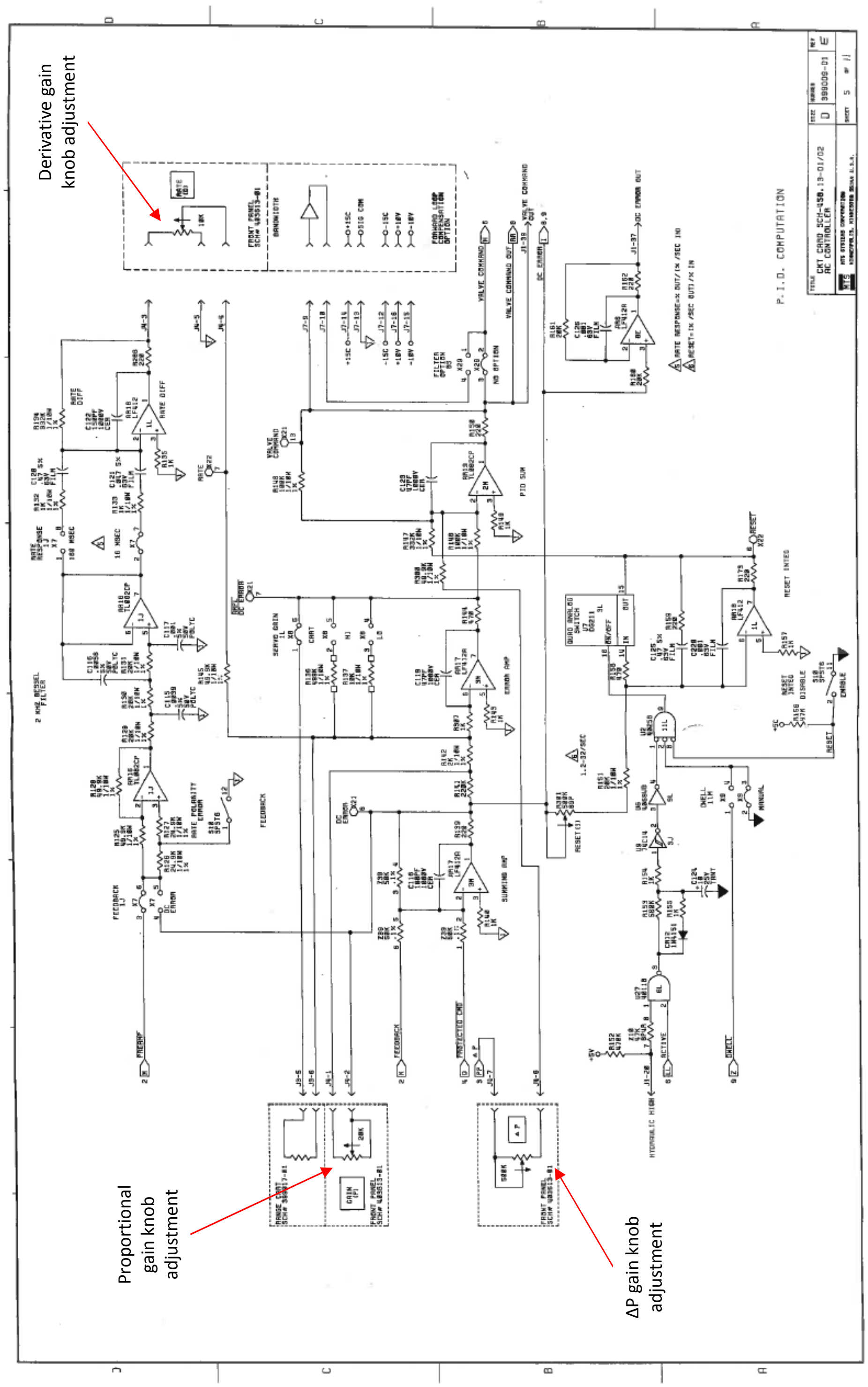

Figure 3.28: Schematic of MTS 458.13 analog controller card

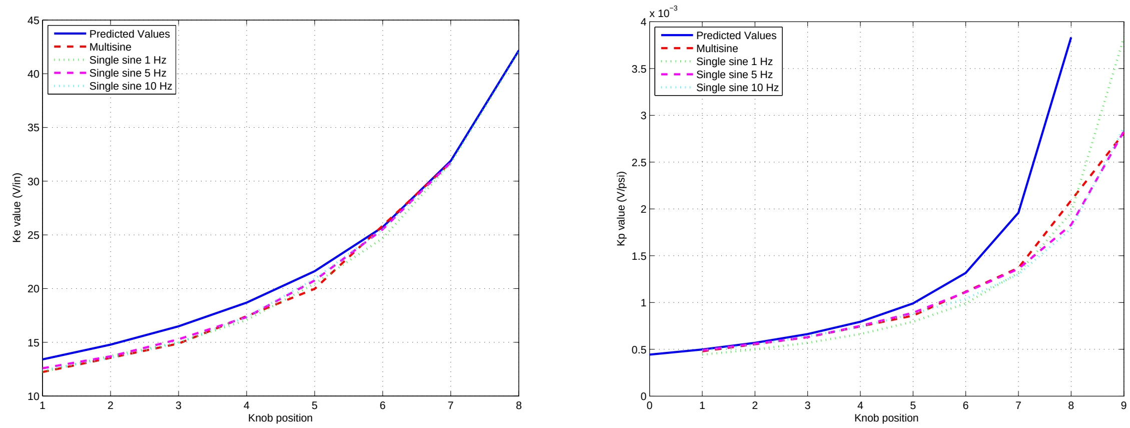

(a) Proportional gain, K_e calibration (b) ΔP gain, K_p calibration

Figure 3.29: Controller knob settings related to gains in engineering units

Knob value	K_e(V/in)	K_p(V/psi)
1	12.24	0.00049
2	13.73	0.00055
3	14.99	0.00064
4	17.07	0.00074
5	20.45	0.00088
6	24.68	0.00104
7	31.67	0.00130
8	42.06	0.00179
9	N/A	0.00283

Table 3.7: Calibration of gains K_e and K_p

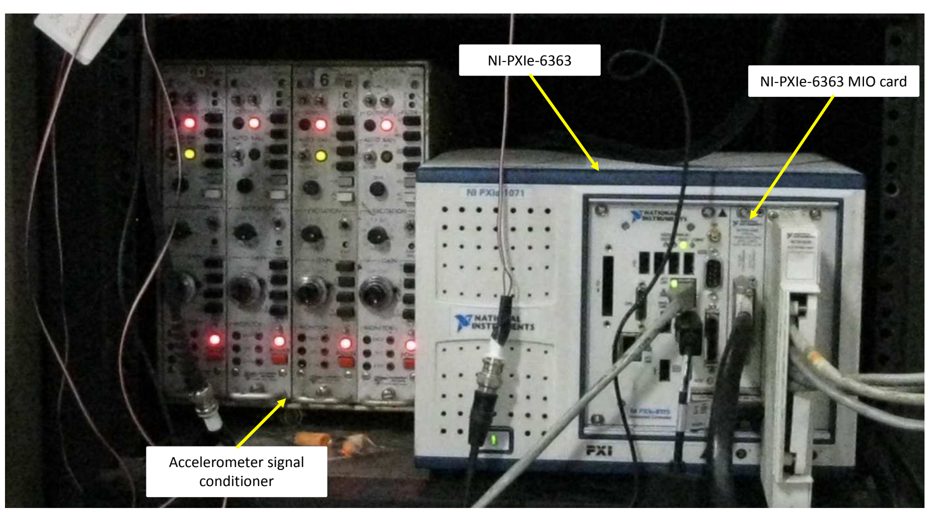

Figure 3.30: Acceleration signal conditioning and NI-PXIe-1071 chassis containing an NI PXI 8115 controller and a NI-PXIe 6363 multifunction IO card

Host PC A PC is used for the application development and the graphical user interface (GUI), as shown in Figure 3.26a.

3.4.3 Software components

LabVIEW RT application A LabVIEW RT application is used as the platform for hybrid simulation, and executes on the PXI controller described above. The application serves multiple functions.

1. Acquire sensor signals
2. Output control signals
3. Implement the DS controller
4. Perform analysis such as frequency response computations
5. Generation of signals such as the multisine
6. Receive commands from and send signal/analysis data to an external GUI application through TCP/IP

The first three functions are implemented in a timed loop, as shown in Figure 3.31, where the controller is implemented as a MATLAB-style script in a MathScript Node [109]. The timed loop executes at a sample rate of 1024Hz. Communication with the GUI is implemented using a standard client-server architecture [110].

Qt graphical user interface (GUI) A lightweight GUI has been developed specifically for the DS application using the Qt toolkit [111]. The application communicates with the LabVIEW RT application through TCP/IP. Screenshots from the GUI application are shown in Figure 3.32. The application consists of the following components.

1. A component that manages the connection to the realtime controller.
2. A function generator to parametrize cyclic (sine, square, sawtooth etc.) signals and multisine signals.

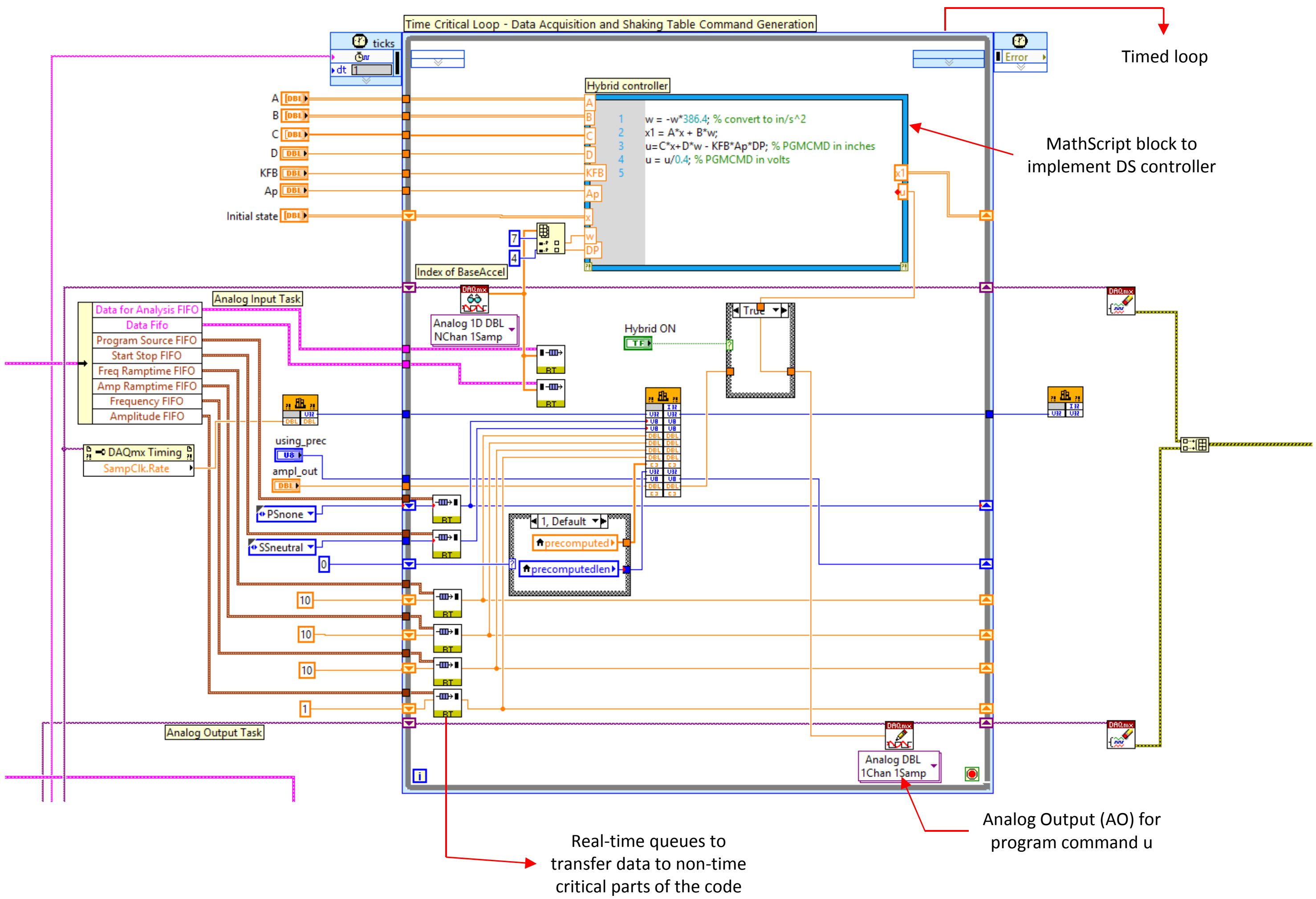

Figure 3.31: Time critical loop

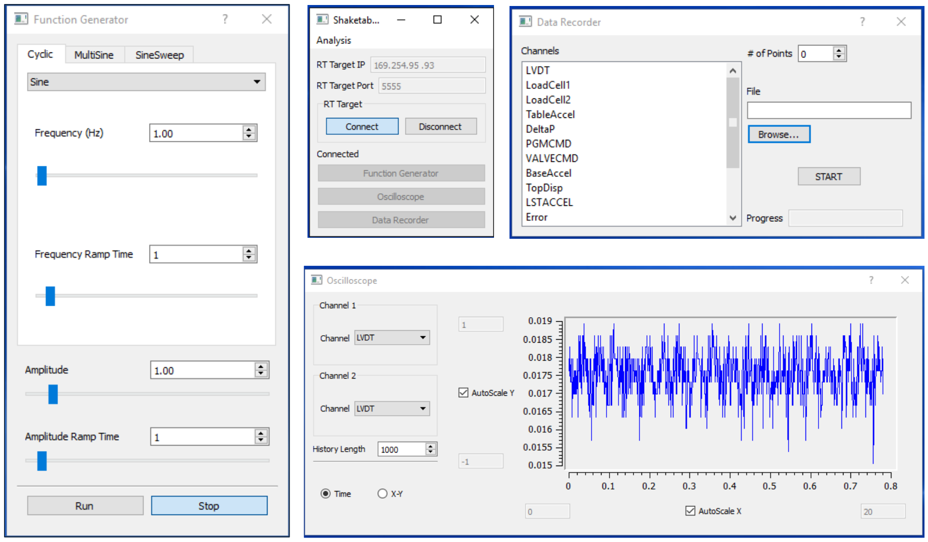

Figure 3.32: Qt GUI for DS controller (Chapter 4)

3. An oscilloscope to view signals.

4. A data recorder to save acquired data in MATLAB .mat format.

5. A spectrum viewer to visualize frequency response plots.

Trigger capability The realtime application is equipped with a trigger that can be toggled from the GUI, so that it can be initiated simultaneously with an input from a different source. For instance, for the proof of concept experiments described in Chapter 5, a digital trigger is set so that the DS controller starts operating when the laminar box excitation begins.

3.5 Experimental evaluation of mathematical models

As stated in Section 3.1, an important goal is an extensive characterization of the testbed, so that it can be used with confidence in the dynamic substructuring experiments presented in Chapter 4. This section provides a description of the experiments carried out to evaluate the mathematical models developed previously.

3.5.1 Friction characterization

Friction in the shaker is present between the recirculating bearings and the rails, in the swivels, and internally in the actuator, for instance in the seals. To characterize this friction, the shaker is driven with the program command is set to be sawtooth signal, so that during the straight edge of the sawthooth, the velocity of the shaker is constant, therefore its acceleration is zero. The actuator force must then equal the friction. Different constant velocities can be obtained by varying the amplitude and frequency of the sawtooth signal. The actuator force is obtained by two different means — (i) $A_{\mathrm{p}}\Delta P$ and (ii) LC1 - LC2 (the difference, since when one of the loadcells is in tension, the other is in compression), and plotted against the shaker displacement in Figure 3.33 for different constant velocities.

The friction measured from the ΔP cell is larger than that measured using the load cells, suggesting that there is friction internally in the actuator. The magnitude of the friction is about 100lb. It can also be seen in Figure 3.33 that for larger velocities, acceleration effects begin to appear at the corners of the hysteresis loops.

Friction is not included in the shaker models developed in Section 3.2.2. DS experiments described in Chapter 4 are carried out at force levels significantly larger than the 100-lb friction, and consequently, DS controllers designed without accounting for friction perform well. However, as seen in Section 4.5.4, friction does play an important role in some situations, such as when the virtual substructure frequency is very low.

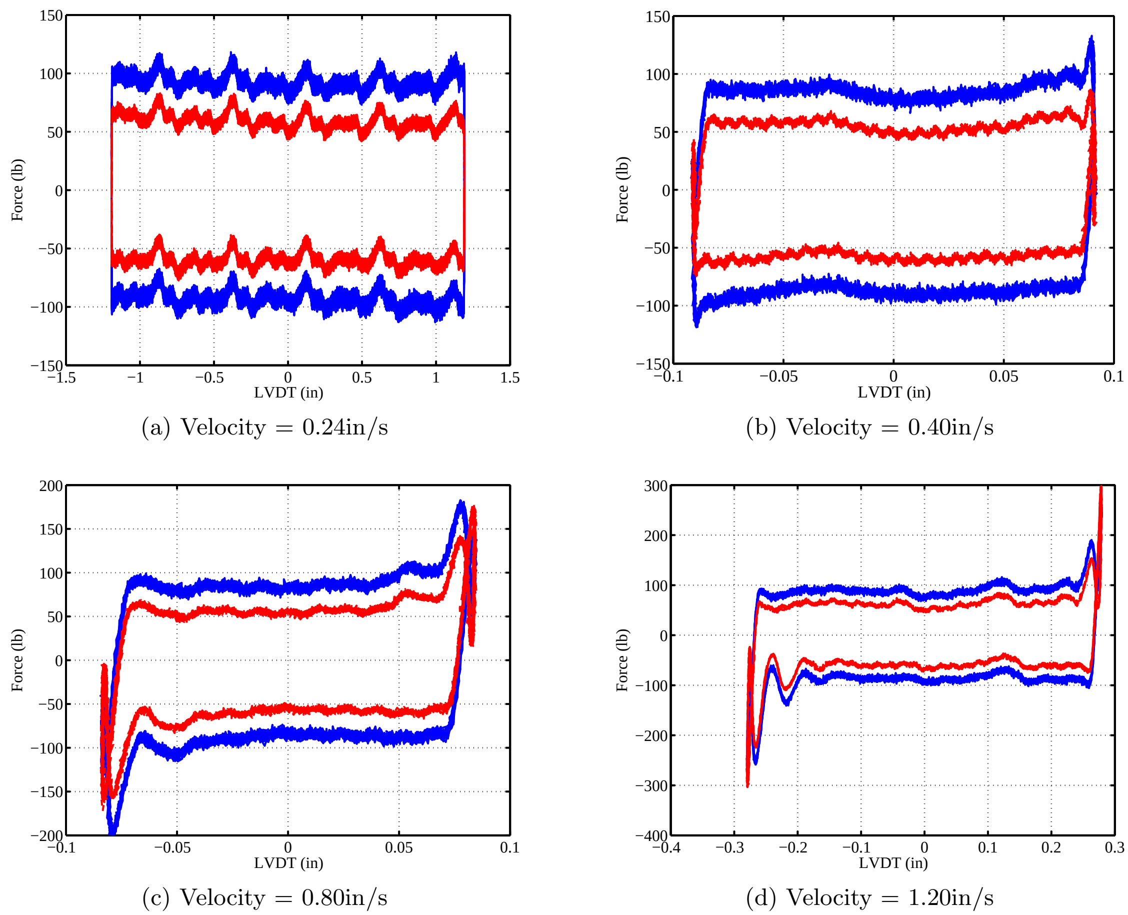

Figure 3.33: Characterizing friction in the shaker; blue lines denote force as measured using the ΔP cell, and red lines the total force from the load cells

3.5.2 Evaluation of AMD model

To evaluate the linear mathematical model of the shaker, important frequency response functions of the shaker are estimated over the bandwidth of interest. Frequency response functions are used to mathematically represent the relationship between the input and the output of linear time invariant (LTI) systems. Real systems, like the hydraulic shaker presented here, are nonlinear as described in Section 3.2.2.1. Assuming however that the system operates within nominal parameters, hence close to the equilibrium point, it has a response close to a linear system and this approach can be used.

3.5.2.1 Multisine signal

For the frequency response measurements described in this section, the program command is set to a multisine signal. The multisine is specially constructed periodic broadband signal consisting of a sum of sines of constant amplitude, and phases selected so that the "crest factor" is minimal; i.e. the ratio of the maximum peak to the minimum peak in the signal is close to one [112]. This helps maximize the signal-noise ratio in the output signals for frequency response estimation [113]. Figure 3.34 shows an example of a multisine signal, where the sampling frequency is 1024Hz, the period is 4s (=4096 samples), and the bandwidth is 128Hz (=512 sine components).

3.5.2.2 Experiments with multisine input

To evaluate the AMD models developed in Section 3.2.2, two types of comparisons are made.

1. Frequency response functions implied by the linear models (3.13) and (3.14) are compared with those obtained experimentally. Frequency response from the program command, u, to (i) the proof mass displacement (LVDT), (ii) the differential pressure, ΔP, and (iii) the proof mass acceleration are considered.

2. Responses predicted by the linear model (3.14) (including servovalve dynamics) as

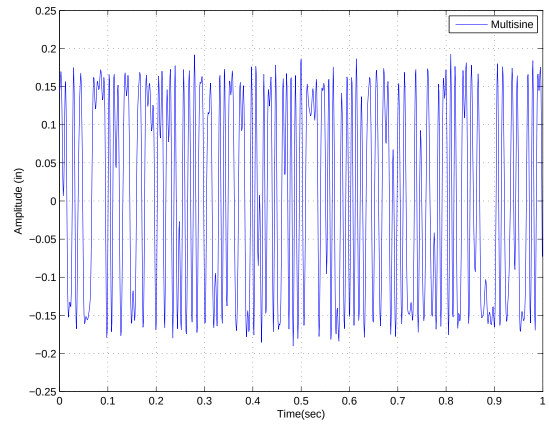

(a) One period (4s = 4096 samples) of multisine signal

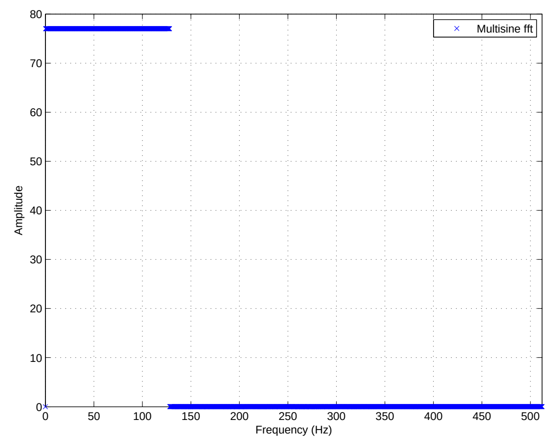

(b) FFT magnitude of multisine signal showing each sinusoidal component in the bandwidth having equal amplitude

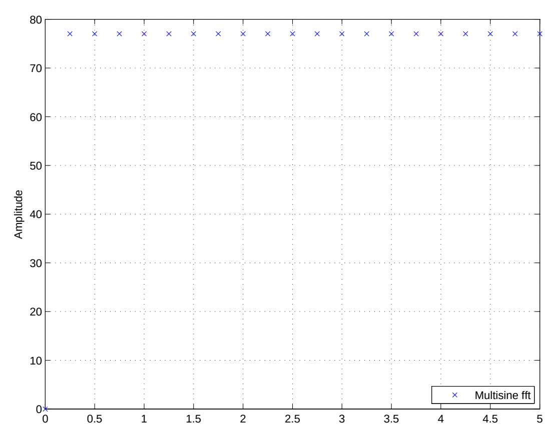

(c) Zoom in of FFT magnitude showing frequency resolution = 1024Hz/4096 = 0.25Hz

Figure 3.34: Example multisine signal of period 4s (=4096 samples), bandwidth 128Hz (= 512 sine components) and 0.2in amplitude

well as the nonlinear model (3.4) with servovalve dynamics appended are directly compared with experimental measurements. Proof mass displacement, ΔP, and valve command are considered, comparison is made in both time and frequency domains.

Experiments are carried out with the program command, u, set to the multisine signal with properties shown in Figure 3.34. Three different gain setting are considered — (i) $K_{\mathrm{e}} = 1$ and $K_{\mathrm{p}} = 0$, (ii) $K_{\mathrm{e}} = 2$ and $K_{\mathrm{p}} = 5$ and (iii) $K_{\mathrm{e}} = 1$ and $K_{\mathrm{p}} = 9$. These values refer to the controller knob settings; the corresponding gain values in engineering units can be obtained from Table 3.7.

Frequency response comparison Figures 3.35, 3.37 and 3.39 compare the measured frequency response with those from the linear models (3.13) (excluding servovalve dynamics) and (3.14) (including servovalve dynamics). It is evident that the addition of the servovalve dynamics in the model significantly improves the ability of the model to represent the response of the system. It is also clear that only the oil column frequency is apparent in the range of frequencies up to 100Hz. Hence, the natural frequencies of the parts of the shaker, such as the platform frequency are indeed higher than the bandwidth of interest, as desired.

Response comparison Figure 3.36 shows the comparison of the proof mass displacement (LVDT), the differential pressure ΔP and the valve command signals, along with the corresponding FFT for each case. The specific results refer to experiments performed with gain values $K_{\mathrm{e}} = 1$ and $K_{\mathrm{p}} = 0$. Similarly, Figures 3.37 and 3.40 show the comparison for tests performed with gain values equal to $K_{\mathrm{e}} = 2$ and $K_{\mathrm{p}} = 5$ and $K_{\mathrm{e}} = 1$ and $K_{\mathrm{p}} = 9$ respectively. It can be observed that there is good agreement between the linear analytical model and the experimental results for all three different gain value sets, for both time and frequency domain. However, there is discrepancy when the experimental results are compared to the nonlinear model. This is more obvious in case (i), when the ΔP gain is smaller. Specifically, in the frequency domain the oil column frequency is correctly estimated, however the amplitude is not predicted well. However, as the ΔP gain increases the effect of the nonlinearities is suppressed and the comparison the nonlinear and linear model become similar. This is due to the fact that the increase of the ΔP gain reduces the effect of nonlinearities in the system.

In general, based on these results, the analytical model is reliable and can be used for the experiments described in Chapter 4.

3.5.2.3 AMD Transfer Functions

The analytical equations of the transfer functions H_{Fw} and H_{Fu} can be derived, and then compared with the ones obtained during the experiment. It should be mentioned that here the derivation of the transfer functions H_{Fw} and H_{Fu} are shown, however they can also be directly obtained using MATLAB.

In order to define the transfer function between the commanded displacement u and the force, $F = A_\mathrm{p} x_3$, applied by the actuator, the equation (3.14) can be written in the Laplace domain:

$$
\begin{aligned}
x_1(s) &= \frac{1}{s^2}\left(\frac{A_\mathrm{p}}{M_\mathrm{t}}x_3 - w\right)\\
x_2(s) &= \frac{1}{s}\left(\frac{A_\mathrm{p}}{M_\mathrm{t}}x_3 - w\right)\\
x_3(s) &= \frac{\frac{M_\mathrm{t}\omega_\mathrm{oil}^2}{A_\mathrm{p}}s^2 + \left(\frac{\alpha_\mathrm{s}\omega_\mathrm{oil}^2 M_\mathrm{t}}{A_\mathrm{p}} + \alpha_\mathrm{s} d K_\mathrm{d}\right)s + \alpha_\mathrm{s} d K_\mathrm{e}}{s^4 + (\alpha_\mathrm{s} + 2\zeta_\mathrm{oil}\omega_\mathrm{oil})s^3 + (\alpha_\mathrm{s} d K_\mathrm{p} + 2\zeta_\mathrm{oil}\omega_\mathrm{oil}\alpha_\mathrm{s} + \omega_\mathrm{oil}^2)s^2 + \left(\frac{A_\mathrm{p}\alpha_\mathrm{s} d K_\mathrm{d}}{M_\mathrm{t}} + \alpha_\mathrm{s}\omega_\mathrm{oil}^2\right)s + \frac{A_\mathrm{p}\alpha_\mathrm{s} d K_\mathrm{e}}{M_\mathrm{t}}} w\\
&\quad + \frac{d\alpha_\mathrm{s} K_\mathrm{e} s^2}{s^4 + (\alpha_\mathrm{s} + 2\zeta_\mathrm{oil}\omega_\mathrm{oil})s^3 + (\alpha_\mathrm{s} d K_\mathrm{p} + 2\zeta_\mathrm{oil}\omega_\mathrm{oil}\alpha_\mathrm{s} + \omega_\mathrm{oil}^2)s^2 + \left(\frac{A_\mathrm{p}\alpha_\mathrm{s} d K_\mathrm{d}}{M_\mathrm{t}} + \alpha_\mathrm{s}\omega_\mathrm{oil}^2\right)s + \frac{A_\mathrm{p}\alpha_\mathrm{s} d K_\mathrm{e}}{M_\mathrm{t}}} u\\
x_4(s) &= \frac{1}{s^2(s+\alpha_\mathrm{s})}\left[\left(-s^2\alpha_\mathrm{s} K_\mathrm{p} - \frac{s\alpha_\mathrm{s} K_\mathrm{d} A_\mathrm{p}}{M_\mathrm{t}} - \frac{\alpha_\mathrm{s} K_\mathrm{e} A_\mathrm{p}}{M_\mathrm{t}}\right)x_3 + \alpha_\mathrm{s} K_\mathrm{e} s^2)u + (\alpha_\mathrm{s} K_\mathrm{e} + s\alpha_\mathrm{s} K_\mathrm{d})w\right]
\end{aligned}
$$

Hence, for zero derivative gain $K_\mathrm{d} = 0$, the equation $F = H_{Fw}w + H_{Fu}u$ is

$$
\begin{aligned}
F = &\frac{\omega_\mathrm{oil}^2 M_\mathrm{t} s^2 + \omega_\mathrm{oil}^2 M_\mathrm{t}\alpha_\mathrm{s} s + d K_\mathrm{e} A_\mathrm{p}\alpha_\mathrm{s}}{s^4 + (\alpha_\mathrm{s} + 2\zeta_\mathrm{oil}\omega_\mathrm{oil})s^3 + (\alpha_\mathrm{s} d K_\mathrm{p} + 2\zeta_\mathrm{oil}\omega_\mathrm{oil}\alpha_\mathrm{s} + \omega_\mathrm{oil}^2)s^2 + \alpha_\mathrm{s}\omega_\mathrm{oil}^2 s + \frac{A_\mathrm{p}\alpha_\mathrm{s} d K_\mathrm{e}}{M_\mathrm{t}}} w\\
&+ \frac{d K_\mathrm{e} A_\mathrm{p}\alpha_\mathrm{s} s^2}{s^4 + (\alpha_\mathrm{s} + 2\zeta_\mathrm{oil}\omega_\mathrm{oil})s^3 + (\alpha_\mathrm{s} d K_\mathrm{p} + 2\zeta_\mathrm{oil}\omega_\mathrm{oil}\alpha_\mathrm{s} + \omega_\mathrm{oil}^2)s^2 + \alpha_\mathrm{s}\omega_\mathrm{oil}^2 s + \frac{A_\mathrm{p}\alpha_\mathrm{s} d K_\mathrm{e}}{M_\mathrm{t}}} u
\end{aligned}
$$

The transfer functions for the AMD system are given by equations (3.22) and (3.23).

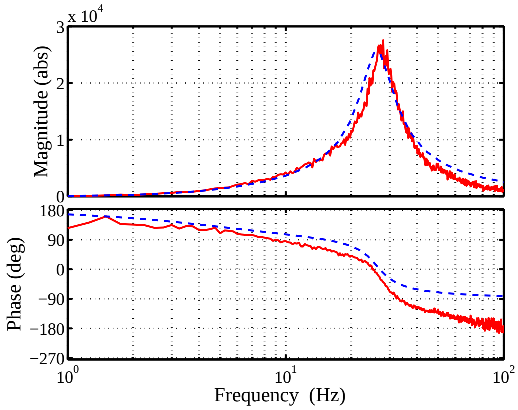

(a) Program command (u) to ΔP comparison with model without servovalve

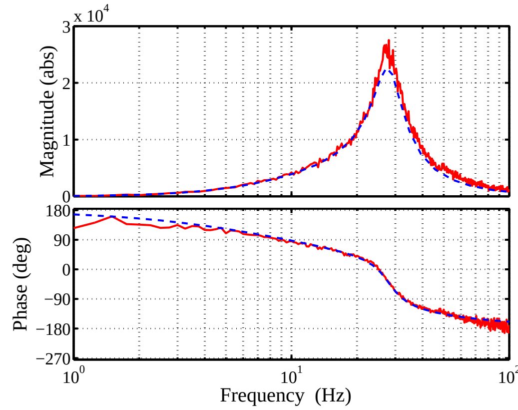

(b) Program command (u) to ΔP comparison with model with servovalve

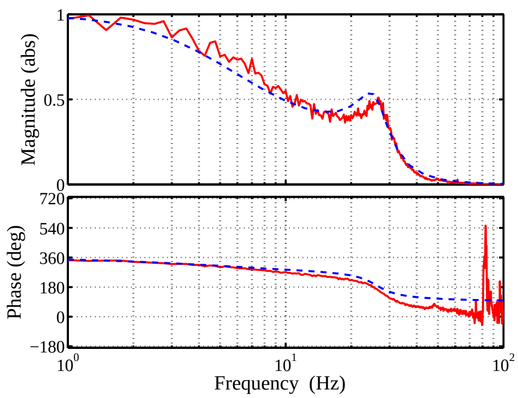

(c) Program command (u) to LVDT comparison with model without servovalve

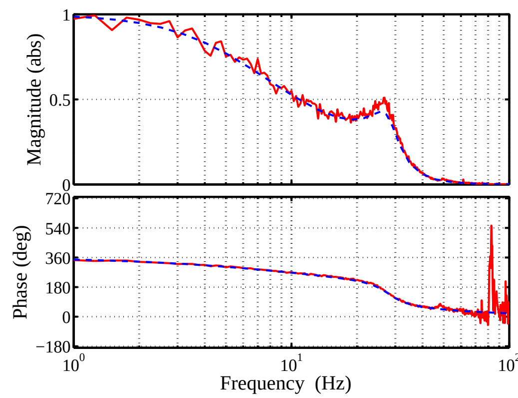

(d) Program command (u) to LVDT comparison with model with servovalve

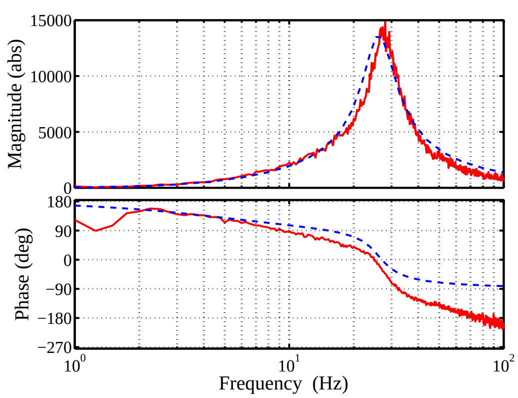

(e) Program command (u) to table acceleration comparison with model without servovalve

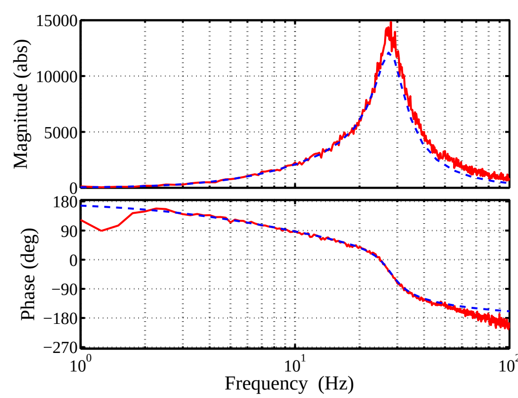

(f) Program command (u) to table acceleration comparison with model with servovalve

Figure 3.35: Evaluation of hydraulic shaker model for gain settings $K_\mathrm{e} = 1$, $K_\mathrm{p} = 0$. Shaker transfer functions, red solid lines show the experimental data and dashed blue lines show the expected response of the linear mathematical model.

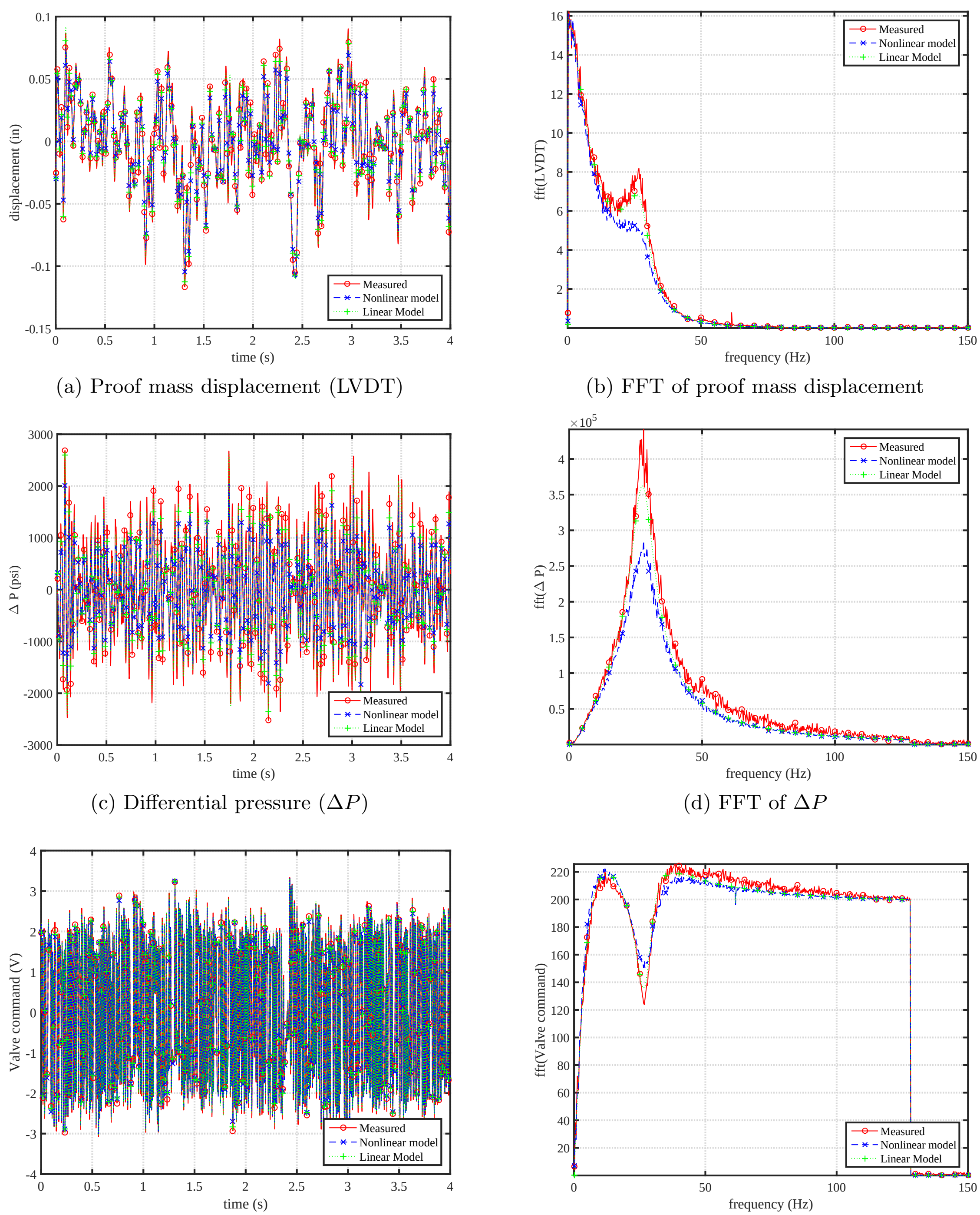

(a) Proof mass displacement (LVDT)

(b) FFT of proof mass displacement

(c) Differential pressure (ΔP)

(d) FFT of ΔP

(e) Valve command

(f) FFT of valve command

Figure 3.36: Comparison of measurements with simulation results from nonlinear and linear models for gain settings $K_{\mathrm{e}} = 1$, $K_{\mathrm{p}} = 0$

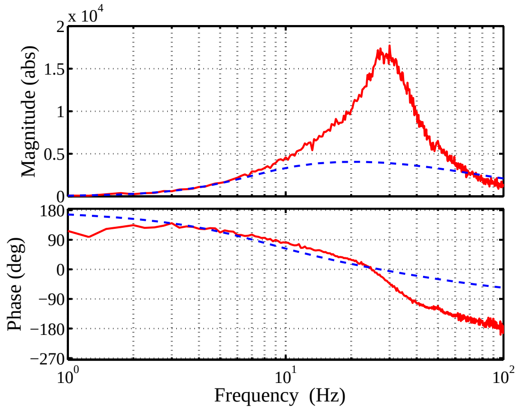

(a) Program command (u) to ΔP comparison with model without servovalve

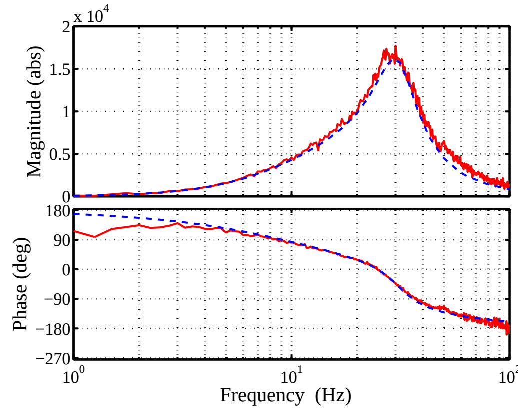

(b) Program command (u) to ΔP comparison with model with servovalve

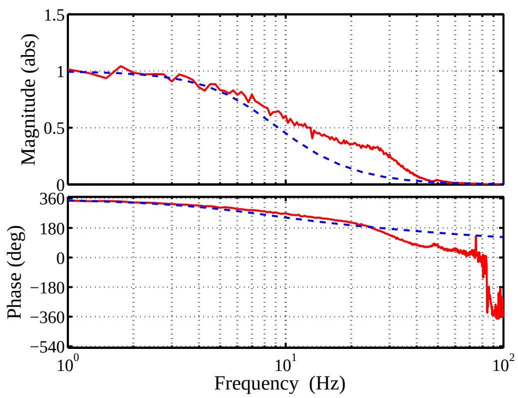

(c) Program command (u) to LVDT comparison with model without servovalve

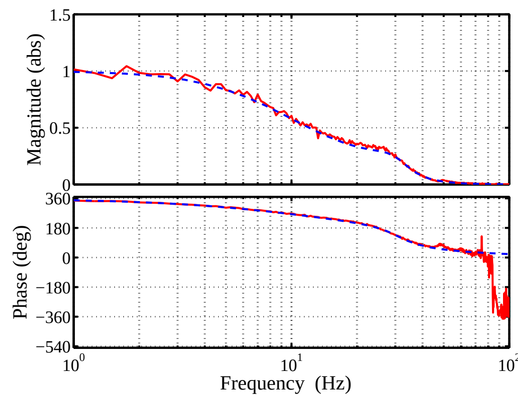

(d) Program command (u) to LVDT comparison with model with servovalve

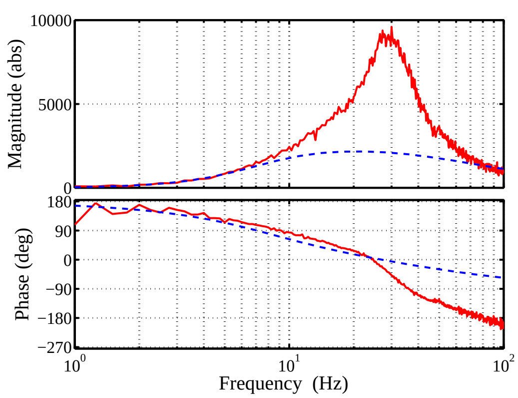

(e) Program command (u) to table acceleration comparison with model without servovalve

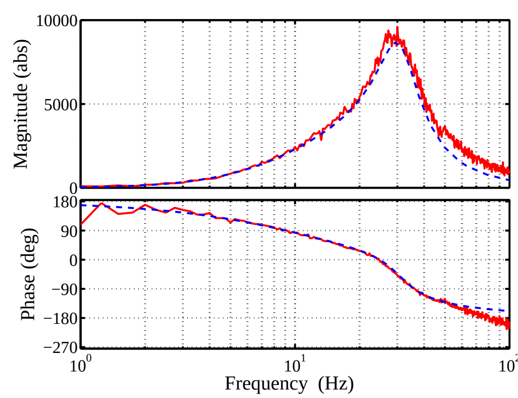

(f) Program command (u) to table acceleration comparison with model with servovalve

Figure 3.37: Evaluation of hydraulic shaker model for gain settings $K_{\mathrm{e}} = 2$, $K_{\mathrm{p}} = 5$. Shaker transfer functions, red solid lines show the experimental data and dashed blue lines show the expected response of the linear mathematical model.

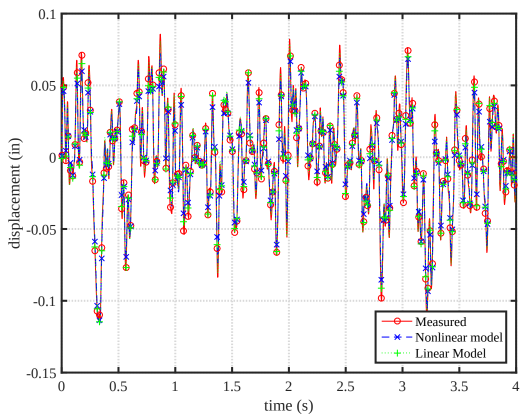

(a) Proof mass displacement (LVDT)

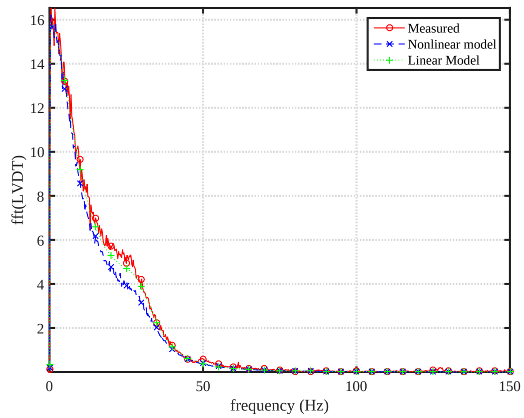

(b) FFT of proof mass displacement

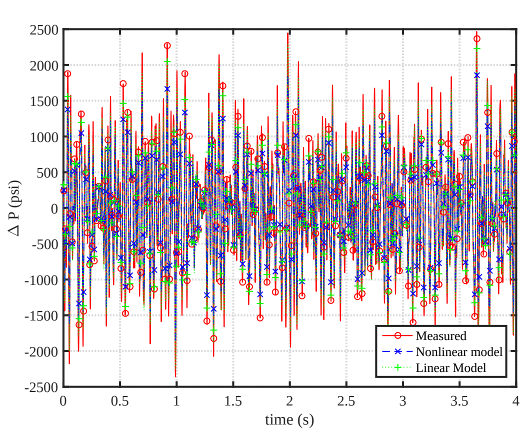

(c) Differential pressure (ΔP)

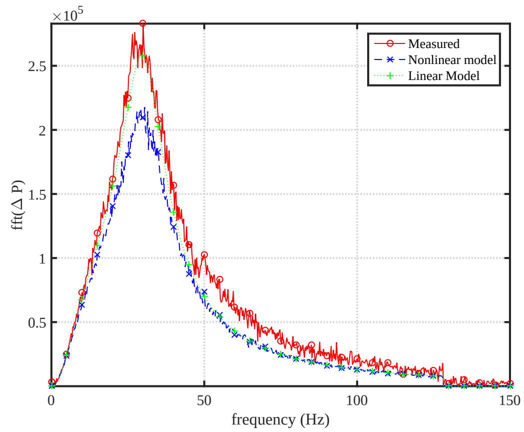

(d) FFT of ΔP

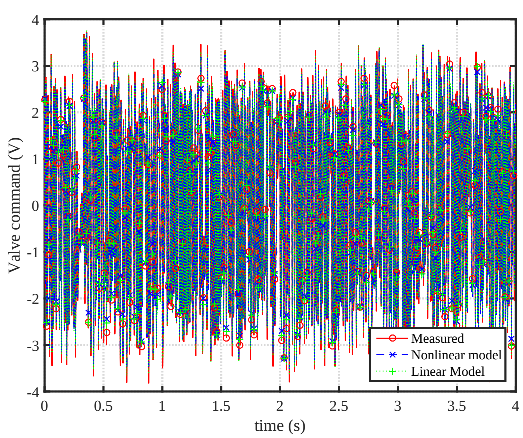

(e) Valve command

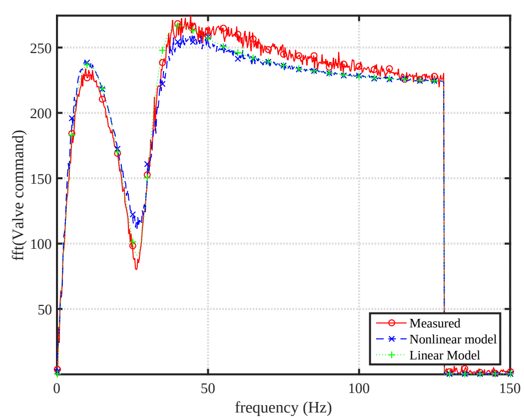

(f) FFT of valve command

Figure 3.38: Comparison of measurements with simulation results from nonlinear and linear models for gain settings $K_\mathrm{e} = 2$, $K_\mathrm{p} = 5$

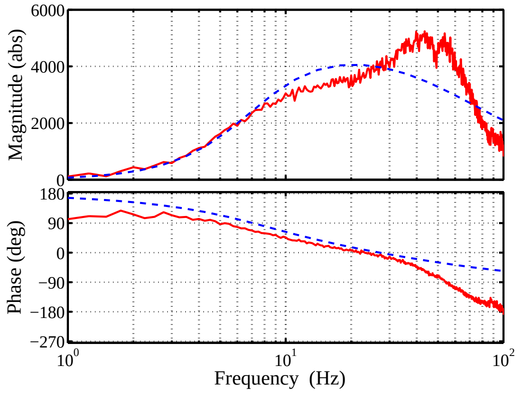

(a) Program command (u) to ΔP comparison with model without servovalve

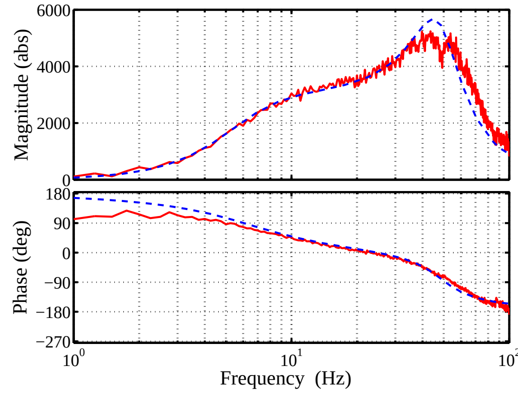

(b) Program command (u) to ΔP comparison with model with servovalve

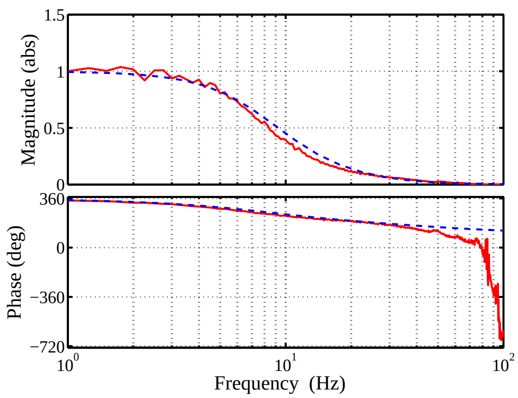

(c) Program command (u) to LVDT comparison with model without servovalve

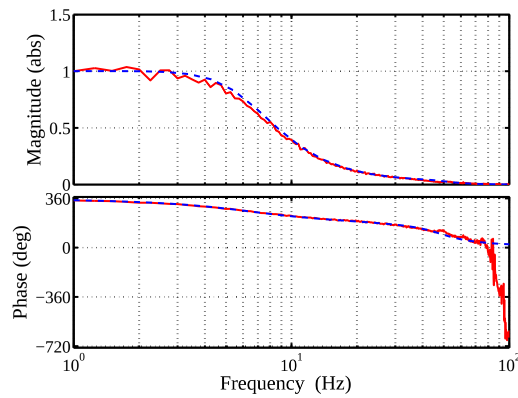

(d) Program command (u) to LVDT comparison with model with servovalve

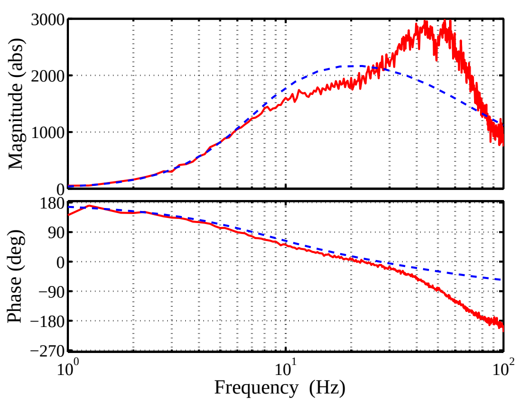

(e) Program command (u) to table acceleration comparison with model without servovalve

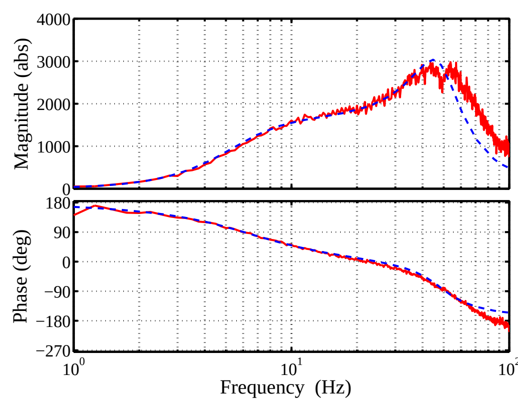

(f) Program command (u) to table acceleration comparison with model with servovalve

Figure 3.39: Evaluation of hydraulic shaker model for gain settings $K_\mathrm{e} = 1$, $K_\mathrm{p} = 9$. Shaker transfer functions, red solid lines show the experimental data and dashed blue lines show the expected response of the linear mathematical model.

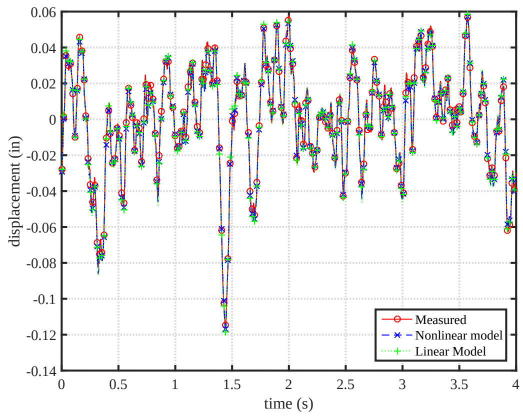

(a) Proof mass displacement (LVDT)

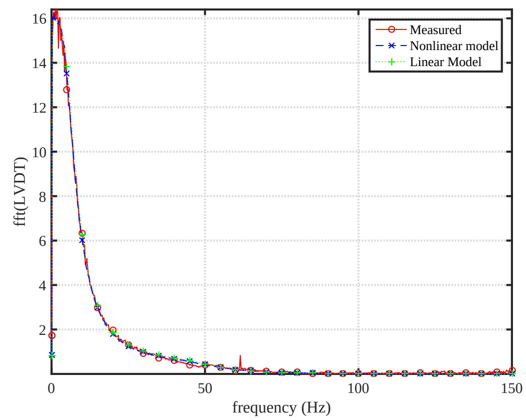

(b) FFT of proof mass displacement

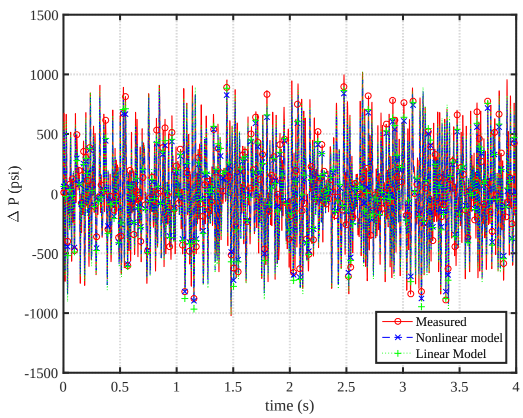

(c) Differential pressure (ΔP)

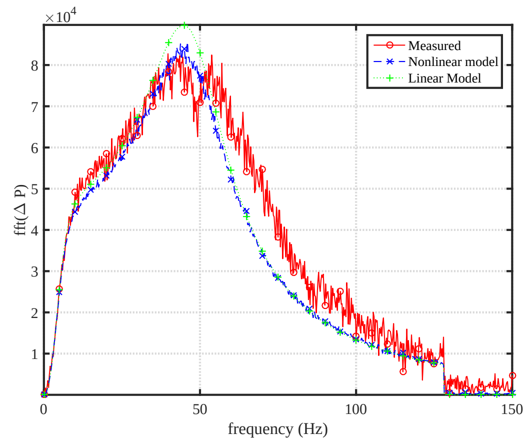

(d) FFT of ΔP

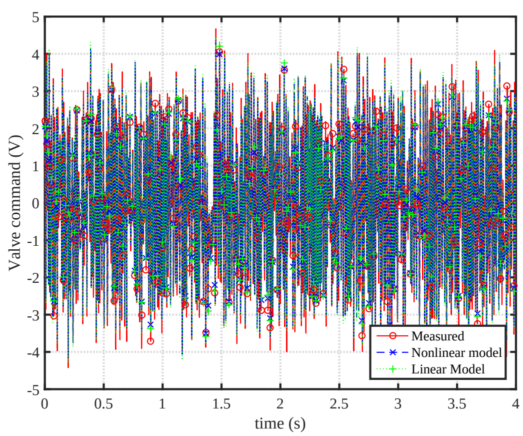

(e) Valve command

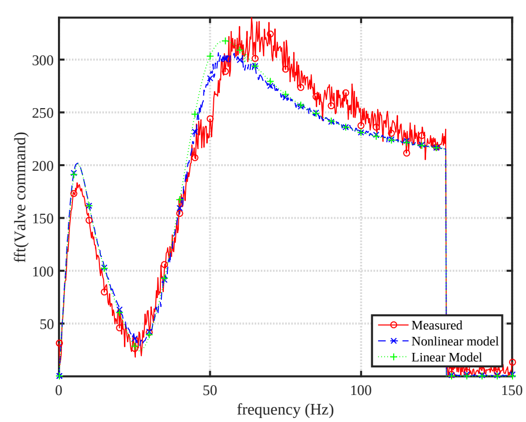

(f) FFT of valve command

Figure 3.40: Comparison of measurements with simulation results from nonlinear and linear models for gain settings $K_\mathrm{e} = 1$, $K_\mathrm{p} = 9$

$$H_{Fw} = \frac{\omega_{\mathrm{oil}}^2 M_{\mathrm{t}} s^2 + \omega_{\mathrm{oil}}^2 M_{\mathrm{t}} \alpha_{\mathrm{s}} s + dK_{\mathrm{e}} A_{\mathrm{p}} \alpha_{\mathrm{s}}}{s^4 + (\alpha_{\mathrm{s}} + 2\zeta_{\mathrm{oil}}\omega_{\mathrm{oil}})s^3 + (\alpha_{\mathrm{s}} dK_{\mathrm{p}} + 2\zeta_{\mathrm{oil}}\omega_{\mathrm{oil}}\alpha_{\mathrm{s}} + \omega_{\mathrm{oil}}^2)s^2 + \alpha_{\mathrm{s}}\omega_{\mathrm{oil}}^2 s + \frac{A_{\mathrm{p}}\alpha_{\mathrm{s}} dK_{\mathrm{e}}}{M_{\mathrm{t}}}} \tag{3.22}$$

$$H_{Fu} = \frac{dK_{\mathrm{e}} A_{\mathrm{p}} \alpha_{\mathrm{s}} s^2}{s^4 + (\alpha_{\mathrm{s}} + 2\zeta_{\mathrm{oil}}\omega_{\mathrm{oil}})s^3 + (\alpha_{\mathrm{s}} dK_{\mathrm{p}} + 2\zeta_{\mathrm{oil}}\omega_{\mathrm{oil}}\alpha_{\mathrm{s}} + \omega_{\mathrm{oil}}^2)s^2 + \alpha_{\mathrm{s}}\omega_{\mathrm{oil}}^2 s + \frac{A_{\mathrm{p}}\alpha_{\mathrm{s}} dK_{\mathrm{e}}}{M_{\mathrm{t}}}} \tag{3.23}$$

For the specific setup, the transfer functions H_{Fw} and H_{Fu} were obtained experimentally for two different controller gain combinations, $K_{\mathrm{e}} = 1, K_{\mathrm{p}} = 0$ and $K_{\mathrm{e}} = 1, K_{\mathrm{p}} = 9$. The calibration of the gain values are shown in Section 3.4.1, however it is reminded here that the specific values do not refer to the actual values but the position of the knob in the controller.

The experimentally obtained transfer functions for AMD are compared with the expected values, as shown in Figure 3.41. In this case, the mathematical model including the servovalve dynamics (equation (3.14)) is used, since it provides a more accurate prediction for a larger range of frequencies. The comparison between the two models and other transfer functions of AMD is given in Chapter 3.

3.5.3 Evaluation of PS model (AMD locked)

Following the evaluation of the AMD, the analytical model of the physical subsystem is examined. This is achieved using the configuration shown in Figure 3.24. The AMD is locked in place using steel brackets, and the only input to the system is the acceleration of the shake table a_{g}.

The experimental results are compared with the analytical model for the case when the AMD is locked, as described in Section 3.3.3.1. Figure 3.42 shows this comparison for the acceleration both at the proof mass and the physical subsystem level. It is observed that there is a mismatch between the analytical and the experimental results, which is more profound when the plots are shown in the db scale. While the fundamental frequency of the physical subsystem is well predicted, there is an additional peak at approximately 45 Hz. It is, hence, desired to investigate this behavior.

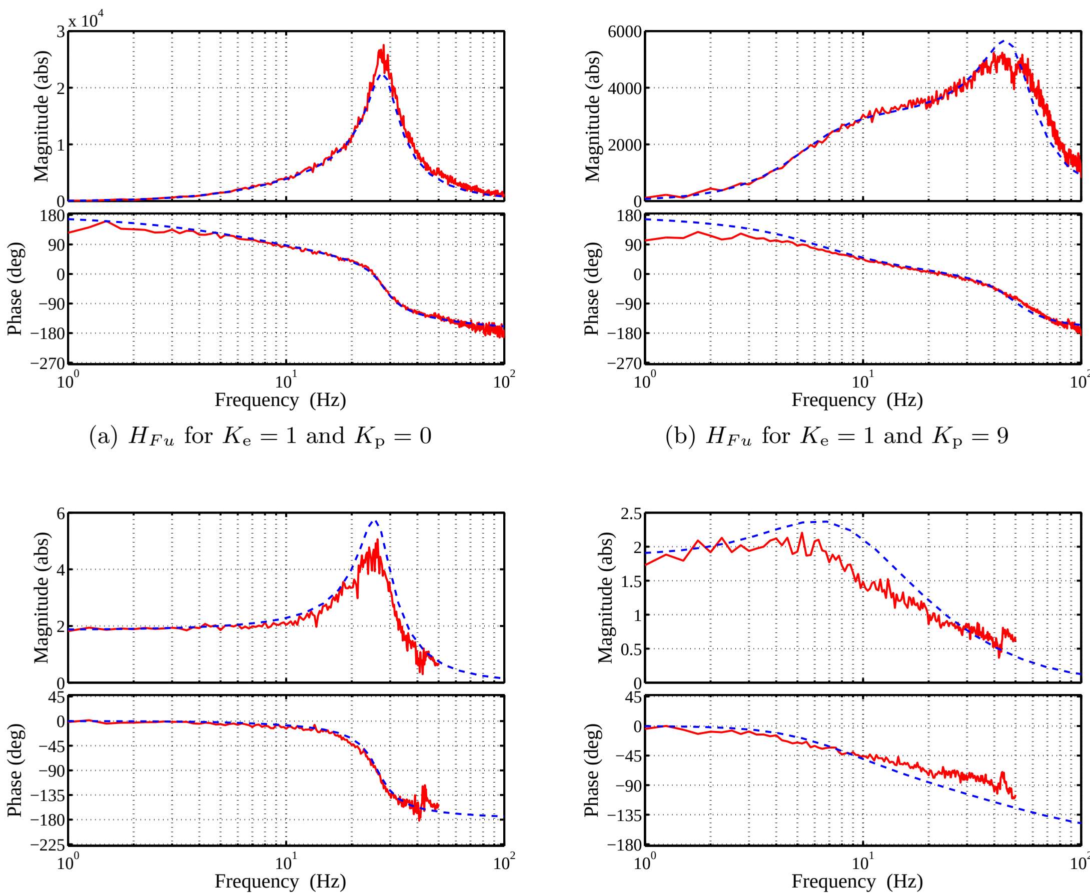

(a) H_{Fu} for $K_\mathrm{e} = 1$ and $K_\mathrm{p} = 0$

(b) H_{Fu} for $K_\mathrm{e} = 1$ and $K_\mathrm{p} = 9$

(c) $\mathrm{HF_w}$ for $K_\mathrm{e} = 1$ and $K_\mathrm{p} = 0$

(d) HF_w for $K_\mathrm{e} = 1$ and $K_\mathrm{p} = 9$

Figure 3.41: Transfer Functions for AMD. Red solid lines show the experimental data and dashed blue lines show the expected response of the linear mathematical model.

For this purpose, the time domain data of the accelerations, at both the proof mass and physical subsystem mass level, are closely observed. As shown in Figure 3.43, the accelerations are similar, however high frequency components are present. To eliminate this effect, a 25 Hz low pass filter is applied to the acceleration signals. Specifically, the filtering is performed in MATLAB without phase distortion using the following code.

```
[b,a] = butter(6,25/1024); % 6-pole Butterworth 25 Hz low pass filter
 at 1024Hz sampling frequency
filtered_signal = filtfilt(b,a,signal);
```

As shown in Figure 3.44, there is very good agreement between the filtered acceleration signals, so it is reasonable to conclude that the proof mass and the physical subsystem have the same acceleration time histories. This response is then compared with the predicted response a 1DOF model with only translational degree of freedom, with mass equal to the mass of the proof mass and stiffness equal to 6000lb/in. The comparison presented in Figure 3.45 reveals that these two responses are not similar which leads to the conclusion that there is an additional degree of freedom not accounted for.

To further investigate this, the acceleration time histories measured at the level of the shake table extension is examined and compared with the acceleration at the proof mass level. It should be mentioned here that these acceleration time histories are measured using two separate data acquisition systems (National Instruments (NI) and Pacific system), which are synchronized as presented in Figure 3.46. It can be observed from Figure 3.46d that the acceleration measurements at the level of the shake table extension are slightly different, due to the position of the accelerometers, as shown in Figure 3.10. Using these two acceleration time histories, the rotational acceleration of the shake table can be calculated as (extension acceleration - table acceleration)/height. It is obvious from Figures 3.46e and 3.46f that there is rotational acceleration of significant amplitude, leading to the conclusion that there is rotation of the shake table, which is the degree of freedom not accounted for in the results shown in Figure 3.42.

To ensure that this is actually the case, the acceleration time histories at the level of

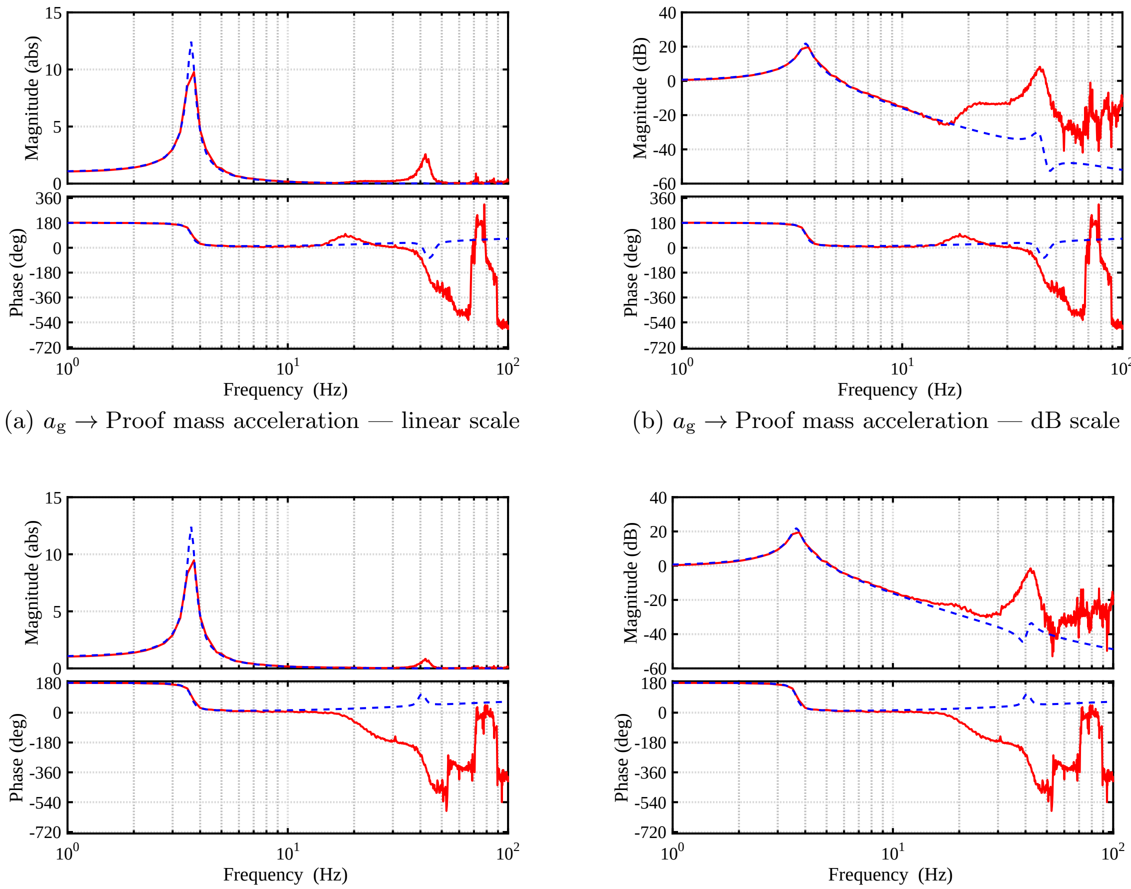

(a) $a_{\mathrm{g}} \rightarrow$ Proof mass acceleration — linear scale

(b) $a_{\mathrm{g}} \rightarrow$ Proof mass acceleration — dB scale

(c) $a_{\mathrm{g}} \rightarrow$ PS-level acceleration — linear scale

(d) $a_{\mathrm{g}} \rightarrow$ PS-level acceleration — dB scale

Figure 3.42: Frequency response from shake table input, a_{g}, accelerations at the proof-mass and PS-mass levels. Red solid lines show the experimental data and dashed blue lines show the expected response of the linear mathematical model.

the proof mass and the physical subsystem are compared to the response of a 2DOF model including the rotational degree of freedom in addition to the translation DOF. As shown in Figure 3.47, there is very good agreement between the predicted and experimental results, hence it is concluded that there is indeed rotation of the shake table during the experiments. This fact was not accounted for at the time of the experiments, however it proves that the analytical model of the physical subsystem is correct.

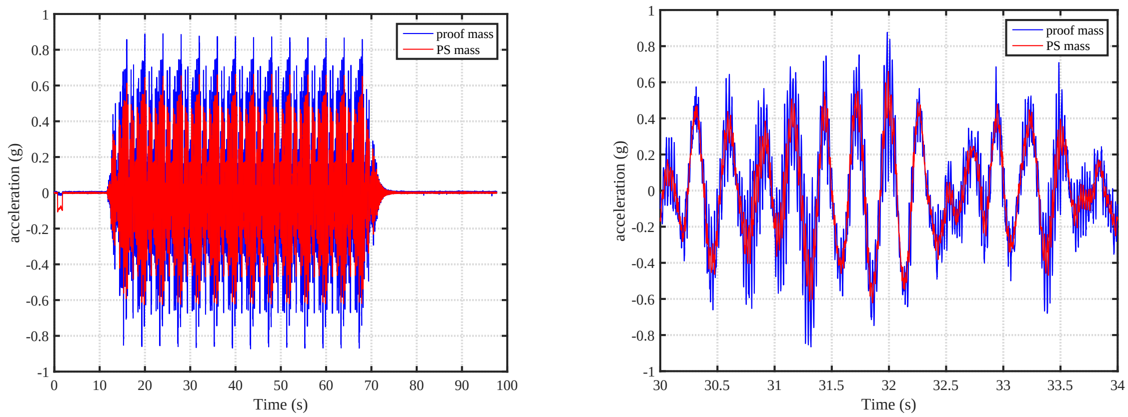

(a) Complete time series (b) One period (4s duration)

Figure 3.43: Measured accelerations at the levels of the proof mass and physical subsystem mass

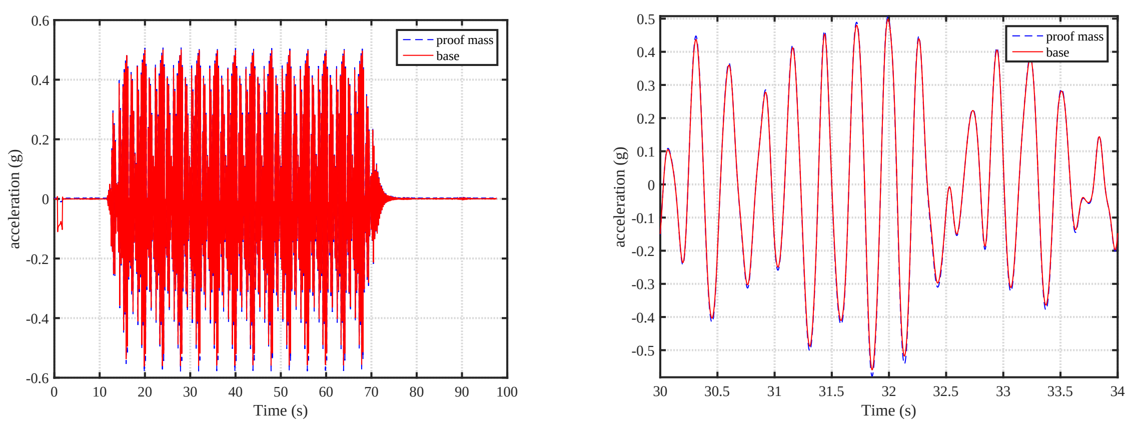

(a) Complete time series (b) One period (4s duration)

Figure 3.44: Measured accelerations at the levels of the proof mass and physical subsystem mass filtered with a 25Hz low pass filter

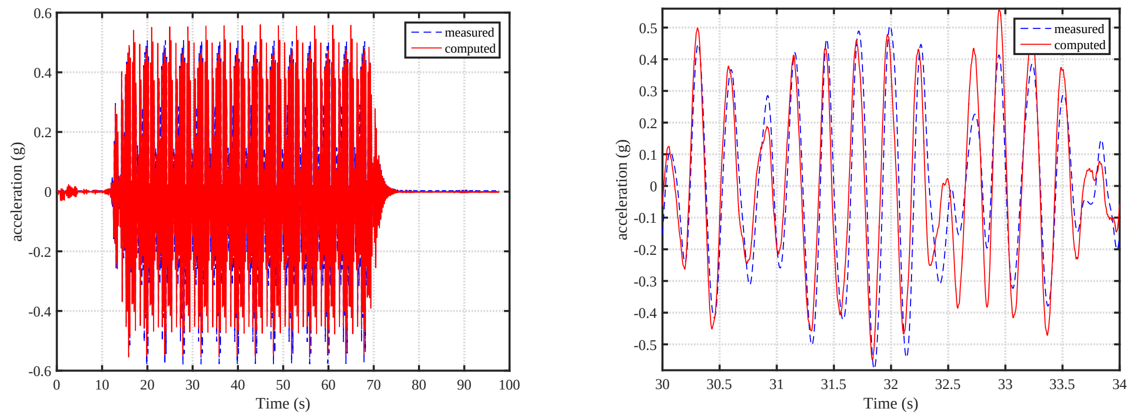

(a) Complete time series (b) One period (4s duration)

Figure 3.45: Filtered measured acceleration (which is the same as the proof-mass and PS levels) compared with acceleration obtained from a 1DOF model with only translational DOF

3.5.4 Evaluation of combined AMD and physical substructure model

After testing the performance of the analytical models of the AMD and the physical subsystem separately, it is desired to evaluate how well the mathematical model of the combined system can predict its behavior during testing.

For this purpose, the transfer functions of the inputs u and a_g to the displacements, accelerations and the differential pressure are calculated and compared against the experimentally obtained data. For the specific experiments, multisine input is used, with amplitude of 0.5V = 0.2in, for which the maximum frequency is 128Hz. The results shown here are for two cases of the ΔP gain, a low value $K_\mathrm{p} = 0$ and a high value $K_\mathrm{p} = 9$. The proportional gain is set equal to $K_\mathrm{e} = 1$, and the derivative gain K_d is set equal to zero. However, the behavior of the system is also well predicted for other values of the gains. It should be noted that the values of the gains correspond to the knob value set in the controller, the values in engineering units are given in Table 3.7.

The comparison is shown in Figures 3.48 through 3.51. The left part of these figures shows the comparison of the model without the addition of the servovalve, while the comparison of the experimental data to the model including the servovalve is shown in the right part. It is evident that when the servovalve dynamics are considered, the prediction is much

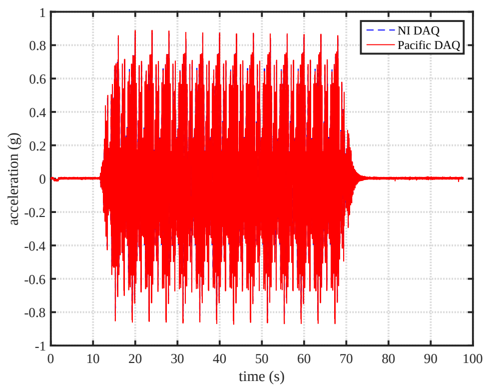

(a) Proof mass-level acceleration from NI and Pacific data acquisition systems for synchronization — complete time series

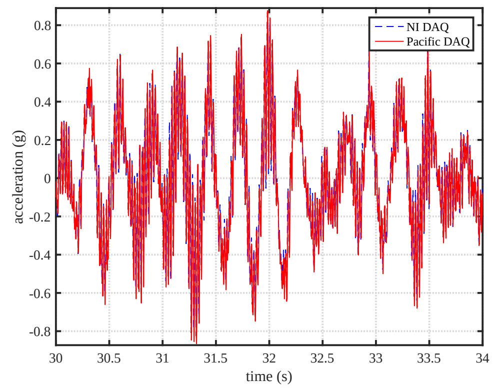

(b) One period (4s duration) of time series on the left

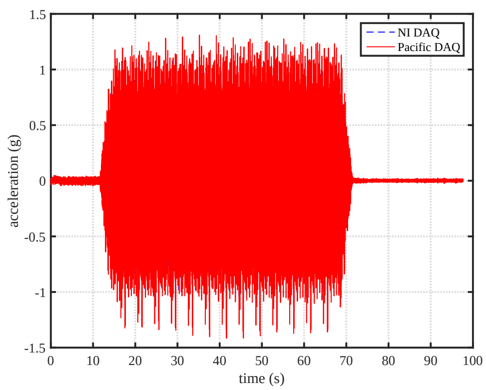

(c) Horizontal acceleration of shake table extension from NI and Pacific data acquisition systems — complete time series

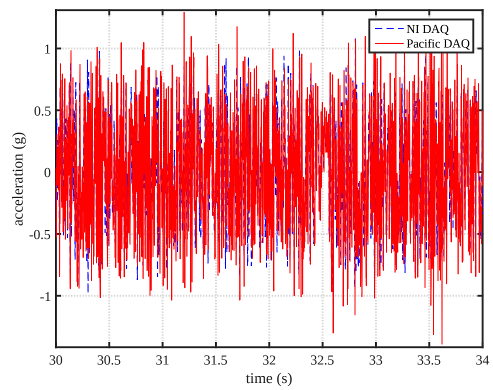

(d) One period (4s duration) of time series on the left — accelerations from NI and Pacific systems are slightly different because the accelerometers are located at different position vertically as shown in Figure 3.10; for all analyses, the acceleration from the NI system is used, since it is exactly at the base of the PS

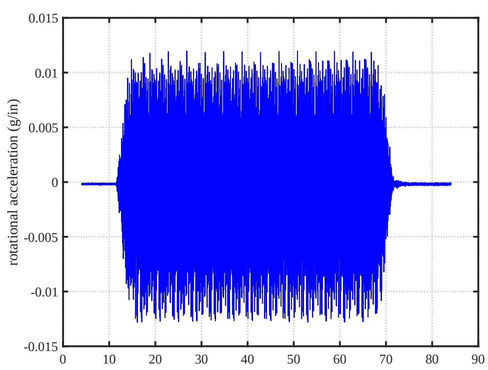

(e) Rotational acceleration of shake table computed as (extension acceleration - table acceleration) / height — complete time series

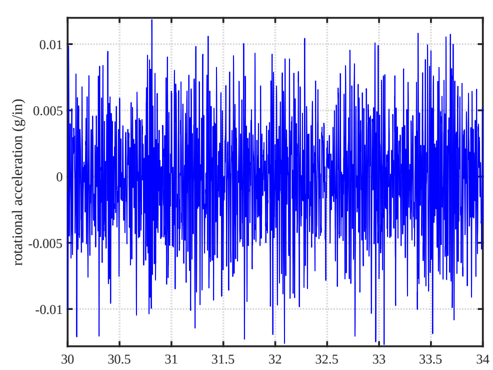

(f) One period (4s duration) of time series on the left

Figure 3.46: Estimating rotational acceleration of shake table

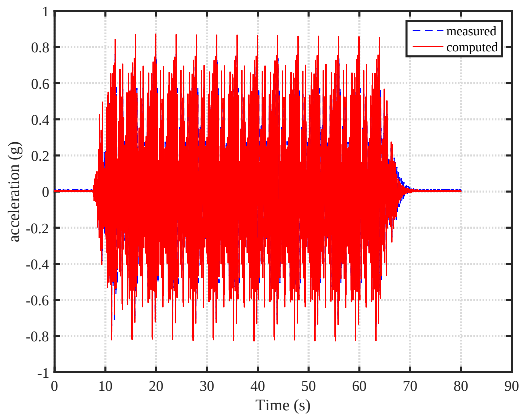

(a) Proof mass acceleration — complete time series

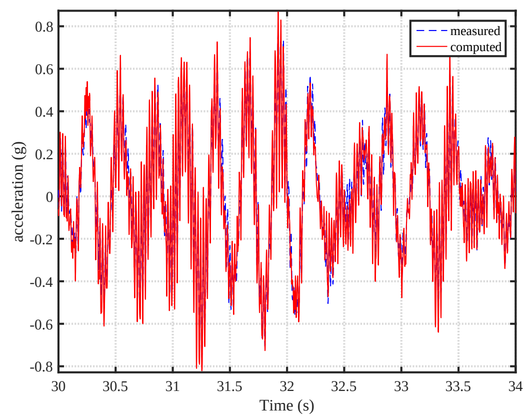

(b) Proof mass acceleration — one period (4s duration)

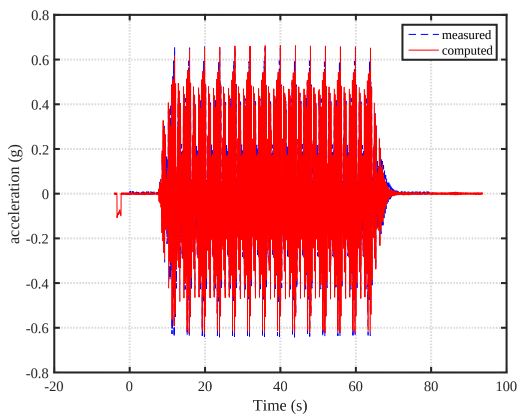

(c) PS acceleration — complete time series

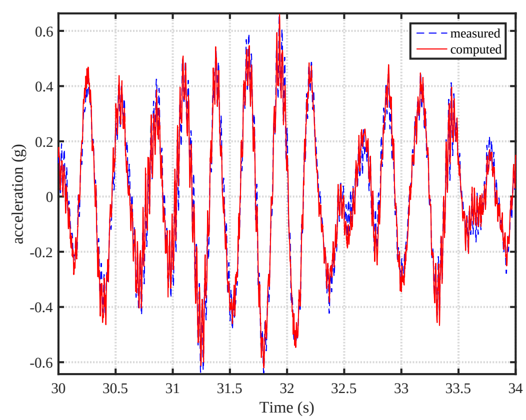

(d) PS acceleration — one period (4s duration)

Figure 3.47: Comparison of measured acceleration and acceleration computed from model including rotation DOF and rotational acceleration input (equation (3.15a))

better, especially for the case with higher ΔP gain, $K_{\mathrm{p}} = 9$.

Figure 3.52 shows the results for the case when the program command u is equal to zero and the only input to the system is the acceleration of the shake table a_{g}. Specifically, it presents the transfer functions with input the acceleration of the shake table and outputs the LVDT, ΔP and the acceleration at both the level of the proof mass and the physical subsystem. Since, in this case, there is no input from the shake table ($u = 0$), comparison for the model with the servovalve is redundant.

It should be mentioned that this case is different than the case presented in Section 3.5.3, where the AMD is locked in place. Here, the AMD is resting on the physical subsystem and the hydraulics are on. For the specific experiment, multisine input of $0.5g$ amplitude is used, for which the maximum frequency is 100Hz. The gains of the shaker are set equal to $K_{\mathrm{e}} = 1$ and $K_{\mathrm{p}} = 0$.

It can be observed from Figure 3.52 that the analytical model is predicting the frequency of the system well, however there is discrepancy at high frequencies. This is attributed to the fact that there is rotation of the shake table extension, as discussed in Section 3.5.3.

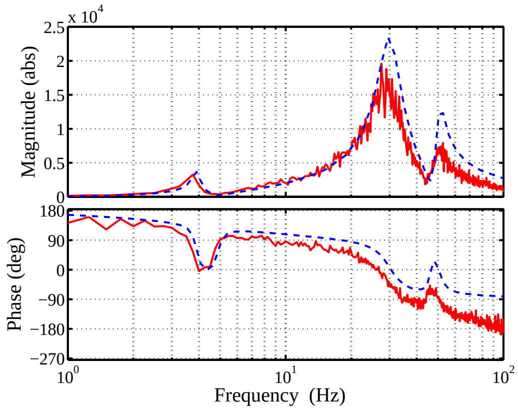

(a) Transfer function: program command (u) to ΔP comparison with model without servovalve

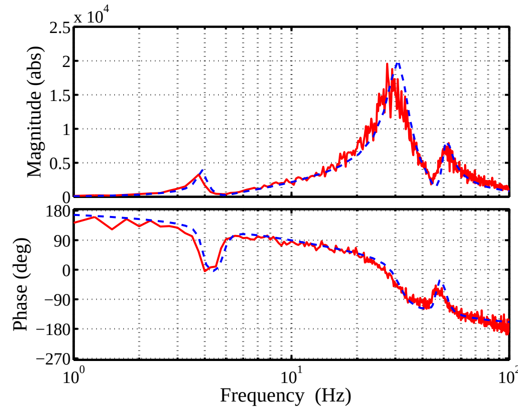

(b) Transfer function: program command (u) to ΔP comparison with model with servovalve

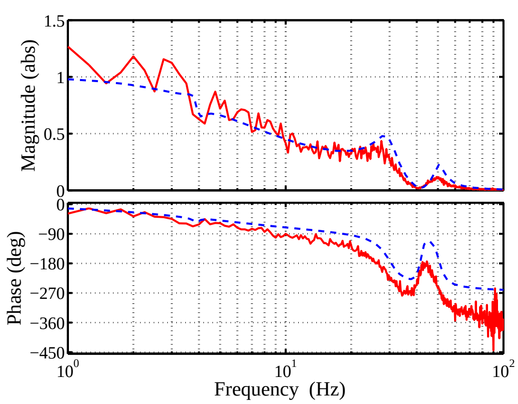

(c) Transfer function: program command (u) to LVDT comparison with model without servovalve

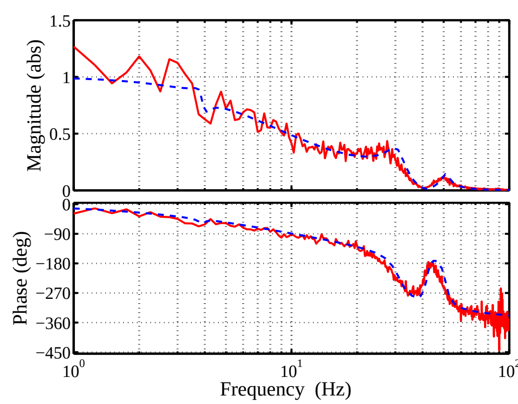

(d) Transfer function: program command (u) to LVDT comparison with model with servovalve

Figure 3.48: Model of AMD and bearings setup evaluation for $K_{\mathrm{e}} = 1$ and $K_{\mathrm{p}} = 0$. Red solid lines show the experimental data and dashed blue lines show the expected response of the linear mathematical model.

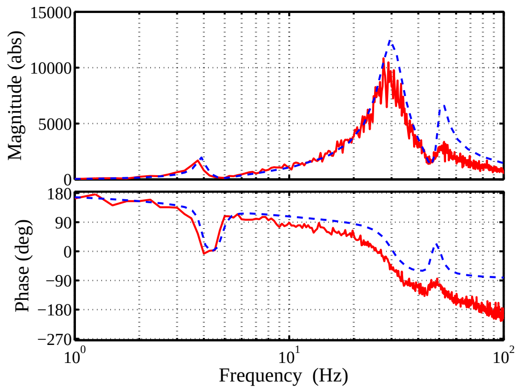

(a) Transfer function: program command (u) to table acceleration comparison with model without servovalve

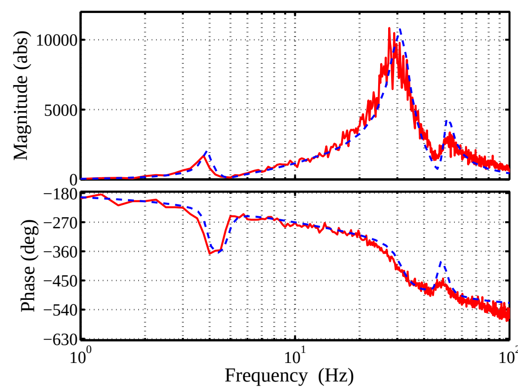

(b) Transfer function: program command (u) to table acceleration comparison with model with servovalve

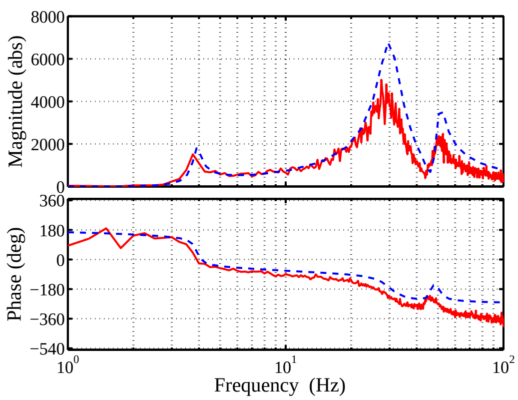

(c) Transfer function: program command (u) to acceleration at steel plates level - comparison with model without servovalve

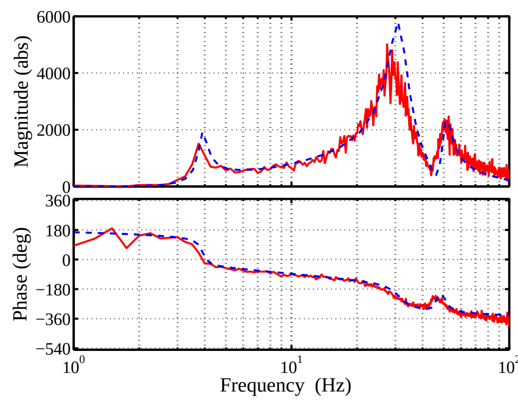

(d) Transfer function: program command (u) to acceleration at steel plates level - comparison with model with servovalve

Figure 3.49: Model of AMD and bearings setup evaluation for $K_{\mathrm{e}} = 1$ and $K_{\mathrm{p}} = 0$. Red solid lines show the experimental data and dashed blue lines show the expected response of the linear mathematical model.

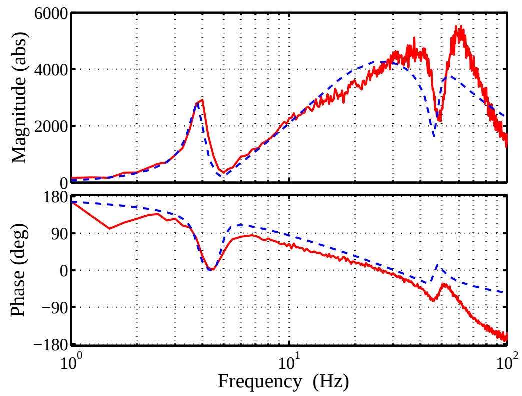

(a) Transfer function: program command (u) to ΔP comparison with model without servovalve

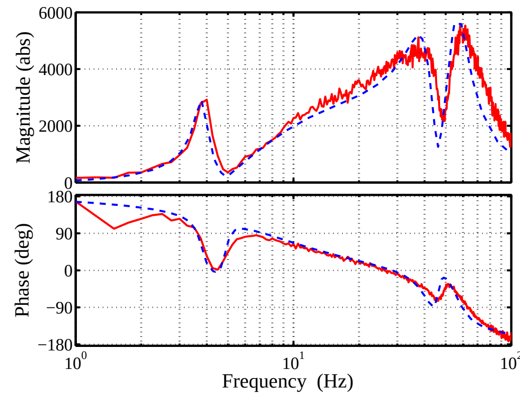

(b) Transfer function: program command (u) to ΔP comparison with model with servovalve

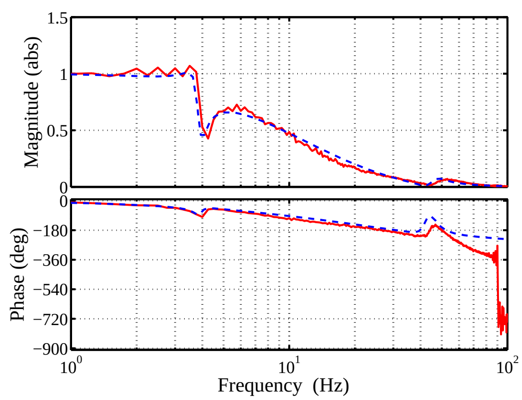

(c) Transfer function: program command (u) to LVDT comparison with model without servovalve

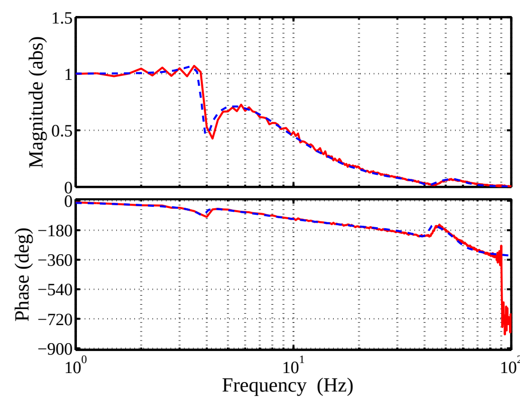

(d) Transfer function: program command (u) to LVDT comparison with model with servovalve

Figure 3.50: Model of AMD and bearings setup evaluation for $K_\mathrm{e} = 1$ and $K_\mathrm{p} = 9$. Red solid lines show the experimental data and dashed blue lines show the expected response of the linear mathematical model.

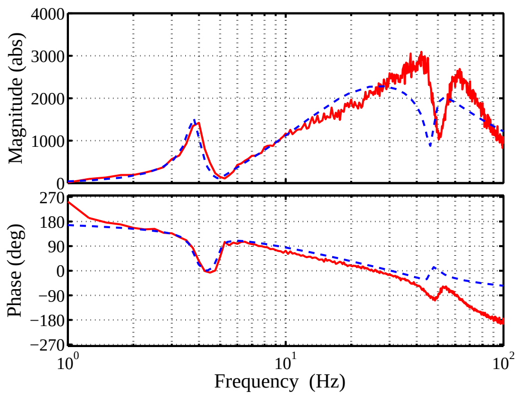

(a) Transfer Function: Program command (u) to table acceleration comparison with model without servovalve

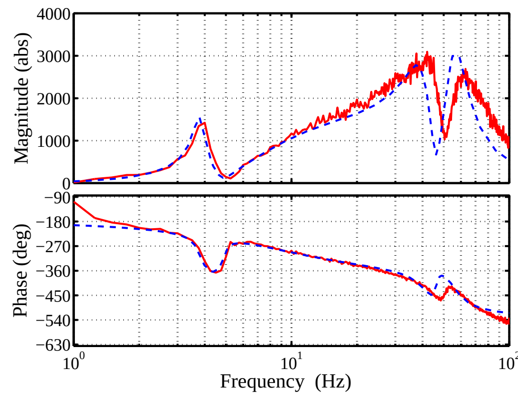

(b) Transfer Function: Program command (u) to table acceleration comparison with model with servovalve

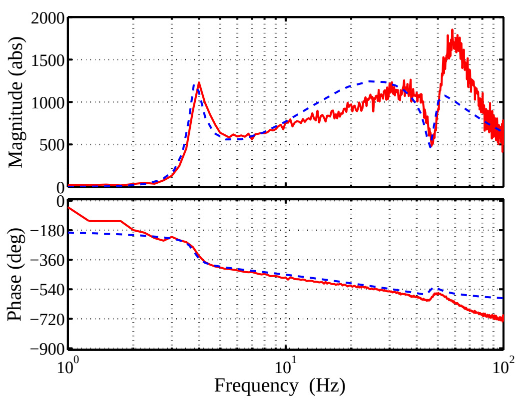

(c) Transfer Function: Program command (u) to acceleration at steel plates level - comparison with model without servovalve

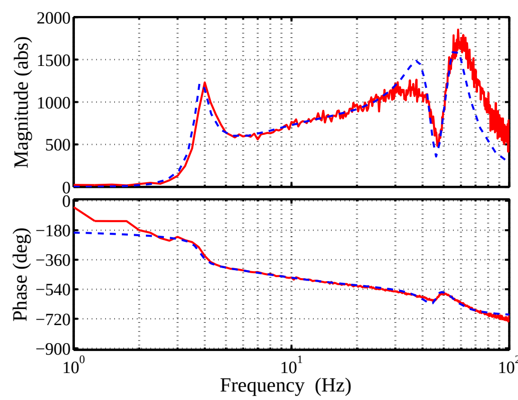

(d) Transfer function: program command (u) to acceleration at steel plates level - comparison with model with servovalve

Figure 3.51: Model of AMD and bearings setup evaluation for $K_{\mathrm{e}} = 1$ and $K_{\mathrm{p}} = 9$. Red solid lines show the experimental data and dashed blue lines show the expected response of the linear mathematical model.

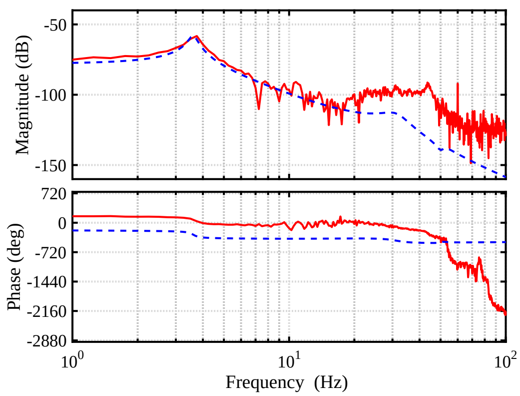

(a) $a_\mathrm{g} \to$ LVDT

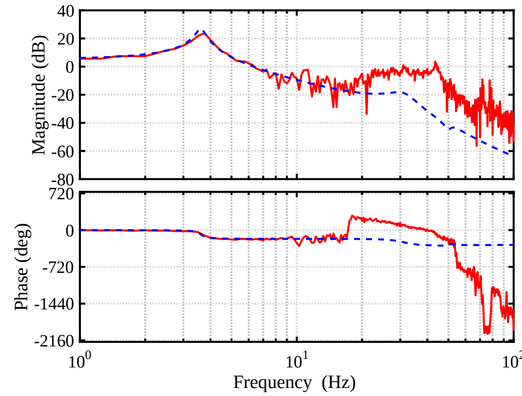

(b) $a_\mathrm{g} \to \Delta P$

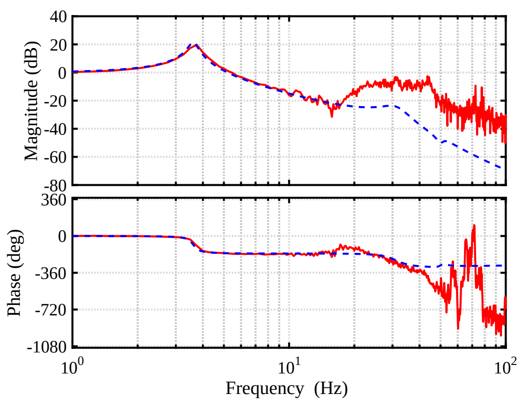

(c) $a_\mathrm{g} \to$ Proof-mass acceleration

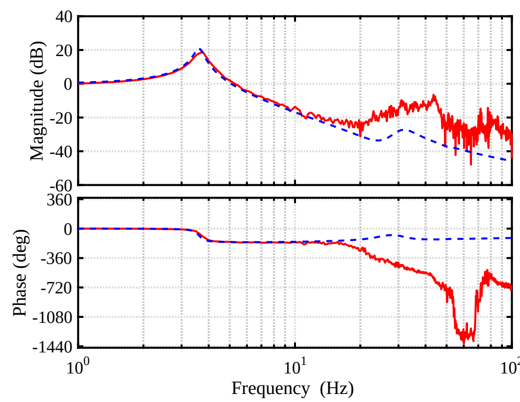

(d) $a_\mathrm{g} \to$ PS acceleration

Figure 3.52: Frequency response from shake table input, a_g, to different outputs of the combined AMD-PS system. Red solid lines show the experimental data and dashed blue lines show the expected response of the linear mathematical model.

Chapter 4

Dynamic Substructuring Strategy

This chapter represents the main contribution of this work, introducing an alternate approach to designing controls for DS. First, the applicability and implementation of the approach are discussed, highlighting its simplicity relative to conventional approaches. Then, two sets of shake table experiments are presented, demonstrating the performance of this approach. These experiments utilize the 1DOF AMD and the resonant physical subsystem of Chapter 3. The first set compares how closely the 1DOF AMD with control resembles different virtual subsystems. As pointed out in Chapter 1, being able to test this independently of any physical subsystem is a feature of this new approach. In the second set of experiments, the resonant physical subsystem is used, and the response of the combined system is evaluated. The experimental results attest to robust stability and accuracy of the new approach.

4.1 Concept

DS is approached here from a different point of view than previous efforts described in Chapter 2. This new approach does not involve a tracking controller, a compensator for the actuator dynamics, or specialized numerical integration schemes. While this approach is applicable more generally, for concreteness, it is described in the context of the configuration shown in Figure 4.1a. This is similar to the SFSI configuration of Figure 5.1.

The AMD has two inputs — the physical subystem motion (acceleration) and a control input. The physical control input to a hydraulic shaker is a valve driver current reference. However, as described in Chapter 3, the AMD is operated in a closed-loop mode with feedback gains on the position error and the differential pressure. In this mode, the control input is a reference position. The intention is however not to track position. The feedback control of the AMD is merely to reduce sensitivity to parameter variations and nonlinearities. The effect of these feedback gains on dynamic substructuring will be discussed later in this chapter. Operating the AMD with position feedback is also convenient in terms of practical matters such as simply being able to power it on before starting a dynamic substructuring test[1].

The new control strategy is based on asking the question,

> What should the control input be, so that the AMD applies the same forces on the foundation as the VS would?

The concept is shown in Figure 4.2. It should be noted that this is a *feedforward* strategy, with no tracking controller, or a compensator to make up for inexact tracking. It will be shown in the following that this greatly simplifies the control design and ensures robustly stable and accurate testing.

4.2 Specialization to linear systems

Rather than attempting to answer the above question in its full generality, several cases are considered where the AMD can be reasonably represented by a linear model. This restriction is made for two reasons.

[1]The idea of driving an AMD with position feedback when the goal is not displacement tracking is not new; this was done in the structural control context in [114]. There, the goal was to regulate the displacements of the actively controlled structure, while the input to the AMD was a position command. Control-structure interaction was taken into account; by contrast, in the present DS strategy, control-structure interaction is *eliminated*. This strategy may therefore also hold promise in active control applications to account for control-structure interaction.

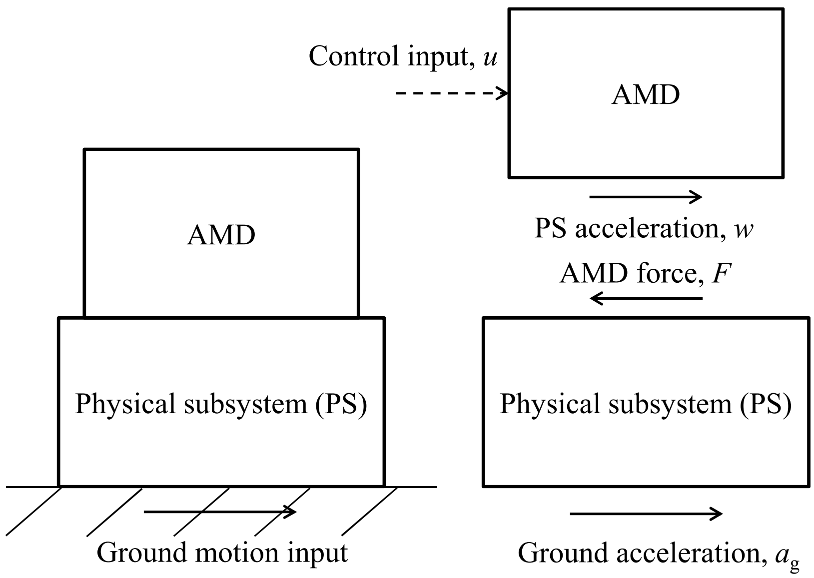

(a) DS configuration that this work focuses on

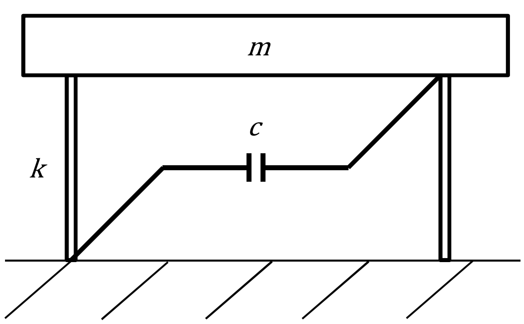

(b) One-DOF virtual subsystem

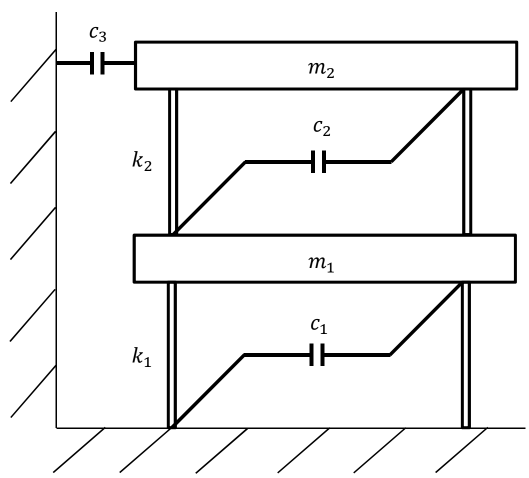

(c) Two-DOF virtual subsystem (the dashpot c_3 is intended to produce a VS with an exaggerated second mode in Section 4.4.2.2)

Figure 4.1: DS configuration used in this work; although the strategy described in this work is more generally applicable, discussions are based on the configure shown here.

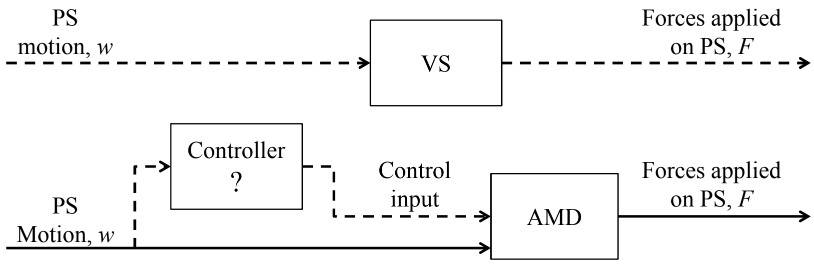

Figure 4.2: Concept of our DS strategy — what should the control input be, so that the AMD applies the same forces on the PS as the VS would?

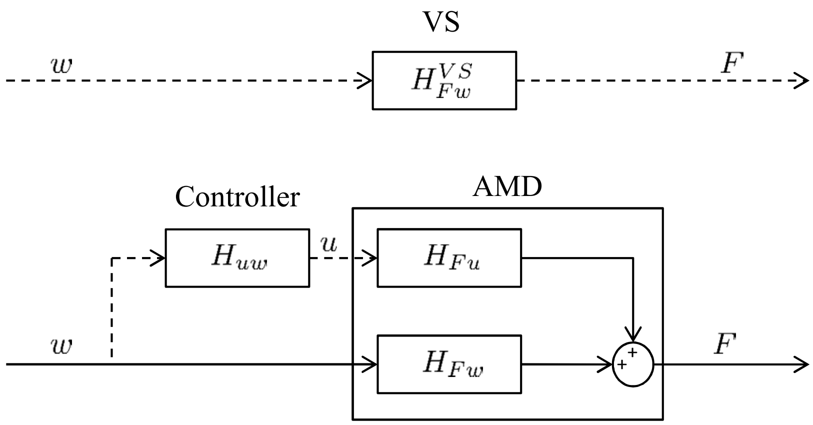

Figure 4.3: Controller concept for linear AMD — when the AMD is considered linear, the force transmitted can be written as $F = H_{Fu}u + H_{Fw}w$; the concept of Figure 4.2 can then be arranged as shown here

1. Since there is feedback control implemented in the AMD itself, the effects of nonlinearities are reduced.

2. As will be demonstrated later, the dynamic substructuring control strategy developed is not very sensitive to model variations; so using a linear model is sufficient.

With this specialization, the concept of Figure 4.2 can be rearranged as shown in Figure 4.3.

In this work, a further specialization is made, considering stable linear virtual subsystems (Section 4.3 briefly suggests how nonlinear virtual subsystems can be considered). This results in a linear controller, and the concept of Figure 4.3 can be written as

$$H_{Fw}^{\mathrm{VS}}w = H_{Fw}w + H_{Fu}H_{uw}w \tag{4.1}$$

where H_{uw} is the dynamic substructuring controller to be designed. This suggests the following for the controller

$$H_{uw} = H_{Fu}^{-1}(H_{Fw}^{\mathrm{VS}} - H_{Fw}) \tag{4.2}$$

raising the question of when the inverse model H_{Fu}^{-1} is meaningful. This has been considered extensively for linear multivariable systems [115–117] and even nonlinear systems [118, 119] in the contexts of inverse feedforward control and model-matching [120] among others. Section 4.3.1 reviews this question in the dynamic substructuring context. Before proceeding further, the next subsection describes the virtual subsystems used later.

4.2.1 Virtual subsystems considered

In the analysis and experiments that follow, two types of virtual subsystems are used — a one-DOF system (Figure 4.1b), and a two-DOF system (Figure 4.1c). Although more complex virtual subsystems can be considered, this is not particularly necessary, because only effects that influence the DOF at the VS-PS interface need to be taken into account. It should be noted that with a one-DOF AMD, i.e., with one control input, only one interface condition can be represented as desired. For example if the base shear transmitted to the physical subsystem is represented actively, the overturning moment is automatically determined by the geometry of the AMD, and does not represent the overturning moment from the virtual subsystem. Vice versa if the overturning moment is represented actively. If multiple interface conditions must be properly represented, then a multi-DOF AMD is required. In the virtual subsystems considered here, properties are chosen so that rotational effects are negligible, and therefore overturning moments need not be properly represented. Thus, the goal is only to represent base shear, and controls are designed accordingly.

One-DOF VS: The equation of motion together with the force transmitted to the base is

$$\begin{gathered} m\ddot{\chi} + c\dot{\chi} + k\chi = -mw \\ F = k\chi + c\dot{\chi} \end{gathered} \tag{4.3}$$

where χ is the displacement relative to the base. The usual state-space representation is

$$\begin{aligned}\dot{\bar{x}} &= \bar{A}\bar{x} + \bar{E}w \\ \bar{y} &= \bar{C}\bar{x}\end{aligned} \tag{4.4a}$$

where the output y is the force transmitted, and

$$\bar{A} = \begin{bmatrix} 0 & 1 \\ -k/m & -c/m \end{bmatrix}, \quad \bar{E} = \begin{bmatrix} 0 \\ -1 \end{bmatrix}, \quad \bar{C} = \begin{bmatrix} k & c \end{bmatrix} \tag{4.4b}$$

The transfer function from the base acceleration to the force transmitted is

$$H_{Fw}^{\mathrm{VS}} = \frac{k + cs}{s^2 + 2\zeta\omega s + \omega^2} \tag{4.5}$$

Two-DOF VS: The mass, damping and stiffness matrices are

$$M = \begin{bmatrix} m_1 & 0 \\ 0 & m_2 \end{bmatrix}, \quad C = \begin{bmatrix} c_1 + c_2 & -c_2 \\ -c_2 & c_2 + c_3 \end{bmatrix}, \quad K = \begin{bmatrix} k_1 + k_2 & -k_2 \\ -k_2 & k_2 \end{bmatrix} \tag{4.6}$$

The equation of motion and force transmitted are

$$\begin{aligned}M\ddot{\chi} + C\dot{\chi} + K\chi &= -M \begin{bmatrix} 1 & 1 \end{bmatrix}^\top w \\ F &= k_1\chi_1 + c_1\dot{\chi}_1 + c_3\dot{\chi}_2\end{aligned} \tag{4.7}$$

where again $\chi = [\chi_1, \chi_2]^\top$ is the displacement relative to the base. The state space representation is as in Equation (4.4a), with

$$\bar{A} = \begin{bmatrix} 0 & I \\ -M^{-1}K & -M^{-1}C \end{bmatrix}, \quad \bar{E} = \begin{pmatrix} 0 \\ -1 \\ 0 \\ -1 \end{pmatrix}, \quad \bar{C} = \begin{bmatrix} k_1 & c_1 & 0 & c_3 \end{bmatrix} \tag{4.8}$$

The transfer function for the force transmitted, H_{Fw}^{VS}, is computed in MATLAB from the state space representation.

4.2.2 Specialization to SISO AMD

The experiments presented in Sections 4.4 and 4.5 use the single input-single output (SISO) AMD designed in Chapter 3. Therefore, a SISO AMD is considered here. The controller given in Equation (4.2) can be written as

$$H_{uw} = \frac{H_{Fw}^{\mathrm{VS}} - H_{Fw}}{H_{Fu}} \tag{4.9}$$

For implementation, we wish for H_{uw} to be *stable* and *causal*. This will be the case if [121]

1. H_{Fw} and H_{Fw}^{VS} are *stable* (all their poles are in the left half plane)

2. H_{Fu} is *minimum-phase* (all its zeros are in the left half plane)

3. The transfer function H_{uw} is *proper* (the order of its numerator polynomial is less than or equal to the order of its denominator polynomial)

For the closed-loop hydraulic AMD, from the equations presented in Section 3.2.2.2, H_{Fw} is stable and H_{Fu} is minimum phase. Therefore, if a stable virtual subsystem is selected, the first two conditions above are satisfied. However, depending on the choice of the virtual subsystem, formula (4.9) may not result in a causal transfer function H_{uw}, i.e. its numerator polynomial may be of greater order than its denominator polynomial. In such cases, the H_{uw} obtained using formula (4.9) should be modified by adding an appropriate number of fast poles. This is illustrated in the next subsection through examples. Further modifications are needed to H_{uw} for other virtual subsystems as discussed in Section 4.2.4. The operator "fix" is used to denote all approximations needed to realize a controller that can be implemented, and the controller can be written as

$$H_{uw} = \mathrm{fix}\left(\frac{H_{Fw}^{\mathrm{VS}} - H_{Fw}}{H_{Fu}}\right) \tag{4.10}$$

4.2.3 Fixing H_{uw} for causality

Here the modifications to H_{uw} to make it causal are illustrated using specific examples. In these examples, the AMD models shown in Section 3.2.2.2 and parameters from Tables 3.4 and 3.6 are used, and a single-DOF VS with the properties, mass $m = M_\mathrm{t} = 3.93\frac{\text{lb-s}^2}{\text{in}}$, stiffness $k = 3879\text{lb/in}$, and damping coefficient $c = 12.35\frac{\text{lb-s}}{\text{in}}$. This results in a VS frequency of 5Hz and damping ratio of 5%, and transfer function based on equation (4.5),

$$H_{Fw}^{\mathrm{VS}} = -\frac{12.35s + 3879}{s^2 + 3.142s + 987}$$

AMD models with and without the servovalve are considered, to show the implication of this on the causality of H_{uw}, i.e., on whether or not it is proper.

Case (1) — AMD model *without* servovalve The AMD transfer functions are obtained from the state-space model $\dot{x} = Ax + Bu + Ew$, where A, B and E are as in equation (3.13). Since the output of interest is the force transmitted, $C = [0\ 0\ A_\mathrm{p}]$. The transfer functions are obtained in MATLAB using

```
H_Fu = tf(ss(A,B,C,[]));
H_Fw = tf(ss(A,E,C,[]));
```

Using the AMD properties in Section 3.2.2.2, we get

$$H_{Fu} = -\frac{3.856{\times}10^6 s^2}{s^3 + 121s^2 + 2.878{\times}10^4 s + 9.811{\times}10^5}$$
$$H_{Fw} = -\frac{1.131{\times}10^5 s + 3.856{\times}10^6}{s^3 + 121s^2 + 2.878{\times}10^4 s + 9.811{\times}10^5}$$

Now, from equation (4.9),

$$H_{uw} = \frac{3.202{\times}10^{-6} s^2 - 0.02794s - 0.8783}{s^2 + 3.142s + 987} \tag{4.11}$$

which is proper. It should be noted that the denominator polynomials of H_{Fw}^{VS} and H_{uw} are identical.

Case (2) — AMD model *with* servovalve By a similar process as in the previous case, but with A, B and E taken from equation (3.14) that includes the servovalve dynamics, and $C = [0\ 0\ A_\mathrm{p}\ 0]$, we obtain

$$\begin{aligned} H_{Fu} &= -\frac{7.268{\times}10^8 s^2}{s^4 + 236s^3 + 5.159{\times}10^4 s^2 + 5.425{\times}10^6 s + 1.849{\times}10^8} \\ H_{Fw} &= -\frac{1.131{\times}10^5 s^2 + 2.132{\times}10^7 s + 7.268{\times}10^8}{s^4 + 236s^3 + 5.159{\times}10^4 s^2 + 5.425{\times}10^6 s + 1.849{\times}10^8} \end{aligned}$$

and formula (4.9) gives

$$H_{uw} = \frac{1.699{\times}10^{-8} s^3 - 1.463{\times}10^{-4} s^2 - 0.02769s - 0.8783}{s^2 + 3.142s + 987} \tag{4.12}$$

Now, H_{uw} is *not* proper, and consequently, not causal. It therefore cannot be exactly implemented for realtime application. To make it proper, it is approximate by adding one fast pole. The frequency of this pole is chosen to be higher than all the dynamics of interest in the system. In the experiments that follow, where needed, this frequency is set equal to 1000Hz ($2\pi 1000$rad/s). Thus, the "fixed" transfer function is

$$\begin{aligned} H_{uw} &= \frac{1.067{\times}10^{-4} s^3 - 0.9191s^2 - 174s - 5518}{(s^2 + 3.142s + 987)(s + 6283)} \\ &= \frac{1.067{\times}10^{-4}(s - 8797)(s + 145.6)(s + 40.37)}{(s + 6283)(s^2 + 3.142s + 987)} \end{aligned} \tag{4.13}$$

A comparison of the frequency responses of the non-causal and causal versions of the controller, H_{uw} are shown in Figure 4.4. The figure also shows the discrete approximation of the causal controller, described in Section 4.2.5.

4.2.4 Other considerations — high pass filtering

It has already been shown that formula (4.9) needs to be adjusted for causality. There are also other occasions when the controller resulting from the direct application of formula (4.9) is not ideal to implement directly. Often integrators appear, which will result in drift of the AMD proof mass. Two such examples are discussed below.

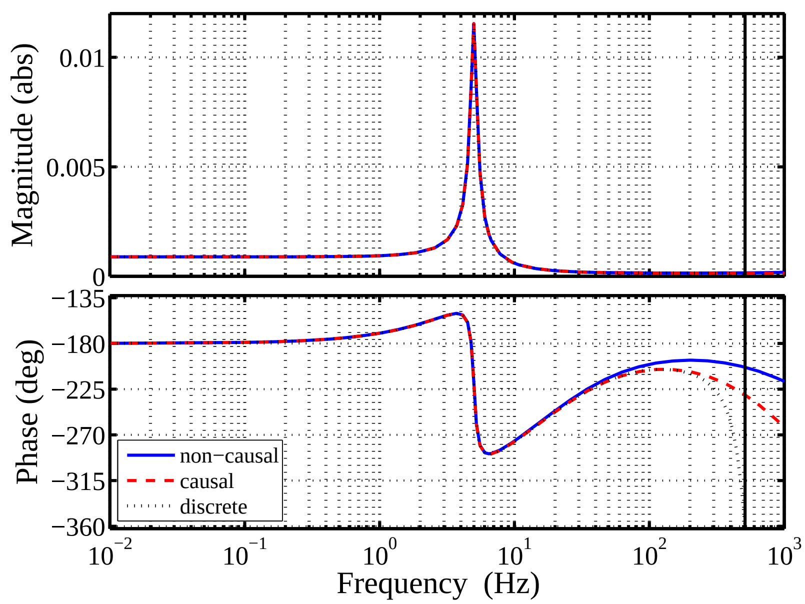

Figure 4.4: Controller for 1DOF VS with servovalve

Example 1 — VS mass not equal to proof mass: Again, AMD properties from Chapter 3 are used, and a single degree-of-freedom VS with the properties, mass $m = 1.97\frac{\text{lb-s}^2}{\text{in}} \neq M_\text{t}$, stiffness $k = 1939\text{lb/in}$, and damping coefficient $c = 6.17\frac{\text{lb-s}}{\text{in}}$ is considered. This results in a VS frequency of 5Hz and damping ratio of 5%, and transfer function

$$H_{Fw}^{\text{VS}} = -\frac{6.17s + 1939}{s^2 + 3.142s + 987}$$

Application of equation (4.9) gives a controller transfer function

$$H_{uw} = \frac{8.494{\times}10^{-9}s^5 - 1.51{\times}10^{-4}s^4 - 0.02876s^3 - 1.062s^2 - 16.05s - 493.5}{s^2(s^2 + 3.142s + 987)}$$

Note that there is a double integrator in the controller. The presence of the double integrator may be understood by recognizing that if $m = M_\text{t}$, then at steady state, i.e. constant base acceleration w, the force transmitted by the AMD is the same as that of the VS with no control action. However, if $m \neq M_\text{t}$, additional control action is needed.

In configurations similar to the canonical configuration of Figure 4.1a, it is likely that the VS mass is equal to or comparable to the proof mass. This is because in this configuration, the weight of the VS must be physical; it is only the lateral dynamics of the VS that is imitated through controls. In the experiments described in Section 4.4, the VS mass is taken equal to the proof mass.

Example 2 — Damping not stiffness-proportional: Let us now consider a 2-DOF virtual subsystem. First, the properties, $m_1 = m_2 = M_\mathrm{t}/2$, $k_1 = k_2 = 7758\mathrm{lb/in}$, $c_1 = c_2 = 12.35\frac{\text{lb-s}}{\text{in}}$, $c_3 = 0$ are used. The damping in this case is stiffness-proportional. The virtual subsystem transfer function is

$$H_{Fw}^{\mathrm{VS}} = -\frac{12.35s^3 + 7913s^2 + 1.95{\times}10^5 s + 6.125{\times}10^7}{s^4 + 18.85s^3 + 1.188{\times}10^4 s^2 + 4.961{\times}10^4 s + 1.559{\times}10^7}$$

and the controller from equation (4.9) is

$$H_{uw} = \frac{1.699{\times}10^{-8}s^5 - 0.0001407s^4 - 0.02855s^3 - 2.601s^2 - 279.2s - 7947}{s^4 + 18.85s^3 + 1.188{\times}10^4 s^2 + 4.961{\times}10^4 s + 1.559{\times}10^7}$$

The controller is not causal and can be implemented after adding a fast pole as described in Section 4.2.3.

Next, a two-DOF VS is considered with the following alternate properties: $m_1 = m_2 = M_\mathrm{t}/2$, $k_1 = 31030\mathrm{lb/in}$, $k_2 = 7758\mathrm{lb/in}$, $c_1 = c_3 = 12.35\frac{\text{lb-s}}{\text{in}}$, $c_2 = 0$. The specific VS is used in Section 4.4.2.2 to exaggerate the influence of the second mode. With these properties, the damping matrix is not stiffness-proportional. The virtual subsystem transfer function is

$$H_{Fw}^{\mathrm{VS}} = -\frac{3.103{\times}10^4 s^2 + 1.95{\times}10^5 s + 2.45{\times}10^8}{s^4 + 12.57s^3 + 2.373{\times}10^4 s^2 + 1.488{\times}10^5 s + 6.234{\times}10^7}$$

and the controller from equation (4.9) is

$$H_{uw} = \frac{-1.129{\times}10^4 s^5 - 0.02095s^4 - 2.458s^3 - 406.7s^2 - 1.105{\times}10^4 s - 9.922{\times}10^4}{s(s^4 + 12.57s^3 + 2.373{\times}10^4 s^2 + 1.488{\times}10^4 s + 6.234{\times}10^7)}$$

When the damping matrix is not stiffness proportional, it can be observed that the controller has again an integrator. A double integrator also appears when causal controller is designed using a state space approach in Section 4.3.

In such cases, in order to prevent drift of the proof mass, the controller should be augmented with a high-pass filter. In the experiments of Sections 4.4 and 4.5, where needed, a cutoff frequency of 0.1Hz is used for such high pass filters.

4.2.5 Controller implementation

The computation and implementation of the controller can be summarized as follows.

1. Calculate the controller H_{uw}, using formula (4.9), implemented in MATLAB as

   ```
   H_uw = minreal((H_VS - H_Fw)/H_Fu,1e-4);
   ```

2. If necessary, make the controller causal by adding a fast pole, as described in Section 4.2.3.

   ```
   omega = 2*pi*1000;
   H_uw_causal = H_uw/(s/omega+1);
   ```

3. If integrators are present, add a high pass filter as described in Section 4.2.4. For example, if a single integrator is present, as in Example 2 in Section 4.2.4, the a first order high pass filter is added.

   ```
   H_highpass = s/(s+2*pi*0.1);
   H_uw_fixed = minreal(H_uw_causal*H_highpass,1e-4);
   ```

4. Discretize the controller.

   ```
   controller = c2d(H_uw_fixed,1/1024,'tustin');
   ```

5. Obtain the state space representation of the discrete-time controller.

```
controller_ss = ss(controller);
```

6. Implement the controller as a LabVIEW MathScript (Figure 3.31).

Before proceeding to evaluate the effectiveness of this control design for DS through experiments, an alternate view of this approach is presented that may serve as a better starting point if nonlinear virtual subsystems and multi-DOF systems need to be considered.

4.3 State space view of controller

To further understand the transfer function inverse and causality considerations involved in constructing the controller H_{uw}, and as a starting point for extending this approach to multiple input-multiple output AMDs and nonlinear VSs, a state space view of the process described above is considered.

We start from state space descriptions of the AMD model

$$\begin{aligned} \dot{x} &= Ax + Bu + Ew \\ y &= Cx \end{aligned} \tag{4.14}$$

and of the VS,

$$\begin{aligned} \dot{\bar{x}} &= \bar{A}\bar{x} + \bar{E}w \\ \bar{y} &= \bar{C}\bar{x} \end{aligned} \tag{4.15}$$

Equation (4.14) may correspond to the equation that includes servovalve dynamics presented in Section 3.2.2.4, or the one presented in Section 3.2.2.3 that does not. Equation (4.15) may correspond to VS models such as the ones given by the equations (4.4b) and (4.8).

In state space terms, the control design concept of Figure (4.2) can be stated as

For $x(0) = 0$ and $\bar{x}(0) = 0$, find u such that $y(t) = \bar{y}(t)$ for $t \geq 0$.

If the model (4.14) had a direct feedthrough term, this can be used to solve for u. However, since (4.14) does not have a direct feedthrough term, the well-established procedure first introduced by Brockett [122] is followed to solve for u. It is required that $\dot{y}(t) = \dot{\bar{y}}(t)$. Since $y(0) = \bar{y}(0) = 0$, this implies that $y(t) = \bar{y}(t)$. From $\dot{y}(t) = \dot{\bar{y}}(t)$, we have

$$C\dot{x} = \bar{C}\dot{\bar{x}}$$

Substituting for $\dot{x}$ and $\dot{\bar{x}}$ from equations (4.14) and (4.15),

$$CAx + CBu + CEw = \bar{C}\bar{A}\bar{x} + \bar{C}\bar{E}w$$

There are now two possibilities.

Case (i) $CB \neq 0$: In this case, the above equation can be solved for u.

$$u = -(CB)^{-1}CAx + (CB)^{-1}\bar{C}\bar{A}\bar{x} + (CB)^{-1}(\bar{C}\bar{E} - CE)w$$

Substituting in equation (4.14) and combined with equation (4.15), the following state space representation for the controller is obtained.

$$\begin{aligned} \dot{\tilde{x}} &= \tilde{A}\tilde{x} + \tilde{E}w \\ u &= \tilde{C}\tilde{x} + \tilde{F}w \end{aligned} \tag{4.16a}$$

where

$$\begin{aligned} \tilde{x} &= \begin{bmatrix} x^\top & \bar{x}^\top \end{bmatrix}^\top \\ \tilde{A} &= \begin{bmatrix} (A - B(CB)^{-1}CA) & B(CB)^{-1}\bar{C}\bar{A} \\ 0 & \bar{A} \end{bmatrix} \\ \tilde{E} &= \begin{bmatrix} (E + B(CB)^{-1}(\bar{C}\bar{E} - CE))^\top & \bar{E}^\top \end{bmatrix}^\top \\ \tilde{C} &= \begin{bmatrix} -(CB)^{-1}CA & (CB)^{-1}\bar{C}\bar{A} \end{bmatrix} \\ \tilde{F} &= (CB)^{-1}(\bar{C}\bar{E} - CE) \end{aligned} \tag{4.16b}$$

Note that this is the case, i.e., $CB \neq 0$, when equation (4.14) corresponds to model of the AMD presented in Section 3.2.2.2 that does not include servovalve dynamics. The transfer function representation of equation (4.16) is identical to that obtained in case (1) in Section 4.2.3.

Case (ii) $CB = 0$: In this case, we require $\ddot{y}(t) = \ddot{\bar{y}}(t)$. Differentiating again,

$$CA\dot{x} + CE\dot{w} = \bar{C}\bar{A}\dot{\bar{x}} + \bar{C}\bar{E}\dot{w}$$

and substituting from equations (4.14) and (4.16),

$$CA(Ax + Bu + Ew) + CE\dot{w} = \bar{C}\bar{A}(\bar{A}\bar{x} + \bar{E}w) + \bar{C}\bar{E}\dot{w}$$

Now if $CAB \neq 0$, we can solve for u.

$$u = -(CAB)^{-1}CA^2x + (CAB)^{-1}\bar{C}\bar{A}^2\bar{x} + (CAB)^{-1}(\bar{C}\bar{A}\bar{E} - CAE)w + (\bar{C}\bar{E} - CE)\dot{w} \quad (4.17)$$

It can be seen that u depends on $\dot{w}$, and therefore, this computation of u is not causal. However, a causal approximation of $\dot{w}$ may be obtained as follows.

$$\begin{aligned} \dot{\tilde{w}} &= -\alpha\tilde{w} - \alpha^2 w \\ \dot{w} &= \tilde{w} + \alpha w \end{aligned} \quad (4.18)$$

where $\alpha \gg 0$, a state-space representation of the transfer function

$$\frac{\alpha s}{s + \alpha}$$

a causal approximation to a differentiator. This can be combined with equations (4.17), (4.14) and (4.15), resulting in the following state-space representation for the controller.

$$\begin{aligned} \dot{\tilde{x}} &= \tilde{A}\tilde{x} + \tilde{E}w \\ u &= \tilde{C}\tilde{x} + \tilde{F}w \end{aligned} \quad (4.19a)$$

where

$$
\begin{aligned}
\tilde{x} &= \begin{bmatrix} x^\top & \bar{x}^\top & \tilde{w} \end{bmatrix}^\top \\
\tilde{A} &= \begin{bmatrix} (A - B(CAB)^{-1}CA^2) & B(CAB)^{-1}\bar{C}\bar{A}^2 & B(CAB)^{-1}(\bar{C}\bar{E} - CE) \\ 0 & \bar{A} & 0 \\ 0 & 0 & -\alpha \end{bmatrix} \\
\tilde{E} &= \begin{bmatrix} (E + B(CAB)^{-1}((\bar{C}\bar{A}\bar{E} - CAE) + \alpha(\bar{C}\bar{E} - CE)))^\top & \bar{E}^\top & -\alpha^2 \end{bmatrix}^\top \\
\tilde{C} &= \begin{bmatrix} -(CAB)^{-1}CA^2 & (CAB)^{-1}\bar{C}\bar{A}^2 & (CAB)^{-1}(\bar{C}\bar{E} - CE) \end{bmatrix} \\
\tilde{F} &= (CAB)^{-1}((\bar{C}\bar{A}\bar{E} - CAE) + \alpha(\bar{C}\bar{E} - CE))
\end{aligned}
\tag{4.19b}
$$

Unlike in case (i), this controller is not the same as that obtained by the transfer function approach. Formula (4.19b) is an alternate causal controller that results in the AMD having the same effect as the VS. For the VS considered in case (2) in Section 4.2.3, the transfer function of this controller is

$$
H_{uw} = \frac{-4.3603\times 10^{-5}(s + 2.155\times 10^{4})(s + 145.5)(s + 40.38)(s^2 + 0.0008976s + 0.5615)}{s^2(s + 6283)(s^2 + 3.142s + 987)}
\tag{4.20}
$$

which has a double integrator. Adding a second order high pass filter with frequency 0.1Hz and damping ratio 0.7, we get

$$
H_{uw} = \frac{-4.3603\times 10^{-5}(s + 2.155\times 10^{4})(s + 145.5)(s + 40.38)(s^2 + 0.0008976s + 0.5615)}{(s^2 + 0.8796s + 0.3948)(s + 6283)(s^2 + 3.142s + 987)}
\tag{4.21}
$$

A comparison of the controllers obtained using the transfer function approach and state space approach is shown in Figure 4.5. The controller designed using the state space approach leads to the AMD more closely resembling the VS. The transfer function-based controller is used in the experiments that follow, because the state space approach was not realized at the time of the experiments.

The state space view could serve as a starting point if it is needed to represent nonlinear virtual subsystems. It also translates readily to multi-DOF systems. The extension of the above approach to multi-axis AMDs is presented in the next section.

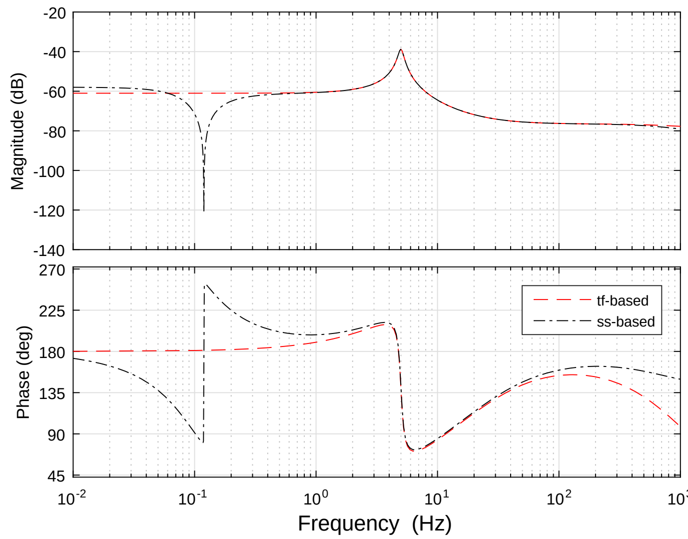

(a) Controller

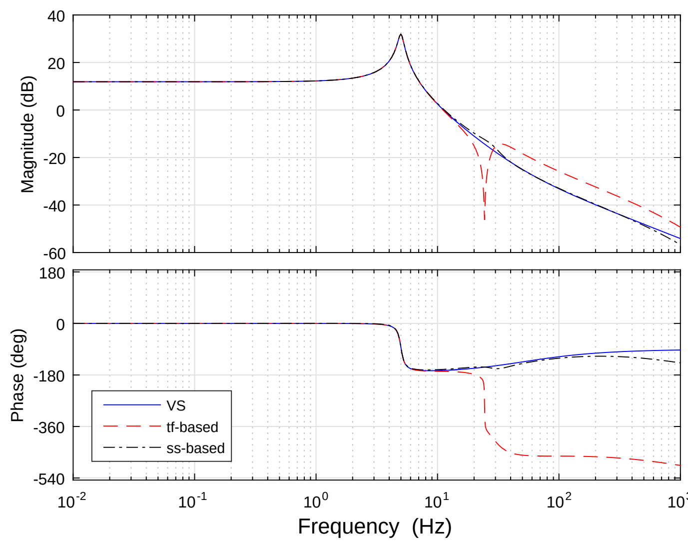

(b) Comparison with VS

Figure 4.5: Comparison of transfer function and state space approaches for controller design

4.3.1 Multi-axis AMD configurations

Consider a multi-axis AMD, for example, as shown in the concept of Figure 1.1, with n_{DOF} degrees of freedom for the proof mass and n_{ACT} actuators ($n_{\mathrm{ACT}} \geq n_{\mathrm{DOF}}$). Let $x_1 \in \mathbb{R}^n_{\mathrm{DOF}}$ be the displacements (and small rotations) associated with the DOF of the proof mass, $x_2 \in \mathbb{R}^n_{\mathrm{DOF}}$ the corresponding velocities, $x_3 \in \mathbb{R}^n_{\mathrm{ACT}}$ the differential pressures in the actuators, and $x_4 \in \mathbb{R}^n_{\mathrm{ACT}}$ the servovalve states in the actuators. Let T denote the $n_{\mathrm{ACT}} \times n_{\mathrm{DOF}}$ kinematic transformation from the proof mass DOF to the actuator displacements, so that Tx_1 represents the actuator displacements. Then the multi-DOF extension of the AMD model (3.14) is

$$\begin{pmatrix} \dot{x}_1 \\ \dot{x}_2 \\ \dot{x}_3 \\ \dot{x}_4 \end{pmatrix} = \begin{bmatrix} 0 & I & 0 & 0 \\ 0 & 0 & M_{\mathrm{t}}^{-1}T^{\top}A_{\mathrm{p}} & 0 \\ 0 & -k_{\mathrm{ACT}}T & -c_{\mathrm{ACT}} & d \\ -\alpha_{\mathrm{s}}K_{\mathrm{e}}T & 0 & -\alpha_{\mathrm{s}}K_{\mathrm{p}} & -\alpha_s \end{bmatrix} \begin{pmatrix} x_1 \\ x_2 \\ x_3 \\ x_4 \end{pmatrix} + \begin{bmatrix} 0 \\ 0 \\ 0 \\ \alpha_{\mathrm{s}}K_{\mathrm{e}}T \end{bmatrix} u + \begin{bmatrix} 0 \\ -R \\ 0 \\ 0 \end{bmatrix} w \quad (4.22a)$$

where now M_{t} is an $n_{\mathrm{DOF}} \times n_{\mathrm{DOF}}$ matrix, A_{p} and α_{s} are $n_{\mathrm{ACT}} \times n_{\mathrm{ACT}}$ diagonal matrices of actuator piston areas and servovalve cutoff frequencies, K_{e} and K_{p} are $n_{\mathrm{ACT}} \times n_{\mathrm{ACT}}$ diagonal matrices of actuator proportional and differential pressure gains, and k_{ACT}, c_{ACT} and d are $n_{\mathrm{ACT}} \times n_{\mathrm{ACT}}$ diagonal matrices of actuator stiffness ($2A_{\mathrm{p}}\kappa/x_{\mathrm{m}}$ from equation (3.9), damping $(2\kappa/(A_{\mathrm{p}}x_{\mathrm{m}})(K_{\mathrm{l}} + K_{\mathrm{f}})$ from equation (3.9)) and flow gain $(4\kappa/(A_{\mathrm{p}}x_{\mathrm{m}})K_{\mathrm{V}}$ from equation (3.11)). The output, the transmitted force ($\in \mathbb{R}^n_{\mathrm{DOF}}$), is given by

$$y = \begin{bmatrix} 0 & 0 & -T^{\top}A_{\mathrm{p}} & 0 \end{bmatrix} \begin{pmatrix} x_1 \\ x_2 \\ x_3 \\ x_4 \end{pmatrix} \quad (4.22b)$$

Equations (4.22) are in the form of (4.14). Since the states of any one actuator are completely uncoupled from those of the others, the analysis of these equations closely resembles case (ii) above. We realize that $CB = 0$, but $CAB = -T^{\top}(A_{\mathrm{p}}\alpha_{\mathrm{s}}dK_{\mathrm{e}})T$ is nonsingular because the kinematic transformation, T, is full rank. The controller therefore has the state space representation (4.19). This, of course, has to be adjusted for integrators and other features before implementation.

4.4 Testing AMD function independently of any PS

This section describes experiments carried out to assess how closely the AMD, using the controller of Section 4.2.5, is able to imitate different virtual subsystems. In these tests, no physical subsystem is used; the capabilities of the AMD are tested independently of any physical subsystem. The ability to do so is a feature of the new strategy.

The experimental setup is shown in Figure 4.6, with the AMD mounted on a shake table. In addition to the AMD displacement (LVDT), acceleration and differential pressure, the shake table acceleration, w, is also measured, and is the input to the DS controller. Different one-DOF and two-DOF virtual subsystems are considered as detailed below. For each target VS, a controller is computed and implemented as outlined in Section 4.2.5. DS performance is assessed in terms of frequency response. The base-motion (w)–applied force ($A_{\mathrm{p}}\Delta P$) frequency response of the AMD together with the controller is obtained experimentally as described in Section 3.5.2.2. This is compared with the corresponding frequency response of the target VS. For all these tests, the shake table is commanded with a 0.5g amplitude multisine acceleration. The bandwidth of the multisine is however 50Hz for some tests and 100Hz for others. The actual measured acceleration of the shake table is used as the input, w, for frequency response calculation.

The effect of gain settings in the hydraulic feedback controller on performance of dynamic substructuring is also explored. At higher amplitudes of motion of the AMD, which result for example when the VS natural frequency or damping ratio is low, nonlinearities are more pronounced in the AMD behavior. The effect of these nonlinearities on dynamic substructuring with a controller designed based on a linear AMD model is examined.

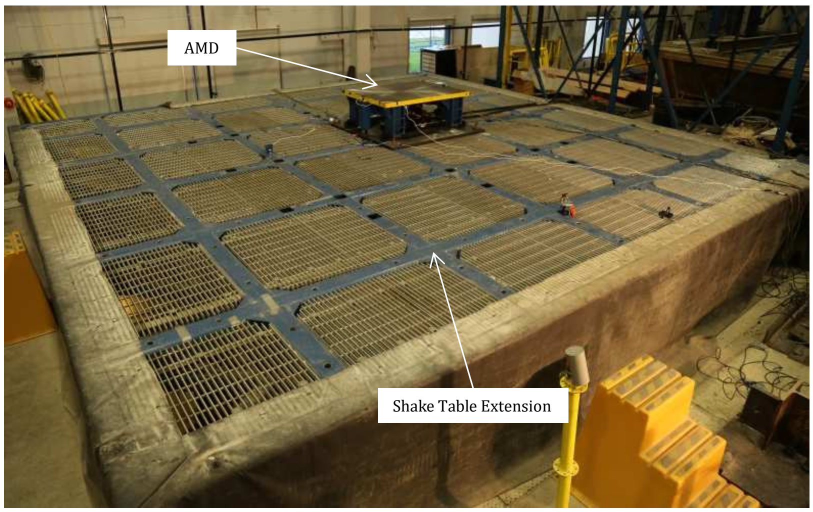

(a) Overview

(b) Closeup

Figure 4.6: Experimental configuration for testing AMD function independently of physical subsystem — AMD mounted on shake table (see [98] for details of shake table extension)

4.4.1 One-DOF virtual subsystems

Eight one-DOF virtual subsystems are considered with natural frequencies 5Hz–40Hz in intervals of 5Hz. The mass of each VS is taken as equal to the proof mass of the AMD, and the damping ratio as 5%. DS experiments are repeated with two sets of hydraulic controller gains settings — $K_{\mathrm{e}} = 1, K_{\mathrm{p}} = 0$ and $K_{\mathrm{e}} = 1, K_{\mathrm{p}} = 9$. There is thus a total of 16 experiments. The w–$A_{\mathrm{p}}\Delta P$ frequency response of the AMD+controller is compared with the base-acceleration–transmitted force frequency response of the corresponding target VS (equation (4.5)). Results are shown in Figures 4.7–4.9. The following can be observed.

1. For all VS natural frequencies and hydraulic controller gain settings, the frequency responses of the AMD+controller match closely those of the target virtual subsystems. Specifically, the amplitude and phase response near the natural frequency are represented well. This demonstrates that the proposed dynamic substructuring controller is effective.

2. For VS with lower natural frequencies, when the ΔP gain, $K_{\mathrm{p}} = 0$ (Figures 4.7a, 4.7c and 4.7e), the AMD+controller frequency response deviates from that of the target VS at frequencies over 20Hz, to the right of the VS natural frequency. For these same VS, when a higher ΔP gain is used (Figures 4.7b, 4.7d and 4.7f) the discrepancy at least in the amplitude response decreases. The fact that the difference in amplitude frequency response decreases with increased K_{p} suggests that the deviation is related to the 27Hz oil-column frequency of the AMD. The DS controller produces very little input at frequencies away from the VS natural frequency. The hypothesis is that nonlinearities in the system result in harmonics that are unmitigated near the oil-column frequency. This requires further work.

3. For VS frequencies in the 20Hz–30Hz range (Figure 4.8), there is not a significant deviation between the AMD+controller and target VS frequency responses. This is presumably because for these VSs, the controller produces substantial input in the vicinity of the oil-column frequency, and the AMD response to this input dominates

any harmonic effects.

4. For even higher VS frequencies of 35Hz and 40Hz (Figure 4.9), the deviation begins to appear to the left of the natural frequency, lending further credence to the hypothesis that this is related to the AMD oil-column frequency.

5. In some of the plots such as Figures 4.7a, 4.7b, 4.8a, 4.8c and 4.8e, there are abrupt changes in the measured phase response. These changes are multiples of 360°, and are just artifacts of plotting.

In summary, the proposed DS controller is effective in imitating virtual subsystems over a wide range of frequencies. When the natural frequency of the virtual subsystem is away from the oil-column frequency of the AMD, there is a small deviation in the frequency response, which is reduced with a sufficiently large ΔP gain, K_{p}, is used.

4.4.1.1 Effect of servovalve saturation

A VS of given natural frequency and mass transmits greater force as its damping ratio decreases for forcing frequencies below $\sqrt{2}$ times its natural frequency. This is shown in Figure 4.10a for a VS of 5Hz natural frequency. Consequently, as the VS damping ratio is reduced, the acceleration needed in the AMD increases. This leads to a higher velocity demand in the AMD, and greater flow demand in the servovalve. Therefore, VSs with lower damping ratio are considered to explore what happens when there is increased flow demand, and potentially saturation of the servovalve. Specifically, when this occurs, the behavior of the AMD is nonlinear, and the goal is to see how a DS controller designed based on a linear model of the AMD would work.

5Hz VS with damping ratios of 5%, 2% and 1% are considered. Experimental results are shown in Figure 4.11 for gain setting $K_{\mathrm{e}} = 1$, $K_{\mathrm{p}} = 0$, and in Figure 4.12 for $K_{\mathrm{e}} = 1$, $K_{\mathrm{p}} = 9$. In these figures, the left columns show the measured AMD+controller and target VS frequency responses, and right columns show corresponding the time series of the servovalve command. A 10V servovalve command indicates saturation. The following

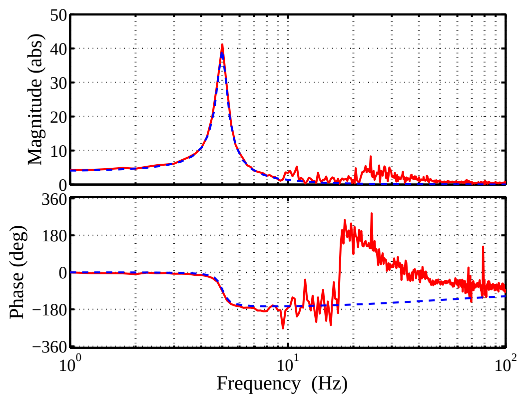

(a) VS frequency = 5Hz, $K_{\mathrm{e}} = 1$, $K_{\mathrm{p}} = 0$

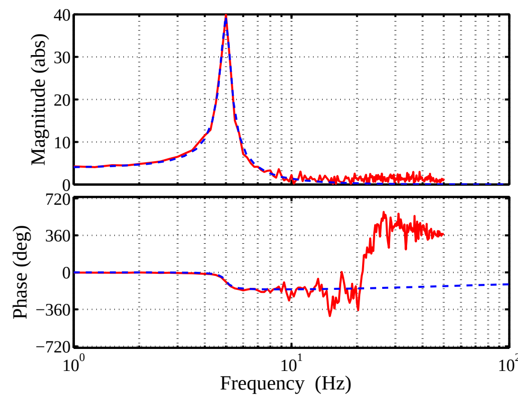

(b) VS frequency = 5Hz, $K_{\mathrm{e}} = 1$, $K_{\mathrm{p}} = 9$

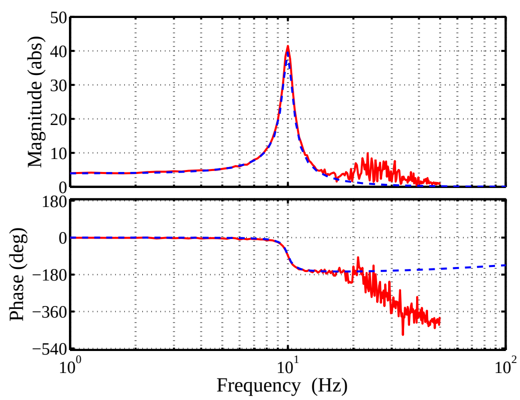

(c) VS frequency = 10Hz, $K_{\mathrm{e}} = 1$, $K_{\mathrm{p}} = 0$

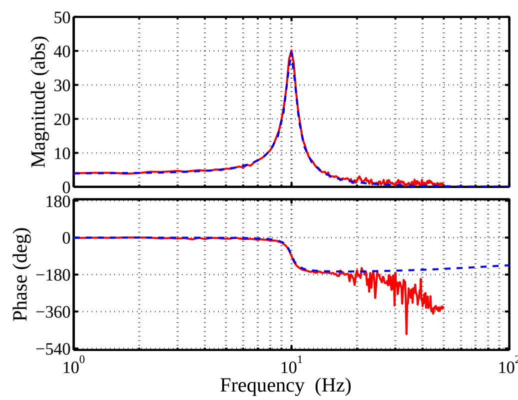

(d) VS frequency = 10Hz, $K_{\mathrm{e}} = 1$, $K_{\mathrm{p}} = 9$

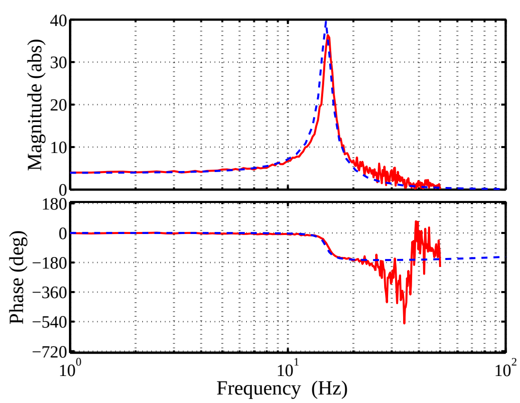

(e) VS frequency = 15Hz, $K_{\mathrm{e}} = 1$, $K_{\mathrm{p}} = 0$

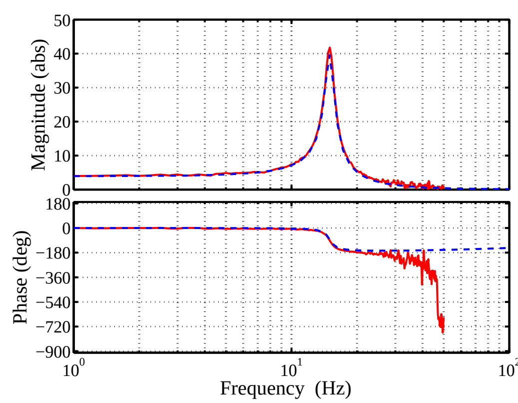

(f) VS frequency = 15Hz, $K_{\mathrm{e}} = 1$, $K_{\mathrm{p}} = 9$

Figure 4.7: DS testing of AMD function independently of physical subsystem for one-DOF VS of frequencies 5Hz, 10Hz and 15Hz and damping ratio 5%; red solid lines represent the measured AMD+controller frequency response, and blue dashed lines, the target VS frequency response

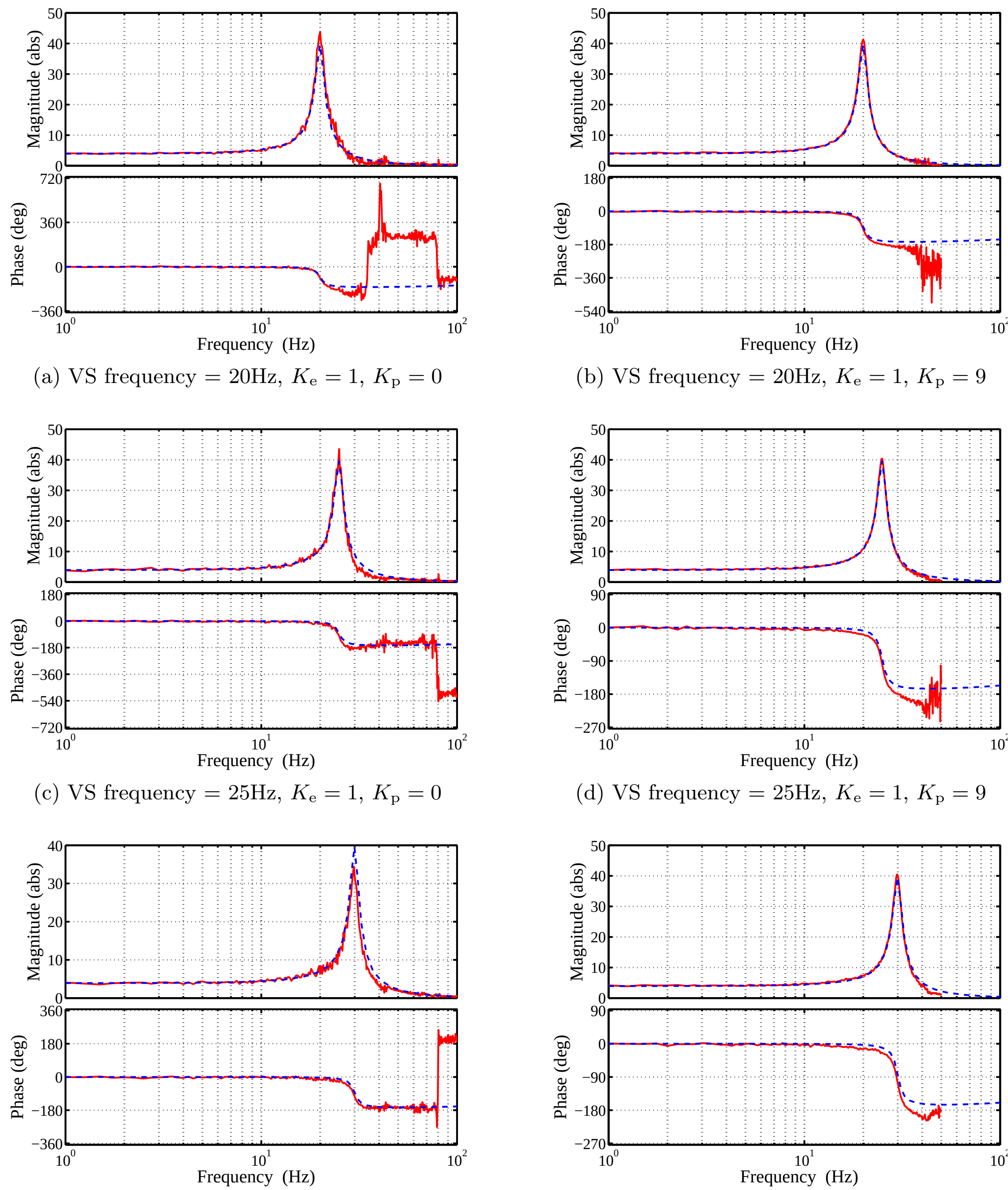

(a) VS frequency = 20Hz, $K_{\mathrm{e}} = 1$, $K_{\mathrm{p}} = 0$

(b) VS frequency = 20Hz, $K_{\mathrm{e}} = 1$, $K_{\mathrm{p}} = 9$

(c) VS frequency = 25Hz, $K_{\mathrm{e}} = 1$, $K_{\mathrm{p}} = 0$

(d) VS frequency = 25Hz, $K_{\mathrm{e}} = 1$, $K_{\mathrm{p}} = 9$

(e) VS frequency = 30Hz, $K_{\mathrm{e}} = 1$, $K_{\mathrm{p}} = 0$

(f) VS frequency = 30Hz, $K_{\mathrm{e}} = 1$, $K_{\mathrm{p}} = 9$

Figure 4.8: DS testing of AMD function independently of physical subsystem for one-DOF VS of frequencies 20Hz, 25Hz and 30Hz and damping ratio 5%; red solid lines represent the measured AMD+controller frequency response, and blue dashed lines, the target VS frequency response

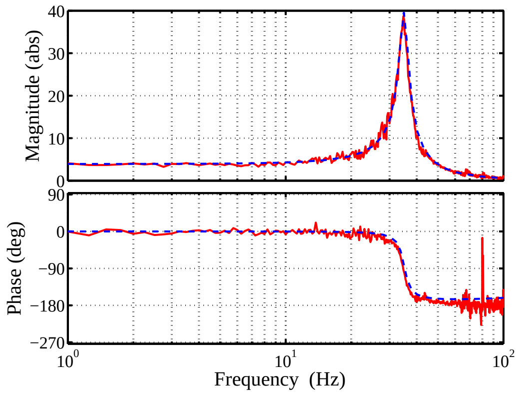

(a) VS frequency = 35Hz, $K_{\mathrm{e}} = 1$, $K_{\mathrm{p}} = 0$

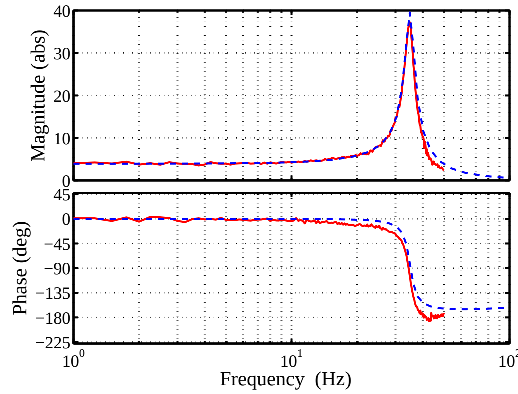

(b) VS frequency = 35Hz, $K_{\mathrm{e}} = 1$, $K_{\mathrm{p}} = 9$

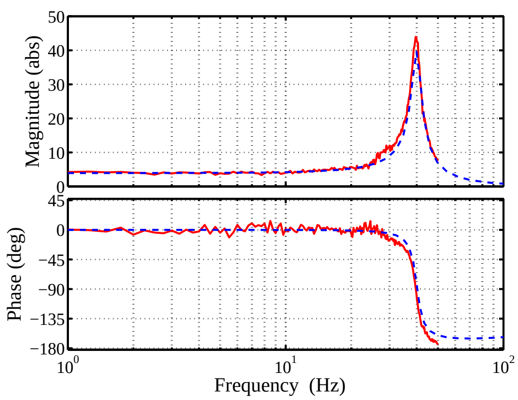

(c) VS frequency = 40Hz, $K_{\mathrm{e}} = 1$, $K_{\mathrm{p}} = 0$

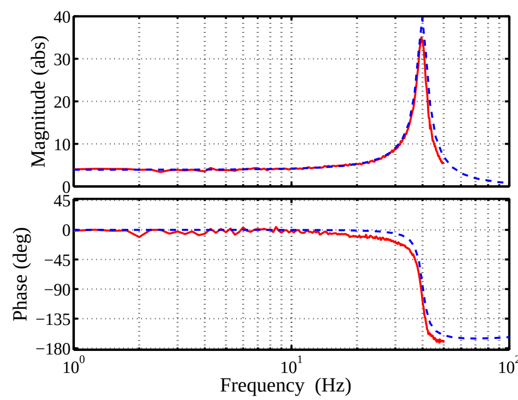

(d) VS frequency = 40Hz, $K_{\mathrm{e}} = 1$, $K_{\mathrm{p}} = 9$

Figure 4.9: DS testing of AMD function independently of physical subsystem for one-DOF VS of frequencies 35Hz and 40Hz and damping ratio 5%; red solid lines represent the measured AMD+controller frequency response, and blue dashed lines, the target VS frequency response

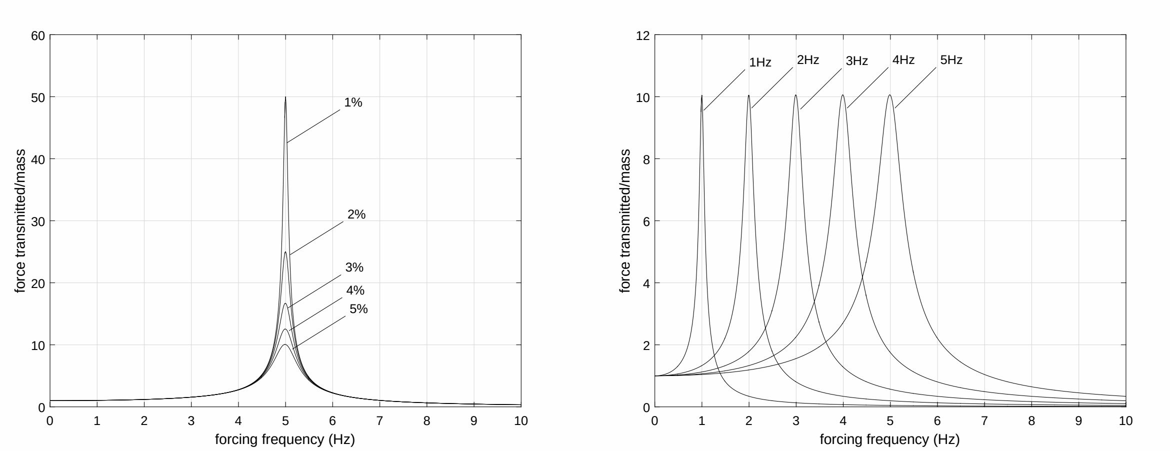

(a) Natural frequency = 5Hz, damping ratio varied from 1% to 5%

(b) Damping ratio = 5%, natural frequency varied from 1Hz to 5Hz

Figure 4.10: Force transmitted/mass for different virtual subsystems with varying natural frequency and damping

observations can be made.

1. For VS with 5% damping ratio, the valve command is only at 50% of saturation (Figures 4.11b and 4.12b). The frequency response of the AMD+controller closely matches that of the target VS, subject to the caveats discussed in Section 4.4.1 (Figures 4.11a and 4.12a).

2. When the damping ratio is decreased to 2%, the valve command just saturates (Figures 4.11d and 4.12d). The natural frequency of the target VS and the corresponding phase change are captured, but the AMD does not achieve the resonant peak (Figures 4.11c and 4.12c). The harmonics resulting from nonlinear effects, as discussed in Section 4.4.1 are more pronounced.

3. When the damping ratio is further reduced to 1%, the valve command saturates over significant periods of time (Figure 4.12f). While the natural frequency and the corresponding phase change are represented, the amplitude of the resonant peak is significantly less, and the the width of the resonant peak is smaller as well (Figure 4.12e). There is also a significant third harmonic.

Even when there is significant nonlinearity in the form of valve saturation, a controller

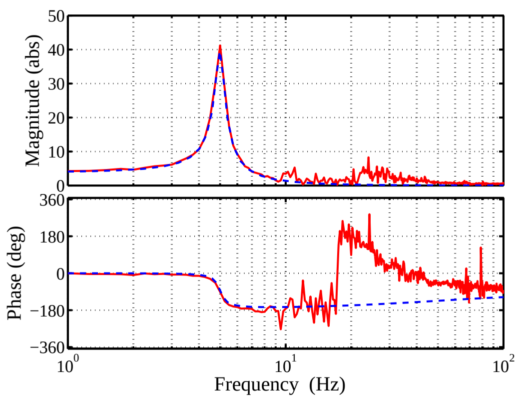

(a) VS damping = 5%: frequency response (same as Figure 4.7a)

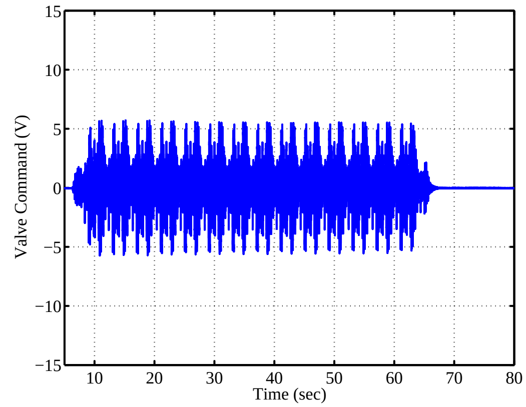

(b) VS damping = 5%: valve command time series

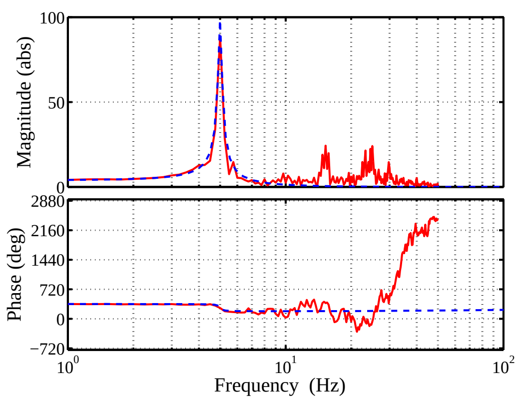

(c) VS damping = 2%: frequency response

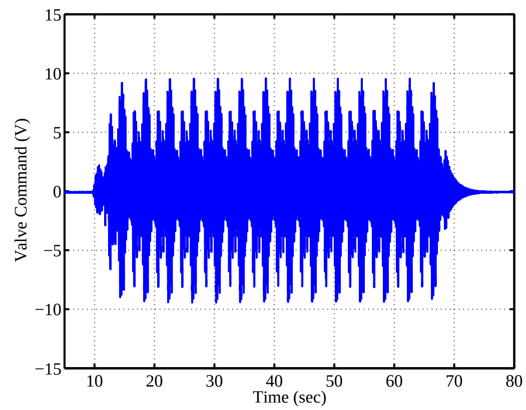

(d) VS damping = 2%: valve command time series

Figure 4.11: DS testing of AMD function for 5Hz one-DOF VS and different damping ratios with $K_{\mathrm{e}} = 1$ and $K_p = 0$; in the frequency response plots, red solid lines represent the measured AMD+controller frequency response, and blue dashed lines, the target VS frequency response

designed based on a linear model of the AMD is effective in capturing the natural frequency and associated phase change of the target VS. This reflects the robustness of such a controller for DS.

It should be noted that even when the damping ratio of the target VS is small, a sufficiently low level base acceleration would not cause saturation. The 360° phase drifts in some of Figures 4.11 and 4.12 are plotting artifacts as mentioned earlier.

Another situation that could cause high servovalve flow demands is when the VS has a low natural frequency. Figure 4.10b shows that the maximum force transmitted, and

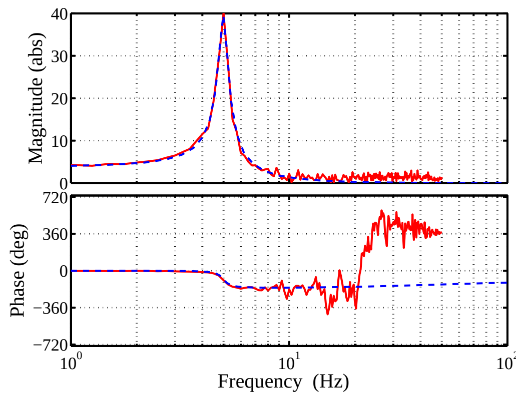

(a) VS damping = 5%: frequency response (same as Figure 4.7b)

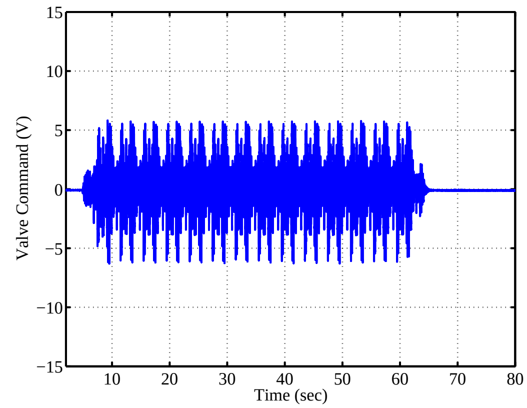

(b) VS damping = 5%: valve command time series

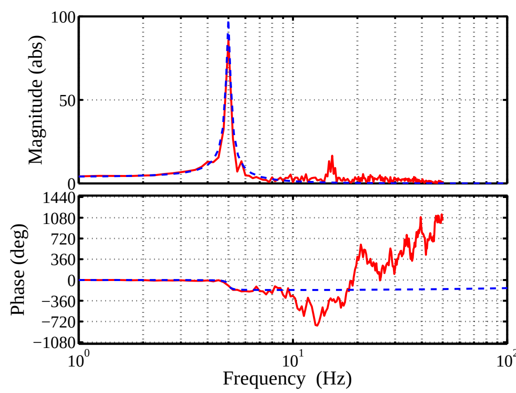

(c) VS damping = 2%: frequency response

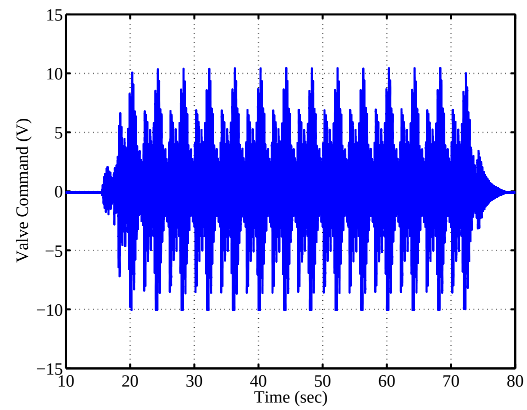

(d) VS damping = 2%: valve command time series

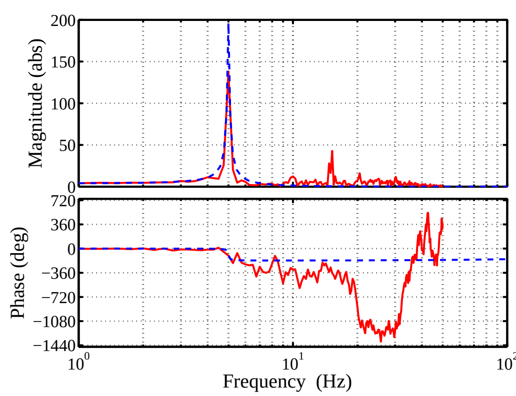

(e) VS damping = 1%: frequency response

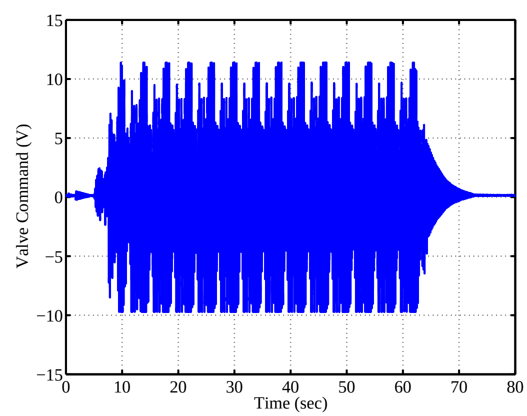

(f) VS damping = 1%: valve command time series

Figure 4.12: DS testing of AMD function for 5Hz one-DOF VS and different damping ratios with $K_\mathrm{e} = 1$ and $K_p = 9$; in the frequency response plots, red solid lines represent the measured AMD+controller frequency response, and blue dashed lines, the target VS frequency response

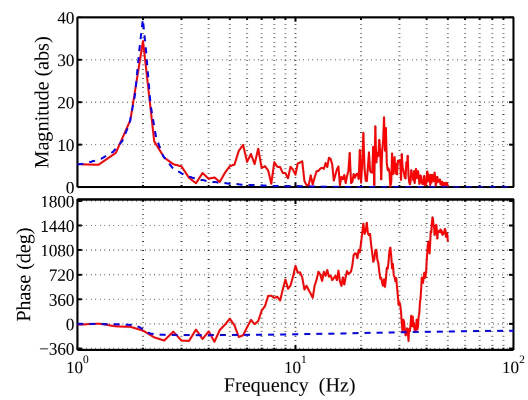

(a) VS damping = 5%, $K_{\mathrm{p}} = 0$: frequency response

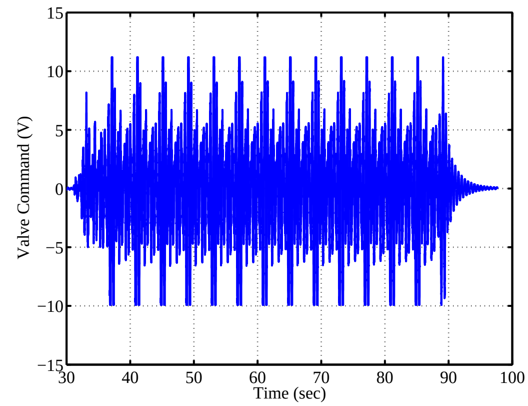

(b) VS damping = 5%, $K_{\mathrm{p}} = 0$: valve command time series

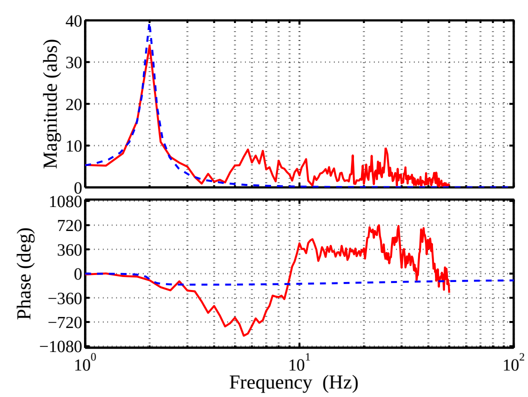

(c) VS damping = 2%, $K_{\mathrm{p}} = 9$: frequency response

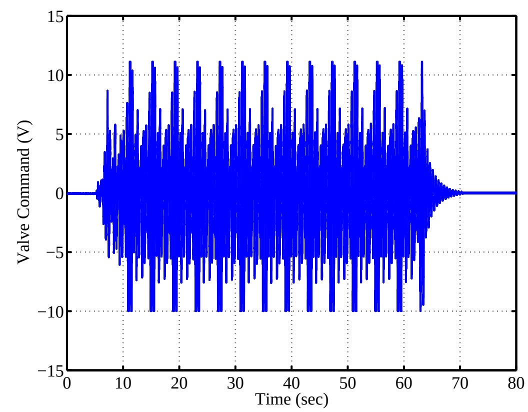

(d) VS damping = 2%, $K_{\mathrm{p}} = 9$: valve command time series

Figure 4.13: DS testing of AMD function for 2Hz one-DOF VS with $K_{\mathrm{e}} = 1$ and varying K_{p}; in the frequency response plots, red solid lines represent the measured AMD+controller frequency response, and blue dashed lines, the target VS frequency response

hence the acceleration demand, is the same irrespective of natural frequency. Therefore the velocity demand increases with decreasing natural frequency. Figure 4.13 shows results for a 2Hz VS. These are similar to the VSs with low damping. The valve command saturates over significant durations; the natural frequency and the resultant phase changes are represented, but the resonant peak is smaller, and harmonics associated with nonlinearities are more pronounced. Again, the fact that the essential dynamic characteristics of the VS are captured well despite significant nonlinear behavior of the AMD attests to the robustness of the proposed DS strategy.

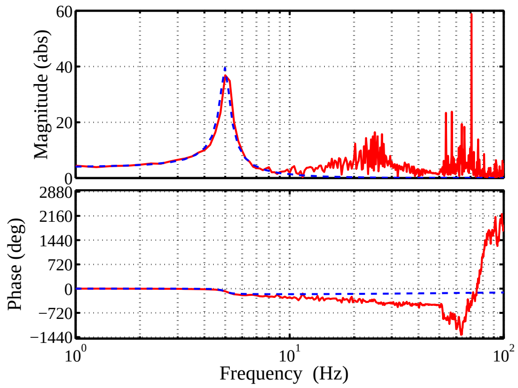

(a) 5Hz VS

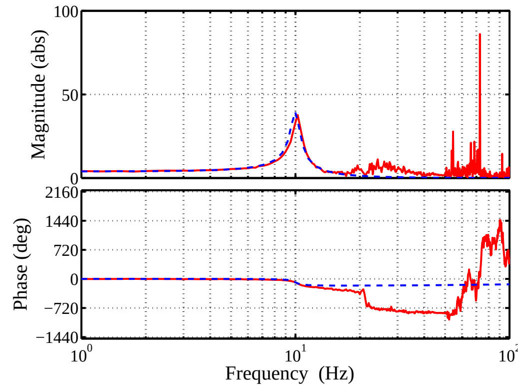

(b) 10Hz VS

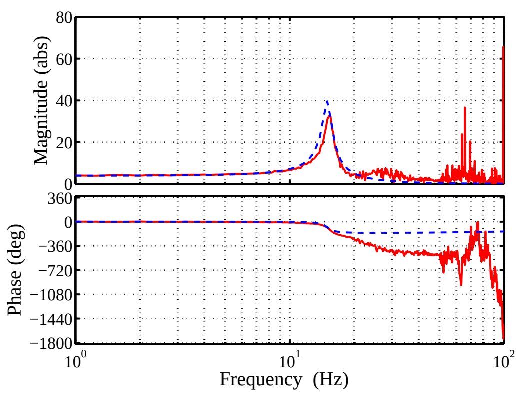

(c) 15Hz VS

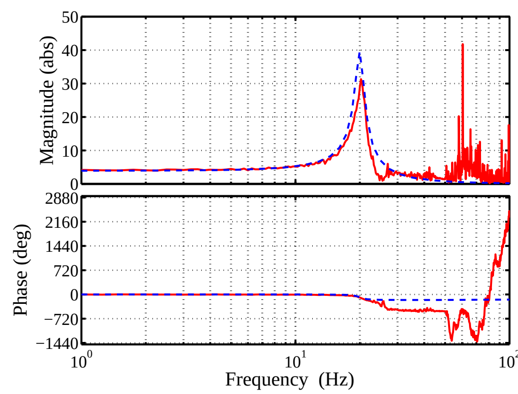

(d) 20Hz VS

Figure 4.14: DS experiments with control design excluding servovalve model

4.4.1.2 Effect of control design excluding servovalve model

As an additional robustness check, DS experiments are performed with a controller designed using the AMD model excluding the servovalve dynamics, according to equation (3.13). As discussed in Section 3.5.2, the AMD model without the servovalve is not as accurate. VS of 5Hz, 10Hz, 15Hz and 20Hz natural frequencies all with 5% damping ratio are considered. Results are presented in Figure 4.14. The main dynamic characteristics of the VSs are still represented closely, further supporting the robustness of the proposed DS strategy.

4.4.2 Two-DOF virtual subsystem

Next, the ability of the AMD+controller to imitate multi-DOF VSs is explored. Specifically two-DOF VSs, as shown in Figure 4.1c, are considered. First, realistic two-DOF models with $c_3 = 0$ are considered. In such two-DOF VSs, the force transmitted to the base is dominated by the first mode of vibration. Therefore these VSs do not truly challenge the ability of the proposed DS strategy to represent multiple resonant frequencies. To do so, somewhat unrealistic two-DOF VSs are artificially constructed with $c_3 \neq 0$ and other properties adjusted, in such a way as to exaggerate the contribution of the second mode in the transmitted force. Both these scenarios are described below.

4.4.2.1 Realistic properties

Two-DOF VSs are constructed by stacking two identical one-DOF structures, each with mass m, frequency f, and damping ratio ζ. The total mass of the two-DOF system is taken equal to the AMD proof mass (so that the weight of the two-DOF system is represented physically as described under Example 1 in Section 4.2.4). Then, $m = M_\mathrm{t}/2$, and in equation (4.6), $m_1 = m_2 = M_\mathrm{t}/2$, $k_1 = k_2 = (2\pi f)^2(M_\mathrm{t}/2)$, $c_1 = c_2 = 2\zeta(2\pi f)(M_\mathrm{t}/2)$ and $c_3 = 0$.

For such a two-DOF VS, a straightforward eigenvalue analysis gives the two natural frequencies to be $0.618f$ and $1.618f$, and the mass normalized mode shapes

$$\Phi = \frac{1}{\sqrt{M_\mathrm{t}}}\begin{bmatrix} 0.743 & 1.203 \\ 1.203 & -0.743 \end{bmatrix}$$

The damping matrix is stiffness-proportional, hence classical, and the damping ratios corresponding to the first two modes are 0.618ζ and 1.618ζ. The participation factors of the two modes are $1.947\sqrt{M_\mathrm{t}}$ and $0.460\sqrt{M_\mathrm{t}}$.

Two two-DOF VSs are considered with $f = 10$Hz and $f = 20$Hz, each with $\zeta = 5\%$. In each case, the transfer function, H_{Fw}^{VS}, of the VS is obtained as described in Section 4.2.1, and the DS controller is designed following the process outlined in Section 4.2.5.

Results are shown in Figure 4.15. The amplitude response is plotted in decibel scale to show the very small contribution of the second mode to the transmitted force. The first mode is well-represented. The magnitude of the second peak is about 100 times less than the first peak, so that from the perspective of the transmitted force, the VS is like a

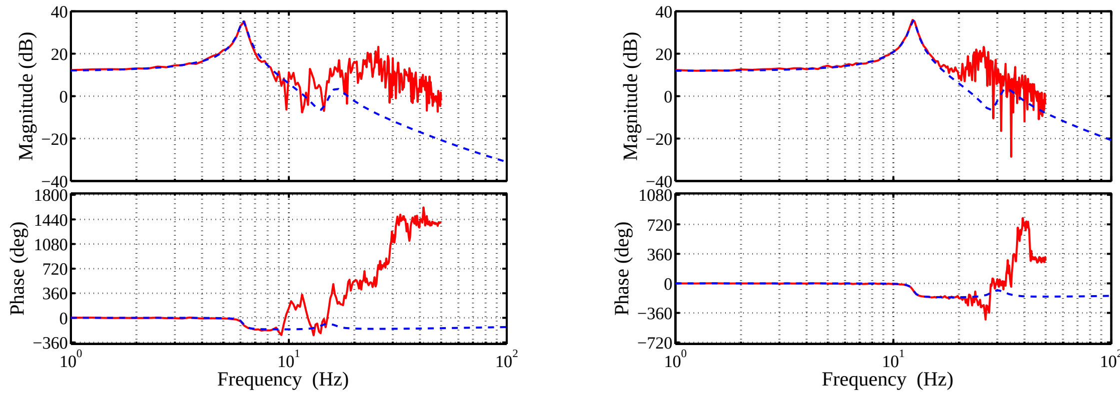

(a) Constituent one-DOF frequency, $f = 10$Hz

(b) Constituent one-DOF frequency, $f = 20$Hz

Figure 4.15: DS experiments with AMD only for 2DOF VS with realistic properties; damping ratio of the constituent one-DOF systems, $\zeta = 5\%$; hydraulic controller gain settings, $K_\mathrm{e} = 1$, $K_\mathrm{p} = 0$; red solid lines represent the measured AMD+controller frequency response, and blue dashed lines, the target VS frequency response; amplitude is shown in dB scale to show the small second-mode contribution

one-DOF system. In the measured response, the second mode is dominated by harmonics resulting from nonlinearities. Such a two-DOF VS does not really challenge the capability of the DS strategy to represent multi-DOF VSs.

4.4.2.2 Exaggerated properties

To truly test the ability of the DS strategy to represent multi-DOF VSs, two-DOF systems with unrealistic configurations are considered, to exaggerate the contribution of the second mode to the transmitted force. Again two one-DOF systems are stacked. The frequency of the top one-DOF system is taken as f, but the frequency of the bottom one-DOF system is taken as $2f$. The total mass is again taken equal to the proof mass, and split equally between the two one-DOF systems. The damping coefficient c_3 is chosen so that the top one-DOF system with fixed base has a damping ratio ζ. c_1 is taken equal to c_3, and c_2 is set to zero. Thus, in equation (4.6), $m_1 = m_2 = M_\mathrm{t}/2$, $k_2 = (2\pi f)^2(M_\mathrm{t}/2)$, $k_1 = 4k_2$, $c_1 = c_3 = 2\zeta(2\pi f)(M_\mathrm{t}/2)$ and $c_2 = 0$.

An eigenvalue analysis shows the two natural frequencies of such a two-DOF VS are $0.874f$ and $2.288f$, and the corresponding mass-normalized mode shapes are

$$\Phi = \frac{1}{\sqrt{M_\mathrm{t}}} \begin{bmatrix} 0.325 & 1.376 \\ 1.376 & -0.325 \end{bmatrix}$$

The damping matrix is mass-proportional, hence classical, and the damping ratios associated with the first two modes are $\zeta/0.874$ and $\zeta/2.288$. The modal participation factors for the two modes are $1.701\sqrt{M_\mathrm{t}}$ and $1.051\sqrt{M_\mathrm{t}}$. The contribution of the second mode to the transmitted force is greater for this arrangement of properties, because its participation factor is larger and damping ratio is smaller.

Three such two-DOF VSs are considered with $f = 3Hz$, $f = 5Hz$ and $f = 10Hz$, each with $\zeta = 5\%$. Results are shown in Figure 4.16. Both modes are represented well in terms of both amplitude and phase. For the low-frequency cases in Figures 4.16a and 4.16b, the peaks in the measured frequency response are shorter because of greater flow demand as discussed in Section 4.4.1.1. Figures 4.16c and 4.16e show the effect of harmonics near the AMD oil-column frequency, resulting from nonlinearities as discussed in Section 4.4.1. Figures 4.16d and 4.16f show how this effect is mitigated by using a higher ΔP gain, again consistent with the description in Section 4.4.1. The abrupt changes is phase observed in some of the phase plots in Figure 4.16, which are multiples of 360°, are, as pointed out earlier, simply plotting artifacts. It can be concluded that the proposed DS strategy is effective for two-DOF, and in general multi-DOF VS.

4.5 Dynamic substructuring with PS

Having established the ability of the AMD together with the DS controller to imitate different virtual subsystems, the next step is to actually perform dynamic substructuring with a physical subsystem. This is done using the tested of Chapter 3, where the physical subsystem is the weights supported by six elastomeric bearings as described in that chapter. The setup with the physical subsystem with an AMD atop it representing a virtual subsystem, placed on the shake table is shown in Figure 4.17. One-DOF virtual subsystems with frequencies 5Hz, 7Hz and 10Hz, each with mass equal to the AMD proof mass and 5% damping ratio are considered.

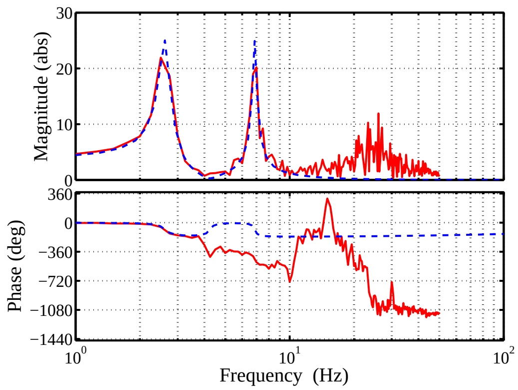

(a) $f = 3\text{Hz},\ K_{\text{e}} = 1,\ K_{\text{p}} = 0$

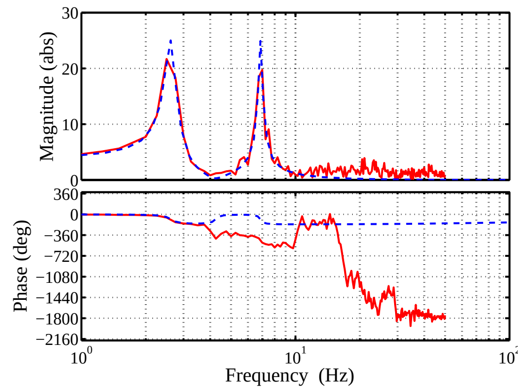

(b) $f = 3\text{Hz},\ K_{\text{e}} = 1,\ K_{\text{p}} = 9$

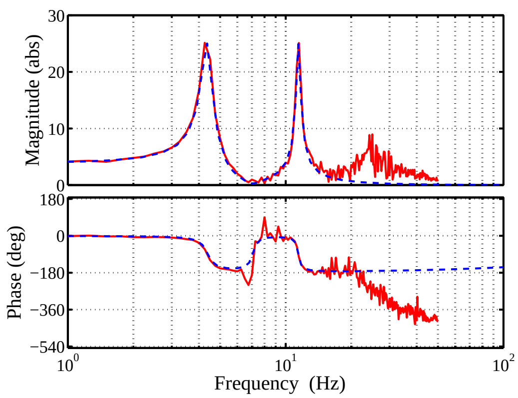

(c) $f = 5\text{Hz},\ K_{\text{e}} = 1,\ K_{\text{p}} = 0$

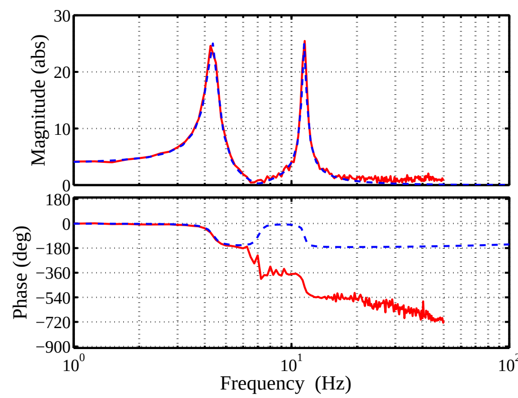

(d) $f = 5\text{Hz},\ K_{\text{e}} = 1,\ K_{\text{p}} = 9$

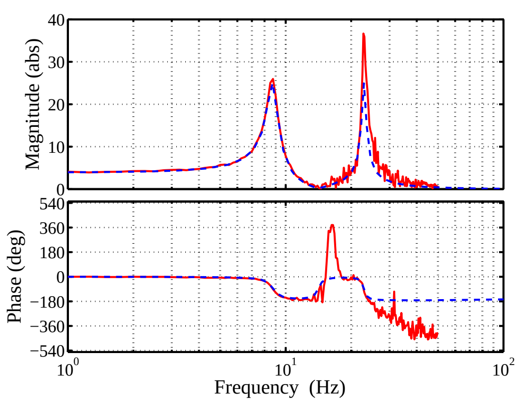

(e) $f = 10\text{Hz},\ K_{\text{e}} = 1,\ K_{\text{p}} = 0$

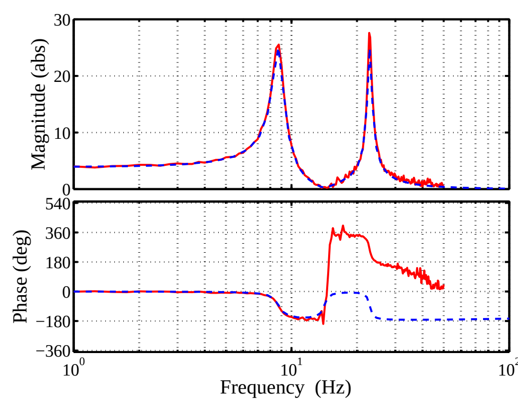

(f) $f = 10\text{Hz},\ K_{\text{e}} = 1,\ K_{\text{p}} = 9$

Figure 4.16: DS experiments with AMD only for 2DOF VS with exaggerated properties; the top one-DOF system frequency f is varied, and its damping ratio $\zeta = 5\%$; red solid lines represent the measured AMD+controller frequency response, and blue dashed lines, the target VS frequency response

(a) Overview

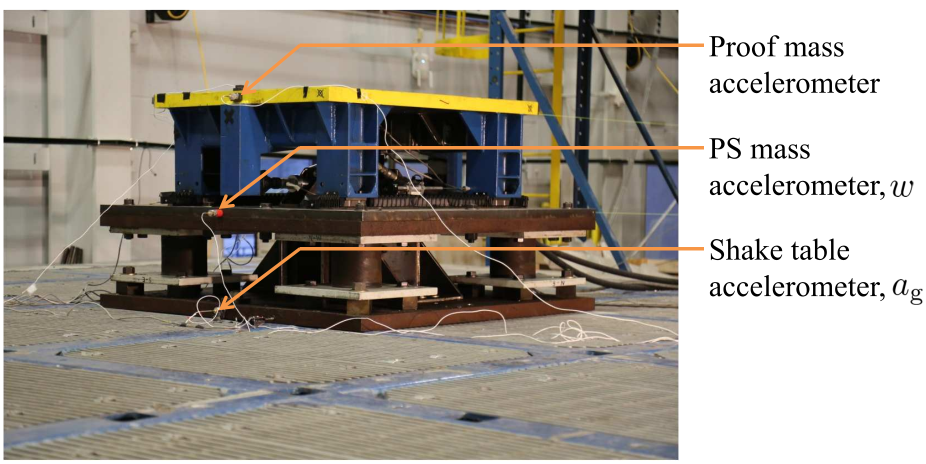

(b) Closeup

Figure 4.17: Experimental configuration for dynamic substructuring — physical subsystem (weight supported by a system of six elastomeric bearings) with an AMD atop representing a virtual subsystem, placed on a shake table; further details are as shown in Figure 3.10

4.5.1 Imitated system model

To assess the performance of dynamic substructuring, a model of the imitated system, consisting of the physical and virtual subsystems interconnected (Figure 4.18), is considered. This model is obtained readily by starting from the combined AMD-PS model equation of motion (3.15) in Section 3.3.3, and

1. letting x_1 and x_5 represent the displacement and velocity of the virtual subsystem (rather than the AMD) relative to the physical subsystem,

2. replacing the proof mass, M_{t}, and its moment of inertia, I, by those of virtual subsystem mass, m and I,

3. letting h denote the elevation of the virtual subsystem mass from the PS center of mass,

4. replacing the actuator force by the virtual subsystem force as

$$A_{\mathrm{p}}\Delta P = -c\dot{x}_1 - kx_1$$

   k and c being the stiffness and damping coefficient of the one-DOF VS, and

5. omitting the differential pressure state, x_9.

The equation of motion of the imitated model is then

$$\mathcal{M}\ddot{x}_{1:4} + \mathcal{C}\dot{x}_{1:4} + \mathcal{K}x_{1:4} + \mathcal{M}e_2 a_{\mathrm{g}} = 0 \tag{4.23a}$$

where the mass matrix

$$\mathcal{M} = \begin{bmatrix} m & m & -hm & 0 \\ m & m + m_{\mathrm{PS}} & -hm & 0 \\ -hm & -hm & I + I_{\mathrm{PS}} + m(h^2 + e^2) & -em \\ 0 & 0 & -em & m + m_{\mathrm{PS}} \end{bmatrix} \tag{4.23b}$$

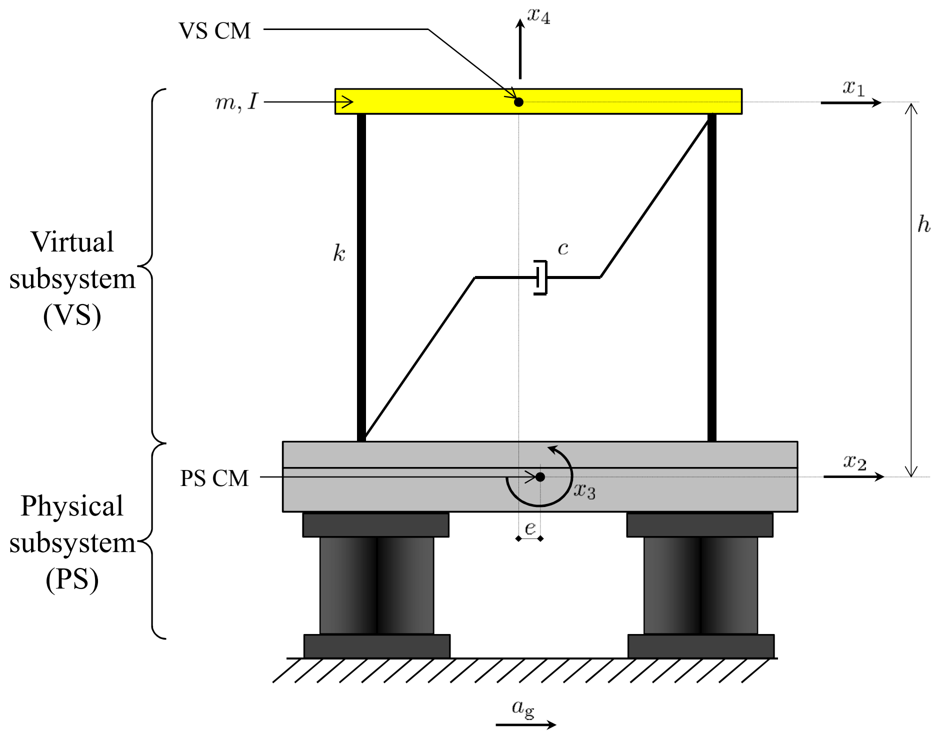

Figure 4.18: Model of imitated system; parameters of the PS are shown in Figure 3.20

the stiffness matrix

$$\mathcal{K} = \begin{bmatrix} k & 0 & 0 & 0 \\ 0 & K_{\mathrm{H}} & K_{\mathrm{H}}\left(\frac{2}{3}h_1 + \frac{1}{3}h_2\right) & 0 \\ 0 & K_{\mathrm{H}}\left(\frac{2}{3}h_1 + \frac{1}{3}h_2\right) & K_{\mathrm{H}}\left(\frac{2}{3}h_1^2 + \frac{1}{3}h_2^2\right) + (K_{1\mathrm{v}} + K_{2\mathrm{v}})\frac{L^2}{4} & (K_{2\mathrm{v}} - K_{1\mathrm{v}})\frac{L}{2} \\ 0 & 0 & (K_{2\mathrm{v}} - K_{1\mathrm{v}})\frac{L}{2} & K_{1\mathrm{v}} + K_{2\mathrm{v}} \end{bmatrix} \tag{4.23c}$$

and the damping matrix, $\mathcal{C}$, is identical in form to the stiffness matrix, $\mathcal{K}$, with the stiffnesses k, K_{H}, $K_{1\mathrm{v}}$ and $K_{2\mathrm{v}}$ replaced with the damping coefficients c, C_{H}, $C_{1\mathrm{v}}$ and $C_{2\mathrm{v}}$. This can be represented in state-space format as

$$\begin{aligned} \dot{x} &= Ax + Ea_{\mathrm{g}} \\ y &= Cx \end{aligned} \tag{4.24a}$$

where

$$A = \begin{bmatrix} 0_{4\times4} & I_{4\times4} \\ -\mathcal{M}^{-1}\mathcal{K} & -\mathcal{M}^{-1}\mathcal{C} \end{bmatrix} \tag{4.24b}$$
$$E = \begin{bmatrix} 0_{1\times4} & -e_2^\top \end{bmatrix}^\top$$

The output y of interest is the total acceleration of the PS mass, and

$$C = \begin{bmatrix} \frac{k}{m_{\mathrm{PS}}} & -\frac{K_{\mathrm{H}}}{m_{\mathrm{PS}}} & -\left(\frac{2}{3}h_1 + \frac{1}{3}h_2\right)\frac{K_{\mathrm{H}}}{m_{\mathrm{PS}}} & 0 & \frac{c}{m_{\mathrm{PS}}} & -\frac{C_{\mathrm{H}}}{m_{\mathrm{PS}}} & -\left(\frac{2}{3}h_1 + \frac{1}{3}h_2\right)\frac{C_{\mathrm{H}}}{m_{\mathrm{PS}}} & 0 \end{bmatrix} \tag{4.24c}$$

For reasonable values of the VS moment of inertia, I, and elevation, h, that are not too large, the imitated system can be approximated simply with the two translational DOF. It is also not important in this case that in dynamic substructuring, the AMD represent overturning moments properly (see Section 4.2.1). The imitated system equation of motion is then

$$\begin{bmatrix} m & m \\ m & m + m_{\mathrm{PS}} \end{bmatrix} \begin{pmatrix} \ddot{x}_1 \\ \ddot{x}_2 \end{pmatrix} + \begin{bmatrix} c & 0 \\ 0 & C_{\mathrm{H}} \end{bmatrix} \begin{pmatrix} \dot{x}_1 \\ \dot{x}_2 \end{pmatrix} + \begin{bmatrix} k & 0 \\ 0 & K_{\mathrm{H}} \end{bmatrix} \begin{pmatrix} x_1 \\ x_2 \end{pmatrix} = -\begin{pmatrix} m \\ m + m_{\mathrm{PS}} \end{pmatrix} a_{\mathrm{g}} \tag{4.25}$$

This model is used as a reference in the following to assess the performance of dynamic substructuring.

4.5.2 DS frequency domain performance

The comparison of the expected transfer function of the emulated model, for input a_g which is, in this case, the acceleration of the shake table and output the acceleration at the level of the steel plates is made to conclude whether the experiments are successful. The DS experiments performed for one degree of freedom virtual substructures, of $5, 7$ and 10Hz fundamental frequency. Virtual substructures with higher frequencies are not considered in the specific case, because for high VS frequencies, the system would respond as a single degree of freedom system. For all the cases studied here, the damping ratio is set equal to $\zeta_{\mathrm{VS}} = 0.05$. The damping and stiffness of the virtual substructure are given by equation (4.26). The input to the shake table is a multisine with amplitude 0.5g for the tests performed for the virtual substructure of 5 and 10Hz, and 0.7g for the virtual substructure of 7Hz. The range of excited frequencies is 0-30Hz for the experiment with 7Hz VS, while for the rest experiments reached 100Hz. These variations are simply made to investigate the performance of the method for higher frequencies and amplitudes of the excitation.

$$C_{\mathrm{VS}} = 2\zeta_{\mathrm{VS}}\omega_{\mathrm{VS}}m_1 \qquad K_{\mathrm{VS}} = \omega_{\mathrm{VS}}^2 m_1 \tag{4.26}$$

The results are shown in Figure 4.19. It is obvious that the match is still good, however one can notice that the peak corresponding to the fundamental frequency of the virtual substructure is a little off (in the order of 0.5Hz).

This can be attributed to the fact that to validate the general model, the amplitude that is used is lower compared to the input of the shake table. The difference in the amplitude of the inputs could be the reason why the specific peak is not very well predicted. It can be observed from Figure 3.42, which shows results for the case when the AMD proof mass is locked, that the same characteristic is present, even without control implementation. This supports the argument that the slight mismatch of the frequency peak is not a result of inaccurate control but is most probably caused by fluctuation in the bearings' parameters.

However, the resulting transfer function follows well the expected values, apart from the range that the oil-column frequency is more dominant. It should be mentioned that these experiments are performed only for gain values $K_{\mathrm{e}} = 1$ and $K_{\mathrm{p}} = 0$, the case of the higher ΔP gain is not examined here.

4.5.3 DS time domain performance

DS experiments with earthquake input are also performed for the same setup considered in the previous section. Similarly to the case of Section 4.5.2, the virtual substructures examined are SDOF systems of 5, 7 and 10Hz frequency. The input to the shake table is a time-compressed El Centro ground motion of 1.4g amplitude for the experiments with 7 and 10Hz virtual substructures and 0.9g for the experiments with 5Hz virtual substructure.

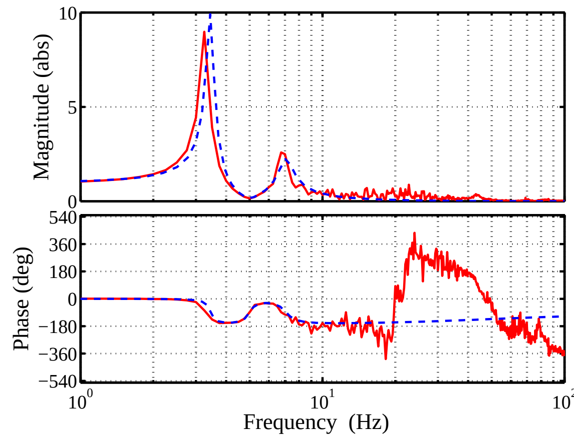

(a) DS test for 5Hz VS

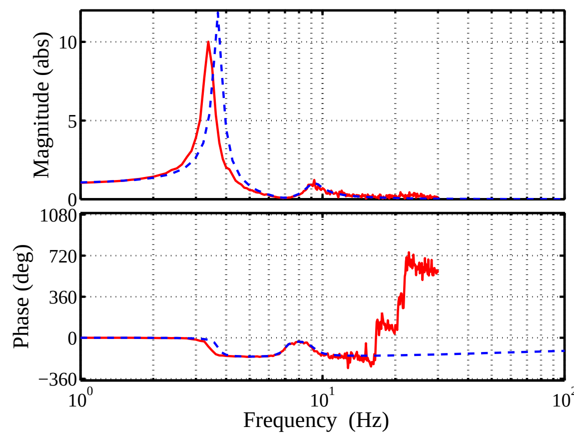

(b) DS test for 7Hz VS

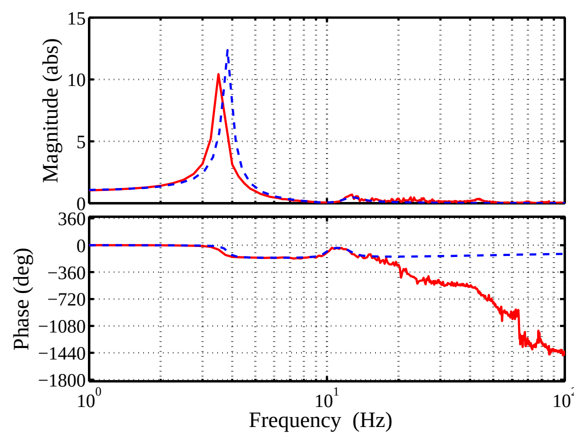

(c) DS test for 10Hz VS

Figure 4.19: DS experiments for AMD and bearings setup for multisine input. Red solid lines show the experimental data and dashed blue lines show the expected response of the linear mathematical model.

The amplitude is decreased in the case of the lower frequency virtual substructure to valve saturation.

In order to examine the effectiveness of the method, the time domain acceleration histories at the PS mass level from the experimental setup and the emulated model are compared for all three VS tested, as shown in Figure 4.20. For all three cases, mismatch is observed, especially in the transient response of the system.

It is, therefore, desired to determine whether this mismatch is an indication that the DS experiment is not successful or whether this effect is related to uncertainties of the elastomeric bearing properties. For this reason, the AMD is isolated from the bearing system and its force is compared to the expected reaction force of the virtual subsystem. Specifically, the reaction force of the virtual subsystem is calculated using its analytical model for the input acceleration at the level of steel plates above the elastomeric bearings. The same acceleration along with the program command u are used to obtain the force from the AMD analytical model. The comparison of the two force time histories together with the measured force during the experiment is shown in Figure 4.21.

It is evident that the match is satisfactory for all three virtual substructures examined. However, it is observed that there are high frequency components in the measured force time history, especially in the transient response, as is clearly demonstrated in Figure 4.22. This is attributed to the oil-column frequency of the AMD. To check this theory, a low pass filter is applied in the measured force history at 25Hz. The filtered force time history also shown in Figure 4.21 follows well the expected values, hence this in fact indicates that the high frequency components are a result of the oil-column frequency.

The fact that Figure 4.21 shows that the comparison between the AMD and the VS model is good proves that the mismatch in the acceleration time histories is a result of the uncertain properties of the elastomeric bearings, and is not an indication of inaccurate DS testing. It is also reminded here that similar effects are recognized in the case with the multisine inputs, as described in Section 4.5.2. It is also worth noticing the limit cycles present in the experimental measurements of the experiment of the low frequency (5Hz) virtual subsystem. This effect is discussed in more detail in Section 4.5.4.

4.5.4 Limit cycle behavior for low-frequency virtual subsystems

Finalizing the discussion of the DS experiments performed using this new approach, it is important to mention an interesting phenomenon observed during the experiments. While attempting to emulate VS with low fundamental frequency and/or damping, self sustained oscillations (limit cycles) are observed for small excitation. The oscillations are of high amplitude in the case when the ΔP gain is low while they are significantly decreased when the ΔP gain is of high value.

An example of this behavior is shown in Figure 4.23, for virtual substructures of 1 and 3Hz. More specifically, this oscillatory effect is present in the program command, u, time history of the AMD. The amplitude of the oscillations decreases significantly when the knob of the ΔP gain is set to the maximum value.

Since such behavior cannot be explained by linear models, this oscillatory effect (limit cycles) is attributed to the nonlinearity of the system which is not included in the model, namely the friction. In order to test this theory, friction is included in the mathematical model of AMD and analytical results are obtained. It should be mentioned that the amount of friction used for this simulation is equal to 100lb as obtained experimentally (Section 3.5.1). As shown in Figure 4.24, a similar effect is observed, even though the amplitude of the oscillation is lower compared to the experimental values. Increase in the ΔP gain causes decrease of the oscillations, similarly to the experimental observations. Of course, in the analytical model, the value of K_{p} can take any value, while in there is a physical limitation to the value of the gain in the experiments.

Hence, by the addition of friction in the model we can qualitatively get similar results, leading to the conclusion that the source of the limit cycles observed is indeed the friction of the system. This is a remarkable observation showing that even a small amount of friction (100lb) can have a significant effect.

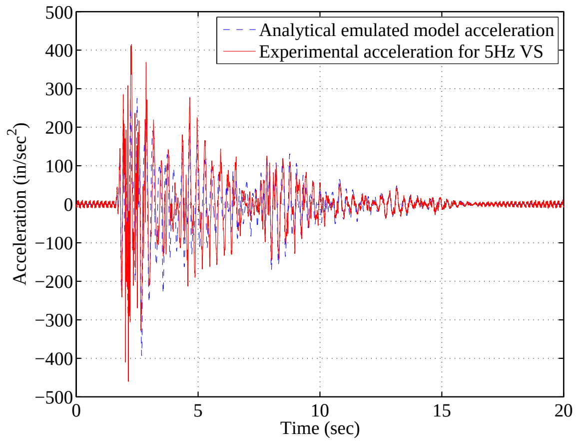

(a) 5Hz VS

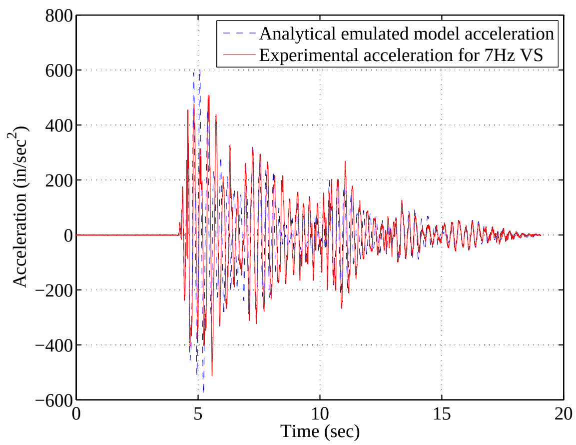

(b) 7Hz VS

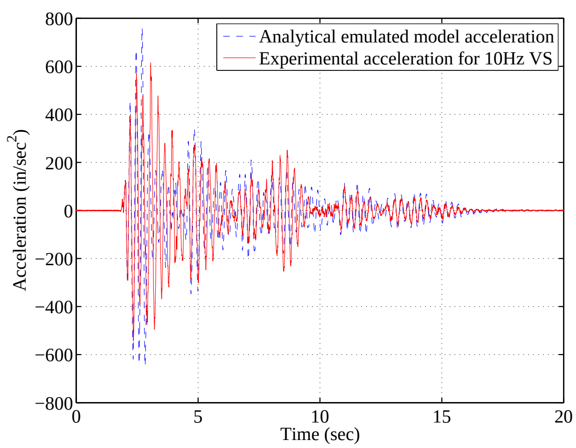

(c) 10Hz VS

Figure 4.20: Acceleration time histories for DS experiments for earthquake input

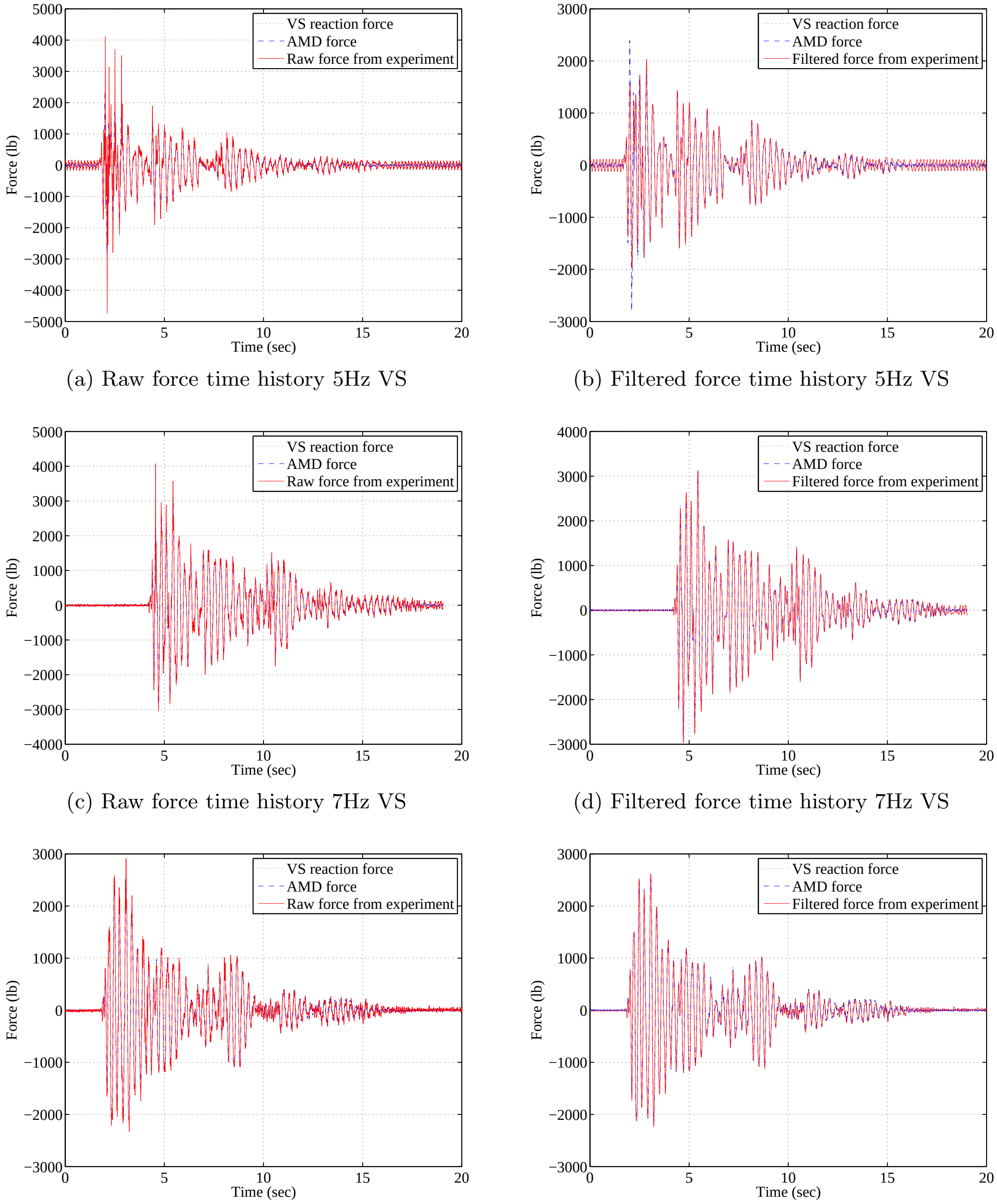

(a) Raw force time history 5Hz VS

(b) Filtered force time history 5Hz VS

(c) Raw force time history 7Hz VS

(d) Filtered force time history 7Hz VS

(e) Raw force time history 10Hz VS

(f) Filtered force time history 10Hz VS

Figure 4.21: Force time histories for DS experiments for earthquake inputs

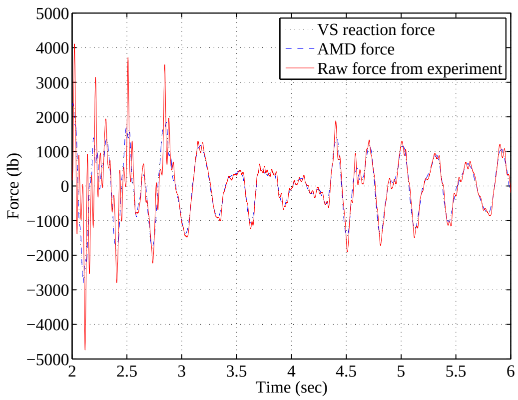

(a) Raw force time history 5Hz VS - closeup view

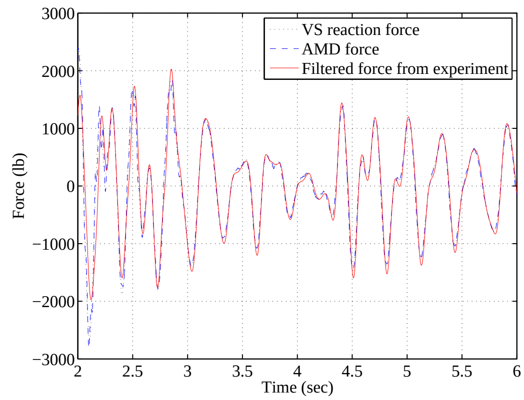

(b) Filtered force time history 5Hz VS - closeup view

Figure 4.22: Closeup view of Force time histories for DS experiments for earthquake inputs - 5Hz VS

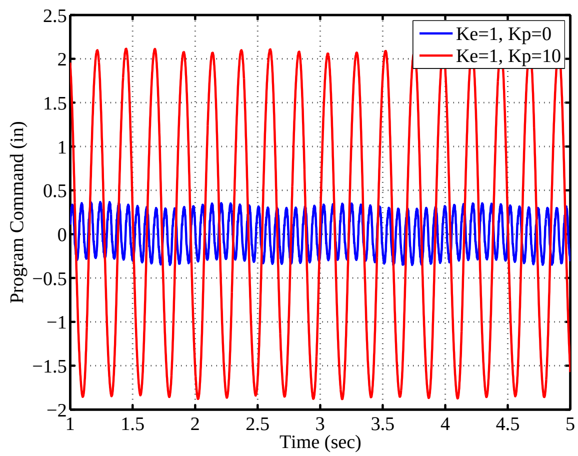

(a) Experimental program command time history for 1Hz virtual substructure

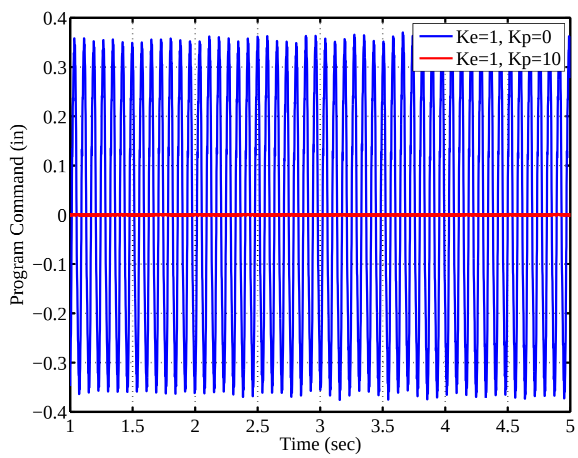

(b) Experimental program command time history for 3Hz virtual substructure

Figure 4.23: Oscillation in program command for high and low K_{p} gain value

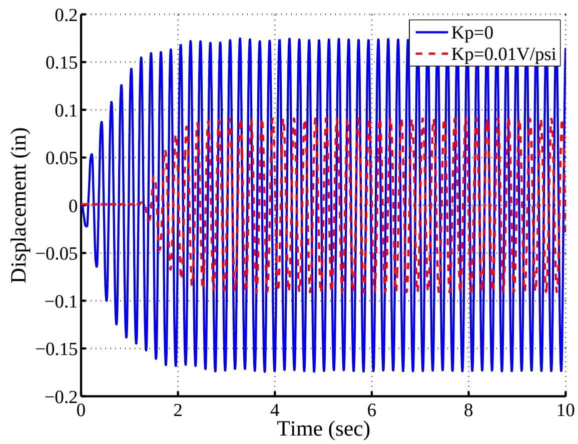

(a) Analytical program command time history for 1Hz virtual substructure

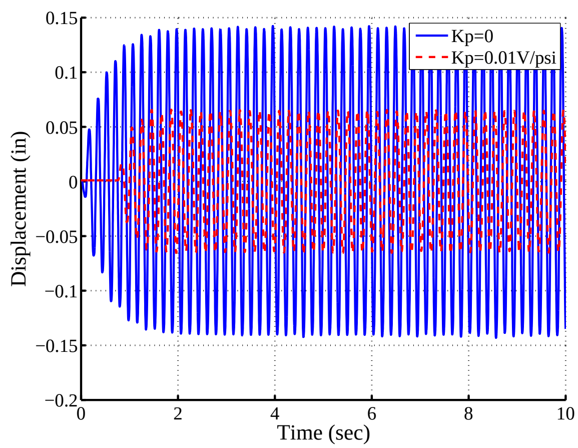

(b) Analytical program command time history for 3Hz virtual substructure

Figure 4.24: Oscillation in program command of analytical model for 100lb friction

Chapter 5

Proof of concept experiments for dynamic substructuring of SFSI

5.1 Introduction

Laboratory testing of soil-foundation-structure interaction (SFSI) has proven to be challenging and expensive. Small-scale (1:50 1:70) testing employing geotechnical centrifuges is limited by scale effects and an inability to control dynamic properties of the structure(s). Much larger-scale testing is possible with 1D geotechnical laminar boxes at a small number of laboratories worldwide. Deployment and operation of such boxes is complex.

Dynamic substructuring offers an added valuable dimension to SFSI testing. The soil-foundation-structure system is partitioned into (a) a physical subsystem: an experimental component representing the soil and foundation, and (b) a virtual subsystem: a computer model of the superstructure, interacting in real-time via actuators, sensors and control systems. Key benefits are (a) foundation models can be tested with multiple virtual superstructures; (b) physical space requirements and costs are reduced; and (c) larger foundation models can be accommodated, minimizing scaling effects. These benefits substantially expand the utility of geotechnical laminar box experiments. A description of SFSI dynamic substructuring concept is given in Chapter 1.

This chapter provides a description of the proof-of-concept tests performed in the Structural Engineering and Earthquake Laboratory (SEESL) at University at Buffalo to demonstrate viability of SFSI dynamic substructuring, and present measurements that (i) elucidate the role of superstructure dynamics in foundation response, and (ii) can be used to validating computational SFSI models. The physical subsystem was a 10-ft deep pile-group foundation model in a 23-ft laminar box filled with saturated sand. One dimensional seismic excitation was applied at the base of the laminar box to represent bedrock input at depth. Interface conditions representative of different superstructures were applied to the foundation using a second shake table.

5.2 Background on SFSI experiments

As mentioned previously, the motivation of dynamic substructuring for SFSI, is driven by the need to obtain experimental data of complete soil-foundation-structure systems. There are clear practical impediments to performing such system-level experiments at full-scale. Various approaches have been taken to study SFSI experimentally.

Centrifuge modeling Centrifuge modeling has a long history in geotechnical engineering [123, 124], stemming from the additional scaling degree-of-freedom resulting in proper stress levels in the soil. Centrifuge modeling has been used to study shallow foundations and deep foundations [125–127], subjected to earthquake shaking. Realistic superstructure models are rarely incorporated in centrifuge models. In a few cases, a cantilevered mass or tower structure is used. Recently, simple frame superstructure models have also been used [128–130]. Although the type of dynamic substructuring technology described herein may become possible in the context of centrifuge testing, such technology for centrifuge testing has not yet been developed to study full SFSI at the system-level.

Role of superstructure in soil-foundation response Even with simple superstructure models, centrifuge tests provide evidence that the superstructure has a considerable influence on the behavior of the soil-foundation system. For example, Madabhushi [131] observed that in saturated soil, effective frequency shift resulting from soil plastification depends on the initial frequency of the combined soil-foundation-superstructure system relative to the predominant earthquake frequency. Madabhushi [132] also observed that the superstructure dynamics influences liquefaction-induced failure mechanisms. Pak and Ashlock [133] noted that the extent to which a uniform equivalent shear modulus can be used to model dry sand beneath a foundation depends significantly on the superstructure. These findings highlight the need to use a variety of superstructure models to obtain comprehensive system-level data.

1-g laboratory and field experiments There have also been a number of SFSI experiments in the 1g environment using shake tables and soil boxes [134–138]. Such tests are also restricted to simple tower-like superstructures due to laboratory space and other limitations. Furthermore, testing with a different superstructure would imply fabricating a new model, leading to additional time and cost. Field experiments have also been carried out to characterize SFSI using ambient and force vibration experiments [139, 140]. Data from such tests have to be limited to low-level excitations. Furthermore, it is difficult to obtain detailed information about the soil-foundation response in the field.

5.3 SFSI dynamic substructuring

As mentioned preciously, dynamic substructuring enables adaptability by allowing a physical soil-foundation system to be coupled with multiple complex virtual superstructure models. It should be noted that an early NEES project [141] utilized all of the approaches presented in Section 5.2 separately to study the SFSI problem. Dynamic substructuring adds an extra dimension by integrating many of these approaches enabling a fully coupled simulation as shown in Figure 1.1. In the case studied here, only one degree of freedom is controlled and the interface conditions are applied using the AMD. The updated schematic with the AMD is shown in Figure 5.1.

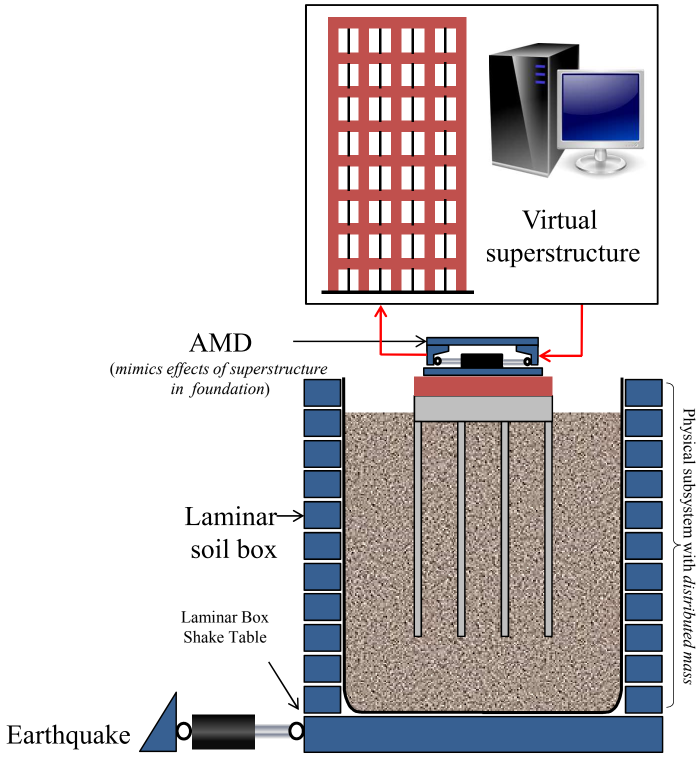

Figure 5.1: Schematic of SFSI dynamic substructuring

5.3.1 Experimental setup

The full system, shown in Figure 5.1, consists of the soil-foundation-structure system can be separated into two subsystems: (i) the numerical subsystem, which is the computer model of the structure and (ii) the physical subsystem, which is the soil-foundation part. For the purposes of this experiment, the pile foundation system was built in saturated soil contained in a large-scale geotechnical laminar box. The total height of the laminar box is approximately 23ft and the saturated soil was 15.5ft high, consisting of 40 six inch wide laminates. Ball bearings are located in between the laminates, allowing each laminate to move with respect to its adjacent laminates. This configuration is used to simulate boundary conditions similar to field conditions. Figures 5.2 through 5.4 show the experimental setup in the Structural Engineering and Earthquake Simulation Laboratory (SEESL) at the University at Buffalo.

The interface conditions can be applied with the active mass driver (AMD), which was

(a) Geotechnical laminar box in SEESL

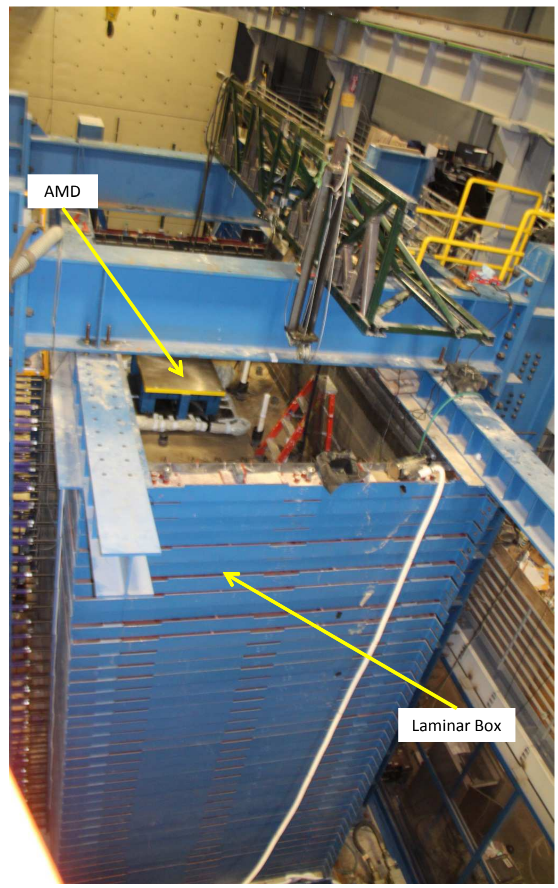

(b) General view of experimental setup

Figure 5.2: Experimental setup

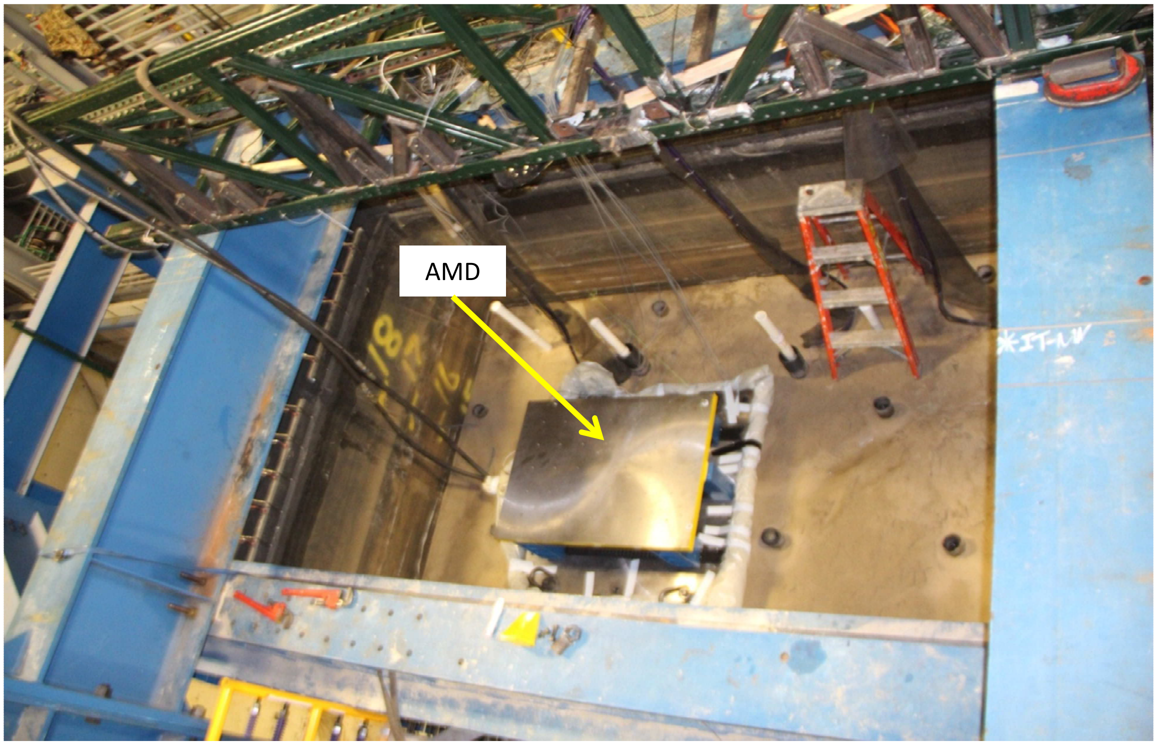

Figure 5.3: Experimental setup plan view

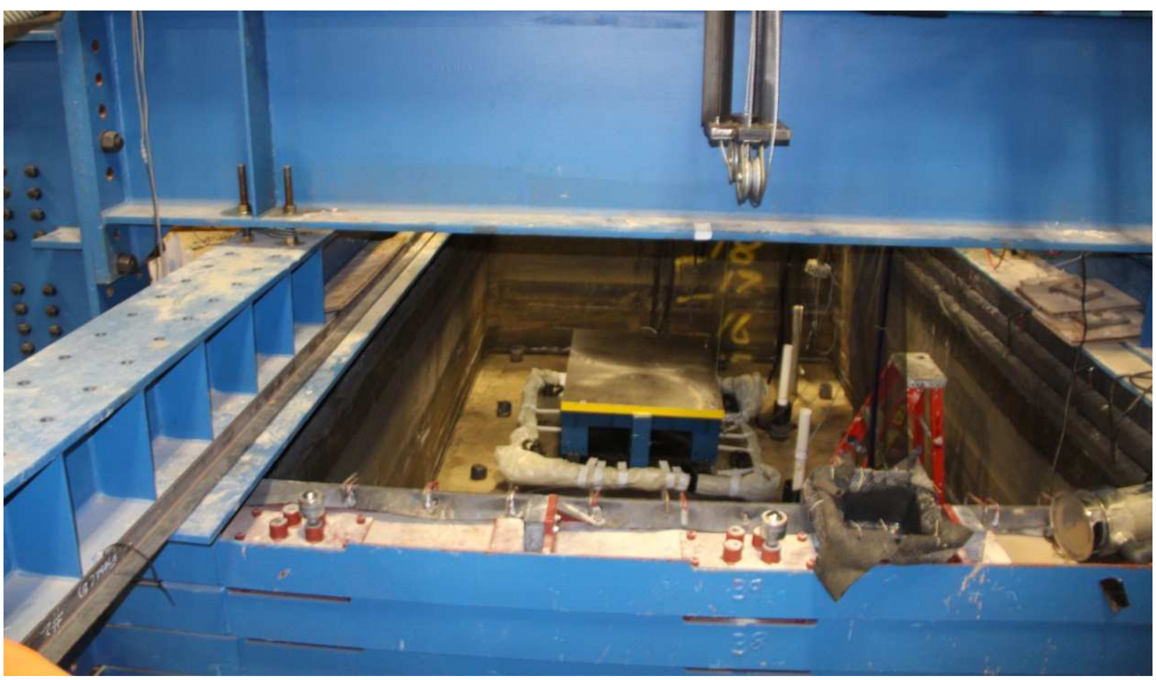

Figure 5.4: Experimental setup side view

designed for such applications as discussed in Chapter 3. In order to isolate variables of interest, instead of using active feedback for the interface conditions, the superstructure impedance is represented by varying the amplitude and phase offset of the interface of the AMD. Employing active feedback is the next logical step, which should be used in future DS experiments.

The foundation consisted of six 10.5ft long schedule 80 steel pipes of 1in nominal diameter. To ensure the necessary pile axial capacity, a cone penetration test (CPT) was conducted prior to their installation. The final configuration after all six piles were driven into the soil, is shown in Figure 5.5. After the placement of the piles, steel plates were attached to the piles to provide support for the AMD. This allowed for errors in the positions of the piles. During the setup preparation several limitations and difficulties had to be taken into consideration and be addressed. The final configuration is shown in Figure 5.6.

5.3.2 Instrumentation

In order to obtain important data to understand the soil-foundation interaction, the four corner piles were instrumented with strain gauges and triaxial accelerometers by embedding these sensors in couplers in the piles as shown in Figure 5.7. These sensors were carefully waterproofed to protect the instruments from the water existing in the soil. The laminar box itself was equipped with string potentiometers at the level of each laminate as well as accelerometers in both horizontal directions. Pore pressure transducers were embedded in the soil to track pore water pressure at different depths.

The AMD representing the superstructure was also equipped with instruments to measure its response during the earthquake shaking. Accelerometers were used in all three directions and string potentiometers were positioned to capture the displacement, rotation, torsion and settlement of the table. The sensors used to measure the response of the AMD are shown in Figure 5.8.

The AMD was equipped with additional sensors, including two load cells measuring the

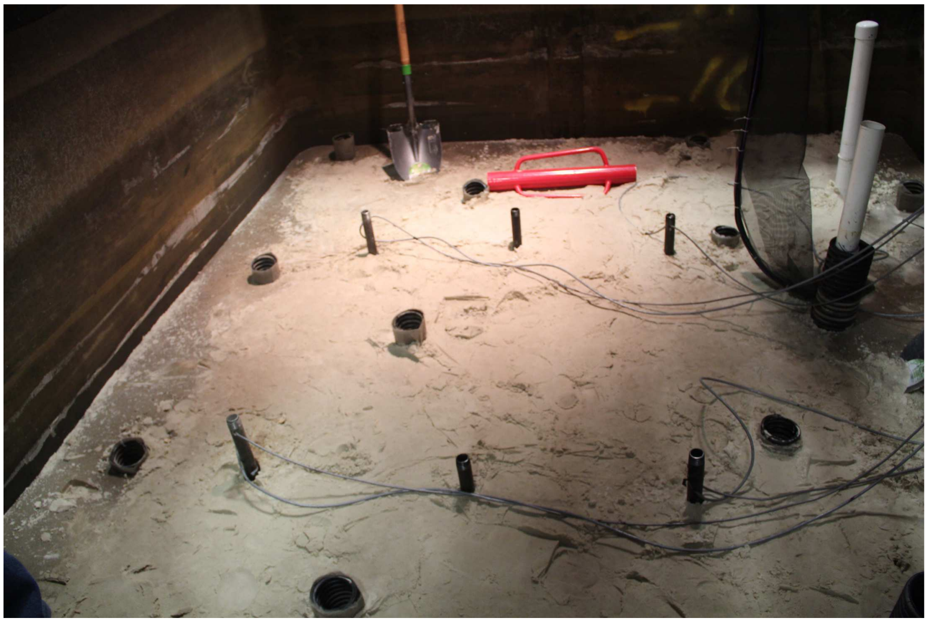

Figure 5.5: Pile foundation installed

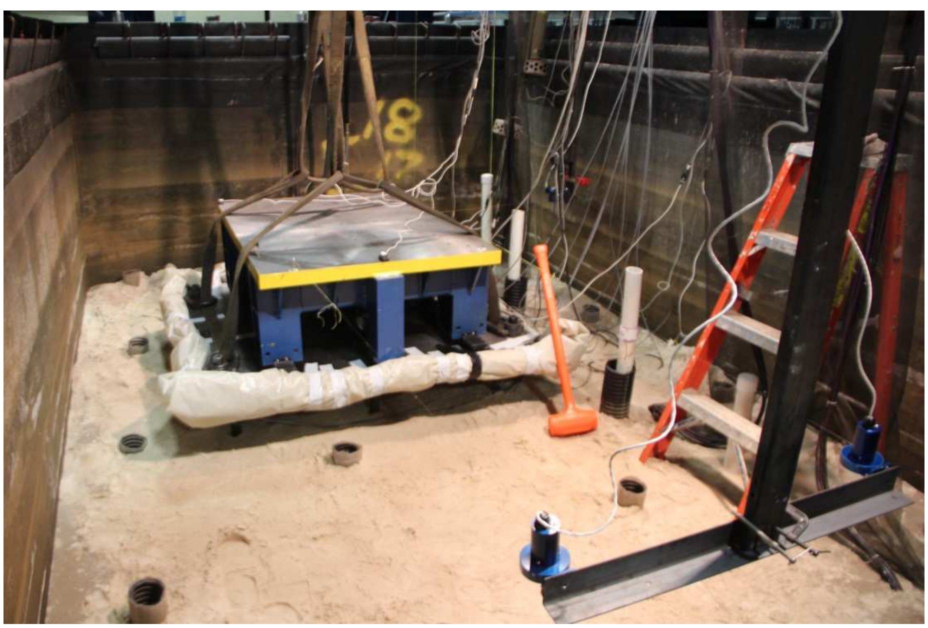

Figure 5.6: AMD mounted on piles

(a) Strain gauges in coupler (b) Waterproof coupler

Figure 5.7: Inside view of instrumented coupler

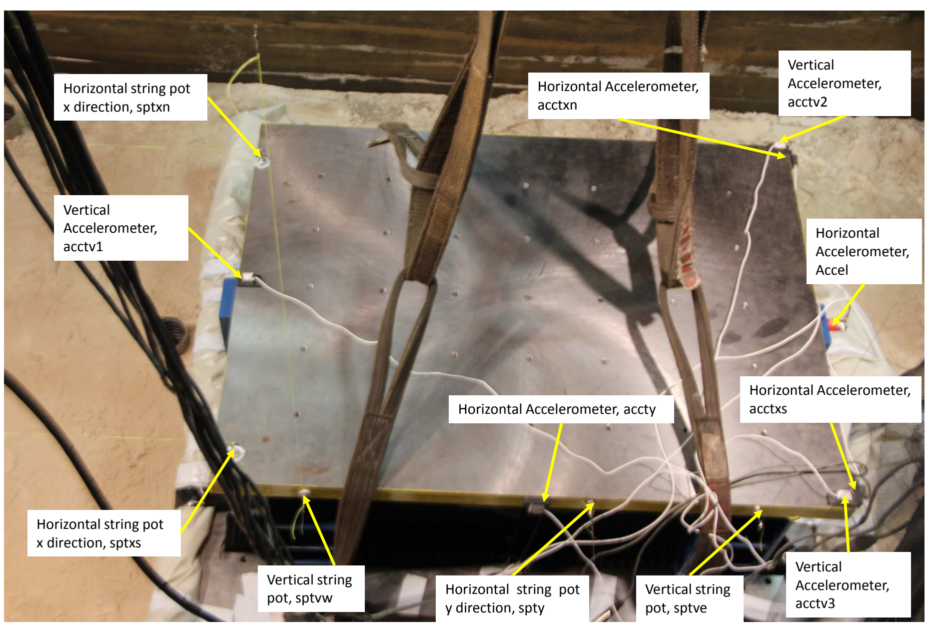

Figure 5.8: AMD instrumentation

applied force. The differential pressure, ΔP, in the actuator chambers was also measured, providing information on the hydraulics and the forces applied on it. The details of the AMD instrumentation are given in Section 3.2.4.

5.3.3 Experimental protocol

Experiments were driven by harmonic input at the base of the laminar box. To represent different superstructures at steady state, the AMD atop the foundation was driven with the same frequency but at different amplitudes and phase offsets relative to the laminar box excitation. Additional experiments were conducted for which there was only input at the base of the laminar box without applying any interface conditions through the AMD, which is equivalent to having a rigid superstructure. The amplitude of excitation was gradually increased through several experiments to a maximum of $0.2g$, which corresponded to 0.12in displacement at the base of the laminar box. Prior to each experiment, free vibration tests were performed to obtain the frequency of the system and to assess how the state of the soil-foundation system evolved over the course of the experiments.

5.4 Analysis and interpretation of experimental data

Experiments were performed parametrically via gradual variation of the shaking input and the superstructure properties. The response of the system during each experiment was captured using the aforementioned sensors and testing protocol. Analysis of the data produced meaningful information through inter-test comparisons. For example, for the same base input excitation, the effect of different superstructures is isolated and identified. The results show that the response of the system varied significantly while changing the superstructure parameters.

Figures 5.9 and 5.10 show comparisons of three different cases: (a) rigid superstructure, for which harmonic excitation was applied to the base of the laminar box and no input was applied to the AMD, (b) harmonic base excitation and a superstructure with natural frequency less than 3Hz (superstructure 1), and (c) harmonic base excitation and a superstructure with natural frequency more than 3Hz (superstructure 2). Data illustrated in the following figures were obtained for harmonic excitation of 3Hz frequency and 0.1g input acceleration, which corresponds to displacement of 0.11in, at the base of the laminar box. The input to the AMD was also sinusoidal with 3Hz frequency and 0.8in amplitude.

Acceleration was measured at both the AMD and at a location approximately 3ft deep in the saturated soil. Comparisons of the measured accelerations for the different superstructures are shown in Figures 5.9b and 5.9d. The embedded pore pressure transducers captured the change in the excess pore water pressure during the experiments, as shown in Figure 5.9c.

Strains were recorded at the level of the instrumented coupler (Figure 5.9a) and the settlements of the AMD are shown in Figure 5.10a for the three subsequent tests. Figure 5.10b shows the change in natural frequency during the progression of the experiments, which gradually decreased until it reached approximately 4Hz, after which no significant change was observed. The settlement progression for all consecutive experiments is presented in Figure 5.10c. The magnitude of the AMD settlement reached a limit value of 0.6in and was measured at two points (east and west side) of the platform. Significant settlement was only observed in trials containing strong ground motions.

In order to investigate the liquefaction potential for different superstructures, the cyclic stress ratio (CSR) was calculated from the obtained experimental data [142] using the following equation:

$$\mathrm{CSR} = \frac{\tau_{\mathrm{cyc}}}{\sigma'_{\mathrm{vo}}} = 0.65 a_{\max} \frac{\sigma_{\mathrm{vo}}}{\sigma'_{\mathrm{vo}}} \left(\frac{W_{\mathrm{L}} + W_{\mathrm{S}}}{W_{\mathrm{S}}}\right) \tag{5.1}$$

Where $a_{\max}$ is the maximum acceleration of each soil layer and σ_{vo} and σ'_{vo} are the total overburden pressure and the initial effective overburden pressure on sand layer under consideration respectively. The CSR value was then multiplied by the ratio of the sum of the weight of the laminar box laminate and the weight of the soil of the specific layer over

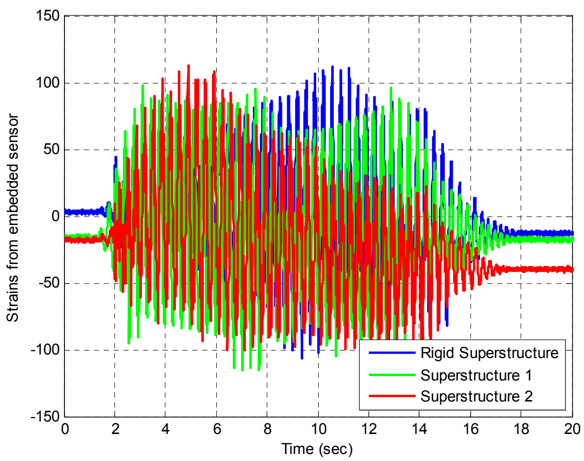

(a) Strains from embedded sensor at 3ft depth

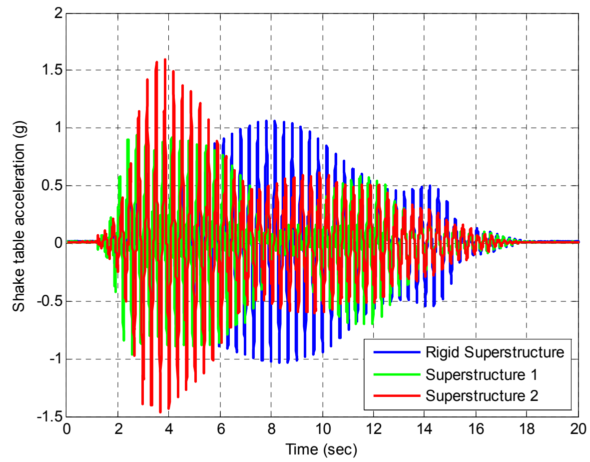

(b) AMD acceleration

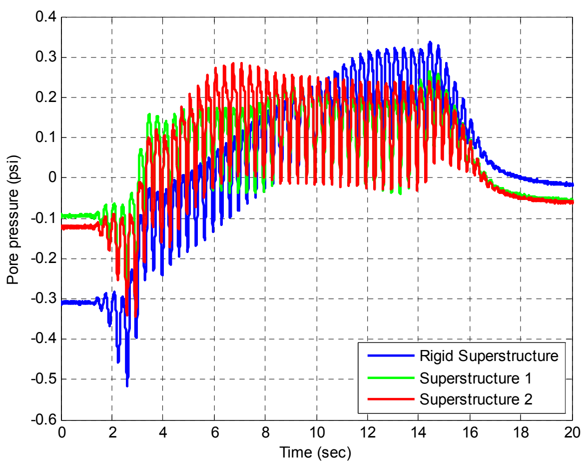

(c) Pore pressures at 10ft

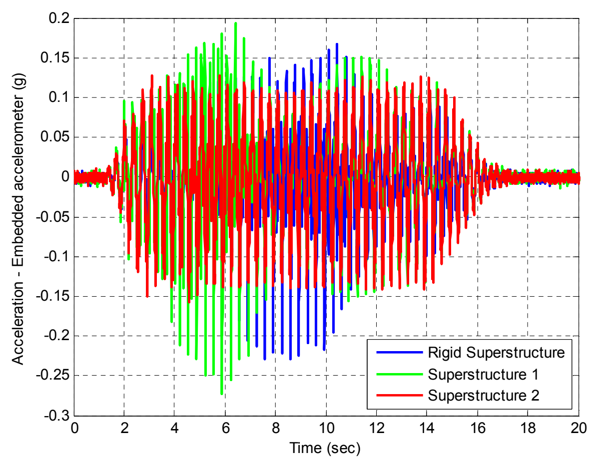

(d) Acceleration from embedded accelerometer at 3ft depth

Figure 5.9: Experimental results

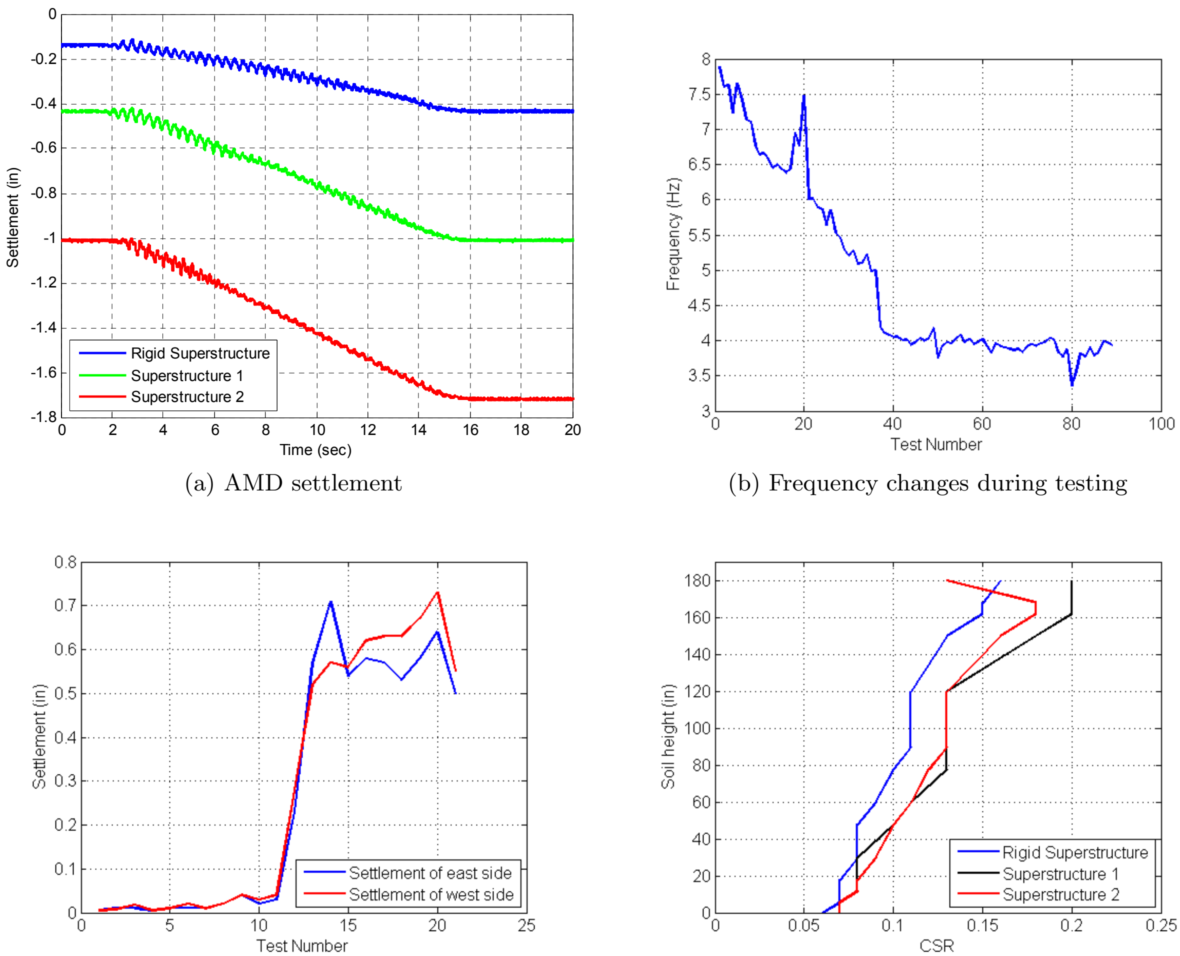

(a) AMD settlement

(b) Frequency changes during testing

(c) Settlement progression during testing

(d) CSR values for consecutive tests

Figure 5.10: Experimental results

the weight of the soil. The soil properties used in this calculation were obtained from a combination of CPT testing and utilizing empirical relationships developed from previous testing in the laminar box. For the specific soil properties and number of testing cycles, the onset of liquefaction will occur at CSR values of 0.2.

Figure 5.10d shows the different CSR values for three different superstructures. The case of the rigid superstructure provides a base case for comparison. Conventional design methodologies often neglect SFSI as they consider it to be beneficial or negligible in terms of energy dissipation; therefore ignoring it is conservative [143]. However this approach does not account for the full behavior of the multiphase system. In the case of superstructure 1, the CSR in the upper layer of the soil reaches the 0.2 limit, indicating that liquefaction has occurred and that excitation past this point would result in catastrophic failure.

Furthermore, the accelerograms (Figures 5.9b and 5.9d) recorded in both the soil and at the AMD for this trial shows a higher peak acceleration compared to the rigid case. The case of superstructure 2 exhibits an equally interesting response including a higher CSR and acceleration at the AMD. The acceleration recorded in 3ft into the soil is much less in this case, however, highlighting the nonlinearity associated with SFSI. These results show that SFSI has a significant impact on the behavior of the system and that it cannot be neglected due to the complex boundary conditions and limit states involved.

5.5 Future research and goals on SFSI DS

It is shown that dynamic substructuring of soil-foundation-superstructure interaction is viable and that interaction with the superstructure can significantly influence soil-foundation response. Active control of the interface will enable more realistic representation of superstructure dynamics and quantification of the effect of interaction under transient conditions.

Experiments on a simplified model, described in Chapter 4, show that using a simple control design approach, robustly stable and accurate dynamic substructuring testing is possible. Hence, this approach could be used to facilitate more complex experiments involving actual soil and foundation systems. This will lead to a better understanding of the mechanics that drive critical SFSI scenarios.

Chapter 6

Summary and concluding remarks

The study presented herein focuses on the development of an effective approach for dynamic substructuring experiments, conceptually different than conventionally used approaches. It involves a simple feedfoward strategy of designing an adequate controller, eliminating the need to use a tracking controller and an explicit compensator for the inherent dynamics of the hydraulic system used. In addition to this, the performance of substructuring is not dependent on specialized numerical integration schemes and their properties.

Experiments performed using the developed strategy demonstrate robust stability and accuracy. As described in Chapter 4, two different configurations are considered during testing, (i) one with the active mass driver (AMD) mimicking the numerical substructure and (ii) one with the AMD sitting on elastomeric bearings, simulating the case when a superstructure is placed on top of a flexible physical subsystem. Similar experiments are performed for both configurations, for which the controller is designed to match the base shear of the virtual superstructures.

For the first configuration, a wide range of single degree of freedom numerical substructures is tested, with fundamental frequencies varying from 2Hz to 40Hz and different damping ratios in the range of 1% to 5% of critical are examined. The comparison between the experimentally obtained data to the expected response is consistently good. Furthermore, it is shown by using a simple control design approach the numerical substructure could be sufficiently represented in the experiments. In addition to this, even for the case when valve saturation is observed, the experiments are performed successfully regardless of the presence of nonlinearity. Additional experiments are performed to emulate two degree of freedom numerical substructures, which are also carried out successfully. As a result it is reasonable to assume that this control strategy can also perform well for higher order numerical substructures. The results are also satisfying for different values of ΔP gains.

With the second configuration, which consisted of the AMD and the flexible physical subsystem, single degree of freedom numerical substructures are emulated, with fundamental frequencies of 5Hz, 7Hz and 10Hz frequency and damping 5% of critical. For these experiments, the numerical substructure is also sufficiently represented.

It is evident that with this simple control design strategy can be used to accurately perform dynamic substructuring experiments. However, it should be mentioned that for the cases when the controller is non causal or when an integrator is present action has to be taken to make the controller proper.

Even though the experiments are successful in general, there are still some issues worth investigating further. Specifically, when the numerical substructure has low fundamental frequency the response of the emulated system does not match the expected behavior in high frequencies. This effect is reduced when the ΔP gain is high, i.e. when the damping in the actuator is large, but this effect is still present. In addition to this, for some numerical substructures with low frequency and/or damping, the response is dominated by a stable limit cycle. This effect is a result of the nonlinearity in the hydraulic system caused by friction. As shown in Section 4.5.4, this effect is reduced for high ΔP gains.

The DS strategy developed here can be used to study more complex structures. The experiments can be performed with multiple actuators to control multiple degrees of freedom in multi-axis configuration in conjunction with more than one shake tables. In addition to this, it is feasible to perform experiments for which the AMD except for the control input can also provide the earthquake input. In such configuration, the use of the shake table would not be required. Such configurations are the subject work in the near future.

Apart from the dynamic substructuring applications, significant effort is made to characterize the testbed used to facilitate these experiments. More specifically, a small scale hydraulic shake table is designed and constructed and a detailed mathematical model is developed and validated through experiments to predict its behavior. Similarly, the behavior of the assembly consisting of the small shake table and the elastomeric bearings is sufficiently predicted with a detailed mathematical model and experimentally evaluated.

Finally, a novel experiment is designed and performed for the first time to test the feasibility of DS experiments in soil-foundation-structure systems. Using such experiments in combination with the strategy for DS developed here, the behavior of these complex systems can be investigated to obtain sufficiently rich experimental data to evaluate numerical models of complete soil-foundation-structure systems.

In summary, the contributions of this work are summarized as follows:

- **Development of a strategy for DS experiments with the following characteristics:**

  1. **The control design is simple and easy**

     – is a feedforward strategy

     – eliminates the use of a tracking controller, a compensator for actuator's inherent dynamics and complicated numerical schemes

     – application is almost trivial for linear systems, theoretical analysis shows it could be also used for more complex systems

  2. **Accurate representation of VS**

     – For both configurations tested (only AMD and AMD-PS) the experimental results matched well the expected response of the various VS: 1DOF and 2DOF VS with varying fundamental frequency and damping ratio

  3. **Method is robustly stable**

     – The results are consistently good even in the case when nonlinearities are present in the system, or when the model used to design the controller is not accurate enough

4. **The physical subsystem does not have an effect on the design of the controller**
   - The actuator with the control can be compared with the virtual subsystem independently of the physical subsystem

- **Development and characterization of testbed**
  - Small scale shake table designed and constructed to be used as an active mass driver (AMD)
  - Elastomeric bearings assembly designed and constructed
  - Development of accurate mathematical model of the testbed (AMD-PS) through extensive experiments
- **Novel SFSI experiment for DS applications**
  - Design of experiment on geotechnical laminar box
  - Preliminary results to support future work

References

[1] Sanchez Ferreira JA. Stability of elastomeric bearings for seismic applications. MS Thesis, University at Buffalo 2010, University at Buffalo.

[2] Warn GP. The coupled horizontal-vertical response of elastomeric and lead-rubber seismic isolation bearings. PhD Thesis, University at Buffalo 2006.

[3] Reinhorn AM, Sivaselvan MV, Liang Z, Shao X. Real-time dynamic hybrid testing of structural systems. *Proceedings of the 13th World Conference on Earthquake Engineering*, 2004.

[4] Shing PB, Nakashima M, Bursi OS. Application of pseudodynamic test method to structural research. *Earthquake Spectra* 1996; **12**(1):29–56.

[5] Mahin SA, Shing PSB, Thewalt CR, Hanson RD. Pseudodynamic test method - current status and future-directions. *Journal of Structural Engineering-ASCE* 1989; **115**(8):2113–2128.

[6] Gawthrop PJ, Wallace MI, Wagg DJ. Bond-graph based substructuring of dynamical systems. *Earthquake Engineering & Structural Dynamics* 2005; **34**(6):687–703.

[7] Murray JA, Sasani M, Shao X. Hybrid simulation for system-level structural response. *Engineering Structures* 2015; **103**:228–238.

[8] Shao X, Griffith C. An overview of hybrid simulation implementations in NEES projects. *Engineering Structures* 2013; **56**:1439–1451.

[9] McCrum DP, Williams MS. An overview of seismic hybrid testing of engineering structures. *Engineering Structures* 2016; **118**:240–261.

[10] Hilber HM, Hughes TJR, Taylor RL. Improved numerical dissipation for time integration algorithms in structural dynamics. *Earthquake Engineering & Structural Dynamics* 1977; **5**(3):283–292.

[11] Bonelli A, Bursi OS. Generalized-alpha methods for seismic structural testing. *Earthquake Engineering & Structural Dynamics* 2004; **33**(10):1067–1102.

[12] Bursi O, He L, Lamarche C, Bonelli A. Linearly implicit time integration methods for real-time dynamic substructure testing. *Journal of Engineering Mechanics* 2010; **136**(11):1380–1389.

[13] Bursi OS, Gonzalez-Buelga A, Vulcan L, Neild SA, Wagg DJ. Novel coupling Rosenbrock-based algorithms for real-time dynamic substructure testing. *Earthquake Engineering & Structural Dynamics* 2008; **37**(3):339–360.

[14] Bursi OS, Jia C, Vulcan L, Neild SA, Wagg DJ. Rosenbrock-based algorithms and subcycling strategies for real-time nonlinear substructure testing. *Earthquake Engineering & Structural Dynamics* 2011; **40**(1):1–19.

[15] Shing PB, Spacone E, Stauffer E. Conceptual design of fast hybrid test system at the University of Colorado. *7th U.S. National Conference on Earthquake Engineering*, 2002.

[16] Chen C, Ricles JM. Analysis of implicit HHT-α integration algorithm for real-time hybrid simulation. *Earthquake Engineering & Structural Dynamics* 2012; **41**(5):1021–1041.

[17] Ou G, Prakash A, Dyke S. Modified Runge-Kutta integration algorithm for improved stability and accuracy in real time hybrid simulation. *Journal of Earthquake Engineering* 2015; **19**(7):1112–1139.

[18] Combescure D, Pegon P. α-operator splitting time integration technique for pseudo-dynamic testing - error propagation analysis. *Soil Dynamics And Earthquake Engineering* 1997; **16**(7-8):427–443.

[19] Zhang YF, Sause R, Ricles JA, Naito CJ. Modified predictor-corrector numerical scheme for real-time pseudo dynamic tests using state-space formulation. *Earthquake Engineering & Structural Dynamics* 2005; **34**(3):271–288.

[20] Wu B, Xu G, Wang Q, Williams MS. Operator-splitting method for real-time substructure testing. *Earthquake Engineering & Structural Dynamics* 2006; **35**(3):293–314.

[21] Kolay C, Ricles JM, Marullo TM, Mahvashmohammadi A, Sause R. Implementation and application of the unconditionally stable explicit parametrically dissipative kr method for realtime hybrid simulation. *Earthquake Engineering & Structural Dynamics* 2015; **44**(5):735–755.

[22] Mosqueda G, Ahmadizadeh M. Iterative implicit integration procedure for hybrid simulation of large nonlinear structures. *Earthquake Engineering & Structural Dynamics* 2011; **40**(9):945–960.

[23] Pegon P, Pinto AV. Pseudo-dynamic testing with substructuring at the ELSA laboratory. *Earthquake Engineering & Structural Dynamics* 2000; **29**(7):905–925.

[24] Shing PSB, Vannan MT, Cater E. Implicit time integration for pseudodynamic tests. *Earthquake Engineering & Structural Dynamics* 1991; **20**(6):551–576.

[25] Chen C, Ricles JM. Stability analysis of SDOF realtime hybrid testing systems with explicit integration algorithms and actuator delay. *Earthquake Engineering & Structural Dynamics* 2008; **37**(4):597–613.

[26] Nakashima M, Kato H, Takaoka E. Development of real-time pseudo dynamic testing. *Earthquake Engineering & Structural Dynamics* 1992; **21**(1):79–92.

[27] Shing PB, Wei Z, Jung RY, Stauffer E. NEES fast hybrid test system at the University of Colorado. *Proceedings of the 13th World Conference on Earthquake Engineering*, 2004.

[28] Bayer V, Dorka UE, Fullekrug U, Gschwilm J. On real-time pseudo-dynamic substructure testing: algorithm, numerical and experimental results. *Aerospace Science And Technology* 2005; **9**(3):223–232.

[29] Sivaselvan M. A unified view of hybrid simulation algorithms. *NEES Hybrid Simulation Workshop, Berkeley, California, USA*, 2006.

[30] Horiuchi T, Inoue M, Konno T, Namita Y. Real-time hybrid experimental system with actuator delay compensation and its application to a piping system with energy absorber. *Earthquake Engineering & Structural Dynamics* 1999; **28**(10):1121–1141.

[31] Horiuchi T, Konno T. A new method for compensating actuator delay in real-time hybrid experiments. *Philosophical Transactions of The Royal Society of London Series A-Mathematical Physical and Engineering Sciences* 2001; **359**(1786):1893–1909.

[32] Nakashima M, Masaoka N. Real-time on-line test for MDOF systems. *Earthquake Engineering & Structural Dynamics* 1999; **28**(4):393–420.

[33] Darby AP, Blakeborough A, Williams MS. Real-time substructure tests using hydraulic actuator. *Journal of Engineering Mechanics-ASCE* 1999; **125**(10):1133–1139.

[34] Darby AP, Blakeborough A, Williams MS. Improved control algorithm for real-time substructure testing. *Earthquake Engineering & Structural Dynamics* 2001; **30**(3):431–448.

[35] Darby AP, Williams MS, Blakeborough A. Stability and delay compensation for real-time substructure testing. *Journal of Engineering Mechanics-ASCE* 2002; **128**(12):1276–1284.

[36] Blakeborough A, Williams MS, Darby AP, Williams DM. The development of real-time substructure testing. *Philosophical Transactions of The Royal Society of London Series A-Mathematical Physical And Engineering Sciences* 2001; **359**(1786):1869–1891.

[37] Nakashima M. Development, potential, and limitations of real-time online (pseudo-dynamic) testing. *Philosophical Transactions of The Royal Society of London Series A-Mathematical Physical and Engineering Sciences* 2001; **359**(1786):1851–1867.

[38] Wallace MI, Wagg DJ, Neild SA. An adaptive polynomial based forward prediction algorithm for multi-actuator real-time dynamic substructuring. *Proceedings of the Royal Society A-Mathematical, Physical and Engineering Sciences* 2005; **461**(2064):3807–3826.

[39] Chen PC, Tsai KC. Dual compensation strategy for real-time hybrid testing. *Earthquake Engineering & Structural Dynamics* 2013; **42**(1):1–23.

[40] Chen PC, Tsai KC, Lin PY. Real-time hybrid testing of a smart base isolation system. *Earthquake Engineering & Structural Dynamics* 2014; **43**(1):139–158.

[41] Mercan O, Ricles JM. Stability and accuracy analysis of outer loop dynamics in real-time pseudodynamic testing of SDOF systems. *Earthquake Engineering & Structural Dynamics* 2007; **36**(11):1523–1543.

[42] Ahmadizadeh M, Mosqueda G, Reinhorn AM. Compensation of actuator delay and dynamics for real-time hybrid structural simulation. *Earthquake Engineering & Structural Dynamics* 2008; **37**(1):21–42.

[43] Gonzalez-Buelga A, Wagg DJ, Neild SA. Parametric variation of a coupled pendulum-oscillator system using real-time dynamic substructuring. *Structural Control and Health Monitoring* 2007; **14**(7):991–1012.

[44] Kyrychko YN, Blyuss KB, Gonzalez-Buelga A, Hogan SJ, Wagg DJ. Real-time dynamic substructuring in a coupled oscillator-pendulum system. *Proceedings: Mathematical, Physical and Engineering Sciences* 2006; **462**(2068):1271–1294.

[45] Wallace MI, Sieber J, Neild SA, Wagg DJ, Krauskopf B. Stability analysis of real-time dynamic substructuring using delay differential equation models. *Earthquake Engineering & Structural Dynamics* 2005; **34**(15):1817–1832.

[46] Pan P, Tada M, Nakashima M. Online hybrid test by internet linkage of distributed test-analysis domains. *Earthquake Engineering & Structural Dynamics* 2005; **34**(11):1407–1425.

[47] Peterson LD. The nonlinear coupled dynamics of fluids and spacecraft in low gravity. PhD Thesis Massachusetts Institute of Technology, 1987.

[48] Plummer AR. Model-in-the-loop testing. *Proceedings of the Institution of Mechanical Engineers, Part I: Journal of Systems and Control Engineering* 2006; **220**(3):183–199.

[49] Carrion JE, Spencer Jr BF. Model-based strategies for real-time hybrid testing. *Technical Report 1940-9826*, Newmark Structural Engineering Laboratory. University of Illinois at Urbana-Champaign. 2007.

[50] Liu J, Dyke SJ, Liu HJ, Gao XY, Phillips B. A novel integrated compensation method for actuator dynamics in real-time hybrid structural testing. *Structural Control and Health Monitoring* 2013; **20**(7):1057–1080.

[51] Gawthrop PJ, Wallace MI, Neild SA, Wagg DJ. Robust real-time substructuring techniques for under-damped systems. *Structural Control and Health Monitoring* 2007; **14**(4):591–608.

[52] Doyle J, Francis B, Tannenbaum A. Feedback control theory, 1992. *Maxwell Communication Group, New York* 2001; .

[53] Gawthrop P. Emulator-based control for actuator-based hardware-in-the-loop testing. *Control Engineering Practice* 2008; **16**(8):897–908.

[54] Wagg DJ, Stoten DP. Substructuring of dynamical systems via the adaptive minimal control synthesis algorithm. *Earthquake Engineering & Structural Dynamics* 2001; **30**(6):865–877.

[55] Neild SA, Drury D, Stoten DP. An improved substructuring control strategy based on the adaptive minimal control synthesis control algorithm. *Proceedings of the Institution of Mechanical Engineers, Part I: Journal of Systems and Control Engineering* 2005; **219**(5):305–317.

[56] Neild SA, Stoten DP, Drury D, Wagg DJ. Control issues relating to real-time substructuring experiments using a shaking table. *Earthquake Engineering & Structural Dynamics* 2005; **34**(9):1171–1192.

[57] Stoten DP, Hyde RA. Adaptive control of dynamically substructured systems: The single-input single-output case. *Proceedings of the Institution of Mechanical Engineers, Part I: Journal of Systems and Control Engineering* 2006; **220**(2):63–79.

[58] Bonnet PA, Lim CN, Williams MS, Blakeborough A, Neild SA, Stoten DP, Taylor CA. Real-time hybrid experiments with Newmark integration, MCSmd outer-loop control and multi-tasking strategies. *Earthquake Engineering & Structural Dynamics* 2007; **36**(1):119–141.

[59] Phillips B, Spencer B. Model-based multiactuator control for real-time hybrid simulation. *Journal of Engineering Mechanics* 2013; **139**(2):219–228.

[60] Gao X, Castaneda N, Dyke SJ. Real time hybrid simulation: from dynamic system, motion control to experimental error. *Earthquake Engineering & Structural Dynamics* 2013; **42**(6):815–832.

[61] Ou G, Ozdagli AI, Dyke SJ, Wu B. Robust integrated actuator control: experimental verification and realtime hybridsimulation implementation. *Earthquake Engineering & Structural Dynamics* 2015; **44**(3):441–460.

[62] Guang L, Herrmann G, Stoten DP, Jiaying T, Turner MC. Application of robust antiwindup techniques to dynamically substructured systems. *Mechatronics, IEEE/ASME Transactions on* 2013; **18**(1):263–272.

[63] Li G, Stoten DP, Tu JY. Model predictive control of dynamically substructured systems with application to a servohydraulically actuated mechanical plant. *Control Theory & Applications, IET* 2010; **4**(2):253–264.

[64] Li G. Dynamically substructured system frameworks with strict separation of numerical and physical components. *Structural Control and Health Monitoring* 2014; **21**(10):1316–1333.

[65] Elorza I. Advances beyond transfer system dynamics compensation in real-time dynamic substructuring tests. *International Journal of Control* 2012; **85**(3):304–319.

[66] Tu JY. Development of numerical-substructure-based and output-based substructuring controllers. *Structural Control and Health Monitoring* 2013; **20**(6):918–936.

[67] Tu JY, Yang HT, Lin PY, Chen PC. Dynamics, control and real-time issues related to substructuring techniques: application to the testing of isolated structure systems. *Proceedings of the Institution of Mechanical Engineers, Part I: Journal of Systems and Control Engineering* 2013; **227**(6):507–522.

[68] Tu JY, Jiang JY. Substructurability and exact synchronisation analysis. *Structural Control and Health Monitoring* 2013; **20**(12):1410–1423.

[69] Chae Y, Kazemibidokhti K, Ricles JM. Adaptive time series compensator for delay compensation of servo-hydraulic actuator systems for real-time hybrid simulation. *Earthquake Engineering & Structural Dynamics* 2013; **42**(11):1697–1715.

[70] Ching IH, Chen-Yu C, Jia-Ying T. The method of identifying the dominative substructure for dynamically substructured systems. *System Theory, Control and Computing (ICSTCC), 2015 19th International Conference on*; 539–544.

[71] Mosqueda G, Stojadinovic B, Mahin S. Real-time error monitoring for hybrid simulation. part I: Methodology and experimental verification. *Journal of Structural Engineering* 2007; **133**(8):1100–1108.

[72] Guo T, Chen C, Xu W, Sanchez F. A frequency response analysis approach for quantitative assessment of actuator tracking for real-time hybrid simulation. *Smart Materials and Structures* 2014; **23**(4):045 042.

[73] Maghareh A, Dyke SJ, Prakash A, Bunting GB. Establishing a predictive performance indicator for real-time hybrid simulation. *Earthquake Engineering & Structural Dynamics* 2014; **43**(15):2299–2318.

[74] Chen C, Sanchez F, Khan M. *Effect of Actuator Delay on Real-Time Hybrid Simulation Involving Multiple Experimental Substructures*. Springer International Publishing: Cham, 2015; 9–17.

[75] Igarashi A, Iemura H, Suwa T. Development of substructured shaking table test method. *Proceedings of the 12th World Conference on Earthquake Engineering*, 2000.

[76] Igarashi A, Iemura H, Tanaka H, Tsuruta D. Experimental simulation of coupled response of structural systems using the substructure hybrid shake table test method. *13th World Conference on Earthquake Engineering, Vancouver, Canada*, 2004.

[77] Lee SK, Park EC, Min KW, Park JH. Real-time substructuring technique for the shaking table test of upper substructures. *Engineering Structures* 2007; **29**(9):2219–2232.

[78] Ji X, Kajiwara K, Nagae T, Enokida R, Nakashima M. A substructure shaking table test for reproduction of earthquake responses of high-rise buildings. *Earthquake Engineering & Structural Dynamics* 2009; **38**(12):1381–1399.

[79] Günay M, Mosalam K. Investigation of the response of electrical insulator posts using real-time hybrid simulation on a smart shaking table. *Proc., 15th World Conf. Earthquake Engineering (15WCEE), International Association for Earthquake Engineering (IAEE), Lisbon, Portugal*, 2012.

[80] Mosalam KM, Günay S. Seismic performance evaluation of high voltage disconnect switches using real-time hybrid simulation: I. System development and validation. *Earthquake Engineering & Structural Dynamics* 2014; **43**(8):1205–1222.

[81] Günay S, Mosalam KM. Seismic performance evaluation of high-voltage disconnect switches using real-time hybrid simulation: II. Parametric study. *Earthquake Engineering & Structural Dynamics* 2014; **43**(8):1223–1237.

[82] Günay S, Mosalam KM. Enhancement of real-time hybrid simulation on a shaking table configuration with implementation of an advanced control method. *Earthquake Engineering & Structural Dynamics* 2015; **44**(5):657–675.

[83] Zhang R, Lauenstein PV, Phillips BM. Real-time hybrid simulation of a shear building with a uni-axial shake table. *Engineering Structures* 2016; **119**:217–229.

[84] Sivaselvan MV, Reinhorn AM, Shao X, Weinreber S. Dynamic force control with hydraulic actuators using added compliance and displacement compensation. *Earthquake Engineering & Structural Dynamics* 2008; **37**(15):1785–1800.

[85] Shao X, Reinhorn AM, Sivaselvan MV. Real-time hybrid simulation using shake tables and dynamic actuators. *Journal of Structural Engineering* 2010; **137**(7):748–760.

[86] Nakata N, Stehman M. Substructure shake table test method using a controlled mass: formulation and numerical simulation. *Earthquake Engineering & Structural Dynamics* 2012; **41**(14):1977–1988.

[87] Wang Q, Wang JT, Jin F, Chi FD, Zhang CH. Real-time dynamic hybrid testing for soilstructure interaction analysis. *Soil Dynamics and Earthquake Engineering* 2011; **31**(12):1690–1702.

[88] De Silva CW. *Control sensors and actuators*, vol. 6. Prentice Hall Englewood Cliffs, NJ, 1989.

[89] Dyke S, Spencer Jr B, Quast P, Sain M. Role of control-structure interaction in protective system design. *Journal of Engineering Mechanics* 1995; **121**(2):322–338.

[90] Spencer BF, Dyke SJ, Deoskar HS. Benchmark problems in structural control: part iactive mass driver system. *Earthquake Engineering & Structural Dynamics* 1998; **27**(11):1127–1139.

[91] MTS. 244 MTS Actuator. URL `www.mts.com/cs/groups/public/documents/library/dev_002093.pdf`.

[92] Blondet M, Esparza C. Analysis of shaking table-structure interaction effects during seismic simulation tests. *Earthquake Engineering & Structural Dynamics* 1988; **16**(4):473–490.

[93] Conte JP, Trombetti TL. Linear dynamic modeling of a uni-axial servo-hydraulic shaking table system. *Earthquake Engineering & Structural Dynamics* 2000; **29**(9):1375–1404.

[94] Rinawi AM. *Shaking table-structure interaction*. Report (University of California, Berkeley. Earthquake Engineering Research Center), Earthquake Engineering Research Center, University of California at Berkeley, 1991.: [Berkeley Calif.].

[95] Merritt HE. *Hydraulic control systems*. New York: Wiley, 1967.

[96] MTS. 252 MTS Servovalve. URL http://www.mts.com/cs/groups/public/documents/library/mts_004922.pdf.

[97] Structural Engineering and Earthquake Simulation Laboratory (SEESL), Geotechnical laminar box. URL http://nees.buffalo.edu/Facilities/Major_Equipment/laminarbox.asp.

[98] Structural Engineering and Earthquake Simulation Laboratory (SEESL), Shake tables. URL http://nees.buffalo.edu/Facilities/Major_Equipment/shaketables.asp.

[99] Servovalve MOOG ; URL http://www.moog.com/literature/ICD/760seriesvalves.pdf.

[100] ABAQUS. ABAQUS - Dassault Systemes. URL http://www.3ds.com/products-services/simulia/products/abaqus/.

[101] IKO. Linear way H bearings. URL http://ikont.com/linear-guides/ball-type-linear-motion-rolling-guides#linear-way.

[102] Shore Western Swivels 981. URL http://www.shorewestern.com/VibeTables.php.

[103] MTS. 249 MTS Swivels ; URL https://www.mts.com/cs/groups/public/documents/library/dev_002128.pdf.

[104] MTS. 601.11 Spiral washers. URL http://www.mts.com/ucm/groups/public/documents/library/dev_003828.pdf.

[105] Kumar M. Seismic isolation of nuclear power plants using elastomeric bearings, University at Buffalo. PhD Thesis 2015.

[106] Reinhorn A, Bruneau M, Whittaker A, Constantinou M, Thevanayagam S, Sivaselvan M, Shao X, Hanley J, Pitman M, Albrechcinski T. The UB-NEES versatile high performance testing facility. *13th World Conference on Earthquake Engng, Vancouver, BC, Canada, August 1*, vol. 6.

[107] Murray RM, Li Z, Sastry SS, Sastry SS. *A mathematical introduction to robotic manipulation*. CRC press, 1994.

[108] Constantinou MC, Whittaker AS, Kalpakidis Y, Fenz DM, Warn GP. Performance of seismic isolation hardware under service and seismic loading. *Report*, MCEER 2007.

[109] National Instruments LabVIEW - Real-Time Module ; URL `http://www.ni.com/labview/realtime/`.

[110] National Instruments - Command-based Communication Using Simple TCP/IP Messaging. URL `http://www.ni.com/white-paper/3098/en/`.

[111] Qt Toolkit website. URL `https://www.qt.io/`.

[112] Schoukens J, Pintelon R, Rolain Y. *Mastering system identification in 100 exercises*. Wiley: Hoboken, NJ, 2012.

[113] Guillaume P, Verboven P, Vanlanduit S, Parloo E. Multisine excitations - new developments and applications in modal analysis. *SEM*; 1543–1549.

[114] Dyke SJ, Spencer BF, Quast P, Kaspari DC, Sain MK. Implementation of an active mass driver using acceleration feedback control. *Computer-Aided Civil and Infrastructure Engineering* 1996; **11**(5):305–323.

[115] Silverman LM. Inversion of multivariable linear systems. *Automatic Control, IEEE Transactions on* 1969; **14**(3):270–276.

[116] Mehra RK. Inversion of multivariable linear dynamic systems using optimum smoothing. *Automatic Control, IEEE Transactions on* 1970; **15**(2):252–252.

[117] Sain MK, Massey JL. Invertibility of linear time-invariant dynamical systems. *Automatic Control, IEEE Transactions on* 1969; **14**(2):141–149.

[118] Chen DG, Paden B. Stable inversion of nonlinear non-minimum phase systems. *International Journal of Control* 1996; **64**(1):81–97.

[119] Devasia S, Degang C, Paden B. Nonlinear inversion-based output tracking. *Automatic Control, IEEE Transactions on* 1996; **41**(7):930–942.

[120] Moore B, Silverman LM. Model matching by state feedback and dynamic compensation. *Automatic Control, IEEE Transactions on* 1972; **17**(4):491–497.

[121] Franklin GF, Powell JD, Emami-Naeini A. *Feedback control of dynamic systems.* 5th edn., Pearson Prentice Hall: Upper Saddle River, N.J., 2006.

[122] Brockett RW. Poles, zeros, and feedback: State space interpretation. *Automatic Control, IEEE Transactions on* 1965; **10**(2):129–135.

[123] Arulanandan K, Scott RF. Project VELACScontrol test results. *Journal of Geotechnical Engineering* 1993; **119**(8):1276–1292.

[124] Taylor RN. Geotechnical centrifuge technology. *Blackie Academic and Professional*, vol. 1st edition.

[125] Boulanger RW, Curras CJ, Kutter BL, Wilson DW, Abghari A. Seismic soil-pile-structure interaction experiments and analyses. *Journal of Geotechnical and Geoenvironmental Engineering* 1999; **125**(9):750–759.

[126] Curras CJ, Boulanger RW, Kutter BL, Wilson DW. Dynamic experiments and analyses of a pile-group-supported structure. *Journal of Geotechnical and Geoenvironmental Engineering* 2001; **127**(7):585–596.

[127] Abdoun T, Dobry R, O'Rourke TD, Goh SH. Pile response to lateral spreads: Centrifuge modeling. *Journal of Geotechnical and Geoenvironmental Engineering* 2003; **129**(10):869–878.

[128] Madabhushi SPG, Lawson CH. Centrifuge modelling-based verification of response spectra design methods for some vulnerable structures. *Geotechnical & Geological Engineering* ; **24**(4):793–808.

[129] Mason HB, Trombetta NW, Chen Z, Bray JD, Hutchinson TC, Kutter BL. Seismic soilfoundationstructure interaction observed in geotechnical centrifuge experiments. *Soil Dynamics and Earthquake Engineering* 2013; **48**:162–174.

[130] Bolisetti C, Whittaker AS. Site response, soil-structure interaction and structure-soil-structure interaction for performance assessment of buildings and nuclear structures. *Report* 2015.

[131] Madabhushi SPG, Schofield AN. Centrifuge modeling of tower structures on saturated sands subjected to earthquake perturbations 1993.

[132] Madabhushi SPG, Haigh SK. Effect of superstructure stiffness on liquefaction-induced failure mechanisms. *International Journal of Geotechnical Earthquake Engineering* 2010; **1**(1):70–87.

[133] Pak RYS, Soudkhah M, Ashlock JC. Dynamic behavior of a square foundation in planar motion on a sand stratum. *Soil Dynamics and Earthquake Engineering* 2012; **42**:151–160.

[134] Shirato M, Nonomura Y, Fukui J, Nakatani S. Large-scale shake table experiment and numerical simulation on the nonlinear behavior of pile-groups subjected to large-scale earthquakes. *Soils and Foundations* 2008; **48**(3):375–396.

[135] Massimino MR, Maugeri M. Physical modelling of shaking table tests on dynamic soilfoundation interaction and numerical and analytical simulation. *Soil Dynamics and Earthquake Engineering* 2013; **49**:1–18.

[136] Chau KT, Shen CY, Guo X. Nonlinear seismic soilpilestructure interactions: Shaking table tests and fem analyses. *Soil Dynamics and Earthquake Engineering* 2009; **29**(2):300–310.

[137] Tang L, Ling X, Xu P, Gao X, Wang D. Shake table test of soil-pile groups-bridge structure interaction in liquefiable ground. *Earthquake Engineering and Engineering Vibration* 2013; **9**(1):39–50.

[138] Gao X, Ling Xz, Tang L, Xu Pj. Soilpile-bridge structure interaction in liquefying ground using shake table testing. *Soil Dynamics and Earthquake Engineering* 2011; **31**(7):1009–1017.

[139] Luco JE, Trifunac MD, Wong HL. Isolation of soil-structure interaction effects by full-scale forced vibration tests. *Earthquake Engineering & Structural Dynamics* 1988; **16**(1):1–21.

[140] Ashlock JC, Fotouhi MK. Characterization of dynamic soil-pile interaction by random vibration methods: Experimental design and preliminary results. *2011 NSF Engineering Research and Innovation Conference*.

[141] Wood SL, Anagnos T, Arduino P, Eberhard MO, Feneves GL, Finholt TA, Futrelle JM, Grant SK, Jeremic B, Kramer BL, *et al.*. Using NEES to investigate soil-foundation structure interaction. *Proceedings of the 13th World Conference on Earthquake Engineering*, Vancouver.

[142] Seed H, Idriss I, Arango I. Evaluation of liquefaction potential using field performance data. *Journal of Geotechnical Engineering* ; **109**(3):458–482.

[143] Wolf JP. *Dynamic soil-structure interaction*. Prentice Hall int., 1985.